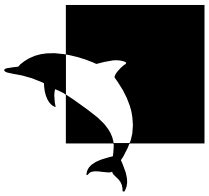

University of Southampton

UNIVERSITY OF SOUTHAMPTON
Faculty of Engineering, Science and Mathematics
Optoelectronics Research Centre

Optical Diffraction-Based Silicon Sensors for the Detection of DNA Sequences

Andrew Mark Weld

A thesis submitted for the degree of Doctor of Philosophy

29th June 2007

UNIVERSITY OF SOUTHAMPTON
ABSTRACT
FACULTY OF ENGINEERING, SCIENCES AND MATHEMATICS
SCHOOL OF THE OPTOELECTRONICS RESEARCH CENTRE
Doctor of Philosophy

Optical Diffraction-Based Silicon Sensors for the Detection of DNA Sequences

by Andrew Mark Weld

This thesis describes the design, fabrication and characterisation of diffraction-based sensors on silicon (100) substrates for the detection of complementary DNA sequences using colloidal gold labels. In-depth analysis of variations of DNA sequence within the human genome and association with diseases is expected to lead to personalised medical treatment. There is a great need for DNA analysis technologies and for techniques to determine whether sequence variations occur on the same chromosomal strand with applications in disease screening and diagnosis.

A novel optical diffraction grating sensor was developed with the aim of being able to detect successful hybridisation of complementary target DNA sequences featuring gold nanoparticle labels using diffraction. Silicon (100) substrates were patterned with DNA diffraction gratings. Subsequent hybridisation of gold nanoparticle-labelled complementary DNA sequences to those immobilised on the grating was observed by measuring the change in diffraction order intensities.

Diffraction theory was extended to model the situation of interlaced diffraction gratings and design the optimum diffraction grating pattern. An optical apparatus was developed for accurate sensor characterisation. DNA diffraction gratings were successfully realised on silicon and characterised. Hybridisation of gold nanoparticle-labelled complementary DNA was achieved and changes in diffraction were evaluated.

Novel two-dimensional diffraction structures are designed and fabricated. It is shown that two-dimensional diffraction approaches may potentially offer multiplexing of DNA detection assays.

Contents

List of Tables

List of Figures

Declaration of Authorship

I, Andrew Mark Weld

Declare that the thesis entitled

Optical Diffraction-Based Silicon Sensors for the Detection of DNA Sequences

and the work presented in it are my own. I confirm that:

- This work was done wholly or mainly while in candidature for a research degree at this University;
- Where any part of this thesis has previously been submitted for a degree or any other qualification at this University or any other institution, this has been clearly stated;
- Where I have consulted the published work of others, this is always clearly attributed;
- Where I have quoted from the work of others, the source is always given. With the exception of such quotation, this thesis is entirely my own work;
- I have acknowledged all main sources of help;
- Where the thesis is based on work done by myself jointly with others, I have made clear exactly what was done by others and what I have contributed myself;
- None of this work has been published before submission

Signed: .....

Date: .....

Nota Bene - Comments on Thesis Content

Some of the details presented in this thesis are based on reconstructed information. The Mountbatten building, Highfield Campus, University of Southampton was devastated by a fire on the 30^{th} October 2005. The fire resulted in complete destruction of my office, including all of my laboratory record books containing details of over 3 years worth of PhD planning, calculations, experimental details, results, analysis and commentaries. Additional paper work, theory and experimental equipment details were also destroyed.

Consequently, only electronic files which I had backed-up have been used for the writing of my thesis. Whilst the main results were well-summarised as work progressed, some of the supporting work, accompanying protocols and fine experimental details are regrettably missing.

The fire also destroyed the cleanroom complex necessary for the fabrication and analysis of both biological and non-biological samples. The bio-laboratory (required for sample fabrication) and optics laboratory (containing the diffraction apparatus I developed for sample characterisation) were rendered unusable and the majority of equipment was damaged beyond use.

Acknowledgements

I would like to express my deepest gratitude to a number of very helpful people within the Optoelectronics Research Centre. It has been a wonderful experience to work in such a thriving research community. I wish to thank Professors James Wilkinson and Rob Eason for their guidance and intellectual input towards the project. I would like to thank Dr Stuart Russell and Dr Corin Gawith for the benefit of their technical skills, experience and wisdom.

I would like to thank technical staff Ed Weatherby and Mark Lessey for helping to make some of the experimental components used. I am grateful for the support of Dave Sager and Neil Sessions related to training on equipment and cleanroom procedures.

I would like to make a special thankyou to Dr Huabing Yin for her immense efforts in developing device fabrication procedures and for her endless encouragement and kind words. I'd also like to thank her for supplying fabrication details and protocols lost in the fire with my lab books. I wish to express my sincere appreciation for the support I have had from my supervisor Dr Tracy Melvin throughout my whole time in Southampton.

I wish to thank my family and friends for all their support, love and interest in what I do.

List of Abbreviations and Symbols

Abbreviation		Definition
1-D	-	One-dimensional
2-D	-	Two-dimensional
3-D	-	Three-dimensional
μCP	-	Micro-contact printing
A	-	Adenine
AFM	-	Atomic force microscope
B	-	B-type DNA conformation
BSA	-	Bovine serum albumin
C	-	Cytosine
CCD	-	Charge coupled device
DAE	-	Double anti-parallel even
DAO	-	Double anti-parallel odd
DCM	-	Dichloromethane
DE	-	Diffraction efficiency
DMF	-	Dimethylformamide
DNA	-	Deoxyribonucleic acid
DNP	-	Dinitrophenyl
DPN	-	Dip-pen nanolithography
DTT	-	Dithiothreitol
DX	-	Double crossover
EDC	-	1-Ethyl-3(3-dimethylaminopropyl)-carbodiimide
EDTA	-	Ethylenediamine tetra-acetic (acid)
EDX	-	Energy dispersive X-ray analysis
EM	-	Electromagnetic
FISH	-	Fluorescent in situ hybridisation
FRET	-	Forster resonant energy transfer
FT	-	Fourier transform
FWHM	-	Full-width half-maximum
G	-	Guanine
HF	-	Hydrofluoric (acid)
HRP	-	Horseradish peroxidase
ICP-MS	-	Inductively coupled plasma-mass spectroscopy
IFT	-	Inverse Fourier transform
LED	-	Light emitting diode
MAPL	-	Molecular assembly patterning by lift-off
mRNA	-	Messenger RNA
NHSS	-	N-hydroxysulfosuccinimide
NIL	-	Nano-imprint lithography
NVOC	-	Nitroveratryloxycarbonyl

OPL	-	Optical path length
OTS	-	Octydecyltrimethoxysilane
PBS	-	Phosphate-buffered saline
PCR	-	Polymerase chain reaction
PDMS	-	Poly-dimethyl siloxane
PEG	-	Poly-ethylene glycol
ppt	-	phosphinothricin
RNA	-	Ribonucleic acid
RT-PCR	-	Reverse transcription-polymerase chain reaction
SA	-	Streptavidin
SAM(s)	-	Self-assembled monolayer(s)
SEM	-	Scanning electron microscope
SERRS	-	Surface enhanced resonant Raman scattering
SERS	-	Surface enhanced Raman scattering
SNOM	-	Scanning near-field optical microscopy
SNP	-	Single nucleotide polymorphism
SNR	-	Signal-to-noise ratio
SPP	-	Surface plasmon polariton
SPR	-	Surface plasmon resonance
SPRI	-	Surface plasmon resonance imaging
T	-	Thymine
TMB	-	Tetramethyl-benzidine
TTN	-	Titin gene
U	-	Uracil
UANHS	-	Undecylenic acid N-hydroxysuccinimide ester
UV	-	Ultra violet (light)
Z	-	Z-type DNA conformation

Symbols		Definition [units]
a	-	Diffraction grating line-width $[m]$
b	-	Diffraction grating line-separation $[m]$
d	-	Diffraction grating period $[m]$
D_p	-	Diffraction plane separation $[m]$
$\underline{\mathbf{E}}$	-	Electric field amplitude $[V/m]$
e^-	-	Electron $[C]$
$\mathcal{F}$	-	Fourier transform operator
I	-	Intensity $[W/m^2]$
I_{input}	-	Incident laser intensity $[W/m^2]$
I_m	-	Intensity of diffraction order m $[W/m^2]$
I_{max}	-	Maximum intensity $[W/m^2]$
I_0	-	Maximum intensity $[W/m^2]$
$\underline{\mathbf{k}}$	-	Wave vector $[m^{-1}]$
m	-	Diffraction order
n	-	Refractive index
N	-	Number of grating lines
N_b	-	Number of nucleotide bases
$\underline{\mathbf{r}}$	-	Point of observation of EM wave $[m]$
r	-	Reflectivity coefficient
R	-	Reflected EM field amplitude $[V/m]$
$R(\theta)$	-	Reflected EM field amplitude with angular dependence $[V/m]$
R_p	-	Radius of particle $[m]$
R_{tot}	-	Total reflected EM field amplitude $[V/m]$
t	-	Time $[s]$
$T(x, y)$	-	Transmission function of aperture
T_m	-	Melting temperature $[^\circ C]$
u_p	-	Electric field amplitude at point of observation $[V/m]$
α	-	Angle [rad]
β	-	Envelope modulation parameter
γ	-	Angle [rad]
δ	-	Periodic modulation parameter
Δ	-	Total optical path length difference $[m]$
ΔDE	-	Change in diffraction efficiency
Δ_i	-	Path length difference on incidence $[m]$
Δ_m	-	Path length for diffracted beam $[m]$
Δn	-	Change in refractive index
ϵ	-	Standard error
λ	-	Wavelength of light $[m]$
λ_{peak}	-	Wavelength of peak reflected intensity $[m]$
ϕ	-	Phase difference between EM waves [rad]
ρ	-	Surface coverage
σ	-	Standard deviation
Σ	-	Summation
z	-	Length $[m]$

Chapter 1

Introduction

1.1 Introduction

DNA (deoxyribonucleic acid) is the material of which the chromosomes and genes of almost all living organisms are composed. The rapid analysis of genomic DNA is a key requirement for heritable disease detection in clinical and research samples. Gene sequencing has been the major goal driving DNA analysis technology for many years and the human genome has been almost completely mapped [1]. One of the next challenges is to correlate known sequence variations, in particular single nucleotide polymorphisms (SNPs), with disease susceptibility. Technological advances in recent years have led to the development of a variety of micro-devices for DNA sensing and analysis. However, because the quantity of DNA isolated from blood samples is low, current DNA analysis methods tend to require polymerase chain reaction (PCR) amplification of genomic DNA samples in order to attain a large enough quantity for detection.

There is therefore a need for more sensitive detection techniques which use smaller volumes of DNA. The aim of this thesis was to develop an optical diffraction-based sensor on a silicon substrate for the detection of complementary DNA sequences.

1.2 DNA Sensors

A range of techniques exist for DNA sensing and analysis, each of which has both advantages and limitations, as discussed below.

Microarrays consist of DNA sequences spotted in an array pattern, enabling multiplexing of up to 500 000 different sequences on one 'biochip' [2]. They typically rely on fluorescent labelling of DNA probes and have enabled parallel analysis of thousands of DNA sequences. However, the fluorescence intensity required for analysing DNA microarrays requires a relatively large quantity of DNA sample, and so PCR is required to amplify fragments of DNA and to incorporate fluorophores.

Sensitive techniques based on single molecule fluorescence have also been developed, for example Forster resonance energy transfer (FRET)[3] and fluorescent in-situ hybridisation (FISH)[4]. These enable the study of individual DNA strands. However, they are inappropriate for use where high-throughput is required in sequencing, or in a disease screening sensor, due to the time required and the laborious nature of targeting individual molecules.

Gold nanoparticles have been used as an alternative to fluorescent molecules as optical DNA probes. They offer better discrimination of single base-pair mismatches [5], and improved sensitivity of detection compared to fluorescent labels, particularly when used in conjunction with silver amplification [6].

Electrical detection of DNA has also been achieved using gold nanoparticle probes. DNA capture sequences are patterned between electrodes and then the target probe gold nanoparticles are hybridised. Generally, silver enhancement procedures are used to fill in the gaps and bridge the electrode, increasing the conductivity, as exemplified by the work by Mirkin *et al* [7]. A drawback of the technique is the need for post-probe binding amplification, rather than direct detection of the probe alone.

It would be advantageous to determine whether two (or more) known polymorphisms of the DNA sequence of a gene occur on the same chromosomal DNA strand as the presence of a number of SNPs within the same strand of a gene sequence defines a specific haplotype [8]. This is of particular significance when investigating the likelihood of a disease being inherited.

Although electrical detection offers excellent sensitivity for detecting the presence of two SNPs, there is not a possibility to extend this to identifying more than two sequences on the same strand in one measurement, since the presence of one or more sequences would result in the same outcome.

Optical methods may offer the advantage of being able to search for several SNPs within one strand simultaneously by using different sized nanoparticles which have different resonant wavelengths.

1.3 Interference-based Biosensors

Optical interference-based techniques have been developed enabling accurate measurement of small-scale changes, which can be exploited for detecting the presence of small biomolecules [9]. Small changes in optical properties are detectable by the effect they have on the propagation of light, for example, causing colour changes by interference, or changes to the spatial intensity distribution of light by diffraction. These changes are often detectable using relatively simple apparatus, and can be visible by eye. Some techniques which exploit interference effects for biomolecule sensing are discussed below.

Biomolecule sensing methods based on optical interference include scattering studies on cells, thin film interference, holographic polymers, diffraction gratings and surface plasmon diffraction [9–14]. Scattering studies carried out on bacterial colonies provide a quick method for identifying which strain is present by observing diffraction in transmission [12]. However, to obtain resolvable features at optical wavelengths, this method can only be applied for relatively large entities. Interference techniques have been used to detect DNA sequences by using the DNA to capture probes which are then used to develop precipitates; this generates a thin film causing interference of reflected light [9]. Whilst this is very sensitive and provides a colour indication of the DNA sequence having been present, there are a large number of steps involved in the process, rendering it time consuming and costly. Holographic polymers containing interference fringes from silver particles have proved very useful for chemical sensing and biomolecule detection [13]. In general, the presence of the analyte causes the holographic polymer to swell, changing the fringe separation distance and therefore altering the peak wavelength of reflection from the hologram. This has proved a sensitive and versatile detection method for bio-chemical sensing.

Sensors based on the principles of diffraction gratings for the detection of biomolecules have also been developed. When relatively large analytes, such as cells, are to be detected the increase in optical density and step height is sufficient to generate a change in diffraction [10]. For smaller molecules such as DNA, labels are required to generate a detectable change in signal upon binding [14]. Grating structures have also been used in conjunction with surface plasmon resonance to develop DNA sensors [11]. This technique does without nanoparticle labels or fluorophores, instead using DNA probes with antibody labels to capture antigens and build up biological matter on the grating, increasing the diffraction. The drawbacks to this technique are the number of layers and steps involved, the complicated experimental apparatus and the lower sensitivity than is likely to be achieved by using nanoparticle probes.

Fundamental to the DNA sensor devices has been the development of surface attachment chemistries such as thiol adsorption to gold, or silane attachment to glass, and the ability to pattern substrates on the micro-scale [15]. The majority of sensors developed to date have been developed on glass substrates. The sensor developed in this thesis uses a silicon substrate as this offers the benefits of higher surface binding coverage of DNA (up to $1.2 \times 10^{13}/cm^2$), a flatter and more homogeneous substrate than glass, and most significantly the integration compatibility with microelectronic devices. The combination of gold nanoparticle labels and diffraction characterisation should offer excellent sensitivity to target DNA sequence detection. A high sensitivity DNA detection system can then be used for haplotyping assays with genomic DNA samples.

1.4 Aims and Sensing Strategy

The main objective of this work has been to create a diffraction-based DNA sensor on silicon, and to develop an analysis method for the detection of haplotype in genomic DNA samples. A novel technique was investigated that utilises the well-known selective hybridisation of DNA with complementary sequences. The requirement was to develop a sensing strategy for the identification of whether two or more known sequences occur on the same DNA strand.

The sensing methodology developed (as summarised in Figure 1.1) works as follows: silicon substrates are patterned and functionalised with DNA oligonucleotide capture sequences complementary to one of the target DNA sequences being searched for. Gold nanoparticles are functionalised with an oligonucleotide sequence complementary to the second target DNA sequence being detected. If a test sample DNA strand features both of the sequences

complementary to those immobilised on the substrate and the gold particles, then subsequent DNA hybridisation attaches the gold nanoparticles on to the surface where it is patterned. The sample is then characterised for a change in diffraction associated with gold nanoparticles bound to the patterned regions.

A more detailed description of the sensing strategy to accompany Figure 1.1 is outlined below.

i A light induced reaction of a functionalised alkene with silicon is used to pattern the silicon surface (down to 10 μm features). This involves illumination of the silicon surface with UV light via a mask, for selective photoreaction causing covalent attachment of functionalised alkenes with the silicon surface, in a diffraction grating pattern.

ii DNA oligonucleotides specific for one of the target DNA sequences (DNA_1) are added to conjugate with the functionalised alkenes immobilised on the silicon substrate.

iii Samples are washed after conjugation and optically characterised.

iv Gold nanoparticles functionalised with oligonucleotides specific for the second target DNA sequence (DNA_2) are added to sample DNA.

v If the sample features the complementary sequence to the oligonucleotide on the nanoparticle (DNA_2), there will be hybridisation of the large DNA fragments ($> 10\,000$ base pairs long).

vi The sample DNA and gold nanoparticle-oligonucleotide conjugates (Au-DNA_2) are added to the diffraction sensor.

vii If the DNA fragment bound to the gold nanoparticles also features the first target DNA sequence, then the nanobead-tagged DNA fragment hybridises with the immobilised oligonucleotide. This forms a diffraction grating of gold nanoparticles on the silicon substrate.

viii The slide is interrogated with a laser. Diffraction patterns will be enhanced due to the presence of the gold nanoparticles where successful hybridisation occurred.

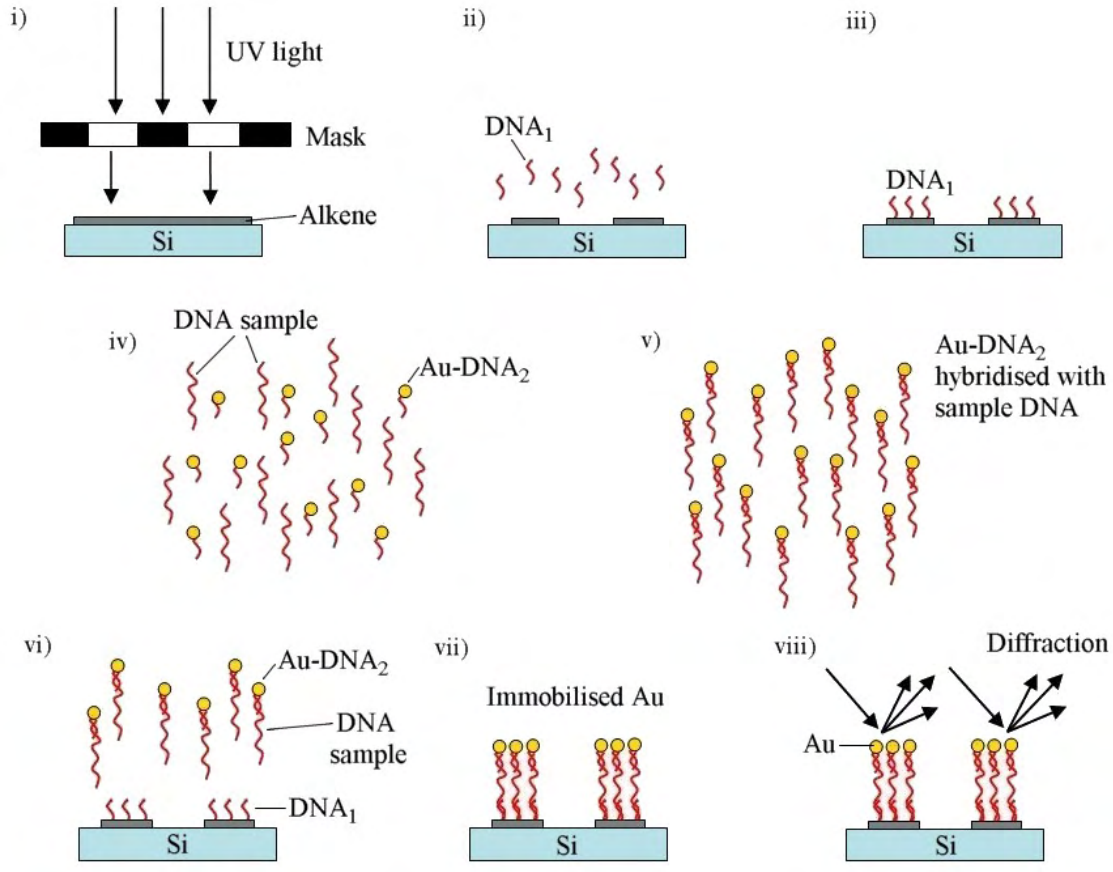

Figure 1.1: Diagrammatic representation of the steps involved for creating the novel device and analysis.

1.5 Summary of Achievements of the Thesis

To summarise, the key achievements and innovations of this thesis work and the development of diffraction sensors on silicon are:

1. A literature review of the state-of-the-art bio-sensor realisation and operation techniques was undertaken.

2. Successful development of a novel method for photo-patterning silicon with DNA using a UV lamp and photolithographic mask was developed in collaboration with Dr H. Yin [16]. Patterning accuracy and uniformity were increased over initial attachment protocol development work by using a UV lamp, 254 *nm* interference filter and close-contact illumination and a new grating design.

3. Diffraction theory was extended and novel modelling was carried out to optimise the design of the diffraction-based silicon sensor, which features two interlaced reflection diffraction gratings.

4. A novel one-dimensional diffraction grating sensor platform was successfully fabricated on silicon using the new fabrication techniques described. DNA was attached to silicon in a neat diffraction grating pattern featuring 10 μm wide lines and a 40 μm period, with excellent discrimination between patterned and unpatterned regions. The surface coverage achieved with DNA of $1.2 \times 10^{13}/cm^2$ was very high, corresponding to one molecule per 8.3 nm^2.

5. Successful hybridisation of gold nanoparticles to DNA sequences immobilised on silicon substrates was achieved. The hybridisation densities were up to 2.5×10^{12} particles/cm^2 for 1.4 nm diameter gold nanoparticles (one gold nanoparticle hybridised to DNA per 40 nm^2). Silver-enhancement procedures were used to increase the diameter by 500 times and verify gold nanoparticle hybridisation *in-situ* by SEM imaging.

6. A novel optical characterisation apparatus was developed to accurately characterise diffraction from reflecting diffraction gratings with an accuracy of ± 0.034 %.

7. Changes in diffraction order intensities of up to $+108.79 \pm 1.98$ % averaged over the entire grating surface, were measured for hybridisation of complementary DNA labelled 1.4 nm diameter gold nanoparticles to the DNA diffraction grating on silicon.

8. A novel two-dimensional diffraction sensor methodology was developed based on reflecting arrays of dots. Test patterns indicated that the technique enables identification of which features are contributing to the diffraction pattern by analysis of the diffraction patterns. Results were then obtained for DNA patterns on silicon substrates. Fourier transform analysis determined that a signal-to-noise ratio increase of 26.7 ± 3.7 % was generated by hybridisation of complementary DNA-labelled gold nanoparticles.

1.6 Synopsis of the Thesis

An optical detection system for diffraction-based analysis of DNA samples is presented. The sensor device developed in this project sits at the interface between genetics and optics. It is necessary therefore to have an understanding of both the biological and optical theory behind the sensor in each of these areas. The underlying diffraction theory, upon which the concept of a diffraction sensor is based, will be covered in Section 4.1.1.

Chapter 2 introduces the necessary information to understand the biochemical processes exploited in the sensor. A review of the literature is then presented which documents existing sensor devices based on optics and/or DNA assembly.

Chapter 3 reviews existing surface functionalisation and patterning techniques. The methods used to fabricate diffraction-based DNA sensors on silicon are detailed and explained. This chapter also describes silver-enhancement procedures to increase the size and reflectivity of gold nanoparticles.

Chapter 4 describes the basic principles of diffraction gratings and extends the theory to cover interlaced diffraction gratings. These are modelled and the optimum grating design is explained for fabricating DNA gratings on silicon.

Chapter 5 documents the progress made in optical characterisation of the diffraction gratings from the initial experiments, through the development stages to the final apparatus. This chapter presents results for 'optimum' metal patterns on silica and silicon substrates and details the results obtained for DNA diffraction gratings on silicon with hybridised gold nanoparticle labels.

Chapter 6 outlines an alternative diffraction sensor methodology using 2-D arrays. Results are given for chrome arrays on glass, gold arrays on silicon and results are presented for DNA patterns on silicon with hybridised gold nanoparticles.

Chapter 7 summarises the progress made with the diffraction-based sensors and the achievements documented in the thesis. Future work is proposed to improve the functionality of the sensor and to exploit it in possible applications.

Chapter 2

Review of Optical Biosensors and DNA Detection

2.1 Introduction

This review chapter first introduces the principles of DNA necessary to understand DNA base-pairing, the significance of DNA analysis and how DNA sensing works. State-of-the-art biosensing strategies are then presented. The main aims of the review are to demonstrate the wide variety of DNA detection methodologies that have been developed, to demonstrate the potential applications of DNA recognition and to provide an overview of optical biosensors.

2.2 The Principles of DNA Structure

The composition of hereditary material from deoxyribonucleic acid (DNA) was discovered in 1944 [17]. Its double-helical structure and complementary base-pairing was proposed in 1953, by James Watson and Francis Crick [18]. Today, the human genome has been almost completely mapped, with the DNA sequence identified for 99 % of the gene-containing part of human DNA [1]. The next step is the evaluation of how differences in the DNA sequences of individuals of the same organism affect size, appearance, ability and predisposition to disease.

Duplex DNA is a double-helical molecule consisting of two anti-parallel polydeoxynucleotide chains, held together by the hydrogen bonding of nucleic acid base pairs. The fundamental building blocks of DNA are the four nucleic acids adenine (A), thymine (T), guanine (G), and cytosine (C) (see Figure 2.1). These nucleic acids are covalently attached to the $C_{1'}$ carbon of the sugar in the sugar phosphate backbone (Figure 2.2(b)).

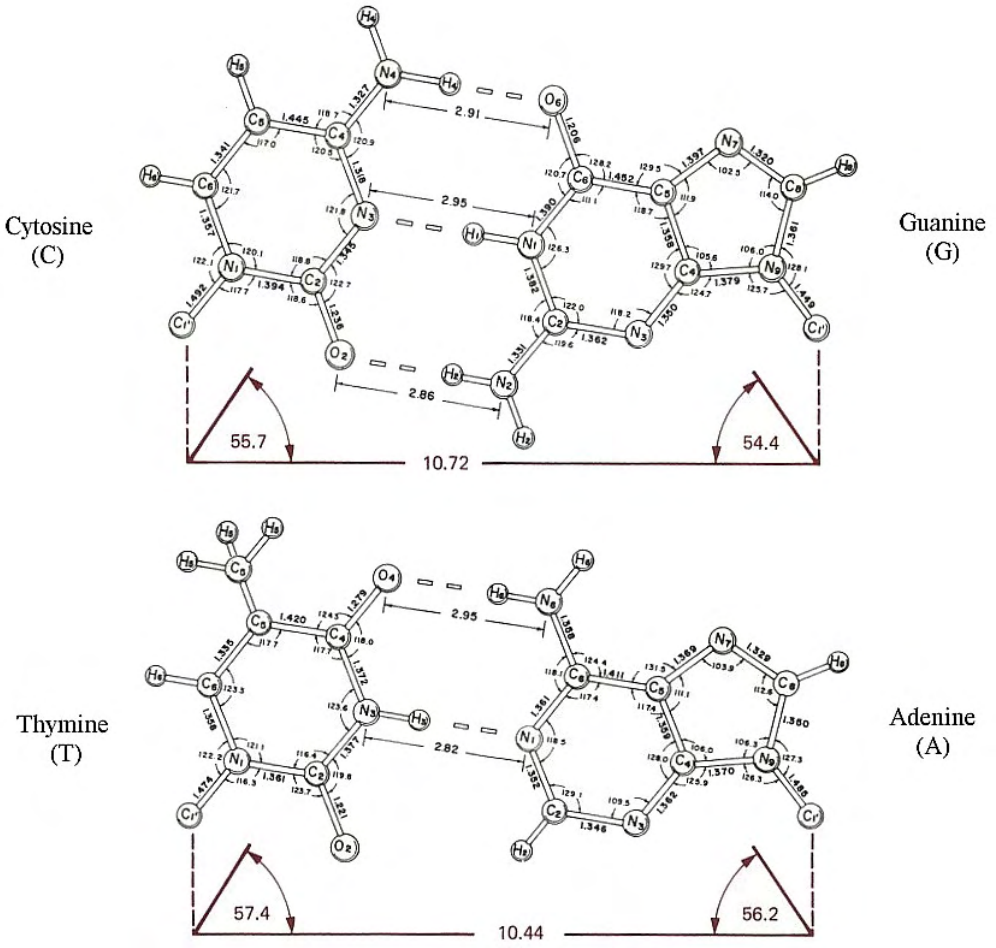

Figure 2.1: DNA bases and complementary base pairs; Cytosine-Guanine (top-row) and Thymine-Adenine (bottom-row) (Figure adapted from Wolfram Saenger, *'Principles of Nucleic Acid Structure'*, Springer-Verlag, 1984 [19])

The bonding of $C \equiv G$ is stronger than between $A = T$, with the total binding energies between the base pairs being 70.3 $kJ/mole$ and 29.3 $kJ/mole$ respectively [19]. This is known as Watson-Crick complementary base pairing.

2.2.1 DNA Hybridisation and Melting

Hybridisation occurs when two different single stranded complementary DNA sequences self-assemble by hydrogen bonding interactions between the nucleic acid molecules by Watson-Crick base-pairing to yield the duplex DNA double helix (see Figure 2.2(a)). DNA melting is

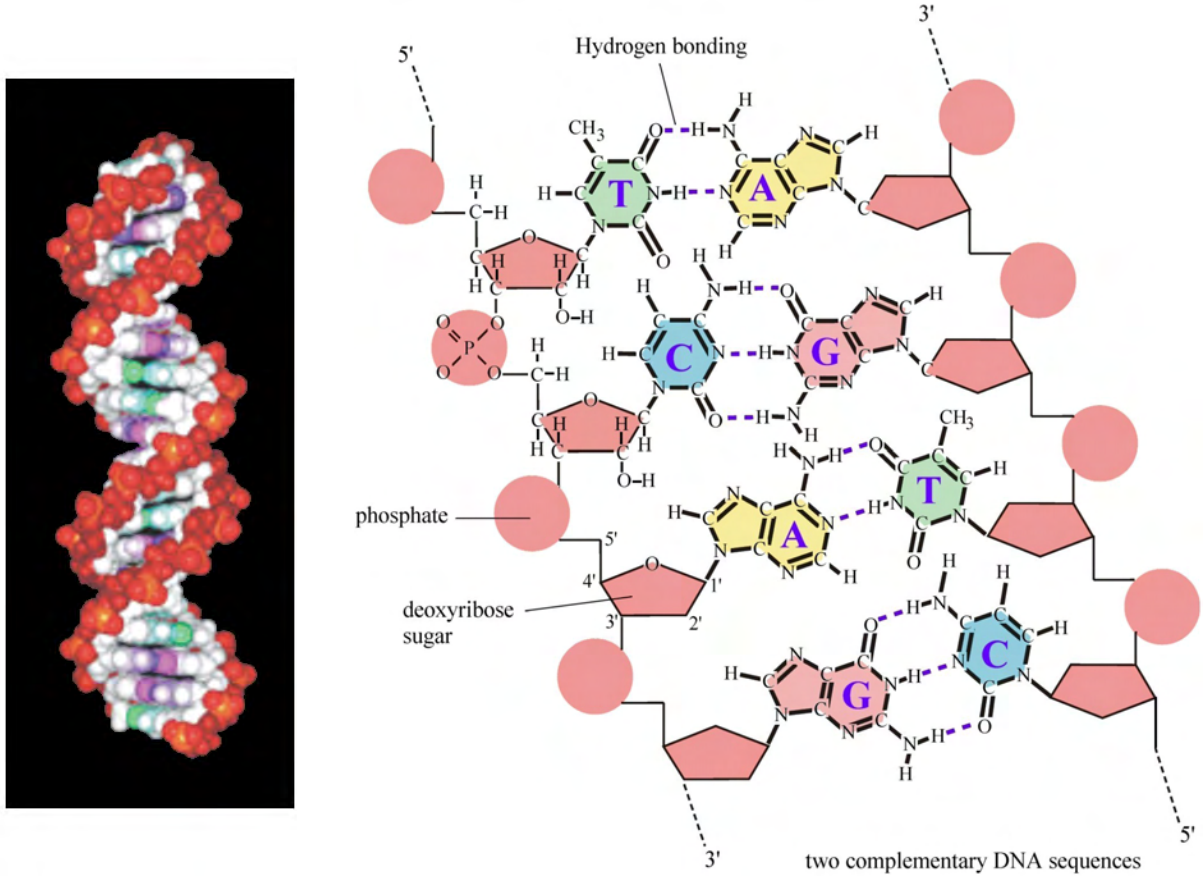

(a) Duplex DNA helix (b) Base pairing of complementary DNA strands

Figure 2.2: The duplex DNA molecule. 2.2(a) The double-helix conformation of hybridised complementary DNA strands (Figure from [20]). 2.2(b) Schematic of nucleotide chain formation and hybridisation. Polynucleotide bonding forms the backbone of a DNA strand and hydrogen bonding between complementary base pairs in duplex DNA (Figure from [17]).

the thermal denaturation of the duplex DNA into two separate strands. The transformation from the double stranded DNA conformation to the single stranded DNA sequences can be detected by an increased UV light absorption at a wavelength of 260 nm, which is caused by reduced base stacking and π orbital overlap of the nucleic acid bases. The melting temperature is defined as the temperature (T_m) at which half of the DNA sample is single stranded (see Figure 2.3). The process is reversible; when the DNA solution is cooled, annealing occurs and the sample returns to its double stranded form.

The melting temperature is dependent upon the G-C content, DNA strand length (number of bases, N_b) and salt concentration of the solution. The melting temperature can be estimated and is dependent upon the DNA strand length of the hybrid region and sequence content [19]. For two oligonucleotide sequences shorter than 18 nucleotides (N_b):

$$T_m(^\circ\mathrm{C}) \approx 2 \times (A + T) + 4 \times (G + C)$$

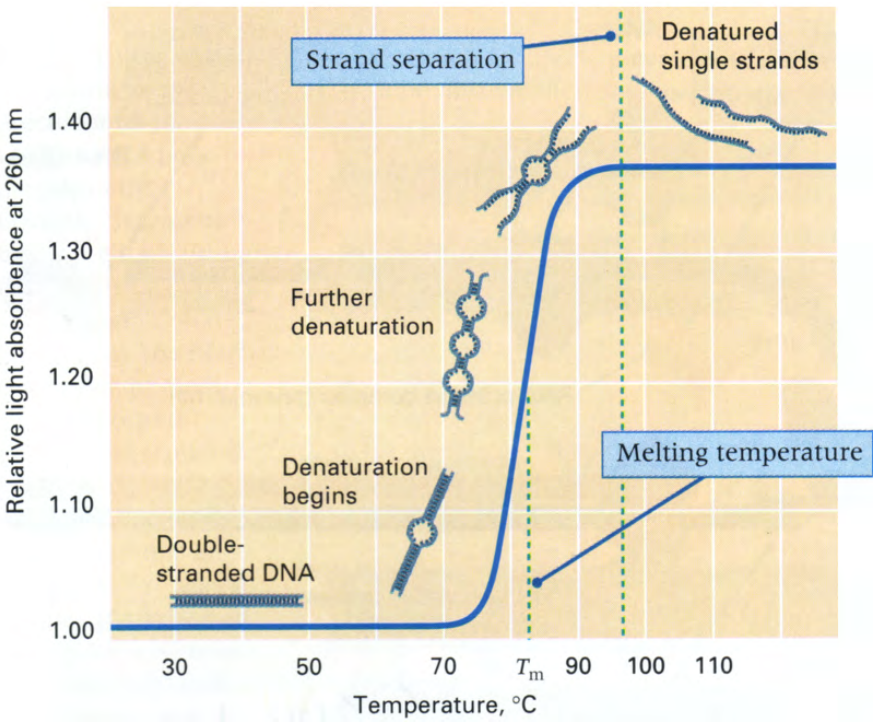

Figure 2.3: Changes in UV absorption of duplex DNA with temperature. As the double helix uncoils and the double strand denatures (indicated schematically), absorption in the UV wavelengths increases (Figure from D L Hartl and E W Jones, *Genetics: Principles and Analysis*, Jones and Bartlett Publishers Inc, 1998 [21]).

For longer hybrid sequences, with chain length (N_b) up to around 70 nucleotides long:

$$T_m = 81.5 + 16.6 \log_{10}(\mathrm{Na}^+\text{Molar concentration}) + 0.41(\text{G+C fraction}) - 600/N_b$$

When large numbers of short oligonucleotide sequences that are complementary to a region in the DNA sequence of interest are added to a melting DNA sample, these will effectively compete for hybridisation because of both the kinetic advantage (smaller sequences will diffuse quicker) and the higher number density that can be added.

The length of a DNA sequence necessary to ensure it is a statistically unique sequence can be estimated as follows [22]; the probability of finding any given base (A, C, G, or T) in a DNA sequence is 1/4. The probability of matching two bases in a row is $1/4 \times 1/4 = 1/16$; the probability of matching N_b bases in a row is:

$$\frac{1}{4^{N_b}}$$

Consequently, when $N_b = 16$, the probability of matching the sequence is approximately once in every 4 billion bases, which is roughly the length of the human genome (3.08×10^9 base pairs [23]). The length of a complementary DNA probe generally used in research to ensure

it is a unique sequence is therefore chosen as at least 17 base pairs. This is simply an estimate of the minimum probe length. Certain sequences of DNA contain repetitive sequences of around $10 - 100$ base pairs, and so longer oligonucleotide probes would be required [24]. When DNA probes are required to decode the amino acid sequences of proteins, $18 - 20$ base pairs is often quoted as a minimum length for a probe to ensure specificity, since amino acids correspond to codons of 3 nucleotides and so probes are prepared based on 6 amino acids or more to ensure specificity [25]. For certain sequences of DNA a complementary probe cannot be prepared as the probe sequence could form hairpins ($5 - 10$ bases apart) or stem-loops (more than 50 bases apart), hybridising with itself [25].

2.2.2 DNA-Templated Assembly

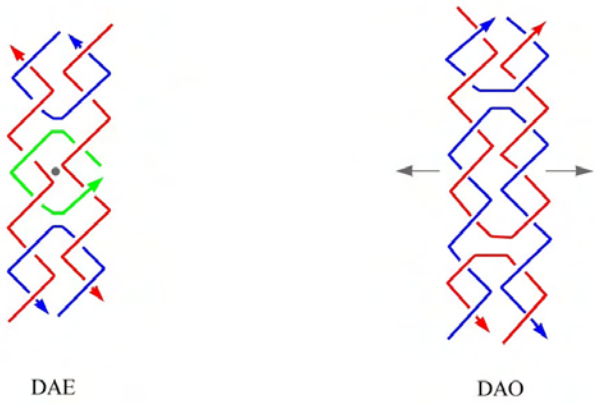

Figure 2.4: Schematic diagrams of DNA strands forming double crossover molecules with antiparallel helices, with even (DAE) and odd (DAO) number of helical half-turns between crossover points (Figure from [26]).

DNA's molecular recognition properties have been exploited to assemble materials in a controlled fashion [27, 28]. Initial development in this field by Seeman and co-workers, exploited DNA's molecular recognition properties to develop structures created solely from DNA. They created branched DNA junctions featuring three to six arms, geometrical objects (e.g. cubes), DNA knots and catenanes [26, 29]. However, these structures are not rigid, so they rely more on topology than fixed geometry due to flexible junctions and linkers. They also created double-crossover (DX) molecules of DNA (Figure 2.4). These consist of two, four-arm branched DNA molecules that contain two crossover sites between each helical domain [30]. It was found that DX molecules with antiparallel helical domains have a rigidity comparable to linear duplex DNA, making them useful for construction of DNA-based materials.

2.3 The Biological Role of Genes

Proteins are the main determinants of the basic structural and physiological properties of an organism. Genes are the functional regions of chromosomal DNA, and most genes are coding regions for proteins [31]. However, the coding sequence of a gene is not continuous and is interrupted by non-coding intron sequences between the coding regions, known as exons. The size and complexity of human genes varies considerably. For example, one of the largest identified is the dystrophin gene which is spread over a DNA sequence of two million base pairs. It consists of 14 000 bases of coding sequence distributed over 79 exons [32]. The longest length of gene coding sequence in the human genome identified to date spans 280 000 base pairs for the TTN gene on chromosome 2 [33].

Proteins are formed from the transcription and translation of DNA. The double-stranded DNA sequence within a gene is transcribed in to a single-stranded primary RNA transcript. The DNA strand is 'read' from the $3'$ end to the $5'$ end, with the RNA transcript being created from the $5'$ end to the $3'$ end, as shown in Figure 2.5 (i). This transcript is then spliced to remove intron regions, the $5'$ end sequence is capped, and the $3'$ end is trimmed and polyadenylated (with $200-250$ adenine bases) to form mature messenger RNA (mRNA) (Figure 2.5(ii)), providing the template for a protein [34]. The mRNA is then translated in to a polypeptide chain, with each 3 nucleotide group (or codon) transcribed coding for a specific amino acid [32]. Post-translational modification, such as folding into a three-dimensional structure and the addition of sugars, forms a functional protein. Consequently, variations of even one base pair will correspond to a different amino acid being transcribed which can potentially alter the functionality of the protein [17].

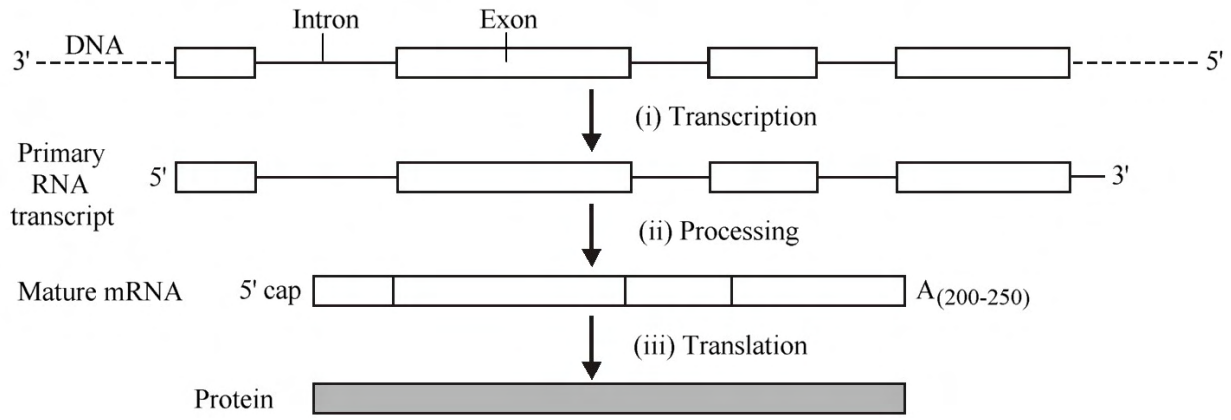

Figure 2.5: Schematic diagram of DNA transcription and translation in to a protein (Figure from [34]).

2.3.1 Single Nucleotide Polymorphisms

A single nucleotide polymorphism (SNP) is one differing nucleic acid base in a given DNA sequence at a particular *locus*; by definition a SNP is a polymorphism that exists in at least 1 % of the population [35]. There are a lot of naturally occurring DNA sequence variations (polymorphisms), which result in genetic variation of the population (size, ability, colour, predisposition to disease). Of these DNA polymorphisms approximately 90 % are due to single nucleotide polymorphism [8]. There is great interest in human genetics research in identifying genome polymorphisms for the understanding of population genetics, heritable diseases and the development of pharmacogenomics. For example, drugs used in cancer therapy could in the future be tailored to an individual to avoid side effects.

Since human cells are diploid, there are two copies of every chromosome and thus two copies of each gene. Alternative versions of a gene are known as alleles, occupying fixed positions within a chromosome. If the copy of a gene on each strand is identical (the same allele) then the individual is homozygous. If the individual has different alleles, it is heterozygous. If a SNP occurs in both alleles, it is known as a biallelic SNP.

There are four different types of biallelic SNPs. Allelic nucleotides x_1 and y_1 of a SNP on one strand have complementary base pairs x_2 and y_2 on the second strand (see Figure 2.6). The SNP change from x_1 to y_1 and complementary base change from x_2 to y_2, i.e. x_1-$x_2 \rightarrow y_1$-y_2 has the following possibilities: C-G → T-A, C-G → A-T, C-G → G-C and T-A → A-T. There is a higher observed occurrence of C-G → T-A, with 2/3 of SNPs found involving this transition [8].

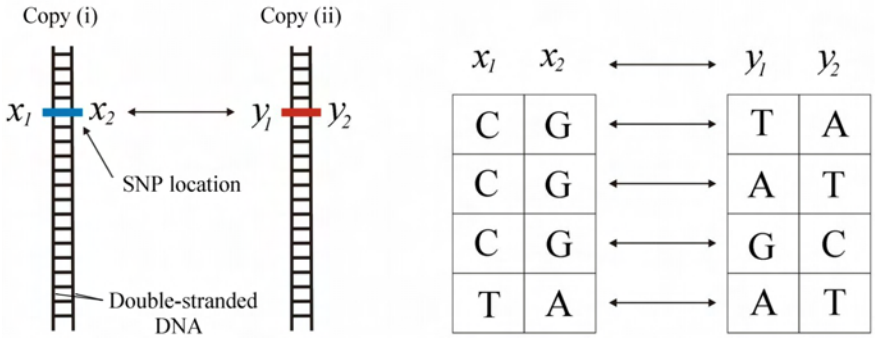

Figure 2.6: Possible SNP combinations of a bi-allelic SNP, with different SNPs on each copy of the chromosome, (i) and (ii). Copy i has SNP x_1 on one strand, with the complementary base x_2 on the other, copy ii has version y_1 of the SNP with complementary base y_2. The table on the right shows the SNP combinations.

The rate of difference between two randomly chosen equivalent chromosomes is known as

nucleotide diversity. The difference in genomic DNA sequence between two equivalent chromosomes is approximately 1 single base change in every 1000 base pairs on average [36]. A single nucleotide sequence variation is not necessarily a SNP, it may be a very rare variation or a single base insertion or deletion (known as 'indels'), or a duplication, as shown schematically in Figure 2.7. Whilst not all of these will be common, many of the polymorphisms will be for alleles of which the least abundant has a frequency of greater than 1 %, making it a SNP. Alleles with a lower frequency presence than this are classified as rare variants. The nucleotide diversity (1/1000 base pairs) means that there is roughly a 0.1 % chance of any one base being different (or heterozygous) in an individual. However, although the nucleotide diversity is on average 0.1 %, there are region specific differences of up to 100 times in SNP density. For example, in vast stretches of DNA, the diversity is much less than 0.1 % - within coding exon regions diversity is 4 times lower. In non-coding regions diversity can be up to $5 - 10$ %. Although this sounds like a low frequency of variation, with around 3×10^9 base pairs in the genome, this creates several million base differences between individuals, generating a hundred thousand or so amino acid differences. Although the human genome shares some 96 % of its DNA gene sequence with Chimpanzees, there is a 10 fold greater nucleotide variation in humans, which highlights the functional significance played by SNPs [37, 38].

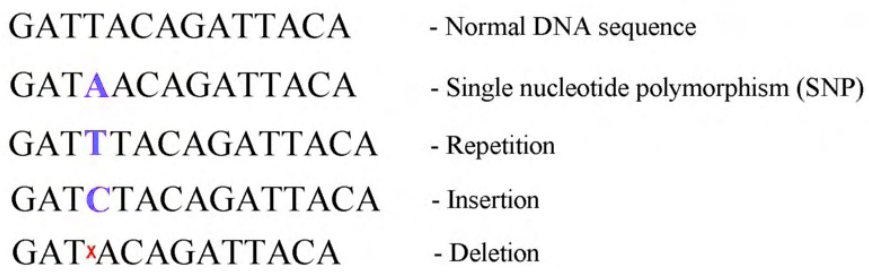

Figure 2.7: Schematic diagram of DNA nucleotide changes; a SNP, repeat and insertion are shown in blue and deletion represented by a red X, in referral to the normal DNA sequence.

The introduction of SNPs is a gradual process, with genomic DNA sequence variations being created continuously. This evolution occurs at a rate of approximately 100 new single base changes per individual, not all of which are guaranteed to be passed on to offspring. Many single base changes only remain for a short time as rare variants before being eliminated in the population. This means that there are only 10^{-8} changes per nucleotide per generation. Additionally, base changing events are often random in nature. This combined with the slow rate of change means that few alleles that were present in early humans will have become fixed yet, reaching either 0 % or 100 % frequencies. It is estimated that around 85 % of human SNPs are common to all humans. Only 15 % of SNPs are population 'private' within human races [8].

Both environmental and genetic factors can generate phenotype variations (physical and chemical characteristics). SNPs are thought to be highly influential genetic factors, modifying risk and susceptibility to diseases, rather than directly causing them [39]. The risks of major common diseases such as cancer and diabetes, are probably due to patterns of SNPs in key susceptibility genes, although there could be many interacting genes involved [40]. Whether an individual suffers from a disease is probably the combined effect of a collection of SNP alleles in key genes and environmental influence [41].

2.3.2 Identification of Haplotype

Each mammalian cell contains two copies of every gene, as one copy is inherited from each of the parents. The genetic constitution of an individual chromosome is termed a haplotype. Determining the presence of a pair, or group of SNPs within a gene sequence on the same chromosomal strand is the essence of haplotype analysis. Establishing which haplotypes a person has in their genes will enable an evaluation of susceptibility to certain diseases, such as heart disease [42], since the genes code for proteins and sequence variations result in different amino acids being transcribed, potentially altering the functionality of the protein. A particular physical characteristic of an individual, a phenotype, may be formed by the presence of two or more linked SNPs on one chromosome [8]. In the simplest case where the phenotype is formed by two SNPs on a single DNA strand, the individual may have four different SNPs within their DNA- two allelic variations for the gene.

SNPs are located at the allele sites indicated in Figure 2.8. If we take the upper case letters to be the SNPs, then an individual inheriting the sequence containing the $A+B$ will potentially inherit a certain phenotype if one parent features the phenotype, but the other does not. The combinations shown in the bottom row of Figure 2.8 are possible in the offspring.

The example in Figure 2.8 shows that both parents feature the same SNPs in their genotype, but they have different haplotypes since the SNPs occur on different chromosomes in each of them. Whether the offspring is likely to develop the phenotype depends on having the specific SNPs for the feature on the same chromosomal strand. It is therefore important to identify an individual's haplotype in order to identify which combination of SNPs influence susceptibility to diseases, such as Alzheimer's or cystic fibrosis [39].

Current DNA analysis methods tend to rely on polymerase chain reaction (PCR) amplification of genomic DNA samples in order to attain a large enough quantity of copies of the same

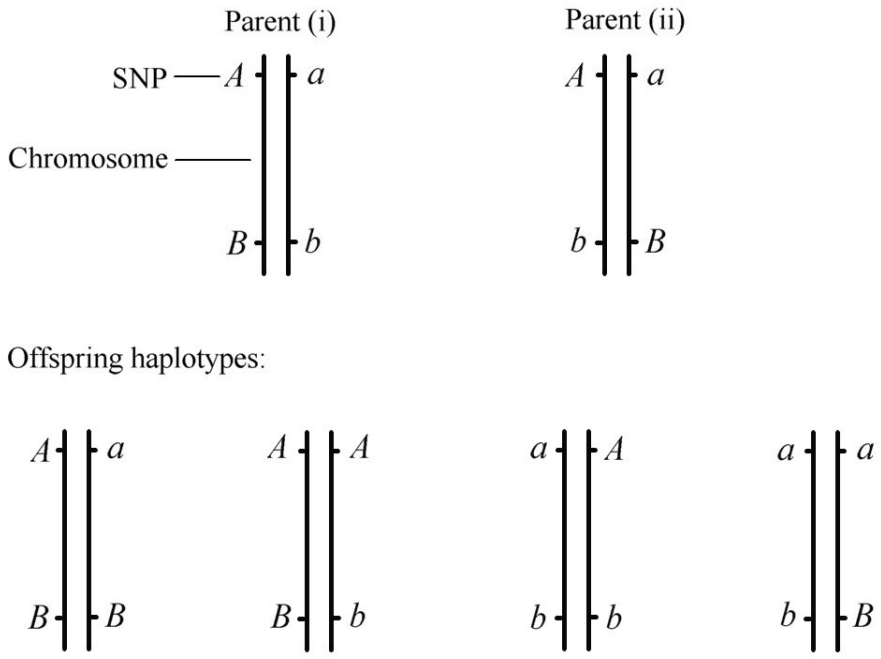

Figure 2.8: Schematic diagram of parental haplotypes (top row); each parent has two copies of a particular chromosome and may have a different collection of SNPs (such as A or a and B or b) for each version of the same gene. The possible offspring haplotype combinations on each copy of the chromosome are shown on the bottom row.

sequence to enable detection. The genomic DNA isolated from blood samples originates from the leukocytes (white blood cells). Blood typically contains up to 5×10^7 leukocyte cells per ml containing 6.6×10^{-12} g of DNA per cell. Commercially available blood preparation kits, for example BloodPrep (Applied Biosystems), isolate 5 μg of DNA per 150 μl [43].

However, PCR commonly uses the enzyme *Taq* polymerase to amplify DNA sequences. The limitation of PCR is that the error rate can become very large as the sequence length increases. *Taq* polymerase has an error rate of 1 in 10 000 and it is very difficult to amplify DNA fragments longer than 10 000 bases long [44]. Consequently, a new sensitive detection method is needed for haplotype analysis which can directly use genomic DNA isolated from blood samples in low copy numbers, without the need for PCR amplification since gene sequences can be much longer than 10 000 bases.

A recent method for haplotyping by Ding *et al* took the approach of diluting genomic DNA samples to the point where diluted samples only contained one copy of DNA, or none [45]. At this point, the isolated single copy featuring several polymorphic markers separated by up to 24 000 bases was used for PCR amplification using only 100 base pairs either side of the SNP. This method avoids amplification of the entire genomic region and ensures all the SNPs identified originate from the same chromosomal strand. Although this method does enable direct molecular haplotyping, PCR is still needed and many of the allocations

contain no DNA. It is a laborious and expensive way around the limitations for sequences up to 24 000 bases, rather than a solution for studying haplotypes of much larger genes.

2.4 Molecular Probes

Molecular probes (or labels) are used for detecting and locating complementary target DNA sequences. DNA strands can be functionalised by attaching molecules to either the 3′ or 5′ end of the sugar-phosphate backbone. This enables attachment of DNA to surfaces or labels, such as fluorophores or nanoparticles, via the functional molecule. Short sequences of DNA, or oligonucleotides, may be functionalised with fluorescent labels and used as molecular probes to track complementary sequences within a large DNA molecule. A key requirement of molecular probes is that they will not adversely interact with the DNA strand, so that it retains its normal functionality. Some commonly used fluorescent dyes include Cy5 (red), Texas Red, fluorescein (green), Cy3 (green), BODIPY-FL (blue) and DAPI (blue).

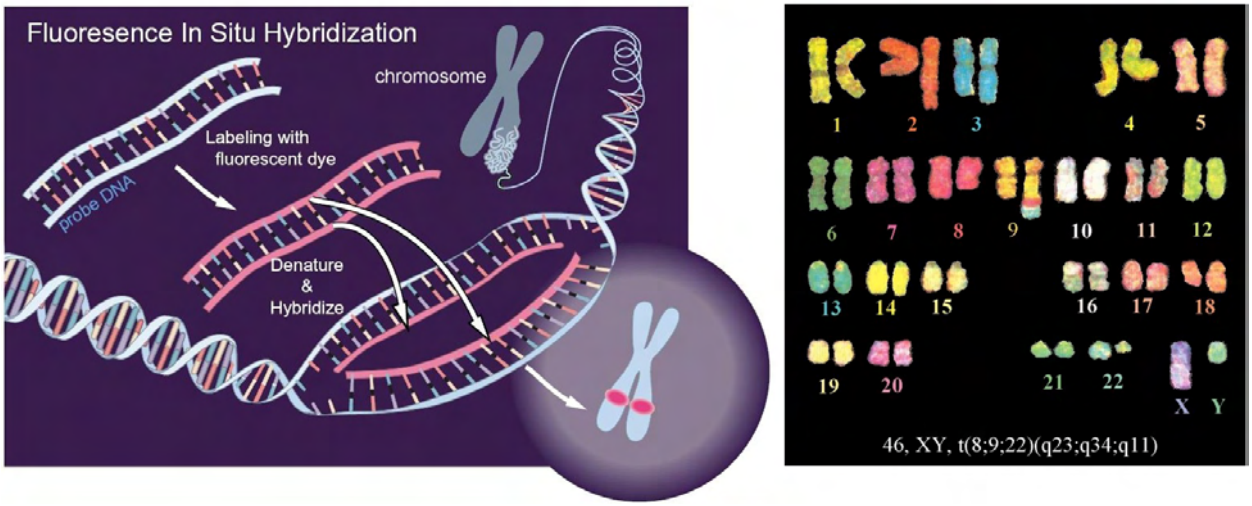

Figure 2.9: Fluorescent in-situ hybridisation (FISH) shown schematically (left, from [46]), can be used to study translocations of chromosomal DNA sequences (right, from [47]). Parts of chromosome 8 and 22 have been translocated to chromosome 9.

Fluorescent in situ hybridisation (FISH) is a technique used to detect and localise specific DNA sequences within chromosomes. A probe DNA sequence and its complementary sequence are fluorescently labelled and added to a chromosome sample. The chromosome is then denatured and the probes hybridise along the chromosome if the complementary target sequence is present. This can be used to observe translocations of DNA sequences between chromosomes, as shown in Figure 2.9 . Fibre-FISH involves attaching the chromosome to a substrate and uncoiling and stretching out the chromosome in a straight line, and examining

where fluorescence occurs along the DNA strand, allowing resolution between two probes down to 1000 bases [4].

Fluorescent probes are detectable on a standard optical microscope, when the appropriate filter is used to pass the fluorophore emission wavelength of light and cut-out the excitation light. However, there are several drawbacks to fluorescent labels. The emission wavelength band can be quite broad, and emission bands from different coloured fluorophores can overlap. This limits the number of different coloured fluorophores that can be used at any one time. Additionally, fluorescent molecules are prone to photobleaching, where the fluorophore is destroyed by high intensity illumination light. An alternative to fluorescent probes is the use of small metal colloids, or nanoparticles, which exhibit valuable physical properties as a function of their size. They exhibit sharp absorption bands of light and appear brightly coloured, and these properties can be exploited for use as molecular probes, as described in the next section.

2.5 Surface Plasmon Resonance and Nanoparticles

In 1979 it was found that noble metal colloids could be used to enhance spectroscopic Raman signals of molecules that attached themselves to surfaces [48]. Since then, the idea has been applied to many different areas, one of the most recent being the idea of tagging gold nanoparticles with oligomers of DNA. Single silver nanoparticles have been used to increase surface enhanced Raman scattering (SERS) by up to a factor of 10^{15} [49]. This makes nanoparticles invaluable for the optical detection of molecules that are themselves relatively undetectable. For example, silver nanoparticles have been used for surface enhanced resonance Raman scattering (SERRS) to quantify detection of dye labelled DNA [50].

In recent years, a lot of research has been undertaken to investigate the fabrication of functional macroscopic materials from assembled nanoparticles. Due to their small size, the properties of semiconductor and metal nanoparticles vary from both the individual atoms of which they are composed and the macroscopic bulk materials [51]. Properties that have been found to depend on the actual size of the nanoparticles include optical, electronic, optoelectronic, catalytic and magnetic behaviour. Furthermore, additional properties arise from the arrangement of nanoparticles into aggregates, where the individual nanoparticles interact with their neighbours [52, 53]. This means that materials can be chemically tai-

lored for their properties by controlling nanoparticle size, chemical composition, interparticle spacing and interaction strength [52, 54, 55]. The shape of nanoparticles can also affect the properties exhibited. For example, slight elongation of nanospheres has been calculated to increase the scattering efficiency [56].

2.5.1 Nanoparticle Plasmon Resonance Effects

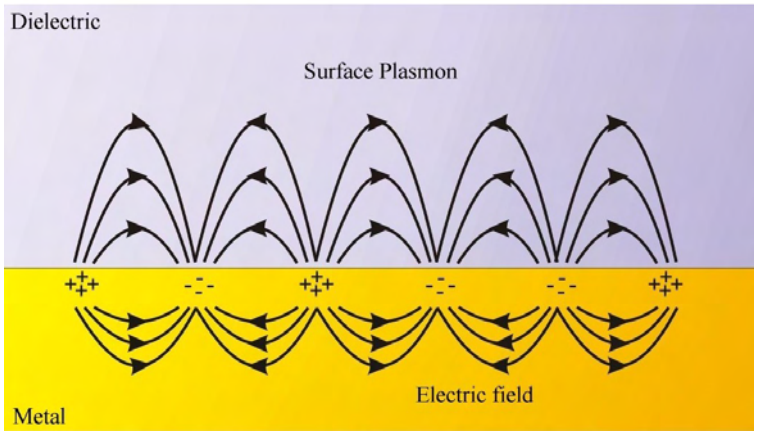

Figure 2.10: Surface plasmons are collective oscillations of nearly-free electrons at a metal-dielectric interface.

Metal colloids with nano-scale dimensions demonstrate plasmon resonance effects. The origin of the surface plasmon resonance effect is believed to be a result of the oscillation of free electrons in noble metals induced by an electromagnetic radiation field [57]. In metals, the almost-free conduction electrons behave similarly to those in a plasma. Density fluctuations in the distribution of free electrons are known as a plasma-oscillation, or a 'plasmon'. When parallel-polarised light strikes the metal-dielectric interface, it generates an evanescent electric field which can interact with the free electrons in the metal layer exciting electron density waves, or plasmons. The resonant coupling of an incident electromagnetic perturbation with a surface plasmon mode induces a propagating wave among the electron plasma known as a surface plasmon polariton (SPP), bound to the metal-dielectric interface (see Figure 2.10). The plasmon tends to occur along the surface region of the metal, due to higher absorption as light travels through a larger distance in the metal material, attenuating the electromagnetic (EM) field.

The wavelength of electromagnetic radiation at which coupling with the surface plasmon occurs is metal and size dependent. In contrast to bulk metals, where electrons are more likely to lose energy by non-radiative processes as a result of collisions and scattering, in nanoscale structures such as a nanoscale thickness film or nano-sized particles, the electrons

are trapped. Consequently, in nanostructures, the interaction between the free conduction electrons leads to collective oscillations between the upper and lower energy states, forming a more intense absorption band typically in the visible region of the spectrum. When illuminated with light of wavelengths in this absorption band, energy is transferred exciting a surface plasmon. This effect is known as surface plasmon resonance (SPR).

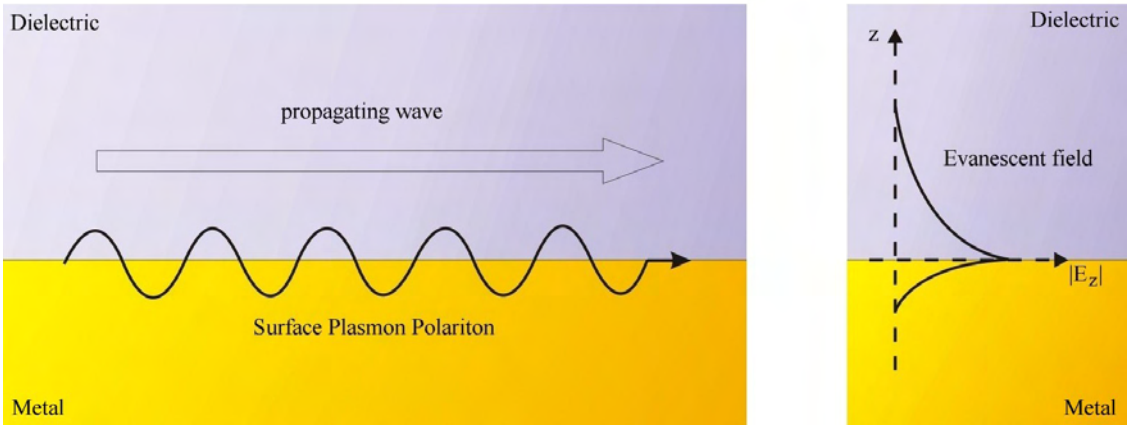

Figure 2.11: When light couples with a surface plasmon mode, a propagating surface plasmon polariton is generated with an evanescent field.

The excited surface plasmon polariton features an electromagnetic wave propagating parallel to the surface with an evanescent field decaying exponentially perpendicular to the interface (see Figure 2.11). The evanescent field penetrates into the adjacent media to a depth of approximately that of the incident radiation wavelength. Consequently, the SPP is very sensitive to the surrounding materials. This affects the wavelengths at which SPR can be excited. At resonance, light is absorbed and the intensity of reflected light is reduced [58].

The reason for the intense colours in the visible region of the electromagnetic spectrum exhibited by metal nanoparticles in solutions, is from their small size. The typical diameter of an atom is a few angstroms (Å$= 10^{-10}\ m$). Nanoparticle diameters used are typically in the range from $1 - 150\ nm$, corresponding to the aggregation of atoms in groups of a few hundred atoms to a few million. When in solution, the particles are isolated from each other resulting in the confinement of free conduction electrons to the surface of the nanoparticle (free electrons accumulate on the surface of an object due to electrostatics) [59]. The collective oscillations between upper and lower energy states accessible to surface plasmons confined on the particle form an intense and sharp absorption band at visible wavelengths. Note that the size of the nanoparticles is much smaller than the wavelength of visible light, which is in the region of $400 - 750\ nm$.

The plasmon band absorption of gold nanoparticles has been studied by Link *et al* in order to

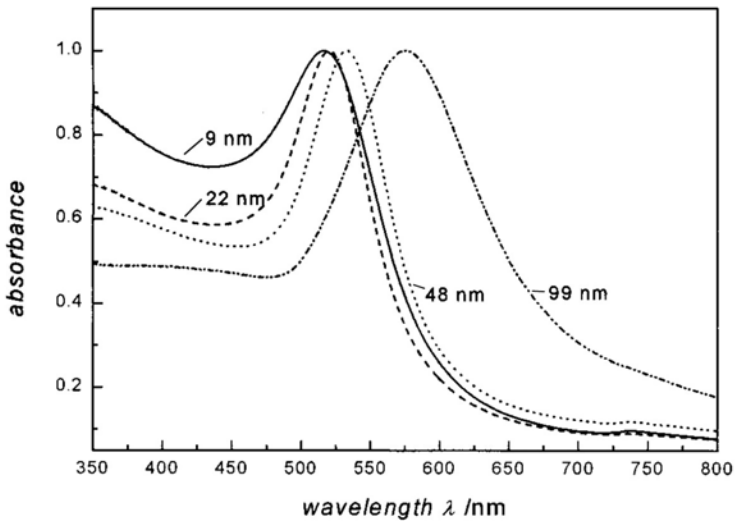

Figure 2.12: The wavelength of the plasmon band absorption maximum is red-shifted with increasing particle diameter, as indicated on the appropriate line (Figure from [57]).

understand the intense colours and optical spectra associated with nanoparticles compared to macroscopic bulk material. The plasmon bandwidth increases with decreasing particle size for 'intrinsic' size particles (less than 25 nm diameter), and increases with increasing particle size for 'extrinsic' size particles (diameter greater than 25 nm)[57]. The plasmon band maximum is red-shifted for increasing particle diameter (see Figure 2.12), creating more absorption at red-wavelengths, and greater transmission at shorter wavelengths of light. For small particles in the region of $10 - 20$ nm diameter, the peak absorption of light is at 520 nm. For larger diameter particles the absorption peak red-shifts to 535 nm for 50 nm particles, and 575 nm for 100 nm particles. A smaller effect of temperature dependence of plasmon absorption is also observed. Increased temperature slightly reduces the maximum absorption of the plasmon band due to greater damping of the collective electron oscillation through increased scattering.

By solving Maxwell's equations with boundary conditions for spherical particles Mie theory was developed, quantifying the extinction cross-section for small particles [57]. The total extinction cross-section is a summation over all electric and magnetic multipole oscillations, incorporating scattering and absorption. When the wavelength of light $\lambda >> 2R_p$ (where R_p is the particle radius), only the dipole absorption contributes to the extinction cross-section. This occurs for gold when $2R_p < 2.6$ nm [60]. In this region, the dielectric function of the nanoparticles is assumed to become size dependent; an intrinsic feature.

Surface Plasmon Resonance (SPR) effects can also be tuned by coating nanoparticles with thin shells of different materials. Composite particles with nanometre thick metal shells

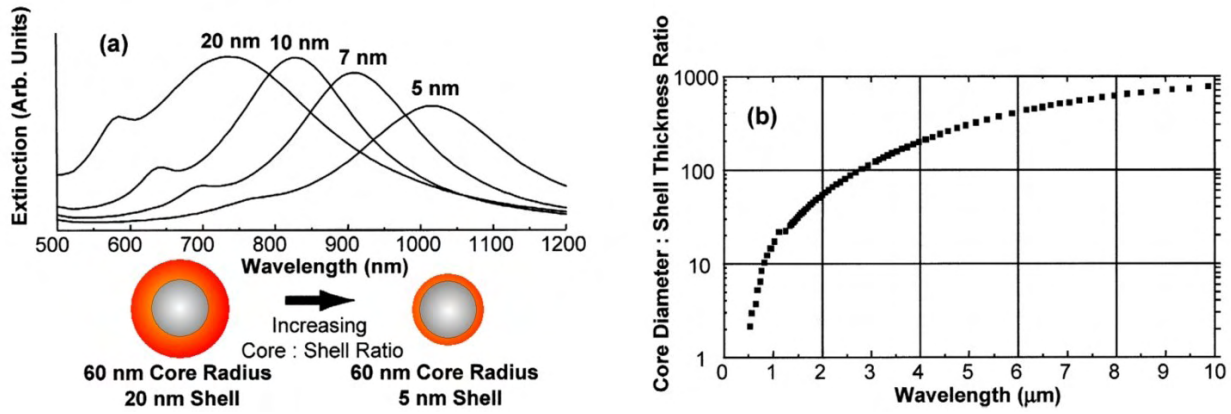

Figure 2.13: (a) Absorption spectra for varying gold shell thickness on silica core. (b) Maximum optical resonance wavelength as a function of the core:shell thickness ratio (Figures from [61]).

and dielectric cores have been created [61]. The optical resonance is selected from visible to infrared wavelengths, by varying the relative dimensions of the core-shell ratio. The composite particles are made from molecular self-assembly and colloid reduction chemistry. For larger core to thin shell ratios, the optical resonance peaks at longer wavelengths, as shown in Figure 2.13. Each nanoparticle type could then be used as a label for a molecular biosensor.

An alternative to metal coating of dielectric cores uses the reverse geometry of coating metal cores with a dielectric shell. By covering the surface of gold nanoparticles with a thin layer of silica, the plasmon band maximum is slightly red shifted in frequency and the intensity strengthened [62].

The exact electromagnetic absorption spectrum observed for sufficiently isolated nanoparticles of a given size depends on the volume and shape of the particle, the chemical composition of the particle and the dielectric constant of the surrounding medium. When the nanoparticles are very close together they exhibit quantum mechanical coupling effects resulting from overlap of the adjacent particles' wavefunctions. Hence, the interparticle distance can have a very significant impact upon the frequency of the plasmon band maximum absorption of incident light. Both particle-particle interactions between close nanoparticles and the aggregation of nanoparticles cause the location of the plasmon band maximum to shift towards longer wavelengths i.e. it is red-shifted [63, 64]. These effects are noted in DNA-nanoparticle aggregate studies by Mirkin *et al* (see Section 2.7.2).

2.5.2 Oligonucleotide-Nanoparticle Devices

The unique molecular recognition by hybridisation of complementary DNA strands has been exploited for assembling nanoparticle aggregates. Gold nanoparticles are used in many experiments owing to the high reflectivity of the element to electromagnetic radiation. Gold surfaces are also easily functionalised with molecules using thiol adsorption chemistry (see later Section 2.6.1) [65]. Additionally, it was discovered that the stability of the gold nanoparticles in the electrolyte solutions required for DNA hybridisation is enhanced by functionalising the surface of the nanoparticles with (alkanethiol)oligonucleotides. The oligonucleotide length and sequence also influence the optimal electrolytic stability of the gold nanoparticles against agglomeration [52]. Stability of gold colloids in electrolyte solutions was found to be highest for thymine nucleotide sequences of $5 - 15$ bases in length. Preparation of trithiol-capped DNA oligonucleotides has enabled the creation of increased stability DNA-gold nanoparticle conjugates, even for particles larger than 30 nm diameter [66].

Nanoparticles also have a pronounced effect on DNA melting temperatures (see earlier, Section 2.2.1). Duplex DNA structures formed between target strands and nanoparticle-labelled probes exhibit exceptionally sharp melting profiles, whether as aggregates or hybridised to DNA strands immobilised on solid substrates [5]. Consequently nanoparticle probes offer a greater ability to differentiate between perfectly complementary targets and those with a single base mismatch, compared to fluorophore based hybridisation. Larger diameter nanoparticles are found to give the sharpest melting transitions, with 50 nm diameter gold particles exhibiting a melting transition over just $1°C$. Interparticle distance (controlled by DNA linker length) also plays a role in DNA melting, with smaller particle separation from 30 base spacers to 0 reducing the melting temperature by $10°C$. These properties have been exploited by Murphy *et al* to study the denaturation behaviour of DNA triplexes [67].

Silver nanoparticles would be advantageous as nanoparticle labels, exhibiting a 4 times larger extinction coefficient than gold nanoparticles for the same sized diameter particle, and a plasmon resonance band at shorter wavelengths ($390 - 420$ nm) than gold nanoparticles ($520 - 580$ nm) [68]. However, oligonucleotide functionalised silver particles are not stable under the conditions needed for DNA hybridisation. Cao *et al* found that by forming a very thin (almost monolayer) gold shell around silver nanoparticles, the particles could be functionalised using well-established gold attachment protocols, but retained the spectral properties of silver particles [68].

Recently, a DNA network template was used to assemble a two dimensional complex of

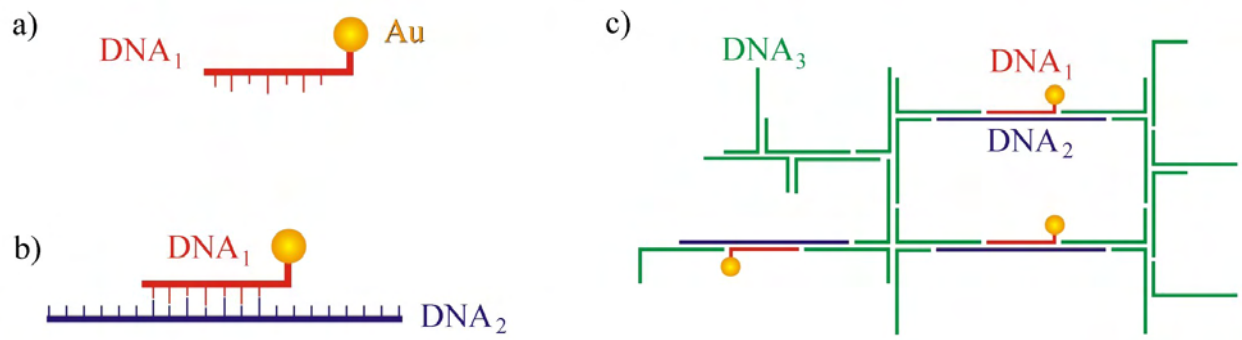

Figure 2.14: Schematic of 2−D assembly of gold nanoparticles (Figures based on [69]).

gold nanoparticles [69]. This was achieved by attaching one oligonucleotide sequence to gold nanoparticles, which was subsequently hybridised to a second, longer oligonucleotide sequence (see Figure 2.14). This second sequence hybridises the nanoparticle's attached complementary sequence along the centre of the strand, leaving free ends either side. These are free to hybridise with the appropriate complementary strands of a third sequence, forming a DNA network, with particles arranged on the template. When the DNA networks were measured on an AFM, the particles had a mean separation of 260 nm, but a large range in location from 60 nm to 600 nm. It was found that the cross-linking could be controlled by modifying the concentrations of the oligonucleotide sequences. At too low a concentration, only linear fragments of gold-DNA complexes were created. At too high a concentration, 3−D aggregates were formed. The intermediate case enabled the formation of two-dimensional networks.

Further examples of DNA construction include self-assembled DNA nanogrids to arrange 5 nm diameter gold nanoparticles in periodic square lattices of $\approx$ 38 nm dimensions [70]. Niemeyer *et al* functionalised gold nanoparticles with a mixture of DNA sequences so that the gold nanoparticles could be immobilised on the substrate by adding one linker sequence and could then be cross linked with an addition DNA sequence [71]. Work by Warner *et al* demonstrated how DNA strands could be used as a scaffold for the assembly of close packed gold nanoparticles [72]. The nanoparticles were coated with a 15 Å ligand shell which electrostatically bound to the DNA backbone, enabling the creation of ribbon-like structures of parallel chains of nanoparticles. DNA has also been used to template the assembly of proteins in linear arrays, and to assemble streptavidin conjugated gold nanoparticles [73], using DNA sequences forming a triple-crossover molecule with biotin binding sites for streptavidin.

A different approach to nanoparticle-based construction has been used to create thin conducting silver wires between two electrodes [74]. Different oligonucleotide sequences derivatised

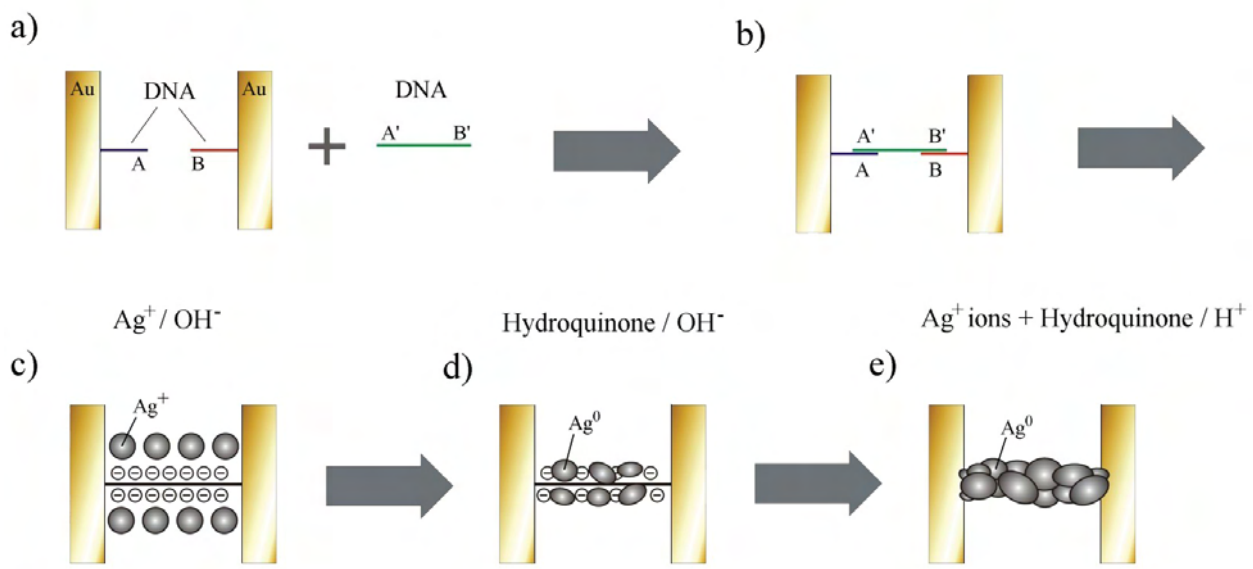

Figure 2.15: DNA-templated construction of a silver conducting wire across a gold electrode gap. (a) Two different oligonucleotides (A and B) are attached to each electrode. (b) An oligonucleotide featuring sequences A' and B', complementary to A and B respectively, bridges the gap. (c) The DNA connection is loaded with silver ions (Ag^+). (d) Hydroquinone causes the silver ions to form metallic silver aggregates bound to the DNA template. (e) Full development results in a conductive silver wire (Figure based on [74]).

with a disulphide group were functionalised on to two gold electrodes through sulphur-gold interactions. A linker sequence featuring 'sticky ends' complementary to the immobilised oligonucleotide sequences was added to bridge the gap between the electrodes, as shown in Figure 2.15. A silver ion (Ag^+) solution was then added; the sodium ion in the phosphate backbone of the DNA was exchanged with a silver ion. A hydroquinone solution was added and oxidised, providing electrons for the reduction of silver ions (Ag^+) in the DNA-wire to silver atoms (Ag^0) producing nanometre sized silver aggregates bound along the DNA template. A hydroquinone and silver ions solution was then used to develop the Ag/DNA-wire. The silver aggregates on the DNA acted as catalysts for reduction of silver ions in solution resulting in a continuous silver wire between the electrodes 100 nm wide.

2.6 DNA and Biomolecule Sensors

New approaches are needed for the detection of single or very low copy numbers of DNA sequences to provide simple, cheap protocols for the study of genetics and for the detection of hereditary diseases. Detection of DNA sequences has been achieved in the past using radioactive, chemiluminescent and fluorescent labels [75]. Despite radioactivity methods

being very sensitive, fluorescence based methods have superseded these due to the problems and health hazards associated with the use of radioactivity, along with the damage done to the DNA sample itself by the radioactive decay products.

Although approaches such as Maxam-Gilbert [76] and Sanger [77] sequencing methods have exploited DNA sequence analysis using radioactive labelling, methods for genetic sequence analysis which use much smaller quantities of DNA and enable massively parallel sample analysis are required. Technological advances in recent years have led to micro-devices and DNA microarrays, with clear benefits for hereditary disease characterisation and diagnosis [78]. Significant effort has resulted in sequencing of the human genome [1, 79–81]. The next challenge is to correlate known DNA sequences with disease susceptibility. For instance the international 'HapMap' project [82], and 'Genomes to Life' program [83] aim to build and use a vast database of common variation in the human genome to identify genetic factors that influence medical traits.

This review investigates the optical sensing approaches used to detect biomolecules and DNA in particular. Nanoparticle properties and nanoparticle-based devices are also explored along with a review of interference, diffraction and holographic based biosensors.

2.6.1 Surface Attachment and Patterning Methods

A broad range of sensors have been developed to enable the detection of bio-molecules. The creation of many of the DNA arrays and devices described in this Chapter have utilised methods developed for the attachment of molecules on surfaces in self assembled monolayers (SAMs)[84]. The fabrication of micro-scale biochips involves the use of surface attachment chemistry with micro-patterning methodologies [15].

The attachment of biomolecules to a solid support surface has been achieved by various methods using different substrate materials. Thiol attachment chemistry is widely used to functionalise gold surfaces and nanoparticles. Modified alkanethiolates form SAMs by adsorption through a sulphur-gold bond [65]; functionalisation with DNA oligonucleotides can then be achieved with thiol substranded DNA molecules. Glass can be functionalised by coating the surface with poly-lysine, amino silanes or amino-reactive silanes [15, 85, 86] as shown in Figure 2.16, and subsequent conjugation of DNA oligonucleotides to the amino group. The patterning of substrates for creating micro-scale biochips can involve photolithography or mechanical spotting techniques. The methods for photo-patterning and

functionalisation of surfaces with biomolecules is covered in more detail later in Chapter 3.

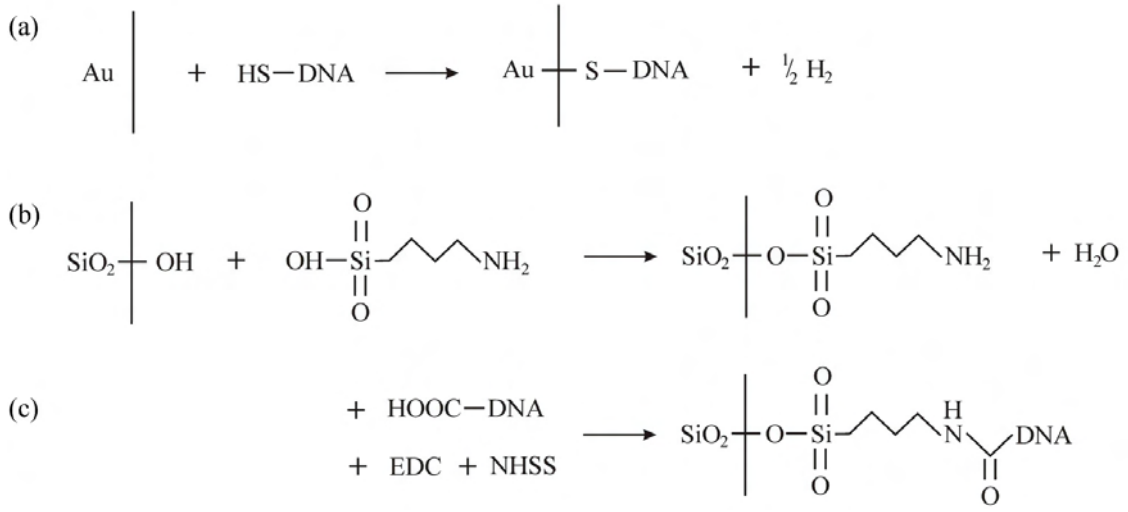

Figure 2.16: Schematic of surface attachment chemistries. (a) Thiol attachment on a gold surface, illustrated by a thiol with a functional group e.g DNA. (b) Glass functionalisation is shown with an aminosilane. (c) Conjugation of carboxylated DNA to aminosilane functionalised glass, in buffer containing EDC and NHSS [85].

2.6.2 DNA Microarrays and Fluorescent Detection

The advent of DNA microarrays has accelerated genetic analysis protocols [87]. They play an important role in DNA sequencing [88, 89], genotyping [90], disease diagnostics [91–93] and studying gene expression analysis [87, 94, 95]. In general DNA microarray systems rely upon fluorescence detection. Fluorescent labels are attractive because optical detection can readily be automated and the need for radioactive reagents was eliminated.

DNA microarrays feature arrays of different nucleic acid sequences spotted in well-defined regions on a surface in a high density ordered fashion with spot feature sizes of between $5 - 100\ \mu m$ diameter [96]. Immobilised DNA sequences act as capture probes for fluorescently labelled target sequences, with tens of thousands of different DNA spots on a single microscope slide (see Figure 2.17). Microarrays provide an approach for many DNA sequences to be probed simultaneously using only small quantities of DNA [86]. Gene sequencing by hybridisation uses arrays of oligonucleotide probes with spots of sequential overlapping sequences. The genomic DNA is fluorescently labelled and those spots which become fluorescent on the microarray can be used to evaluate the DNA sequence [97].

Different coloured fluorescent dyes are used for different sequence probes. Commercial systems scan the whole array with laser beams (or a white light excitation source) using filters

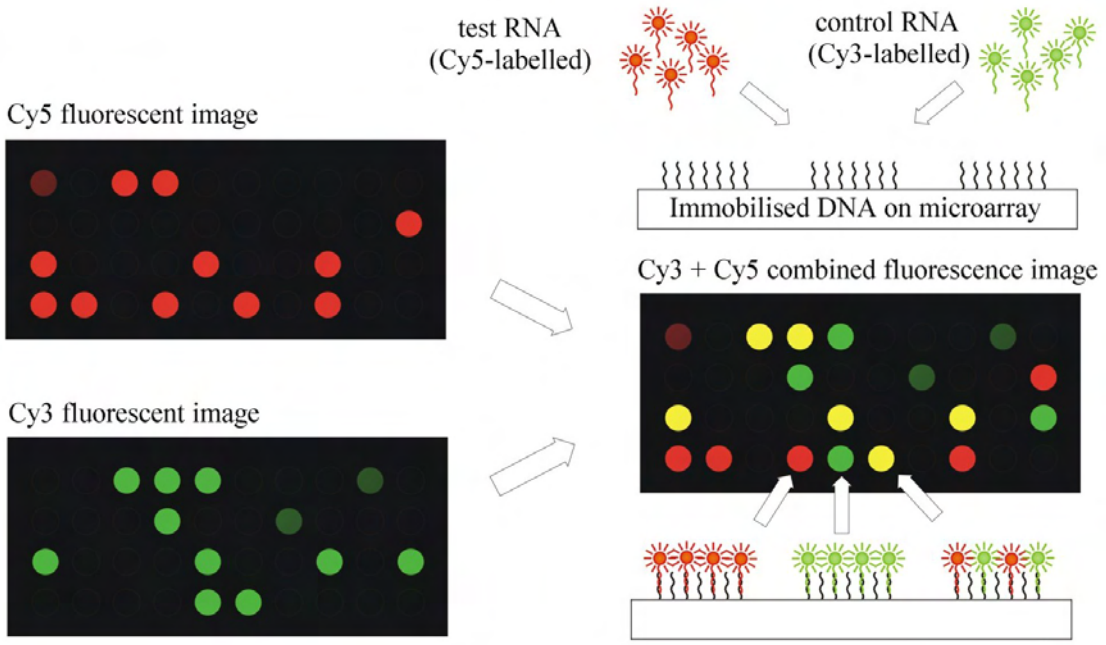

Figure 2.17: Microarrays feature different DNA sequences spotted on a glass substrate. Differential hybridisation between a sample RNA and control RNA can be used to study gene-expression. Yellow indicates no difference in hybridisation between the sample and control, green indicates the gene is down-regulated and red indicates the gene is up-regulated (Figure based on [86]).

for each dye and photodetectors to detect emission, which are used to identify regions with fluorescent labels hybridised to immobilised oligonucleotide sequences. Images are captured for each emission wavelength separately then software is used to calculate the intensity of each spot and combine the images to produce a pseudo-coloured merged image. For gene expression analysis DNA microarrays are used to detect fluorescently labelled DNA sequences created by an RT-PCR reaction from messenger RNA sequences [98]. Different DNA gene sequences are spotted in microarrays, and two-colour fluorescent hybridisation is performed to compare two samples e.g. DNA created from the RT-PCR reaction from mRNA created from a cancerous cell, and a second DNA sample created from the RT-PCR reaction of the mRNA from a healthy control cell. The two DNA samples are fluorescently labelled different colours such as Cy3 (green) or Cy5 (red), mixed together and hybridised to the microarray, as shown in Figure 2.17. Fluorescent images are captured for Cy3 (green) and Cy5 (red) and then combined enabling visualisation of up-regulated and down-regulated genes in one go.

Since it is reasonably straightforward to label DNA strands with fluorescent molecules, many other DNA hybridisation methodologies have been confirmed and tested by fluorescence [75]. Fluorophores are readily available and detection is possible with simple optical technology, such as an epifluorescence microscope. The limitations of fluorescence include photobleaching

and the limited number of different differentiable colour fluorophores available.

An important recent development is the creation of single nucleotide polymorphism (SNP) chips [2, 99]. These are DNA microarrays in which DNA oligonucleotides containing the single nucleotide polymorphism are attached in spots on the array. Commercial chips containing arrays for 10 000 SNP sequences, with a detection accuracy of 99.5 %, have been developed by companies such as Affymetrix™ (see Figure 2.18). The Affymetrix GeneChip™ microarrays were introduced in 1994 with a spot size of 100 μm diameter lithographically patterned on to a quartz glass substrate. Current chips consist of spot sizes down to 5 μm diameter, increasing the amount of content in an array by 400 times. The newest GeneChip features 500 000 SNPs within the array [100].

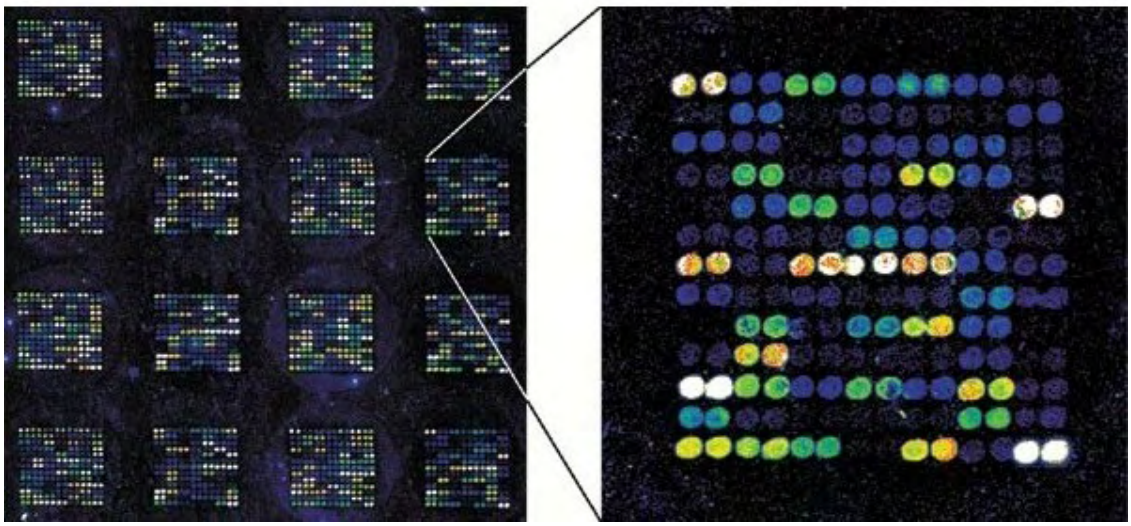

Figure 2.18: Microscope fluorescence image of a DNA microarray by Affymetrix (Image from [99]).

However, the fluorescence intensity required for analysing DNA microarrays requires a relatively large quantity of DNA sample and so PCR is required to amplify fragments of DNA. PCR is also used to fluorescently label the strands.

A recent development by Redkar *et al* is the application of optical interference coatings to microarray substrates prior to surface functionalisation to improve sensitivity. A multilayered dielectric thin-film coating was applied to the substrate to reflect excitation light that would normally pass through the substrate, thus maximising the absorption of the fluorescent dye molecules within 60 nm of the surface. The interference coating also reflected the fluorescent emission back towards the detector further increasing sensitivity. The optical interference coating was found to increase the observed intensity by a factor of over 8 times that of an un-coated control array. The detection limit for target DNA was better than 1 pM concentration, corresponding to 6 ng of fluorescently labelled DNA [101].

2.6.3 Single Molecule Fluorescence

Although microarrays require a strong fluorescent signal, alternative methods have been developed for much higher sensitivity. Single molecule fluorescence detection has been developed and applied to the study of DNA [102] and nucleic acids [103], observing Forster resonant energy transfer (FRET) using scanning near-field optical microscopy (SNOM). FRET is the non-radiative transfer of electronic excitation energy between donor and acceptor dye molecules in close proximity (between $1 - 10\ nm$), such as in Figure 2.19. The donor is excited by light absorption at its excitation wavelength. When an acceptor molecule is within 10 nm, a dipole-dipole coupling interaction between the two molecules transfers excitation energy from the donor to the acceptor molecule, which then returns to the electronic ground state by fluorescent emission [3]. The distance between the donor and acceptor affects the level of energy transfer and hence fluorescent intensity of the acceptor.

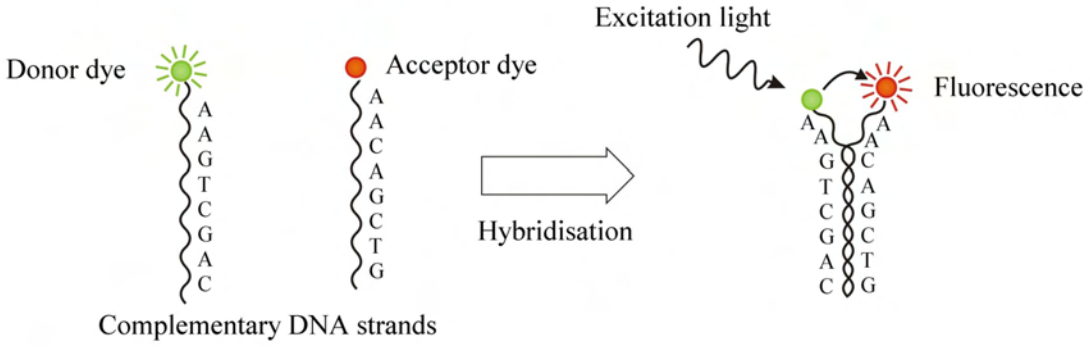

Figure 2.19: Forster resonant energy transfer (FRET) can be used to monitor DNA hybridisation. When an acceptor dye is in close proximity to an donor dye molecule, the donor molecule non-radiatively transfers excitation energy to the acceptor molecule, which then fluoresces instead.

There are two approaches to single molecule fluorescence; either studying free molecules that diffuse in and out of a small volume illuminated by a laser beam, or studying the characteristics of molecules immobilised on a surface. Free diffusing molecules are only detected when they traverse the focused excitation laser beam, giving short fluorescence bursts. This information gives a distribution of molecular properties unimpeded by surface attachment effects [104]. It is possible to observe Brownian motion of individual fluorescent molecules using fluorescence correlation spectroscopy [105]. The second method involves spatial confinement of molecules by surface attachment [102], trapping the molecule in a matrix [106], or optical trapping [107]. This enables observation of the behaviour of individual molecules over time, for example in response to changes in buffer conditions.

Whilst single-molecule techniques provide advantages for studying the dynamics of individual molecules, it is not suitable for high-throughput analysis. In order to reduce errors and false

positives multiple copies are needed, which would be laborious with this method. In addition to this, the assay would need to be done for two strands since there are two versions (and haplotypes) of each chromosome.

2.6.4 Fibre Optic Biosensors

Fibre optic biosensors have been developed based on fluorescence at both optical [108] and infrared wavelengths [109]. They have been developed for sensing specific target molecules rather than mass-sequencing, which has driven DNA microarrays. Fibre optics have been used for the optical detection of DNA, featuring DNA capture sequences immobilised on the end surface of the fibre [110]. Hybridisation with complementary target DNA is detected by fluorescence emission from either fluorophore labelled sequences [111], or intercalating dyes which emit enhanced fluorescence upon hybridisation [112].

The general principal of operation of fluorescent fibre optic sensors involves coupling excitation light from a laser, light emitting diode (LED), or white light source into an optic fibre via total internal reflection (see Figure 2.20). The excitation light excites fluorescent molecules that have been immobilised at the distant end of the fibre from a sample solution. Fluorescence emission within the angular acceptance range of the optic fibre is guided back down the fibre to a photo-detector [113]. For example, a DNA fibre optic sensor featuring a 25-mer oligonucleotide sequence immobilised on the exposed core was used to capture $\sim$ 300-mer genomic DNA fragments from *Escherichia Coli* featuring a complementary 25-mer sequence [114]. Fluorescence emission was detected within 20 s of adding the complementary DNA mixed with the intercalator ethidium bromide.

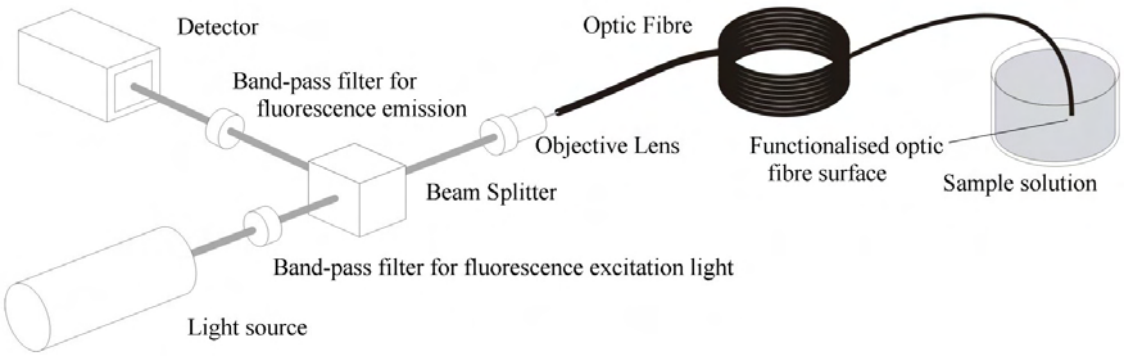

Figure 2.20: General optic fibre sensor experimental setup (Figure based on [113]).

Multiplexing of different assays is possible through optic fibre bundles or multi-core fibres

consisting of around 50 000 fused optical fibres [115]. The cores of bundled fibre arrays were selectively etched to form wells in the cladding material to house 3 μm diameter microbeads functionalised with capture sequences for different fluorophore labelled probes (see Figure 2.21)[110]. This approach enables multiplexing of detection assays, but requires a lot of differently functionalised microbeads. It is more complex and offers less capacity than microarray chips, but has the advantage of very low detection levels. Epstein *et al* achieved the detection of just 600 DNA copies per microbead, corresponding to 10^{-21}mol [113].

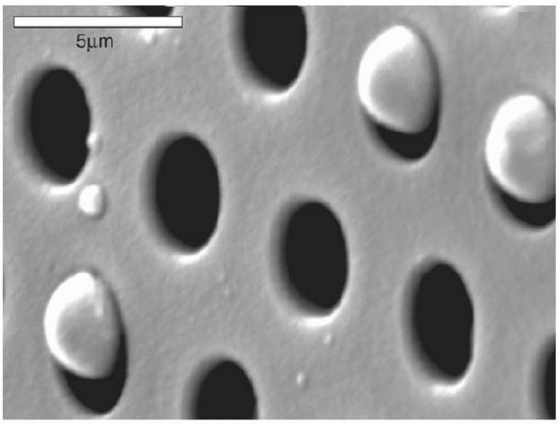

Figure 2.21: SEM image of the end face of a bundled fibre optic array with etched core wells to house 3 μm diameter functionalised microbeads (Image from [110]).

2.7 Gold Nanoparticle-Based Biosensors

Fundamental to the development of biosensors (using nanoparticle labels), biomaterials and DNA assembly of non-organic components is the interaction between the particle and oligonucleotide sequences. Functionalisation of the surface of various types of particles with DNA enables construction of nanoscale structures via the unique molecular recognition properties of DNA. This technology enables the development of mesoscale features smaller than currently available using lithographic techniques (because resolution is limited by the wavelength of light and the effects of chemical etching), but larger than chemically synthesised molecular structures. Consequently, programmed self assembly is very useful for the development of nano-devices by the 'bottom-up' approach [116, 117]. DNA-gold nanoparticle conjugates also offer an alternative labelling technique to fluorophores for more reliable DNA-chip detection [118].

2.7.1 Nanoparticle Enhanced SPR Sensors

Nanoparticles offer a valuable label for SPR based biosensor systems. An example of this was the chip-based optical detection method for nanobead-oligonucleotide hybridisation developed by Reichert *et al* [119]. A glass substrate was patterned with DNA capture sequences, which were hybridised to complementary DNA sequences attached to 30 nm diameter gold nanoparticles. The patterns of hybridised particle-DNA conjugates were observed by using both transmission and reflectance microscopy. This produced easier detection of hybridised sequences, than by using fluorescence, due to simplified optical apparatus; the approach proved suitable for high throughput DNA analysis methods.

Recently, nanoparticle enhanced surface plasmon resonance imaging was used for single nucleotide polymorphism genotyping by Li *et al* [120]. The use of gold nanoparticles with surface plasmon resonance imaging (SPRI) enabled oligonucleotide detection at a concentration as low as 1 pM. Capture oligonucleotide sequences were immobilised in a microarray structure on a gold SPR surface. When the complementary target DNA molecules (T) were present, the enzyme *Taq* DNA ligase ligated a probe sequence (L) to the immobilised oligonucleotide, as shown in Figure 2.22. After denaturing the targets, the ligated oligonucleotides were used to capture complementary DNA-labelled gold nanoparticles, enhancing the plasmon resonance measured.

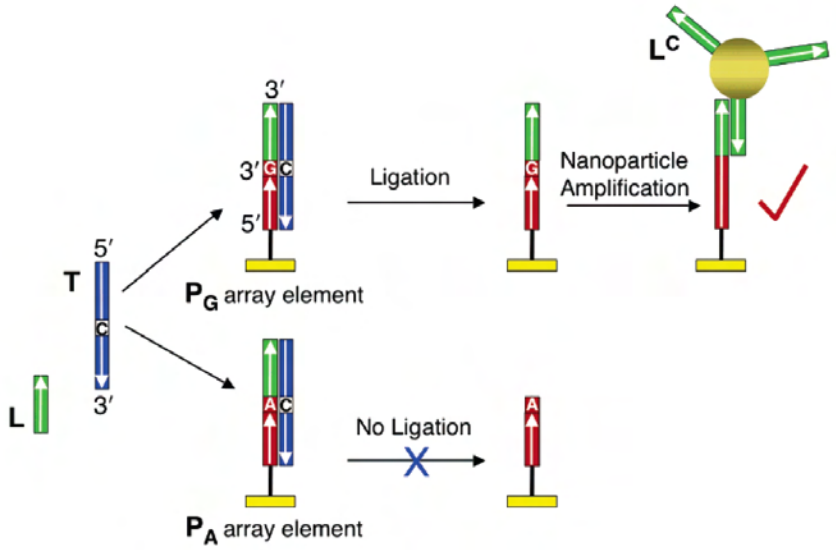

Figure 2.22: Ligation only occurs when the target DNA sequence (T) is complementary to the immobilised sequence, and does not contain a single base-pair mismatch which prevents ligation of the nanoparticle capture sequence (L). Figure from [120].

Gold colloids have also been used as 'topographic labels' to characterise DNA hybridisation [121]. Capture oligonucleotide sequences were immobilised on a sputtered gold sub-

strate. Target gold particles functionalised with complementary DNA sequences were then hybridised to the surface. Non-specific binding of pure gold particles, and probes with non-complementary sequences was low. However, detection relied on the use of atomic force microscopy (AFM) which can be very laborious.

2.7.2 DNA-Particle Devices and Plasmon Effects

A major contributor to the field of new technology for DNA analysis using gold particles is the Mirkin group. Mirkin *et al* developed a DNA-based method for assembling nanoparticle aggregates [122]. Two non-complementary DNA oligonucleotides (A and B) were capped with thiol groups, which covalently bound to 13 *nm* gold colloids. Upon addition of an oligonucleotide linker, featuring sequences A' and B' complementary to the two groups of functionalised gold nanoparticles, an aggregate was formed. A schematic of this process is shown in Figure 2.23. The main advantages of using DNA oligonucleotides over other molecules are the high degree of discrimination between binding, the relative ease of oligonucleotide synthesis, and reversibility of hybridisation. This approach combined the chemistry of DNA and colloidal materials, rather than simply using molecular recognition to build geometric structures from DNA. Instead, hybrid materials were created whose properties are dependent upon their constituents, but different to both.

Figure 2.23: Gold nanoparticles were functionalised with two different oligonucleotide sequences A and B. A linker sequence was added featuring sequences A' and B', complementary to sequences A and B respectively on the gold nanoparticles, enabling aggregate formation.

It was found that the gold colloids functionalised with DNA were stabilised against agglomeration compared to bare nanoparticles when heated or in solutions of high salt concentration. Upon addition of a complementary DNA linker sequence hybridisation caused aggregate growth, changing the colour of the solution from red to purple and forming a precipitate upon full aggregate growth (shown schematically in Figure 2.24). When heated, the DNA-colloid aggregates disassemble as the DNA bonds 'melt', and the colour changes from a clear liquid with the precipitate at the bottom, to a purple and then red solution, showing reversibility of the process. The explanation of this effect is that plasmon absorption band of the gold particles is sensitive to the interparticle spacing and aggregate size. The plasmon band absorption maximum red-shifts and broadens as the aggregate size increases, making

the colour the particles appear change from red to blue [30, 123]. Storhoff *et al* modelled the UV-visible extinction spectra for DNA-linked gold nanoparticle aggregates and calculated a red-shift of the peak absorption wavelength from 540 nm to 630 nm with an increase in aggregate size from 0.6 μm to 2.4 μm [124].

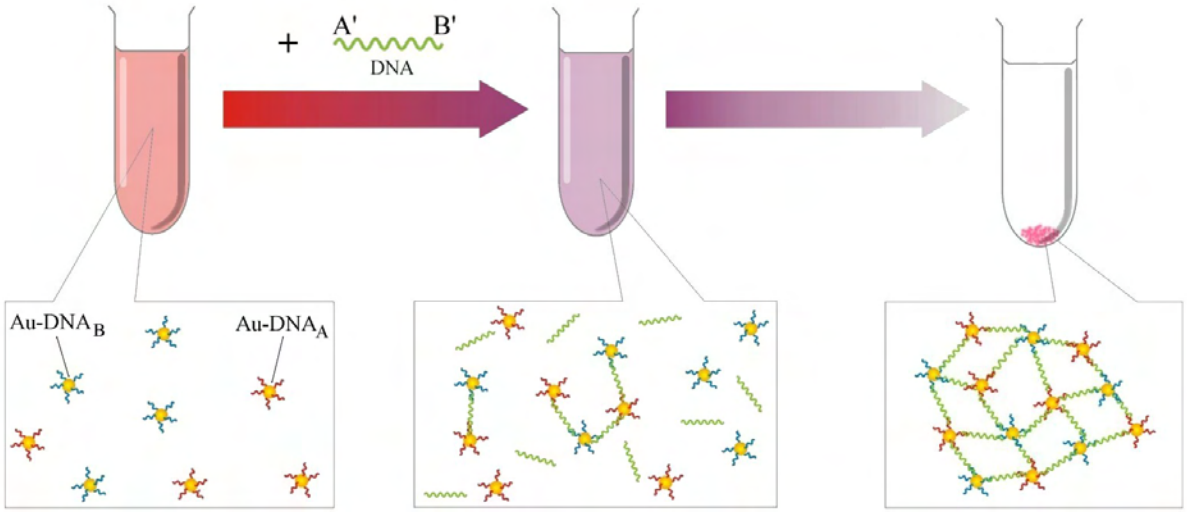

Figure 2.24: Gold colloids in suspension appear red in colour. As complementary DNA hybridisation causes aggregate formation, the particles become closer together, shifting the plasmon band and changing the appearance to purple. Upon full aggregation a precipitate was formed.

Mirkin's group have also developed a colourimetric DNA detection assay [30]. The DNA-labelled particles act as probes to bind with a target linker strand. The nanoparticle probes feature a complementary sequence to the target; the probes are added to a solution of the linker strands, and if the sequences are complementary aggregation occurs. When the particles are deposited on a reverse-phase silica gel plate they form a blue spot. Mismatched sequences remain red since there is no aggregation. The spots are evaluated as a function of temperature, to map the melting temperature of the aggregates. Perfectly complementary sequences will hybridise more efficiently and remain aggregated at higher temperatures than for the slightly mismatched sequences. Two oligonucleotide sequences can be differentiated providing there is at least $1°C$ difference in melting behaviour and by the associated colour change of the gold colloidal aggregate.

An in-depth study investigated the impact of the oligonucleotide linker length and aggregate size on the optical properties of DNA-linked 15 nm gold nanoparticle assemblies [124]. By using oligonucleotide linkers of different lengths to form aggregate assemblies, the aggregate growth rate (at room temperature) was found to be under kinetic control and inversely proportional to linker length. The plasmon frequency of the nanoparticle assemblies was observed to shift towards the red wavelengths as aggregates formed (see Figure 2.25)[124]. The extent of the plasmon shift was found to be inversely dependent upon linker length, so

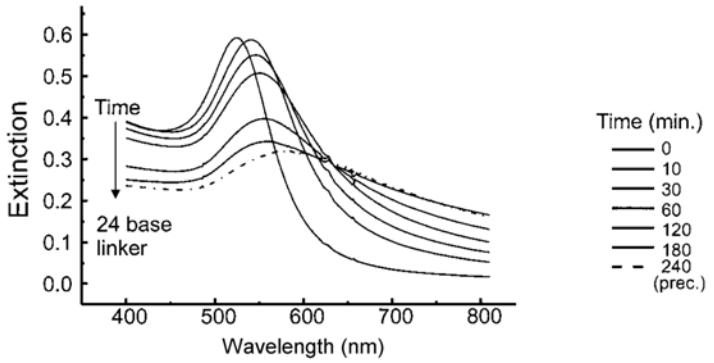

Figure 2.25: The plasmon band absorption maximum of 15 *nm* diameter gold nanoparticles functionalised with DNA is red-shifted over time with increasing aggregate size resulting from hybridisation of a DNA linker sequence (Figure from [124]).

that aggregates using the shorter linker exhibited the largest spectral change. This shows that the aggregate size is kinetically controlled by the linker length. At room temperatures the shorter DNA linkers will form larger aggregates, and hence feature larger red shifts. In this way, the optical properties can be determined by linker length.

Assemblies of the DNA-gold aggregates were studied for their temperature dependence. Upon heating the assemblies exhibited further red shifting of the plasmon band absorption maximum. This effect was examined by annealing the DNA-gold nanoparticle aggregates at a temperature just below the melting temperature. It was hypothesized that as the temperature was increased the larger aggregates grew at the expense of smaller ones (Ostwald ripening), generating a larger red-shift due to increased aggregate size. After annealing, the properties remain fixed (below the melting temperature) and are virtually identical for all linker lengths tested. It was concluded that a red-shift in the plasmon frequency is related to an increase in the aggregate size, independent of the linker length upon annealing of the structures. The plasmon frequency itself was therefore found to be determined by the aggregate size.

More recently, Mirkin's group have developed a homogeneous oligonucleotide detection method, useful for monitoring and quantifying the amount of a product produced by the polymerase chain reaction (PCR) [125]. DNA fragments are amplified using primer sequences to hybridise with denatured DNA. The polymerase enzyme extends the primer sequences to produce the complementary strand of the initial DNA fragments. The PCR product detection method developed uses gold nanoparticle probes functionalised with two non-complementary oligonucleotide sequences. The PCR product being amplified is complementary to both sequences such that it will cause aggregation of nanoparticles (see Figure 2.26). The size of gold nanoparticle aggregates formed was controlled by varying the ratio

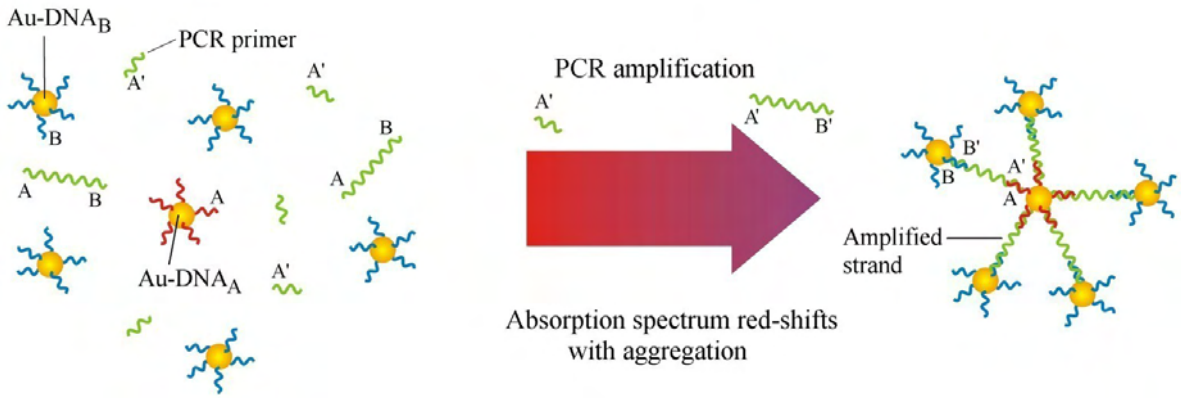

Figure 2.26: Before PCR, there aren't enough target DNA sequences (A'-B') to hybridise with the gold nanoparticles functionalised with complementary DNA sequences A or B. As PCR amplification of target DNA occurs, aggregates form red-shifting the plasmon absorption of the gold nanoparticles, observable by a red to purple colour change of the solution [125].

of the two non-complementary oligonucleotide functionalised particles. The smaller aggregates did not precipitate enabling colourimetric detection of linker sequences in solution. By observing the extinction at 640 nm for a 5 : 1 probe ratio, the concentration of the target molecule can be determined. Before PCR amplification there is a large excess of nanoparticle probes compared to the target linker sequence. As the target sequence is amplified more aggregates are able to form. A colour change of the solution from red to purple is noticeable as enough PCR product has been amplified to enable large numbers of aggregates to form. The detection limit is around 50 pM [125].

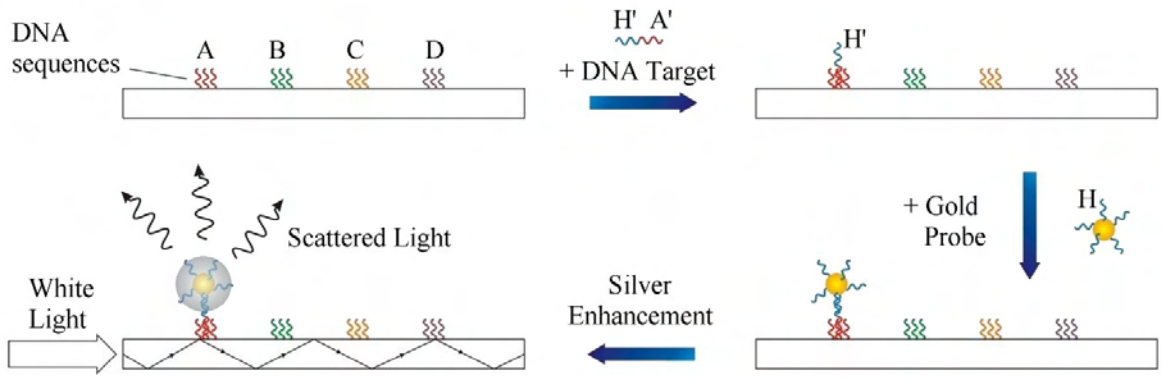

Figure 2.27: Schematic illustration of target DNA hybridisation to microarrays and optical scattering detection using silver enhanced gold nanoparticle probes (Figure based on [126]).

Gold nanoparticles have been used for the detection of genomic DNA in a sandwich-assay; combining DNA microarrays, gold nanoparticle labels and silver enhancement with optical detection [6]. Nanosphere Inc (founded by C. A. Mirkin and R. L. Letsinger) developed a detection methodology based upon immobilising oligonucleotide capture sequences on a glass substrate, these immobilised sequences were targets for complementary DNA sequences. The

presence of the target sequence was detected by subsequent hybridisation of gold nanoparticle probes. Silver enhancement of the gold nanoparticles enabled quantification of the amount of immobilised probes by measuring scattered light [126]. The glass slides are illuminated from the side, generating an evanescent field perpendicular to the plane of the test slide which is scattered by the silver-amplified gold nanoparticles [127]. The scattered light can be focused on to a CCD camera to capture an image [128].

The basic principles of this detection system are shown in Figure 2.27. Different non-complementary oligonucleotide sequences, for example A, B, C and D, are spotted on to a glass substrate and sample DNA is added. If the sample DNA contains the target sequence A' complementary to A, it will be immobilised on the slide. The presence of the target sequence is detected by adding a gold nanoparticle probe functionalised with an oligonucleotide sequence H, complementary to H' in the target DNA. Silver enhancement procedures (similar to those described in Chapter 3) were used to grow silver around the gold nanoparticles amplifying the optical scattering. When using a conventional flatbed scanner the increase in scattering of immobilised gold nanoparticles by silver amplification was up to a factor of 10^5 over gold nanoparticles alone [129]. The detection limit of this methodology was found to be 50 fM corresponding to around 200 probes per spot, an average of 0.001 gold particles per μm^2, compared to a fluorescence detection limit using Cy3 of 7.2 particles per μm^2 (1.4 million per spot) [6]. Recently, this methodology has been used for detecting a biomarker of Alzheimer's disease [130].

An alternative approach for a nanoparticle-based DNA sensor is to create a dry-reagent strip biosensor for DNA analysis [131]. Glynou and colleagues developed a strip-based hybridisation assay as shown in Figure 2.28. The bottom end of the strip is immersed in buffer solution (i), which rehydrates the strip. DNA functionalised gold nanoparticles hybridise to the added sample DNA, which has already been hybridised with biotinylated oligonucleotides (ii). Streptavidin is immobilised in the test zone and captures the biotinylated DNA-nanoparticle conjugates forming a red line due to the presence of colloidal gold (iii). Another zone acts as a control to capture excess nanoparticles, featuring a DNA sequence directly complementary to the functionalised gold nanoparticles (iv). A positive red line can only be seen in the test zone when the target biotinylated DNA is present and has hybridised with the nanoparticles. Target DNA concentrations as low as 2 $f$mol were detectable.

The advantages of nanometre-scale gold or silver particles as bioconjugation labels are that they can be tailored for spectra, they have strong absorption and scattering, and unlike fluorescent labels do not suffer photobleaching [132]. Silver plasmon resonant particles have been

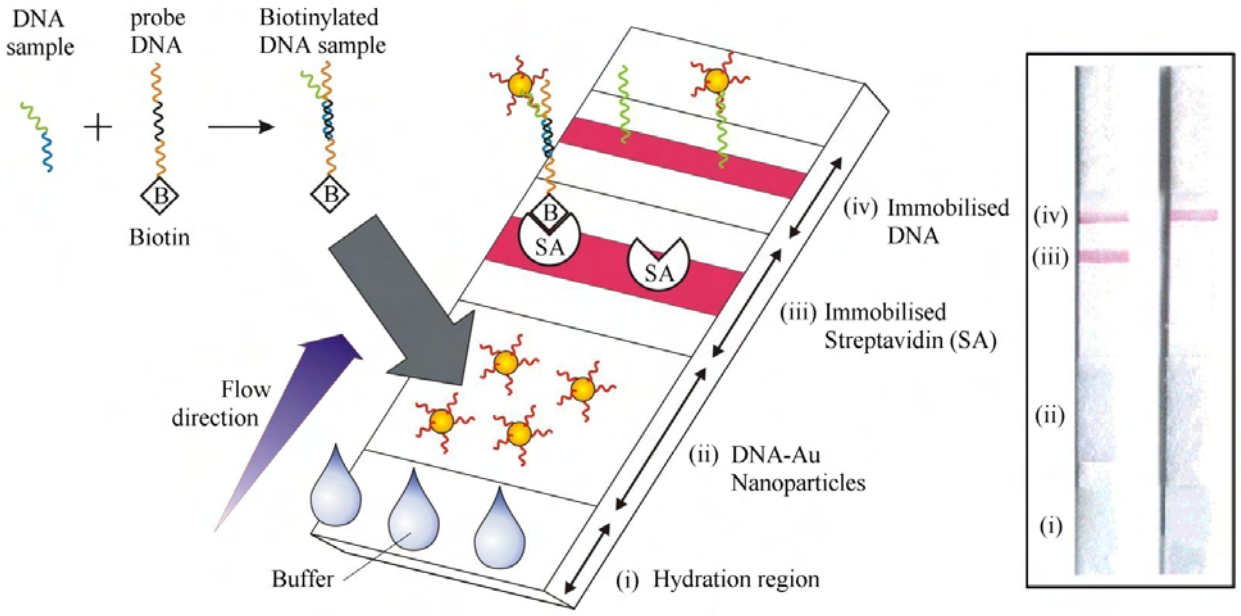

Figure 2.28: Strip-based hybridisation assay for DNA detection. A schematic diagram is shown on the left with positive and negative results shown in images of the strips on the right hand side (Figure from [131]).

used for base-pair mismatch recognition achieving a sensitivity of 1×10^6 oligonucleotides per spot, around 60 times greater than using Cy5 fluorescent labelling (6×10^7 oligonucleotides per spot) [133]. DNA microarrays were used in a hybridisation assay to screen for a known SNP site in the breast cancer gene BRCA1. The silver plasmon resonant particles used were $\approx 55\ nm$ in diameter, grown around a $5\ nm$ gold core and were functionalised with anti-biotin. The detection oligonucleotide was biotinylated and bound to the colloids. Heating and washing of the microarray removed sequences featuring mismatches, leaving immobilised colloids only where the sequence was exactly complementary.

Gold nanoparticles have been used as molecular beacons to quench fluorophore emission [134]. In this technique a single stranded DNA sequence has a fluorophore at one end and a gold nanoparticle at the other. The sequence is chosen such that it will form a hairpin loop when single stranded, and the gold nanoparticle will be in close proximity to the fluorophore, quenching emission (Figure 2.29 (a)). When complementary target DNA hybridises to this molecule the gold nanoparticle and fluorophore become spatially separated and the fluorescent emission can be seen (see Figure 2.29 (b)). This technique has been used for single mismatch detection of oligonucleotide hybridisation [135].

Automated systems have been developed to read DNA chips using silver enhancement of hybridised gold nanoparticles to bridge electron gaps, and then measure which electrodes have a drop in resistivity [136]. The 10 μm region between the electrodes is functionalised

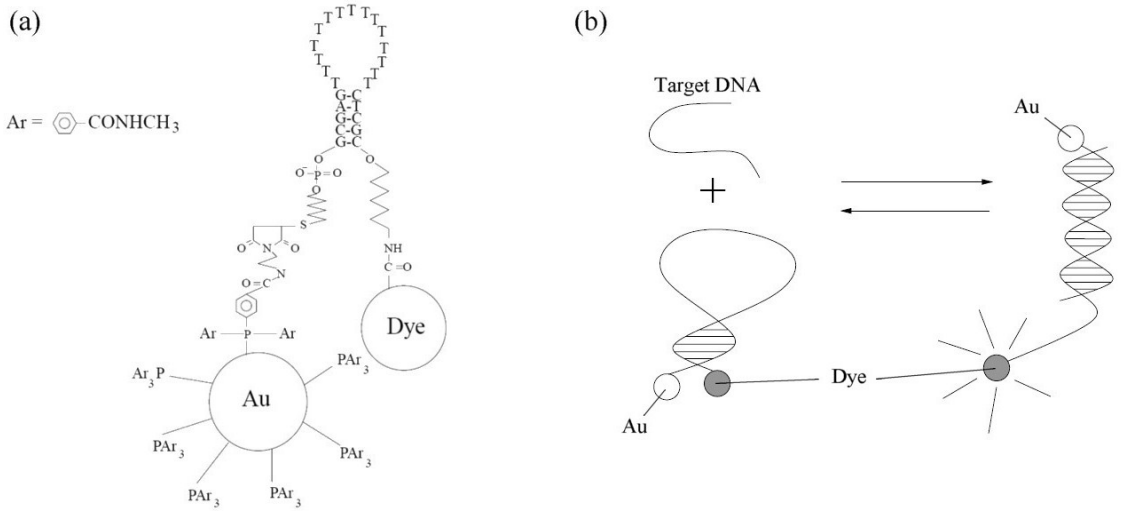

Figure 2.29: Gold nanoparticles can be used as molecular beacons for quenching fluorescence emission (Figure from [135]).

with DNA capture sequences, as shown schematically in Figure 2.30 (a). Biotin-modified complementary oligonucleotide target sequences are hybridised to the immobilised sequences on the chip (b). Streptavidin-modified gold nanoparticles are added which bind to the biotin (c). Moeller *et al* also found that streptavidin-modified gold nanoparticles were more stable than thiol-modified particles, and that this labelling procedure was easier and less time consuming than functionalising gold nanoparticles with thiol-modified oligonucleotides [137]. Silver enhancement was then used to bridge the electrode gap (d). The chips featuring 42 electrodes fabricated from gold on a silicon dioxide substrate have a sensitivity of 5 pM [137].

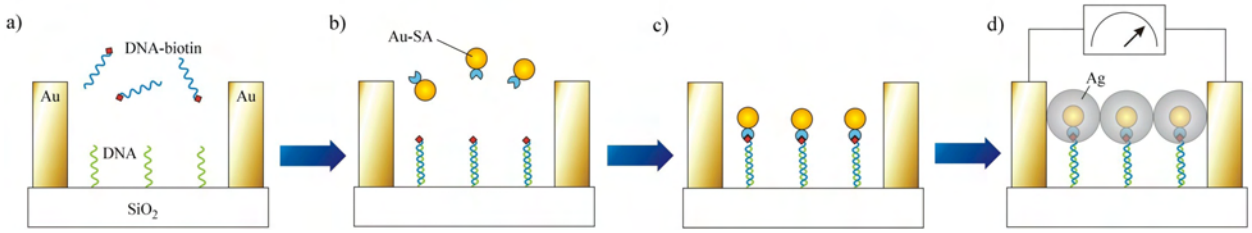

Figure 2.30: A DNA sensor based on a decrease in resistivity across an electrode gap following silver enhancement of captured complementary DNA labelled gold nanoparticles (Figure based on [137]).

Using a similar methodology, it is possible to develop electrical sensors to detect DNA sequences at concentrations as low as 500 $f$mol [7]. The approach taken by Park *et al* used 13 nm diameter gold colloids functionalised with thiol-modified oligonucleotide sequences, and filled-in gaps on electrodes for successful DNA probe-target binding events (see Figure 2.31). Silver deposition around the nanoparticles was then used to generate measurable changes in electrical conductivity. Although a greater sensitivity was achieved than that by

Moeller *et al*, this was an experimental setup rather than an automated detection system for commercial use.

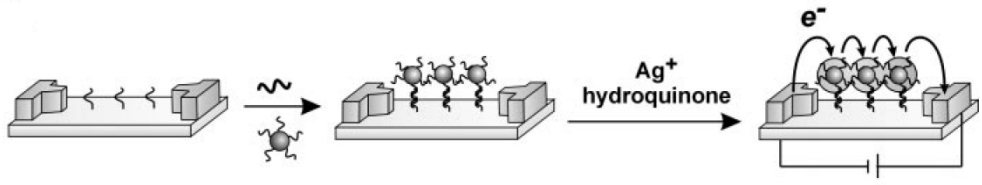

Figure 2.31: Electrical detection of DNA hybridisation using gold nanoparticle labels (From [7]).

Recently, Tsai *et al* showed that gold nanoparticle binding across electrodes could be used for DNA detection without silver-enhancement. Thiol modified gold nanoparticles were immobilised in a monolayer across a 300 nm electrode gap. Upon addition of DNA, functionalised gold nanoparticles were captured forming a multilayer of gold nanoparticles and lowering the resistivity across the contact [138]. Target DNA sequences were detected at concentrations as low as 1 fM. Whilst this detection method is very sensitive, it does not enable identification of more than two SNPs within one strand, whilst this may be achievable optically using nanoparticle probes with different plasmon resonances or different coloured fluorophores.

2.7.3 Barcoded-Particle Sensors

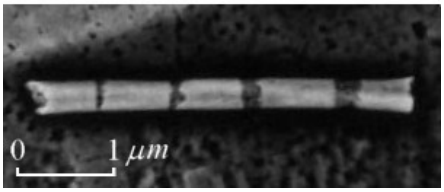

Figure 2.32: SEM image of a metallic barcode micro-rod used as distinguishable molecular label, with thin silver regions separated by gold regions (Image from [139]).

An alternative to DNA arrays is the use of oligonucleotide-particle based metallic barcodes [139]. The target oligonucleotide DNA capture sequence was fixed onto a metallic cylinder ($\sim 5\ \mu m$ long) with a uniquely identifiable submicrometre barcode pattern of different metal bands (minimum size 50 nm). If there was successful hybridisation, then it was identifiable by captured fluorescent probes in a barcode pattern. The number of assays that can be done at once are not limited by the different colours of light that are distinguishable, hence extremely high multiplexing is achievable. The rods were fabricated by sequential electrochemical deposition of different metal ions into template pores ($\sim 200 - 300\ nm$ diameter), giving stripes of different metals, as shown in Figure 2.32.

A recent example of this method used metallic barcodes for an immunoassay [140]; unique barcode patterns of gold and silver bands of differing sizes were created along a nanowire (see Figure 2.33). This barcode was observable on an optical microscope in reflectance, enabling identification of the antibody it had been functionalised with. A sandwich assay was carried out in which the immobilised antibody on the nanowire bound to target antigens tagged with fluorescently labelled antibodies. Fluorescence image analysis was then used to determine which antigens were present in a multiplex assay in conjunction with the unique identifying barcode.

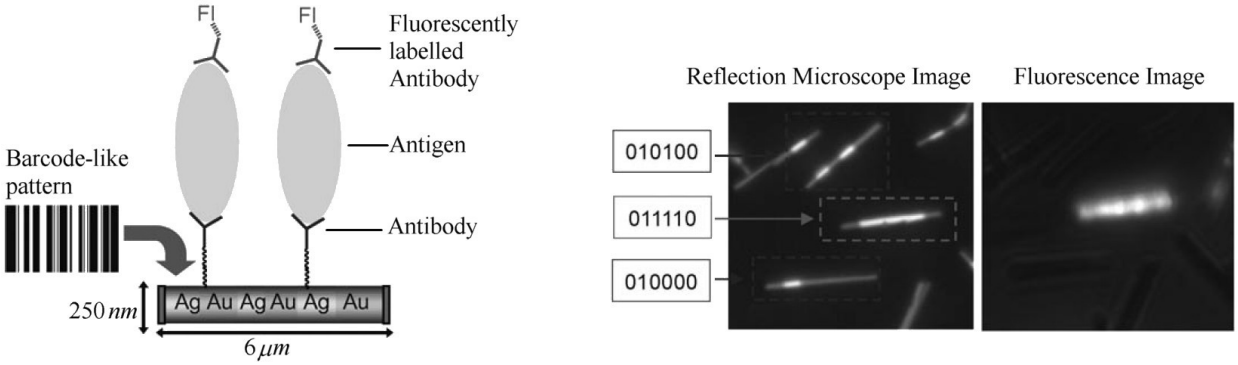

Figure 2.33: Barcoded nanowire labels for identification of individual immunoassays. The barcode pattern identifying which assay is associated with each nanowire is visible on an optical microscope, with fluorescent imaging providing the outcome of the test (Figure adapted from [140]).

An alternative approach to the electrodeposition of alternating layers of different thicknesses to make up a composite nanowire barcode is to simply to etch a barcode pattern through an evaporated layer of metal. Hoffmann *et al* have developed barcoded silicon microbeads as identifiers in a microfluidic detection and characterisation system [141]. They plan on using the microbeads as a platform for the detection of target DNA molecules. The microbeads (measuring 1000 μm × 500 μm × 100 μm) were fabricated by evaporating an aluminium layer on a silicon substrate and photolithographically patterning a barcode. A 200 nm layer of silicon nitride was then deposited on top to protect the barcode and to generate a substrate for chemical modification. As the bead passes down a microfluidic channel, it is identified by observing the reflected laser beam intensity with time as the bead passes, reading the barcode and identifying the assay (as shown in Figure 2.34).

The concept of barcoding particle labels has also been extended to quantum dots [142]. Four different sizes of quantum dots (featuring unique emission wavelengths) were coated on to 8 μm diameter microbeads in different ratios. Consequently, the beads can be identified by looking at their emission intensity ratios for each of the four quantum dot emission wavelengths.

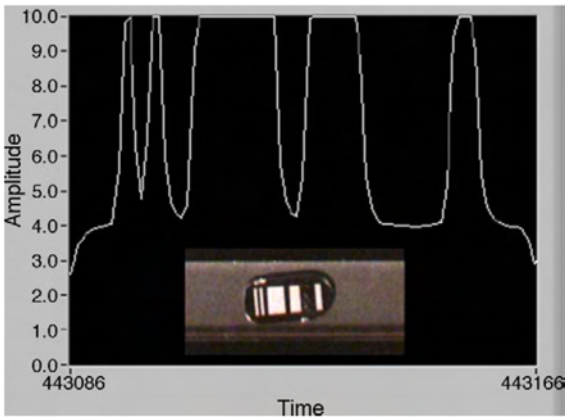

Figure 2.34: Barcoded microbeads are detected by a change in reflected laser intensity measured on a photodiode as the microbead passes along a fluidic channel (inset). Figure from [141].

2.8 Interference and Diffraction-Based Biosensors

Optical biosensors have been developed for the detection of biomolecules based on scattering, interference, holograms, and diffraction gratings. The optical biosensors reviewed below rely on optical properties changing upon the capture of target probes. The binding of target molecules results in a change of the optical signal being measured.

A recent development similar to the approach taken in this project is the "Chemoresponsive" diffracting grating sensor developed by Bailey *et al.* This is based on modulating the transmission of light through a grating upon binding of a target analyte to the pattern [14, 143, 144]. The sensor is based upon an array of 5 μm squares forming a two-dimensional diffraction grating matrix with a 10 μm periodicity. The diffraction methodology (see Figure 2.35) was developed for examining colloidal gold films [14].

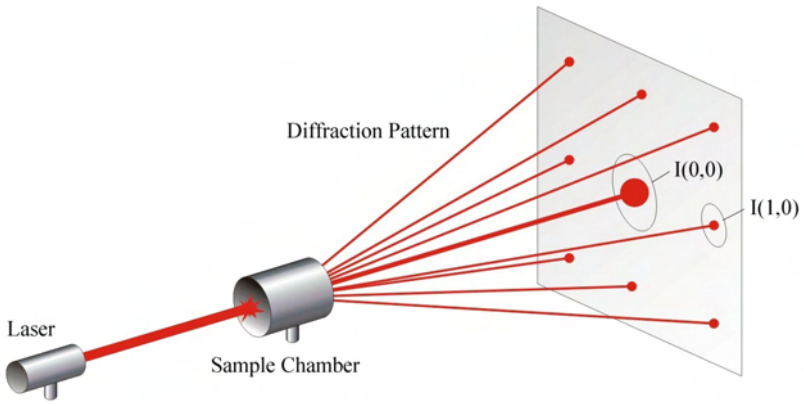

Figure 2.35: Diffraction sensor based on modified transmission and change in diffraction efficiency upon analyte binding (Figure based on [143]).

The grating patterns were created by electrophoretic deposition of gold nanoparticles on

a conducting substrate using photoresist barriers created with a poly-dimethyl siloxane (PDMS) stamp. The substrate (indium tin oxide) was patterned with a photoresist lattice by micro contact printing. The patterned substrate was then subjected to electrophoretic deposition. A voltage was applied across the sample to make the patterned face positively charged, attracting negatively charged gold colloids from the solution. After removal of photoresist, the resulting gold films (15 nm thick) were found to exhibit significant diffraction visible by eye. This led to the development of a sensor whereby analyte binding would further modulate the refractive index contrast periodically and increase the diffraction signal.

The chemoresponsive diffraction gratings were created by placing the PDMS stamp on top of cleaned glass microscope slides and capillary action drew in a solution containing suspended material to create a grating lattice as the solvent evaporated. This was done with vapochromic charge-transfer salt [143] and with various polymers [144] for detection of volatile organic compounds such as chloroform. In this situation the square pattern was left uncovered and the surrounding lattice structure acted as the receptor region. Upon the addition of various analytes the refractive index of the lattice increased, resulting in an increase in diffraction efficiency, monitored in real-time.

Recently, this diffraction sensor has been developed for the detection of hybridisation of gold nanoparticle probes to DNA patterns on glass [145]. This was done as a sandwich-assay which could be applied to haplotyping. In this configuration a photoresist lattice was patterned on to glass microscope slides. A 2 nm seed layer of titanium was then thermally evaporated, followed by 10 nm of gold. The photoresist was then removed with acetone to create the 4×4 mm array of 5 μm gold squares by 'lift-off' photolithography (see Section A.2.2). The substrate was passivated with octydecyltrimethoxysilane (OTS) 2 % in toluene to minimise nonspecific binding. Single stranded DNA modified with an attached thiol was then attached to the thin gold film. The sample was then immersed in a solution of gold nanoparticle probes functionalised with DNA oligonucleotides non-complementary to the immobilised strands on the surface. Complementary target DNA was added to cause both hybridisation of the gold nanoparticles to the target, and the target with the immobilised sequence on the surface (see Figure 2.36). Diffraction was monitored in real-time as the target DNA was added and hybridisation occurred, causing immobilisation of the gold nanoparticles in spatially defined areas on the substrate.

Owing to the two-dimensional nature of the surface patterning the sample acted as a diffraction grating in both the x and y directions. For ease of monitoring the diffraction efficiency was only calculated for one direction, normalising $I[m = (1, 0)]$ to the zeroth order trans-

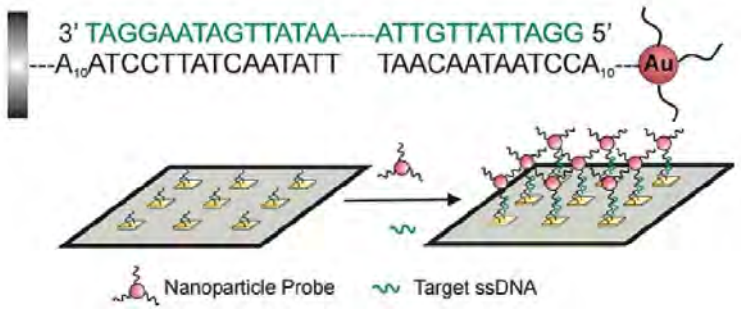

Figure 2.36: Schematic diagram of the sandwich-assay developed by Bailey *et al.* for immobilising gold nanoparticles in a 2−D diffraction grating array (Figure from [145]).

mission $I[m = (0, 0)]$, as shown in Figure 2.35. The diffraction intensities were monitored simultaneously at three different wavelengths ($\lambda = 632.8\ nm$, $543.5\ nm$ and $532\ nm$ using a red HeNe, green HeNe and blue Nd/YAG lasers respectively). The diffraction intensities that were measured were found to be wavelength and concentration dependent. This is because the resonant frequency of the particle (and consequently its absorption spectrum) depends upon both the particle size and neighbouring particle interactions (which is distance dependent). At a fixed concentration the diffraction intensities were monitored in real-time as hybridisation occurred. All three wavelengths initially showed a small decrease in diffraction efficiency (less than 5 %) up to approximately 8 hours (see Figure 2.37). The largest observed change in diffraction efficiency (ΔDE %) was observed after around 14 hours for each wavelength, with red 633 nm showing the largest change of nearly 30 % reduction. Interestingly, the two shorter wavelengths showed an increase in diffraction efficiency after 8 hours.

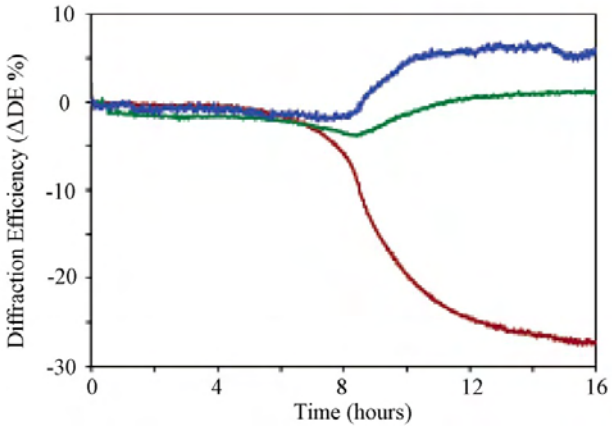

Figure 2.37: The change in diffraction efficiency (ΔDE %) with time as gold nanoparticles hybridised to the grating was monitored simultaneously at 633 nm (red), 543 nm (green) and 532 nm (blue) wavelengths (Figure from [145]).

As the concentration of target DNA was increased, and more nanoparticle conjugates were

hybridised to the grating, the interparticle distance and therefore the resonance of the particles changed. This behaviour accounts for the different diffraction response at each wavelength as the change in resonance led to more or less absorption. When the maximum diffraction change for each concentration was plotted out, it was found that at low concentrations (around 1 particle per μm^2), the particles were spread out enough that little interaction occurred between particles and the plasmon absorption was almost the same as particles in solution, not generating a significant change in diffraction. At higher binding densities, the plasmon absorption of the particles was red-shifted and the magnitude in the change of diffraction increased. At even higher concentrations, the diffraction change reduced as the plasmon absorption moved off resonance.

2.8.1 Scattering-Based Sensing

Optical forward-scattering in transmission has been used for the detection of bacterial colonies [12]. Banada *et al* developed a non-invasive optical scattering system for the identification of bacterial species. In particular, they investigated detecting *Listeria monocytogenes* and exploited phenotypic differences with other *Listeria* species. The bacterial cultures were grown and then plated on Agar plates. A laser beam (635 nm wavelength) was then transmitted through the plate and the diffracted or scattered light was observed on an image plane at a distance of 30 cm away. Diffraction theory was used to model the scattering patterns and was found to be in good agreement with the patterns observed. A database of 108 different strains was created for 6 species of *Listeria*, with a 91 % or greater accuracy in determination of species.

2.8.2 Interference-Based Detection

Interference sensors are based upon thin films on a reflective substrate. Interference is generated between white light entering the film and light reflected from the bottom surface, which interfere with a phase difference dependent on the wavelength and film thickness. Changes in the thickness of the film leads to a change in the apparent colour of the sample. Thus as layers of biomolecules are absorbed on the surface the film thickness increases and the resulting surface yields a colour change as a result of constructive and destructive interference of the different wavelengths of light.

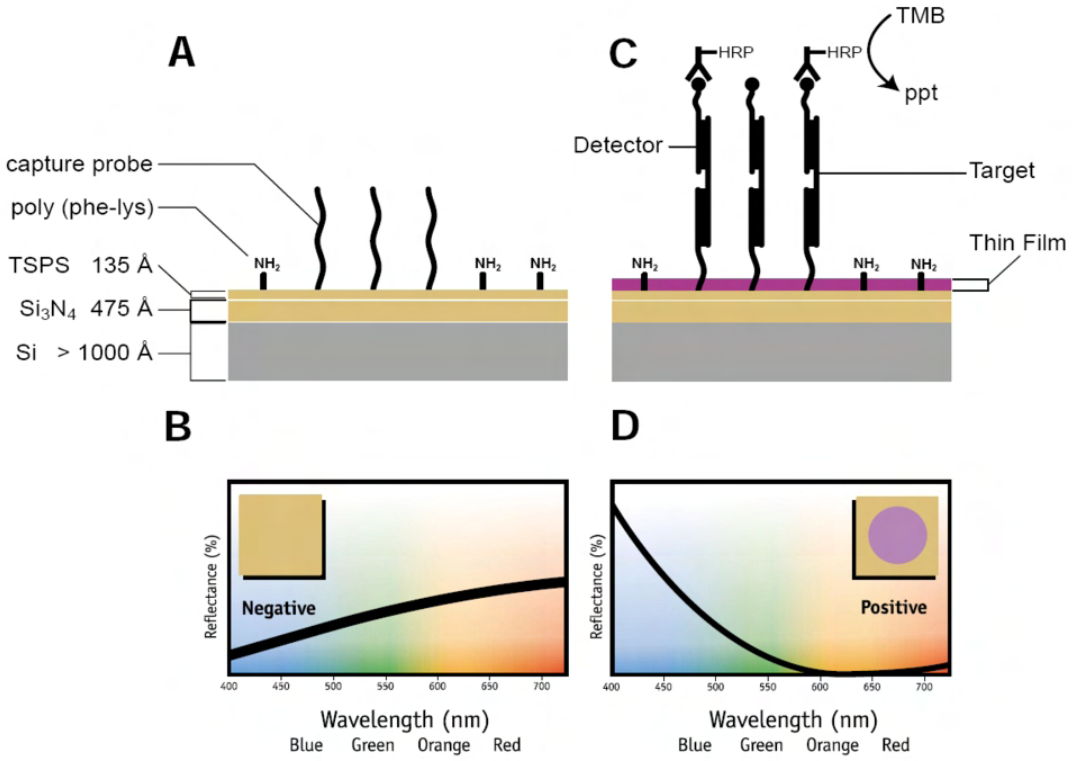

Figure 2.38: (A) Unreacted surface with capture probe. (B) Reflection spectrum for unreacted surface. (C) A thin film is formed when the surface reacts with the target, changing the spectrum as shown in (D), producing a coloured spot (inset). Figure from [9].

An interference-based detector for oligonucleotide sequences has been developed by Jenison *et al* [9, 146]. Capture oligonucleotides were attached to a silicon surface that had been anti-reflection coated with 475 Å silicon nitride (Si_3N_4) so that it appeared gold in white light, as can be seen in Figures 2.38 (A) and (B). In order to detect hybridisation the complementary oligonucleotide was labelled with biotin. Upon addition of anti-biotin antibody conjugated to the enzyme horseradish peroxidase (HRP) a thin film was precipitated by the conversion of tetramethyl-benzidine (TMB) to phosphinothricin (ppt), as shown in Figure 2.38 (C). Due to a change in optical path length very small thickness changes (20 Å) in the film result in destructive interference of some of the wavelengths of light, and so the colour changes from gold to blue. The advantage of this detector is that the colour change can be seen by eye and it is extremely sensitive; fluorescence detection is sensitive to around 500 $f$mol [75], but the interference-based sensor has a sensitivity as low as 0.1 $a$mol [9]. This equates to detecting 60 000 DNA copies, or a concentration of 10 fM [146]. A drawback of this method is the significant number of post-probe capture steps to enable film precipitation following DNA hybridisation.

2.8.3 Holographic Sensors

Holography is a more complex form of interference and has been used to develop holographic sensors. A coherent light source (usually a laser) in two beams is used to illuminate a photo-sensitive material from different angles. Interference fringes generated between the two beams form a diffraction grating.

A series of holographic sensors have been developed by Lowe *et al* [13, 147–152], in which the presence of a sample is indicated by a shift in the peak reflection wavelength from the hologram. Holographic elements are constructed from gelatin and act as biochemical sensors, providing a direct visual output with a change in wavelength and/or a change in brightness. Any physical, chemical, or biological reaction that alters the structure of the gelatin (or 'Smart' polymer) changes the fringe separation of the silver particles in the hologram (see Figure 2.39). This results in a change in the peak wavelength of reflection λ_{peak}, as related by the Bragg equation: $\lambda_{peak} = 2nD_p \cos\theta$, where D_p is the fringe plane separation within the medium, n is the refractive index and θ is the angle of incidence of the illuminating beam to the fringe plane [153]. The peak wavelength of reflection corresponds to the largest summation of reflected components, $R_{tot} = \sum R_1 + R_2 + R_3....$ The highest total reflected intensity occurs when the reflected components from each plane have the same phase and interfere constructively. The wavelength for which this occurs depends on the fringe separation.

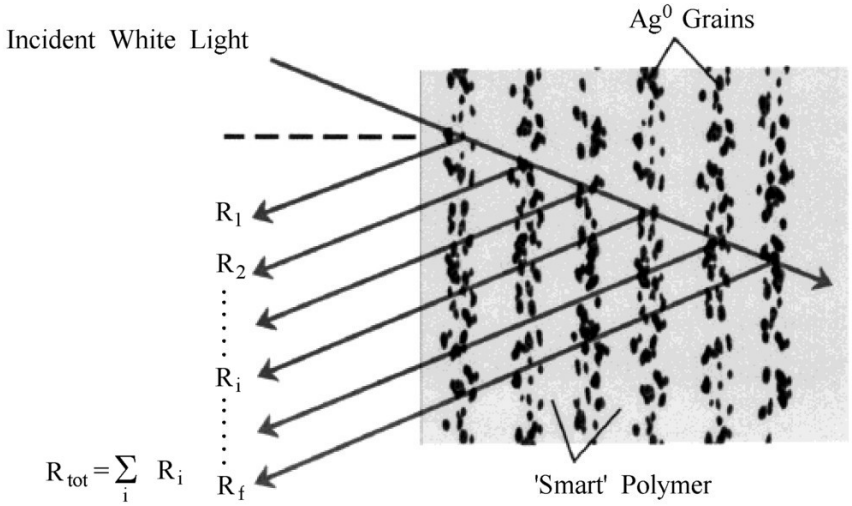

Figure 2.39: The holographic sensor fringe planes of Silver particles ($\leq 20\ nm$). Figure from [147].

Holographic sensing has been used to detect trypsin concentrations down to 25 nM in the short time of 20 minutes [13]. Detection of trypsin levels lower than normal duodenal fluid levels of around $18 - 115\ \mu$M is important since it aids diagnosis of pancreatic disease of

cystic fibrosis [13]. In the holographic sensor trypsin cleaves peptide bonds within the gelatin causing the hologram to swell. When the holograms are illuminated with white light, the rate of change in peak wavelength of reflection indicates the trypsin concentration. As the hologram swells, the peak wavelength of reflection is red-shifted. If the hologram is illuminated with a narrow band source, then the brightness of the hologram is observed to change.

The diffraction hologram system developed by the Lowe group was used to measure water content in solvents [148]. The hologram was immersed in hydrophobic solvents and the water content altered, changing the swelling of the hologram and therefore the peak wavelength of reflection. A visible colour change was observed when the water content in xylene was increased from 47 to 120 ppm. The principles of the gelatin based holographic sensor were extended by investigating alternative synthetic polymers instead of gelatin as the basis of the hologram matrix [150]. This was applied to the measurement of alcohol content in liquids, using a hologram constructed of a polymer film that swells with ethanol concentration [151]. The sensor was illuminated from the back, enabling analysis of turbid and non-transparent liquids. Alcohol concentrations for commercial beverages were determined to be within 0.3 % of their stated values, with the sensor itself accurate to 0.05 %.

The addition of crown ethers incorporated into polymeric hydrogels has enabled sensors to be developed for the detection of Na^+ and K^+ ions [147]. Within 30 seconds, a 200 nm shift in peak wavelength was obtained for ion concentrations less than 30 nM. It was possible to develop a sensor that could quantify K^+ levels, independently of Na^+ concentrations, providing a possible low cost blood K^+ level sensor without interference from Na^+ present.

Further investigation into the types of polymer used to form the basis of the hologram and to tailor its response to different analytes has lead to the development of a pH-sensitive sensor [152]. Variation of the ionisable co-monomer of the polymer can make the sensor sensitive over a wide range, or sensitive to milli-pH in a narrow range. This type of sensor also has the advantage of being tunable for wavelength response, sensitivity, or dynamic range by changing the composition of the polymer film and conditions of hologram formation. The holographic sensor is also very robust, easily stored and inexpensive.

The holographic pH sensor has been demonstrated for clinical diagnostics to detect urea and penicillin over physiologically relevant concentrations [154, 155]. The respective enzymes urease and penicillinase were each immobilised to different holographic pH sensors. The action of urease on urea causes acidification, and the action of penicillinase on penicillin

causes alkalinisation. Changes in pH associated with enzymatic reactions were detectable by a change in the peak reflection wavelength of each hologram.

A recent development of the holographic sensor has been for the detection of glucose by incorporating phenylboronic acid derivatives as recognition elements in the hydrogel matrix of the hologram [156]. As glucose binds with the boronic acid groups, the charge distribution changes cause absorption of water and the hologram swells. The appearance of the hologram changed colour from green to red as the blood glucose level increased over a range of physiologically significant levels $(2 - 10$ mM)[155]. This has been applied to clinical testing of blood sugar levels in diabetics where the holographic sensor has been incorporated into contact lenses [157].

2.8.4 Diffraction-Based Sensors

Biosensors have been developed based on optical diffraction from periodic grating structures. Cells are detected from the diffraction pattern caused by selective binding with antibody arrays immobilised on the substrate [10]. The adsorption of cells to the surface changes the intensity and distribution of the diffraction pattern produced by illuminating the slide with a laser beam. This variation was used to quantify the the amount of cells adsorbed from solution, to the substrate.

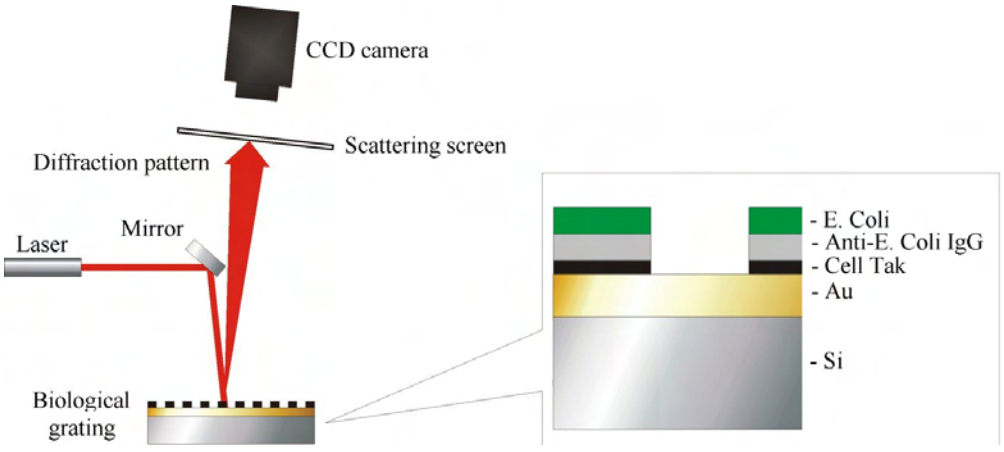

Figure 2.40: Diffraction patterns produced by laser illumination of biological gratings were imaged on a scattering screen using a CCD camera. Surface patterning (inset) was created using microcontact printing of Cell Tak followed by adsorption of anti-*E.Coli* as a recognition element for *E.Coli* in solution (Figure based on [10]).

Microcontact printing was used to pattern a gold-coated silicon wafer with alkanethiol patterns. A PDMS stamp was inked with 'Cell Tak' (containing adhesive proteins from the sea shell *Mytilus edulis*) and then placed in contact with the gold coated silicon substrate.

The Cell Tak micropatterns were used to non-specifically bind receptor proteins or antibodies at well-defined adsorption sites to detect specific proteins in solution. Thus, a periodic biochemically active surface (a biological grating) was created (see Figure 2.40). The diffraction pattern produced is sensitive to the period of the scattering elements, their shape and height. The micropatterns were illuminated with a 632.8 nm HeNe laser. Surface reactions (site specific cell adsorption) affect the shape of the scattering objects, affecting the diffraction pattern in the Fraunhofer regime. The diffraction pattern image was captured on a CCD camera.

The substrate was patterned with anti-*E.Coli* IgG as a receptor recognition element for *Escherichia Coli* bacteria. Observing the formation and intensity of diffraction orders enabled study of the effect of solution concentration and time dependence on protein density. The anti-body was immobilised in an array of lines, with 10 μm line width and 20 μm grating period. As binding occurred a diffraction pattern built up with diffraction orders appearing after $10 - 20$ minutes incubation time.

Diffraction has also been used previously for detecting bacterial *Escherichia Coli* by producing antibody diffraction gratings [158]. In this experiment oxidised silicon substrates were patterned by microcontact printing of antibody cells in a diffraction grating structure. The grating pattern used featured 10 μm wide lines of antibodies separated by 30 μm and diffraction was measured using a 632.8 nm HeNe laser. Gratings were characterised (prior to the attachment of target cells) for reflected ($m = 0$) and first order ($m = 1$) diffraction intensities. After attachment of target cells, diffraction intensities were measured again and the increase in intensities were correlated to the number of captured cells per unit area.

Studies have been conducted that use both the phenomena of diffraction and surface plasmon resonance for label-free detection of biomolecules. One such study coupled light in to the surface plasmon modes of a gold film via a prism and featured a grating structure on the reverse side of the gold [159, 160]. The grating structure was created by microcontact printing a biotin-thiol grating (100 μm period, 42 μm or 6 μm line width) directly on to an evaporated gold film (50 nm thick [161]) and a spacer thiol was used to passivate the unpatterned region. The contrast between the biotin thiol and spacer thiol was insufficient to generate detectable diffraction. Upon binding of anti-biotin antibody to the biotin lines sufficient optical contrast was generated to diffract the surface plasmon field and create a detectable diffraction pattern. The diffracted intensity was found to rise quadratically with the increase in antibody binding (at initial stages before saturation of binding sites was approached). A schematic for the experimental setup used is shown in Figure 2.41.

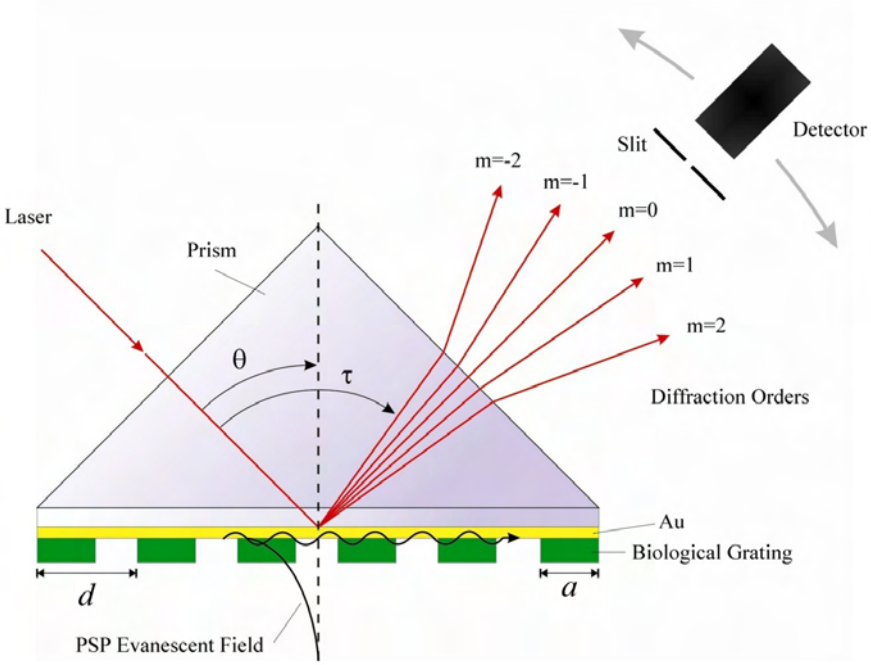

Figure 2.41: Schematic of the Surface Plasmon Diffraction Sensor based on a Kretschmann configuration (Figure based on [11]).

This methodology was also applied to the label-free detection of DNA oligonucleotides [11]. The grating pattern was created in the same way as above, with thiol-biotin grating lines on a gold film and thiol spacer molecules covering regions in between. Streptavidin was then flowed over the grating and associated to the biotin regions. Probe DNA consisting of a biotinylated oligonucleotide sequence was then added to associate to the immobilised streptavidin. Upon addition of target DNA sequences, changes in diffraction intensities measured were correlated to hybridisation efficiencies. The lowest detectable coverage was calculated to be 1.1×10^{11} molecules per cm^2 with a maximum coverage of 1.2×10^{12}. This type of sensor is interesting, but to develop a more accurate sensor, the use of target DNA labels such as gold nanoparticles would introduce a much larger refractive index change. A further improvement would be to have the DNA probe layer closer to the gold surface where the evanescent field has a higher intensity and would offer lower detection limits.

Neuschafer *et al* developed 'Evanescent Resonator' chips and found that the fluorescence yield was enhanced up to 100 times over normal microarray chips [162]. By patterning the substrate for the hybridisation assay with sub-micron periodic structures in a thin dielectric layer, interference creates a resonant angle at which transmitted light destructively interferes, and virtually all light is reflected as it interferes constructively (see Figure 2.42). The concentration of light in specific directions means that the observed fluorescence signal is stronger at certain viewing orientations. These chips utilise diffraction effects resulting from the corrugated structure; a period of 360 nm, step height of 20 nm and width of 150 nm.

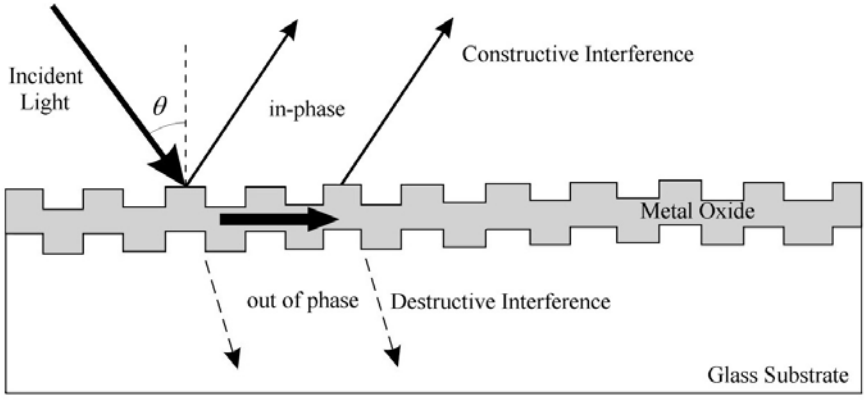

Figure 2.42: Evanescent resonator chips have been used to enhance fluorescent emission [162].

A fibre-optic biochemical sensor has been developed by Tang *et al* featuring a gold colloid modified fibre grating [163]. The resonant wavelength of the long period fibre grating created in the fibre core is sensitive to the refractive index of the cladding. In the grating region of the fibre, the cladding was removed and the core coated with $\approx 8\ nm$ diameter gold nanoparticles, to act as a sensing region. The bulk refractive index of the gold colloids is sensitive to biomolecular binding at the surface of the gold colloids and affects the transmission loss along the fibre. When there is a maximal refractive index contrast between the core and gold colloid cladding (such as in air), there is a minimum in the transmitted light intensity. As the refractive index surrounding the grating increases, the transmission loss reduces and the resonant wavelength at which the minimum transmission occurs is blue-shifted to shorter wavelengths. When the gold colloids were coated with dinitrophenyl (DNP), the detection limit of anti-DNP was found to be 9.5×10^{-10} M.

Sarov *et al* developed a microfluidic device using a reflecting diffraction grating to sense changes in the refractive index of the fluid flowing under the grating [164]. A gold reflecting diffraction grating (10 μm period) was patterned on top of a microfluidic channel window of Si_3N_4. The transparent region in between the gold grating lines enables light to interact with the fluid flowing through the channel, changing the amplitude and phase of light reflected from this region. The reflection properties from the gold regions remain constant and so a change in the optical properties of the fluid changes the optical contribution from the transparent region of the grating, changing the first order diffraction efficiency $I_{m=1}/I_{m=0}$ of the grating. A linear relationship was found between the change in diffraction efficiency and the change in refractive index of a sucrose solution as the sucrose content of the water was increased. The accuracy of diffraction efficiency change measurement of 5×10^{-3} correlated to a change in refractive index of the fluid of $\Delta n = 1.7 \times 10^{-3}$, a concentration of 1.2 % by weight.

An alternative diffraction-based optical biosensor is the optical grating coupler [165]. A planar waveguide was patterned with a surface relief diffraction grating. Laser light was incident on the bottom surface of the waveguide substrate at a variable angle of incidence. As light is diffracted by the grating on the surface, it can propagate along the waveguide by total internal reflection when the incident angle is such that constructive interference occurs and a guided mode is excited. This angle is affected by the refractive index on top of the grating. Consequently, the angle of incidence at which a guided mode is excited can be used to sense changes in refractive index associated with biomolecule binding on the grating. This sensor was used to detect the pesticide simazine with a detection limit of 0.25 $\mu g/l$ [166] and for salmonella detection with a limit of 1.3×10^3 CFU/ml [167].

2.9 Conclusions

DNA plays a vital role in the body as the genetic code that is transcribed in to amino acid sequences to form functional proteins. Many types of sensors have been developed for the detection and analysis of DNA sequences. Microarrays were one of the key technologies which have enabled rapid advances in DNA sequence analysis and aided sequencing of the human genome. With such vast data-banks of information, the new challenge is to correlate known DNA sequences with disease susceptibility to make use of this important resource. Relating DNA sequences to specific features or functions requires not only knowledge of sequence polymorphisms, but also of whether these variations occur within the same gene on the same chromosomal strand.

This review covered key techniques related to DNA analysis and biosensing strategies. A summary of the best current sensing techniques is given in Table 2.1. Whilst single molecule techniques provide optimum sensitivity, they are not suitable for haplotyping where two strands need to be studied for their sequence, and multiple copies are desired for ensured accuracy. Gold nanoparticle labelling offers sensitivity as low as 1.5×10^{-18} mol [133]; over 100 times higher compared to 1×10^{-16} mol for conventional fluorescence [133] and exceeding even the 5×10^{-17} mol sensitivity of radioactive labelling [75]. Fibre optic sensors provide the optimum fluorescence detection, with a sensitivity of 1×10^{-19} moles. Even greater sensitivity of DNA detection has been achieved via silver enhancement of captured gold nanoparticle probes, with DNA targets detected down to 3×10^{-22} mol (200 copies) [129]. This highlights the sensitivity achievable using nanoparticle probes, providing strong optical scattering.

Technique	Ref	Analyte	Volume	Probe label	Post-probe Amplification?	Detection Limits moles	copies	other
Single molecule fluorescence	- Mollova [3]	DNA	-	Fl	N	1.7×10^{-24}	1	
Nanosphere Inc (Ag enhanced Au scattering)	- Taton [129]	DNA	20 μl	Au-NP	Y	3×10^{-22}	200	5×10^{-14} M
Optic fibre sensors	- Epstein [113]	DNA	-	Fl	N	1×10^{-21}	600	
Interference film	- Jenison [9]	DNA	25 μl	HRP	Y	1×10^{-19}	6×10^4	1×10^{-14} M
Ag particle microarray labels	- Oldenburg [133]	DNA	2 μl	Ag-NP	N	1.5×10^{-18}	1×10^6	60× > fluorescence
Radioactive labels (^{32}P)	- Urdea [75]	DNA	20 μl	^{32}P	N	5×10^{-17}	3×10^7	
Colourimetric Au nanoparticle aggregates	- Reynolds [125]	DNA	5 μl target 1 ml probe	Au-NP	N	5×10^{-17}	3×10^7	5×10^{-11} M
Microarrays (fluorescent probes)	- Oldenburg [133]	DNA	2 μl	Fl	N	1×10^{-16}	6×10^7	
Dry-reagent strip biosensor	- Glynou [131]	DNA	5 μl	Au-NP	N	2×10^{-15}	1.2×10^9	
Nanoelectrodes with Au particles	- Tsai [138]	DNA	100 μl	Au-NP	Y			1×10^{-15} M
Anti-reflection coated microarray	- Redkar [101]	DNA	-	Fl	N			1×10^{-12} M or 6 ng
Nanoparticle enhanced SPRI	- Li [120]	DNA	-	Au-NP	N			1×10^{-12} M
Holographic sensor	- Millington [13]	trypsin	1 ml	-	N			2.5×10^{-8} M
Barcode labels	- Tok [140]	antigen	100 μl	Fl	N			1×10^{-11} g/ml
Protein diffraction grating	- Morhard [10]	*E. coli*		-	N			1×10^6 cells/ml
Chemoresponsive gratings	- Bailey [145]	DNA		Au-NP	N			1 particle/μm^2
SPR with surface grating	- Yu [11]	DNA	3 ml/min	-	N			1100 molecules/μm^2
Evanescent resonator	- Neuschafer [162]	DNA	20 μl	Fl	N			100× > fluorescence

Table 2.1: A summary of the detection limits for a range of biomolecule sensing techniques. Detection limits are given by the absolute quantity of molecules (moles, number of copies, or weight) or concentration in solution (Molar or number per volume). Probe labels: Fl = fluorophore, Au-NP = gold nanoparticle, Ag-NP = silver nanoparticle, HRP = horseradish peroxidase.

The optical interference film detection methodology developed by Jenison *et al* offers a simple colour indication, and good sensitivity (1×10^{-19} *mol* [9]), but requires further processing after hybridisation of the target DNA in order to precipitate a thin film. This technique would prove to be time consuming and costly due to the large number of processing steps involved. Electrical DNA detection methods using gold nanoparticle labels and silver enhancement achieved detection limits of 5×10^{-13} *mol* [7]. Using additional gold nanoparticle hybridisation, rather than silver enhancement, enables a detection limit of 1×10^{-15} M [138]. These electrical detection limits are not as sensitive as those achieved optically by Taton *et al* for silver-enhanced gold nanoparticles [129] when considering the larger volume of analyte necessary for detection. A drawback of these techniques is the requirement for post-probe binding amplification processes, rather than direct detection of the DNA with the probe alone.

Label free detection of DNA has been achieved by Yu *et al* with diffraction grating enhanced surface plasmon resonance, but the detection limit of 1100 molecules/μm^2 is a lot higher than for using nanoparticle labels. Bailey *et al* achieved a detection limit of 1 particle/μm^2 by using gold nanoparticles and DNA diffraction gratings, showing the benefit of using diffraction gratings with gold nanoparticle labels for DNA detection.

Whilst many techniques have been developed for DNA sequencing by fluorescence, or oligonucleotide detection using nanoparticle labels, or even using DNA as a construction tool, relatively little work has been done on SNP genotyping and haplotyping. There is the need to develop a sensor offering the ability to use small quantities of DNA with the aim of developing a haplotype sensor for DNA isolated from blood samples without the need for PCR amplification. Diffraction caused by DNA binding of gold nanoparticles can be very sensitive (detecting 1 particle per μm^2) as recently demonstrated by Bailey *et al* [145] developing a similar concept sensor device to detect complementary DNA sequences using gold nanoparticle labels. However, work on silicon rather than glass remains highly desirable for future integration in microelectronic devices. Glass also has variable surface chemistry yields for DNA attachment, where as the crystalline structure of silicon offers high densities of DNA in uniform attachment [16]. The combination of gold nanoparticle probes, diffractive interrogation and silicon technology promises the development of a very sensitive DNA sensor.

Chapter 3

Fabrication of DNA-Modified Silicon Diffraction Sensors

3.1 Introduction

In order to develop a diffraction sensor for DNA analysis for this project, methods were needed for the surface functionalisation and patterning of silicon with DNA. Neat, reproducible patterns with feature sizes down to 10 μm were required, with good discrimination between patterned and un-patterned regions and a lack of non-specific attachment to form a DNA sensor platform.

Existing research describes a wide variety of techniques that have been developed for micro-scale patterning the attachment of biomolecules on planar surfaces for use in biomolecule detection and analysis systems [15]. This chapter reviews the existing patterning techniques and then describes the stages involved with fabricating DNA modified regions on a silicon substrate for this project, from the initial pattern design through to the attachment of DNA on the final samples. The biological protocols required for the biochemistry and DNA hybridisation are described, resulting in the successful realisation of DNA gratings on silicon and detection of complementary sequences with gold nanoparticle labels. Silver enhancement of gold nanoparticles is also investigated to enable observation of the hybridised particles using an SEM.

3.2 Surface Chemistries and Characteristics

The method for functionalisation of a substrate with the desired biomolecule depends on both the surface chemistry and the type of molecule being patterned. Substrates such as glass, gold, silicon and diamond all have different surface chemistries and morphologies. Amorphous surfaces such as silicon dioxide (silica) tend to have larger variations in surface flatness and density of reactive sites for molecular functionalisation. Crystalline structures tend to be flatter and have a more uniform structure, offering the potential for a higher surface functionalisation with biomolecules. Diamond substrates offer the potential of very high uniformity as single-crystalline diamond (100) may be grown by chemical vapour deposition. The surface coverage of carbon bonds (or potential reactive sites) is $1.5 \times 10^{15}/cm^2$ [168]. Shin *et al* demonstrated covalent functionalisation of hydrogen terminated diamond with nitrophenyl groups for subsequent DNA conjugation and achieved a density of 8×10^{13} molecules/cm^2 [168].

Methods for the surface attachment of biomolecules on gold and glass were summarised in Section 2.6.1. DNA attachment by thiol reaction with gold results in a coverage of up to 2×10^{13} molecules/cm^2, but the uniformity of attachment can vary and a coverage of 4×10^{12} DNA molecules/cm^2 was most common [169]. The surface coverage can also suffer instability problems due to the reversible process of the adsorption/desorption of the thiol layer. Glass surfaces functionalised with groups that contain reactive amines have been used for the covalent attachment of DNA molecules and were quantified by hybridisation with complementary radioactive P^{32} labels at a density of $6.7 \times 10^{12}/cm^2$ [170]. Glass (or silicon oxide) also suffers from inhomogeneity of the surface and variability in the surface coverage of active sites for silane attachment [16].

3.2.1 Alkene Functionalisation of Silicon

Achieving surface modification of silicon substrates with biomolecules is desirable due to the benefits of integration with microelectronic devices and excellent crystalline surfaces, making them ideal for uniform patterning and stable functionalisation. Early work by the group of Chidsey on alkene attachment to silicon (111) and (100) surfaces demonstrated the type of attachment chemistry necessary to form a uniform monolayer of covalently bound biomolecules [171–174]. This was achieved by thermal incubation (at temperatures between $100°C - 200°C$) of alkenes with hydrogen-terminated silicon substrates [172], generating

adsorption of the alkene to the silicon surface via a Si-C covalent bond [173, 174].

Sieval *et al* worked on the preparation of monolayers from dilute alkene solutions on hydrogen-terminated Si(100) using a variety of solvents [175]. The Si-C bonded monolayer has been shown to be thermally stable up to 615 K [176]. Diluting the alkene down to 2.5 % concentrations reduced the quantity required by a factor of 40 compared to using neat alkenes and yet still formed well-ordered monolayers. Sieval *et al* also demonstrated that monolayers of alkynes could be formed on Si(100) forming a double bond (Si=C) [177].

Cicero *et al* demonstrated the formation of monolayer hydrocarbon films by UV illumination of unsaturated hydrocarbon solutions on hydrogen-terminated silicon [178]. The H-Si bond is found to dissociate when illuminated with 350 nm wavelength light, providing enough energy to break the H-Si bond of $\sim 80\ kcal/mol$. The number of silicon atoms per surface area as potential binding sites is $7.8 \times 10^{14}/cm^2$. The UV attachment methodology is particularly beneficial as it offers the ability to not only form a monolayer coating, but to also pattern the substrate by selective illumination, for example through a photolithographic mask. The homogeneity of silicon, high density of binding sites, ability to be photo-chemically patterned and potential integration in microelectronics devices, makes it an ideal substrate for developing as a biosensor.

The attachment of DNA oligonucleotides to silicon (100) substrates for the biosensor developed in this thesis, was developed in our group by Dr H Yin at the University of Southampton [16, 179, 180]. Silicon was coated with alkenes functionalised with succinimide groups and UV illuminated via a photolithographic mask for selective photo-patterning. Amino-modified oligonucleotides were subsequently attached to the photo-patterned alkene by displacement of the succinimide group. This is explained in more detail in Section 3.5.

3.3 Surface Patterning of Biomolecules

This section reviews existing techniques that have been developed for the attachment and patterning of biomolecules on rigid substrates. There are several main approaches for surface modification and the patterning of biomolecules. These are either mechanical, such as 'soft-lithography' techniques which directly transfer molecules from a mechanical pattern to the substrate through contact with the surfaces or alternatively photo-based. Photo-patterning includes photolithographic techniques (which can be used to generate barriers of photore-

sist for either lift-off or etching as a method to pattern biomolecules), photo-deprotection of self-assembled monolayers (SAMs) in defined regions to enable subsequent binding of biomolecules, or direct attachment of biomolecules to the substrate when illuminated by UV light.

3.3.1 Mechanical Patterning of Biomolecules

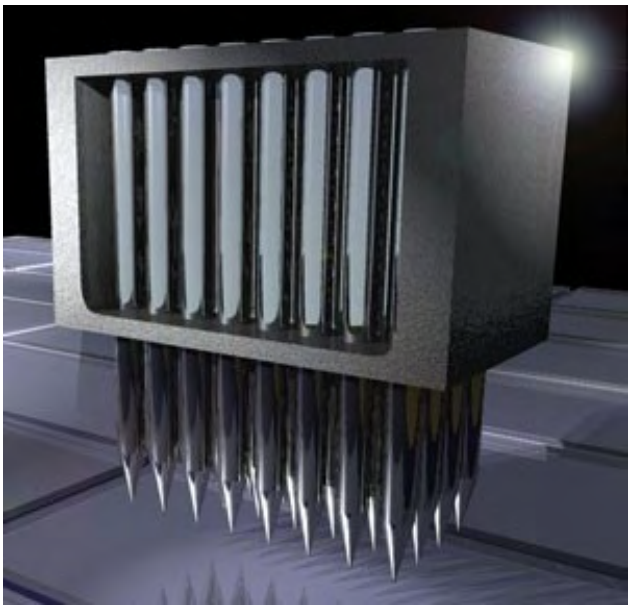

Figure 3.1: Schematic illustration of the arrayer developed by Brown *et al* (Image from [181]).

Mechanical patterning techniques provide an alternative method for patterning to light initiated methods. Mechanical patterning of DNA on surfaces typically involves spotting using arrays of tips, microcontact printing using polymer stamps (featuring micro-scale patterns), or inkjet printing of DNA.

Printing of DNA solutions has been achieved using standard inkjet printers [182]. Microarray sensors were produced using thermal inkjet (bubble-jet) printing to deliver 20 nl droplets of DNA solution with a resolution of 600 dots per inch [183]. Inkjet printing of DNA has also been used for functionalising cantilevers with DNA sequences for developing a nanomechanical sensor [184]. The printing of spots of approximately 70 μm diameter [185] is readily achievable, but only the patterning of spots and arrays of spots are possible and pre-functionalised slides are necessary. The uniformity and repeatability are also not ideal, with the resolution limited by the printhead.

The Patrick Brown group at Stanford University, USA, produced a mechanical arrayer for producing DNA microarrays of spots through contact printing. A 4×8 array consisting of

32 metal tips $\sim 1.6\ mm$ diameter with fine slots cut in the end of a sharp tip have been used to produce spot sizes with ranges from $50 - 250\ \mu m$ diameter (see Figure 3.1). Glass slides were treated with poly-L-lysine adhesive solution and an array of DNA spots were printed on the substrate by bringing the array head in to contact with the substrate [186]. Such mechanical spotters have also been adapted for micro-contact printing protein microarrays too [187]. Arrayers offer very good reproducibility of circular spots, with separation distances generally around 300 μm.

Microcontact printing (or μCP) is useful for creating biological patterns on substrates with feature sizes of several microns of any shape, not just arrays of spots [188, 189]. A rigid master pattern created photolithographically is replicated using a soft polymer (most frequently polydimethyl siloxane (PDMS)) to create a stamp [190]. The stamp is 'inked' with the solution to be printed and deposited by placing in contact with the substrate. The pattern is thus transferred from the elastomeric stamp material to the rigid substrate, hence the technique is also referred to as soft lithography [188]. Soft-lithography has been used routinely for the patterning of proteins or cells [188, 191]. In addition to these applications, microcontact printing of DNA using PDMS stamps has been achieved for the creation of diffraction grating patterns on glass [14] and silicon [10], as reviewed in Section 2.6. Pattern sizes down to 1 μm wide have been achieved for stamping oligonucleotides on amine-derivatised mica substrates with a density of 9000 molecules/μm^2 [192].

3.3.2 Nanolithography Techniques

To achieve even smaller patterns than those possible with photolithography (which are limited by the wavelength of light and diffraction) contact techniques have been developed to pattern on the nanoscale. Mirkin *et al* developed dip-pen nanolithography (DPN) [193], a process in which an AFM (atomic force microscope) tip is used to transfer molecules from the tip to a substrate, enabling the writing of features down to 30 nm [194]. This technique enables the creation of small patterns, but is very laborious and not suitable for mass production. A similar technique to this is nanografting, in which a SAM is imaged using an AFM in a solution containing a different thiol. When the force applied via the AFM tip is greater than the displacement threshold of a thiol SAM on gold (2 nN), the adsorbed molecules are displaced, and the other thiol in solution is able to self-assemble in the exposed sites. This technique has been used to generate features as small as 10 nm wide [195] and has been used to immobilise enzymes on a gold substrate retaining catalytic activity [196].

Nano-imprint lithography (NIL) uses hard moulds (rather than soft polymers) to physically imprint the pattern from the rigid stamp into a polymer material [197]. These hard moulds are typically made of Si or SiO_2. The pattern embossed in the resist is then transferred to the substrate by etching. Using rigid moulds enables feature sizes to be replicated down to 10 nm, but macroscopic features are hard to reproduce and rigid moulds can be brittle and fragile.

3.3.3 Photoresist Barriers

Photoresist is commonly used at various stages for patterning surfaces with biomolecules. This approach exploits high-resolution imaging materials and processes from microelectronics engineering, forming arrays with very high oligonucleotide densities ($10^6/cm^2$)[198]. The resist is typically used as a physical barrier to protect the underlying surface from adhesion of biomolecules in solution. The photoresist is then removed with a solvent which will not damage the bio-functional layer, lifting-off any adsorbed molecules and leaving a bio-patterned surface [199, 200]. Falconnet *et al* created photoresist patterns using standard photolithographic techniques [200]. The photoresist-patterned sample was then dipped in a solution containing the desired biochemical, for example poly(L-lysine)-*graft*-poly(ethylene glycol) (PLL-*g*-PEG) functionalised with biotin, which spontaneously adsorbs to the surface. The photoresist was then lifted-off in an organic solvent and the background was subsequently filled with non-functionalised PLL-*g*-PEG to inhibit non-specific interactions. They achieved feature sizes of down to 2 μm, imaged using fluorescently labelled streptavidin bound to the biotin. The term MAPL - molecular assembly patterning by lift-off was used to summarise this procedure.

An approach for synthesising DNA probe arrays, combining oligonucleotide synthesis with photoresist films was developed in 1996 [198]. Previous optical patterning limited oligonucleotide growth regions by preventing light exposure with photolithographic masks. The approach by McGall *et al* instead used photoresist as a physical barrier to the chemicals used for oligonucleotide synthesis. This worked better since photoresist is non-linear in its response to light intensity (low intensity illumination weakens molecules, but high intensity breaks bonds and causes a chemical conversion), and achieved greater contrast in reactions than from the contrast of illumination alone, improving the resolution of patterning. Firstly, the glass substrate was derivatised with hydroxyl-terminated linker molecules, protected by a trityl group. A protection layer was coated before the photoresist to protect the biological layer. Once a photoresist pattern had been created on top, acid was applied to detritylate the

hydroxyl groups in exposed regions. The photoresist and protection layer was then removed and oligonucleotides attached to the slide where it had been detritylated, thus forming arrays to which DNA hybridisation can occur. This process is summarised in Figure 3.2.

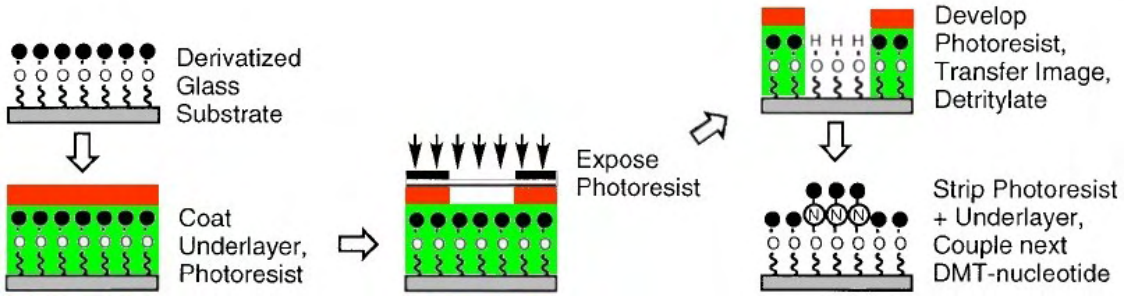

Figure 3.2: Light-dependent patterning of substrates using photoresist as a barrier to activation chemicals (Figure from [198]).

In addition to the use of conventional photoresist polymers, new biocompatible photoresists have been developed which enable use with a wider range of biomolecules [199]. In this method, the positive photoresist poly(*t*-butyl acrylate) is patterned using UV illumination via a mask. The resist is developed and then the biomolecules are deposited on the substrate, attaching to the substrate on bare regions not covered with resist. The remaining resist is then exposed to UV light and developed again, lifting-off any biomolecules attached to it and leaving a bare surface behind and biomolecules only on the substrate at locations patterned in the first exposure stage.

An alternative to the lift-off process, etching of photoresist can be used to enable biopatterning. Sorribas *et al* immobilised protein on a glass substrate, then protected the protein with a layer of sucrose before spinning on a photoresist layer, UV illuminating and developing the resist [201]. Following the photolithography step, the sample was then etched in an oxygen plasma to transfer the resist pattern through to the substrate. The remaining resist and sucrose was then removed from the sample leaving a patterned protein substrate.

3.3.4 Photo-deprotection

Photo-deprotection is a technique in which a layer that protects either the surface or SAM below is destroyed (or made active) by illumination with either a UV lamp via a patterned mask or even by laser ablation. For example, Dillmore *et al* created SAMs of alkanethiolates on gold [202]. A SAM was formed on the gold substrate consisting of nitroveratryloxycarbonyl (NVOC)-protected hydroquinone. When illuminated, the photochemical reaction resulted

in the underlying hydroquinone being revealed. Subsequent oxidisation of the hydroquinone to benzoquinone generated sites for the immobilisation of ligands.

Another example of photo-deprotection was used to pattern proteins on top of self-assembled monolayers on gold [203]. A SAM functionalised with carboxylic acid end groups was coupled to a caged biotin ester. The caged biotin was then deprotected in regions where it was illuminated by UV light, allowing binding of streptavidin to exposed regions. The spatial resolution achieved was down to approximately 6 μm.

Alternative approaches to biomolecule patterning have been developed using laser ablation systems. Self-assembled monolayers of alkanethiolates on a thin (56 nm) gold film were desorbed by laser (390 nm wavelength) ablation at energy levels low enough not to damage the gold, producing 10 μm features [204]. Schwarz *et al* used laser ablation to deprotect a surface covered with a blocking BSA coating such that subsequent incubation with Avidin resulted in protein attachment only at regions where the BSA coating had been ablated [205]. Laser ablation of a protein resistant layer of poly(ethylene oxide) enabled spatial control of biological cells. The 248 nm wavelength Excimer laser used for the ablation enabled patterning with a resolution of approximately 1 μm and cell attachment was only possible where it had been ablated [206].

Another alternative to using a photolithographic mask to create a spatial pattern of illumination is to use micromirror arrays [207]. By switching on certain mirrors within the array, a pattern can be transferred from the mirrors to the substrate. The illumination can be controlled by switching the mirrors on or off. This technique generates a virtual mask by only providing an illuminating reflection from mirrors that are switched on. This has obvious advantages for creating many different patterns, compared to a fixed illumination pattern created from a photolithographic mask. This technology was used to UV illuminate an NVOC group and deprotect the underlying amine-group functionalised surface from subsequent biotin adsorption. The patterned biotin surface was then used to capture fluorescently labelled streptavidin.

3.3.5 Photo-Attachment of Biomolecules

Photo-patterning offers the ability to pattern a substrate with biomolecules without the need for physical barriers such as photoresist. This can be achieved either by direct photo-attachment of a molecule to the illuminated substrate, or by photo-deprotection so that

subsequent bio-molecule attachment becomes possible in patterned areas.

Direct attachment of certain molecules to a substrate can be achieved through UV illumination. When a monolayer is illuminated with UV light via a mask plate the substrate is only patterned in exposed regions. This principle of attachment has been used for photo-attachment of organics on silver [208], patterning of enzymes in microfluidic channels [209], and UV attachment of the polymer PEG on glass [210].

An alternative approach to surface modification without the need for a mask in the photolithographic procedure uses interference of a UV laser beam to create a periodic line pattern [211]. A carbon electrode was patterned with enzyme domains, separating electron transfer sites. First of all, photobiotin was applied to the whole surface of the electrode. An interference pattern was created by splitting a 325 nm wavelength laser beam into two parallel beams and then focusing the beams through a lens to a spot where they interfered. The spacing of the interference maxima can be varied by adjusting the angular separation of the incident beams (determined by the focusing lens). Illuminated photobiotin attaches to the surface, whilst unexposed photobiotin is unreacted and is washed off. To bind an enzyme to the surface, it was attached to biotin. The biotinylated enzyme was then bound to the electrode by avidin, forming periodic 'biotin/avidin/enzyme nanostructures'. The line pattern produced was then observed by adding fluorescent labels. When different electrodes are patterned with different enzymes, they exhibit differential electronic responses [212]. Non enzyme-modified sites feature enhanced electron transfer. Binding of enzymes impedes current flow, and different enzymes cause differing responses to current. The enzyme modified electrode acts as an 'Amperometric biosensor'.

Patterning of photobiotin on 'glassy-carbon' electrodes has also been achieved with UV laser interference [213]. The biotin patterned lines had a period of just below 2.0 μm and a line width of 840 nm. A biotin/avidin/biotin-IgG patterned substrate was then used to capture alkaline-phosphatase labelled Anti-IgG (see Figure 3.3). This binding was studied electrochemically, with a change in conduction upon binding and confirmed with fluorescence imaging.

The principles behind this study were then extended to vary the line intensity and size of patterns produced by scanning the laser beam across the surface at varying speeds [214]. This enabled creation of larger patterns than just the interference region of the focused spot. The enzyme attachment method remained the same but the method of creating the illuminated pattern for photoreaction changed. Interference was no longer used. Instead, a tight spot

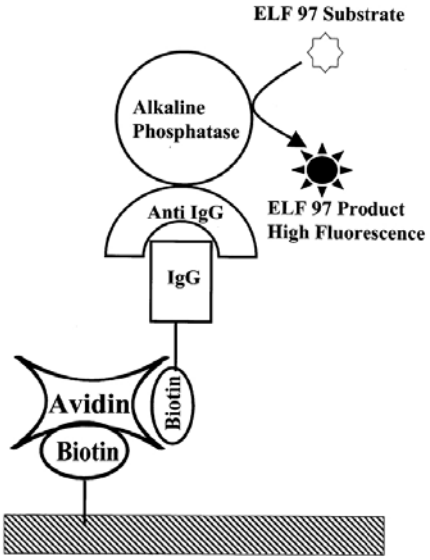

Figure 3.3: Schematic of Biotin/Avidin/Biotin-IgG binding structures (Figure from [213]).

size was focused onto the substrate through a confocal microscope setup, illuminating only a small region (as low as $\lambda/2$). The sample was moved to illuminate specific regions only for photoreaction of the photobiotin, creating line widths from $5 - 20\ \mu m$.

3.3.6 Summary of Surface Patterning

The methods outlined above show the wide variety of techniques that have been developed for the attachment and patterning of biomolecules. The feature size and uniformity of the main surface patterning techniques are summarised in Table 3.1. Whilst mechanical contact techniques offer simplified apparatus and ease of use for repetition of a set pattern they do not enable flexibility in patterning or the accuracy of optical patterning, with the exception of nano-lithographic techniques which are not appropriate for large features. The technique used for surface patterning depends to a large extent on the biomolecule being patterned. Inkjet printing offers a quick method of patterning, but the smallest feature size is 70 μm and repeatability and accuracy is poor [185]. Arrayers offer better repeatability and uniformity of features of 50 μm in diameter [186]. Micro-contact printing can achieve feature sizes of 1 μm in width, but the uniformity of patterning tends to be inconsistent [192]. Whilst nanolithography offers a resolution of down to 10 nm, pattern creation is very laborious [195]. Photo-patterning techniques offer the best resolution for quickly generating neat, large scale patterns, with sub-micron resolution (eg. 840 nm [213]).

Technique	Ref	Feature size	Uniformity
Inkjet printing	- Okamoto [185]	70 μm	Poor
Arrayer	- DeRisi [186]	50 μm	Good
μCP	- Lange [192]	1 μm	Reasonable
Photolithography	- Dontha [213]	840 nm	Excellent
Nanolithography	- Xu [195]	10 nm	Poor (large scale)

Table 3.1: A summary of the feature sizes and uniformity of surface patterning techniques.

Diamond offers the most uniform substrate for surface patterning, with the highest surface area coverage of binding sites (for biomolecule attachment) of 1.5×10^{15} molecules/cm^2 [168]. Silicon offers a similarly high density of 7.8×10^{14} molecules/cm^2 [178] and is also a highly homogeneous crystalline structure. Gold and glass offer lower surface coverage, with DNA surface coverage of 4×10^{12} molecules/cm^2 [169] and 6.7×10^{12} molecules/cm^2 [170], respectively. Gold and glass substrates also suffer from uniformity variations compared to diamond or silicon. The cost of diamond is however prohibitively expensive and it does not offer the microelectronic device compatibility benefits of silicon.

The crystalline uniformity of silicon, high surface coverage of binding sites and potential integration in microelectronics devices makes it an ideal substrate for developing as a biosensor. In order to attach DNA to silicon a monolayer of a cross-linker alkene molecule must first be formed. Owing to the photo-liable nature of the alkene cross-linker molecule being used for this project photolithographic masks were used to selectively UV illuminate the alkene to achieve patterning of the substrate in a single illumination step. The adsorption of the alkene molecule to the surface only at regions where it is illuminated enables the replication of any desired mask pattern on the silicon substrate. The desired mask pattern simply needs to be fabricated for use with UV patterning of the alkene, as detailed in the following section.

3.4 The Fabrication of Photolithographic Masks for Silicon Patterning

The patterns fabricated for this project were designed theoretically for their diffraction properties (detailed later in Chapter 4), and then a photolithographic mask design was produced

using L-Edit^{TM} software. The mask design was then produced by either Innos^{TM} or the Rutherford Appleton Laboratory. Replica masks were made on fused silica (UV grade, UQG Ltd) for use in patterning silicon samples for DNA attachment, and gold test patterns were created on glass and silicon substrates. Patterns were either one-dimensional diffraction gratings or two-dimensional diffraction arrays.

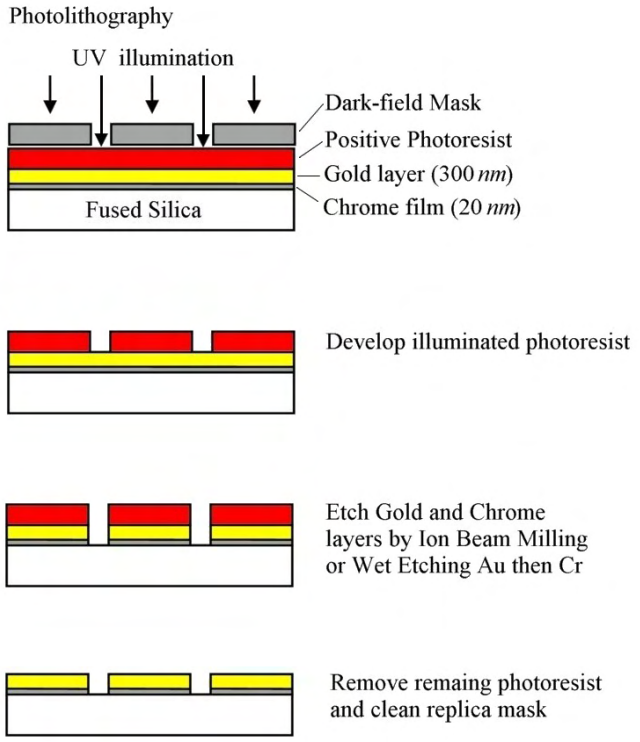

Figure 3.4: Schematic illustration of the photolithography process used for the fabrication of replica masks for DNA patterning were created using positive photolithography on fused silica.

Chrome-gold coating was used for producing replica masks on fused silica for use in UV patterning of silicon with DNA (see Appendix A for further details). Positive photoresist was used to replicate the mask patterns and then samples were dry-etched using Ion-Beam Milling. An outline schematic of the steps involved in fabricating a dark-field replica mask from the original dark-field design is detailed in Figure 3.4. Wet etching was used for creating test gratings on silicon and glass, where the feature accuracy was less critical than for the replica masks used for DNA patterning. An example of a gold on silicon diffraction grating is shown in Figure 3.5.

An example of a replica chrome-gold dark-field mask on fused silica featuring a two-dimensional diffraction structure is shown in Figure 3.6. This is a light-field transmission microscope image showing 100 μm diameter circular apertures ion-beam milled through the chrome-gold layer on the silica substrate. Masks were inspected in transmission to ensure there was a good optical contrast between the milled region compared to transmission through the gold. This enabled quality control of the masks; replicas where the gold featured pinholes or where

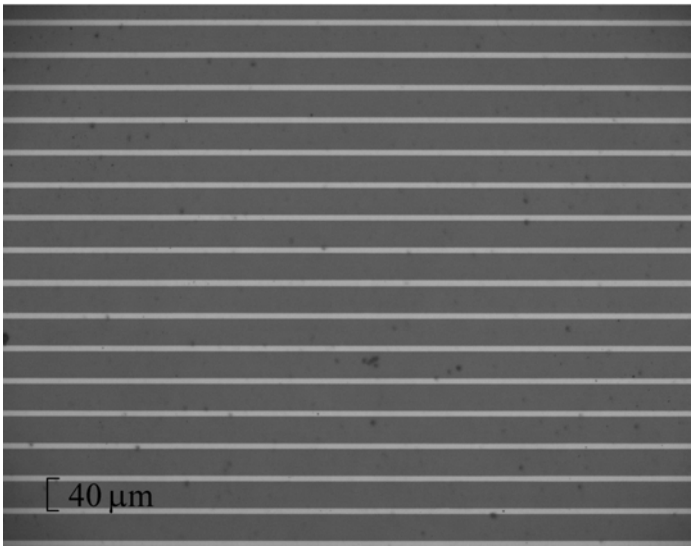

Figure 3.5: Optical microscope reflection image of a trial diffraction grating fabricated from solid gold films on silicon, with a period of 40 μm and 10 μm wide gold lines.

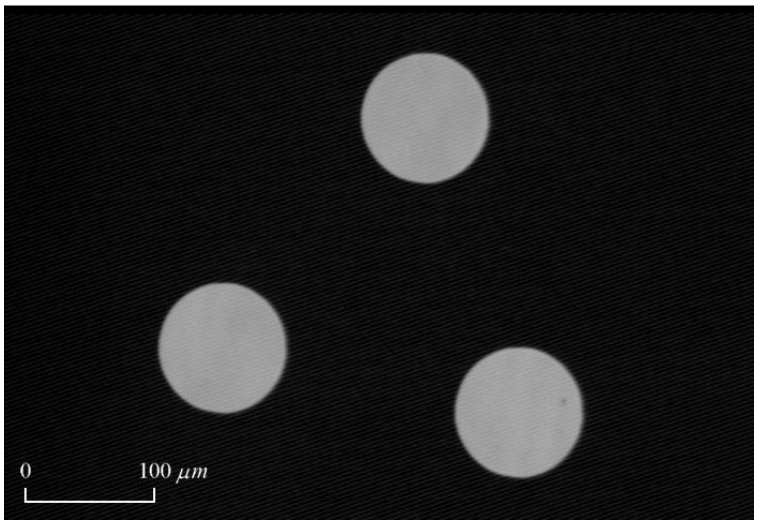

Figure 3.6: Optical microscope transmission image of an ion-beam milled chrome-gold replica mask on fused silica used for DNA patterning of silicon, featuring 100 μm diameter apertures.

windows were partially obscured were rejected.

It was important to have an accurate replica mask as this limited the feature quality achievable by DNA patterning of silicon with the fused silica mask. A KLA-Tencor P-16 Profiler was used to examine the surface topography of the replica masks. The profiler was fitted with a 100 nm radius tip, but had a 1 nm height resolution. The surface profile of a diffraction grating mask is shown in Figure 3.7 (the noise originates from the cleanroom fan vibrations).

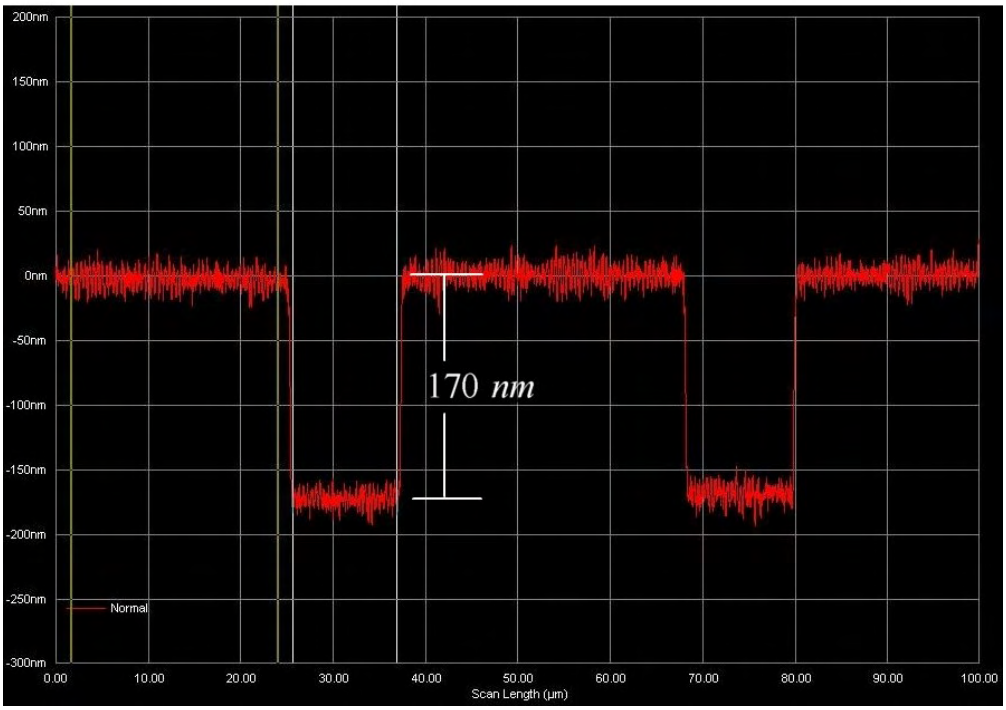

Figure 3.7: Surface topography of a diffraction grating mask fabricated with gold on fused silica, featuring a period of 40 μm, 10 μm line width and a step height of 170 nm. Ion-beam milling was used to ensure the vertical edges of the apertures.

3.5 Fabrication of DNA Patterns on Silicon

Attachment of DNA oligonucleotide sequences to silicon was achieved using an organic cross-linker molecule. The functionalised alkene used for this purpose was undecylenic acid N-hydroxysuccinimide ester (UANHS) synthesised in-house; attachment protocols were developed by Dr Huabing Yin [16, 179, 180]. The DNA sequences used were short chain 5′ Aminohexyl oligonucleotides (17-mer) synthesised by the team of Professor Tom Brown, Department of Chemistry, University of Southampton.

3.5.1 Sample Preparation

The silicon wafers used were (100) crystalline orientation, p-type doped with boron and had a resistivity in the range of $1 - 100\ \Omega cm$. Wafers were diced in to 10 $mm \times$ 10 mm squares for sample fabrication. Samples were cleaned in acetone at $50°C$ in an ultrasonic bath for 30 minutes then rinsed in fresh acetone, followed by isopropanol and dried under a stream of nitrogen. Samples were then cleaned in fuming nitric acid for 30 minutes, followed by removal of the native silicon dioxide layer ($\sim$ 1 nm thick [215]) with diluted (20 : 1) hydrofluoric (HF) acid for 10 minutes (see Figure 3.8).

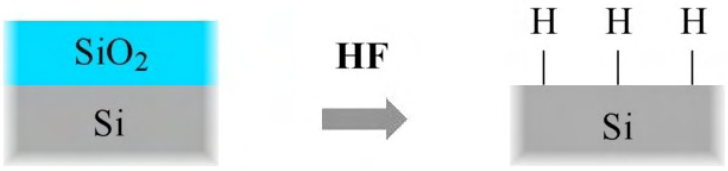

Figure 3.8: The thin native silicon dioxide layer was removed using hydrofluoric acid resulting in a hydride-silicon surface.

3.5.2 Surface Functionalisation

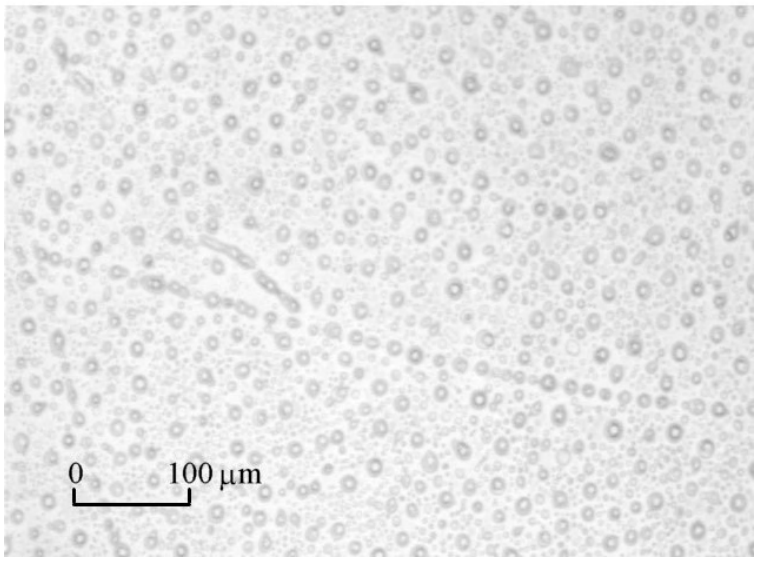

Figure 3.9: The UANHS alkene layer forms 'islands' of material after spinning, rather than a perfectly continuous thin film.

After removal of the native oxide layer by HF, the silicon was left with a hydrogen terminated surface. The UANHS alkene molecule was dissolved in dichloromethane (DCM) at 1% by weight. Immediately after oxide removal, 40 μl of the alkene solution was deposited on the top surface of the 1 cm square silicon sample by a pipette. It is then spun for 30 s at 2000 rpm immediately after deposition to form a relatively uniform layer compared to that formed by allowing the solvent to evaporate. Even using the optimised spin coating parameters the alkene layer tended to form islands of material, rather than forming a continuous thin film (as shown in Figure 3.9).

3.5.3 Photopatterning

Samples were patterned by UV illumination of the alkene layer through a replica photolithographic mask (made from gold on fused silica) using a 500 Watt mercury lamp. Samples were exposed via an interference filter (with a 10 nm wide transmission band centred on a wavelength of 253.7 nm) to an intensity of 1.0 mW/cm^2 (measured at $\lambda = 250$ nm with a UV power meter) for 6 minutes in a nitrogen environment (see Figure 3.10). Where illuminated, photo-attachment of the alkene functionalised with an N-hydroxysuccinimide ester group occurs covalently to the silicon substrate (shown schematically in Figure 3.12 i). UV illumination below 350 nm wavelengths provides sufficient energy to dissociate hydrogen from the silicon surface (Si-H) [178]. This generated free radicals which initiated a covalent bond between the silicon and a carbon atom of the alkene molecule.

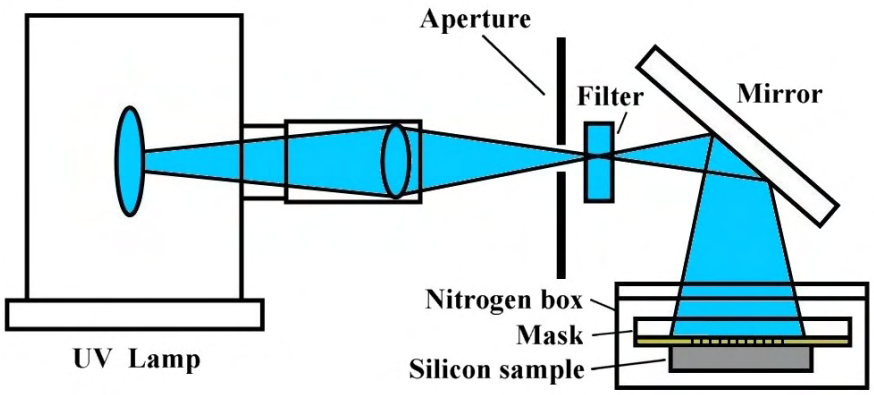

Figure 3.10: Experimental layout for UV illumination and photo-patterning of the UANHS alkene on silicon.

The UV photo-desorption of the hydrogen requires shorter illumination times for shorter wavelengths. However, if too high an energy is used it can impair the reactivity of the UANHS functional groups of the alkene succinimide group. The UV spectrum of UANHS in acetonitrile shows that there is no absorption around 250 nm, so this wavelength region was used for illumination using a 254 nm interference filter (see Figure 3.11). The alkene forms a monolayer on the surface 14 Å thick (as determined previously by Ellipsometry measurements [16]) and acts as a template for DNA conjugation. Unreacted alkene was removed from the sample by sonication in DCM for 60 seconds followed by washing for 60 seconds in fresh DCM and 10 seconds in dimethylformamide (DMF).

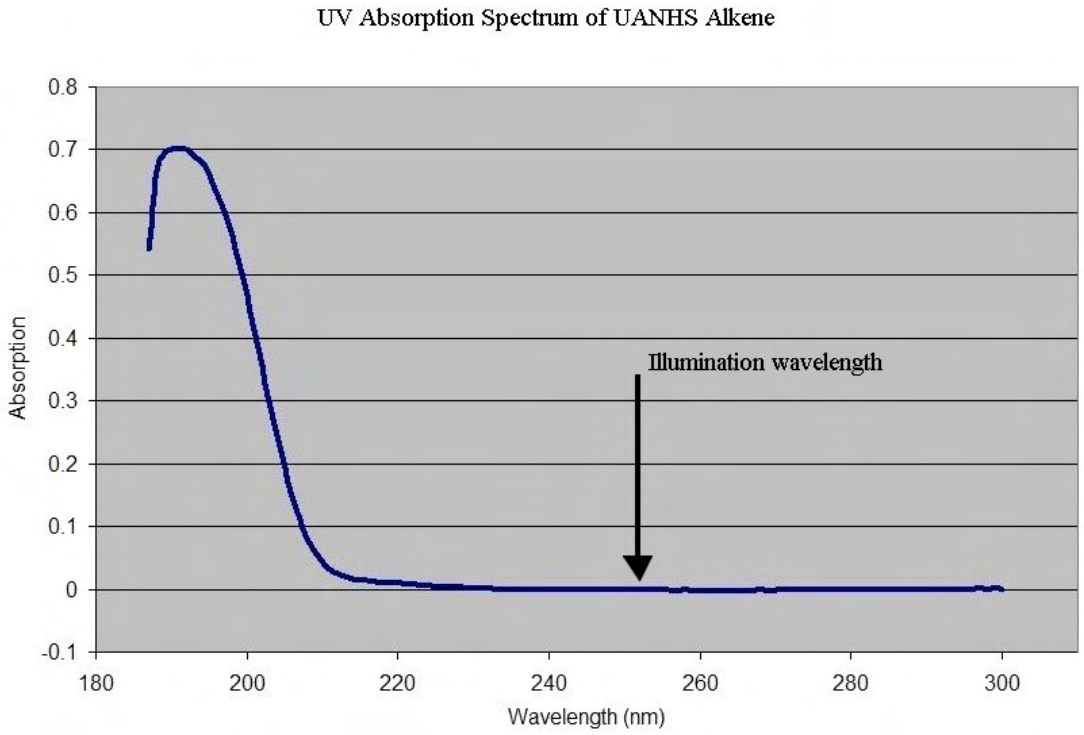

Figure 3.11: UV absorption spectrum for UANHS functionalised alkene dissolved 1 % by weight in acetonitrile and normalised to the spectrum for pure acetonitrile. With no absorption at $\sim 250\ nm$, this region was used for illumination to avoid damage of the functional groups.

3.5.4 DNA Conjugation

The DNA sequence used was $5' -$ T GCA GAT AGA TAG CAG T $- 3'-$PEG-amino link. Note that this sequence included a poly-ethylene glycol (PEG) linker molecule prior to the amino group for reaction with the immobilised alkene molecule. The PEG linker was added to improve the accessibility of the immobilised oligonucleotide to the DNA in solution during hybridisation. This extended the distance from the surface giving the DNA greater freedom for movement and capture of a complementary target sequence.

DNA sequences were stored in the freezer and defrosted prior to use. DNA solutions were prepared at 50 μM concentration in 0.1 M $NaHCO_3$ buffer (10 % DMF). The pure DNA oligonucleotides were diluted to 50 μM by adding 1.0 M $NaHCO_3$ and DMF with the correct volume of de-ionised water.

The surface functionalised silicon substrates were dried under a stream of nitrogen, following which 7.0 μl of DNA solution was applied. Glass cover slips were placed on top of samples and they were incubated face-down for $18 - 20$ hours in a sealed humid chamber at room temperature to facilitate the DNA conjugation with the patterned alkene. In this process,

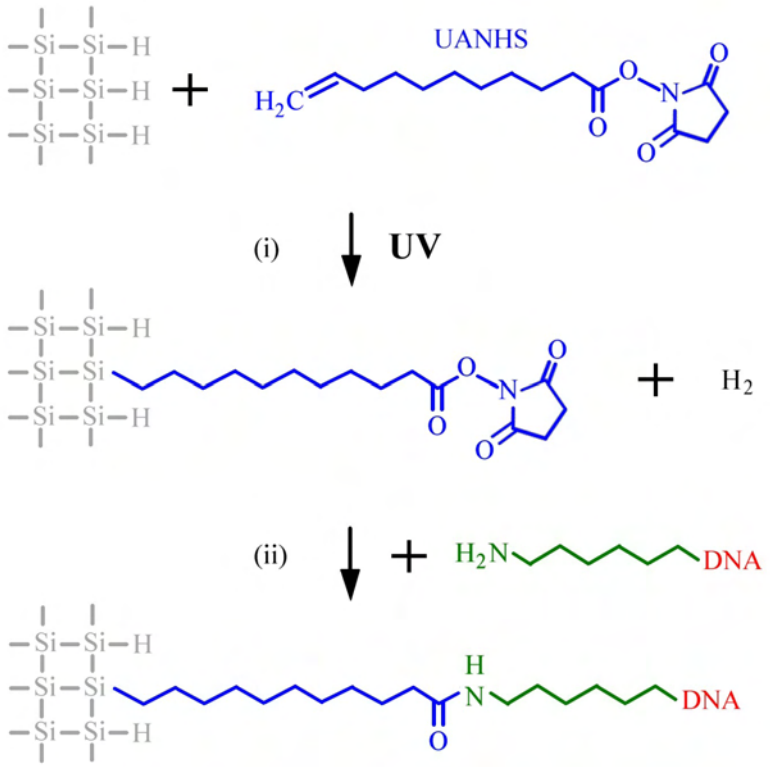

Figure 3.12: A schematic diagram for the attachment of DNA on silicon. (i) UV initiated reaction between the double carbon bond of the alkene (UANHS) and the hydrogen terminated silicon substrate. (ii) The amino-modified DNA oligonucleotide was added in an aqueous solution to displace the succinimide ester group to yield covalently attached oligonucleotides.

the 3′amino-hexyl-DNA oligonucleotide displaces the succinimide ester group of the UANHS alkene yielding covalently attached oligonucleotides (see Figure 3.12 ii). After incubation samples were washed in de-ionised water for 30 minutes, exchanging for fresh water every 10 minutes. Samples were inspected under a light-field microscope to determine the outcome of the fabrication batch. The steps involved in DNA patterning are shown in Figure 3.13.

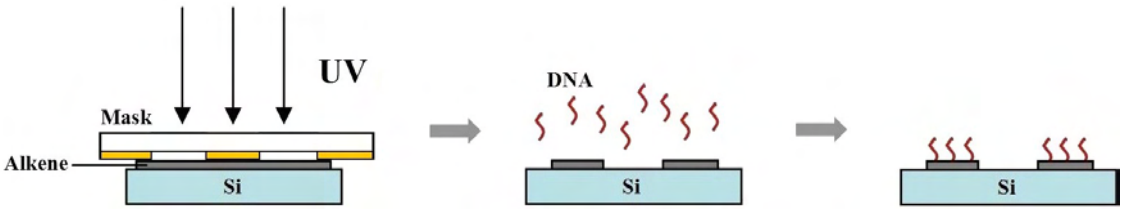

Figure 3.13: DNA patterns are created on silicon by conjugating oligonucleotides on to a UV photo-attached alkene substrate.

The fabricated diffraction gratings consisted of a 3×6 mm array of 150 DNA functionalised lines 10 μm wide, with 30 μm separation giving a 40 μm period and a grating area of 18 mm^2. A light-field microscope reflection image of a typical DNA grating on silicon is

shown in Figure 3.14. A fluorescent image of the grating is shown in Figure 3.15 featuring hybridised fluorescent labelled DNA probes with a complementary oligonucleotide sequence to the DNA patterned on the surface.

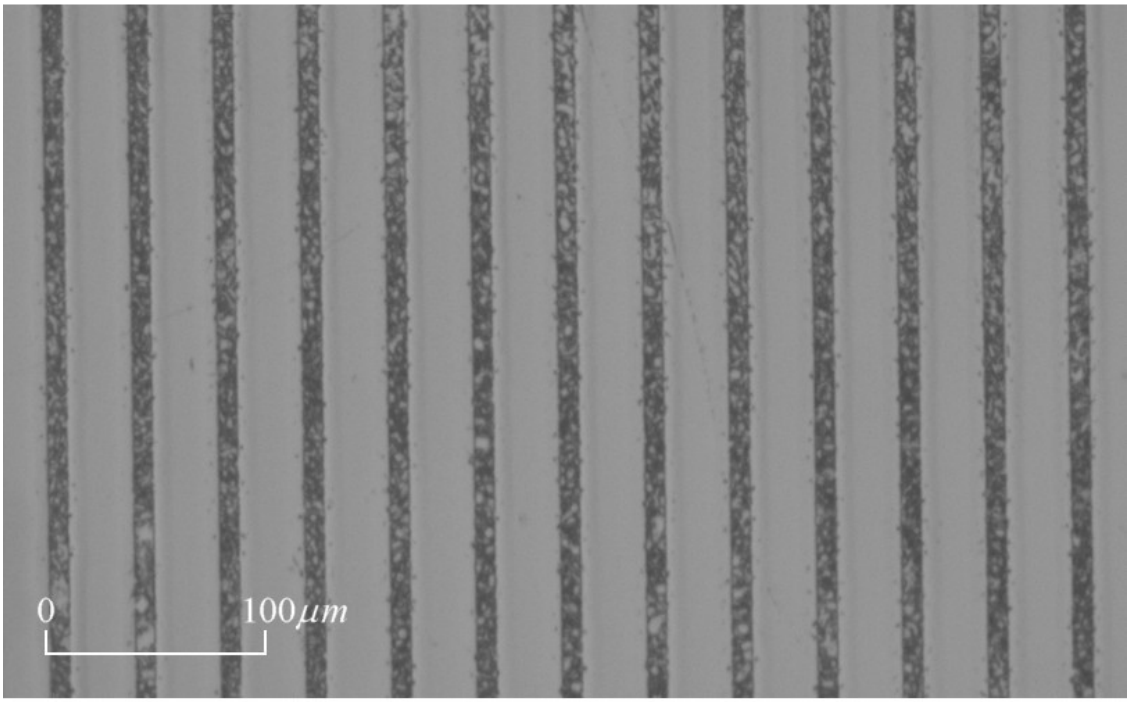

Figure 3.14: Optical microscope reflection image (10× magnification) of DNA functionalised diffraction grating lines on a silicon substrate.

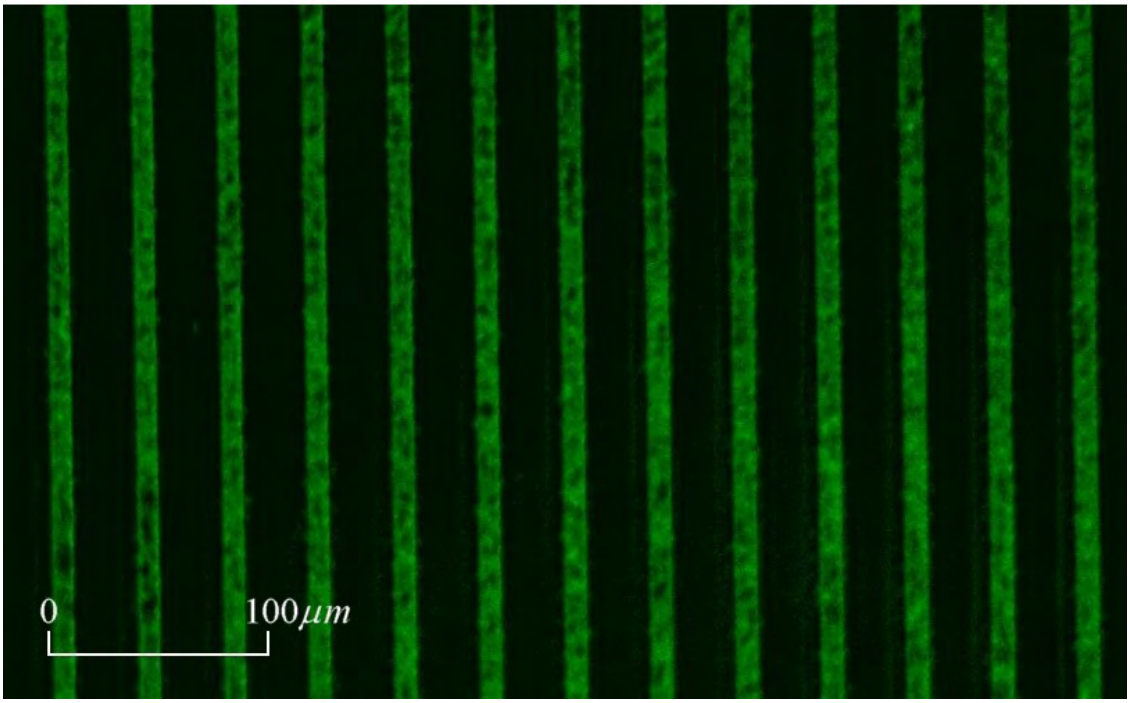

Figure 3.15: Epifluorescent reflection microscope image of a DNA diffraction grating with hybridised complementary fluorescent labelled DNA.

The microscope images of the DNA gratings show that the biological patterning is very well defined. The grating lines are continuous and the DNA attachment is only on the grating lines as desired, with virtually no non-specific attachment visible. The uniformity achieved is good for biomolecule patterning.

3.6 DNA Hybridisation

Prior to the hybridisation of complementary DNA, samples were washed in 2.5 % bovine serum albumin (BSA) solution to reduce non-specific attachment to the silicon surface. Labelled DNA sequences complementary to those immobilised on the silicon were prepared in a hybridisation buffer 0.3 M NaCl 10 mM phosphate pH 7.0 (phosphate buffered saline). Samples were rinsed in de-ionised water and dried under a stream of nitrogen. DNA sequences for hybridisation were either fluorescently labelled (see Figure 3.15) or attached to gold nanoparticles (see Figure 3.16). A volume of 7.0 μl of the DNA solution was added on top of the samples, which were subsequently covered with a glass coverslip and placed face down in a humid chamber at room temperature for 4 hours.

Figure 3.16: Gold nanoparticles featured oligonucleotide sequences complementary to those immobilised on the silicon.

After hybridisation, samples were washed in fresh 0.3 M NaCl 10 mM phosphate buffer pH 7.0 to remove non-hybridised DNA from the samples. The buffer was exchanged 3 times whilst agitating gently for 30 minutes. Samples were then stored in a fridge in 0.3 M NaCl 10 mM phosphate buffer pH 7.0 ready for use in diffraction experiments. Figure 3.17 shows a schematic illustration of hybridising gold nanoparticles to the DNA sensor for diffraction analysis.

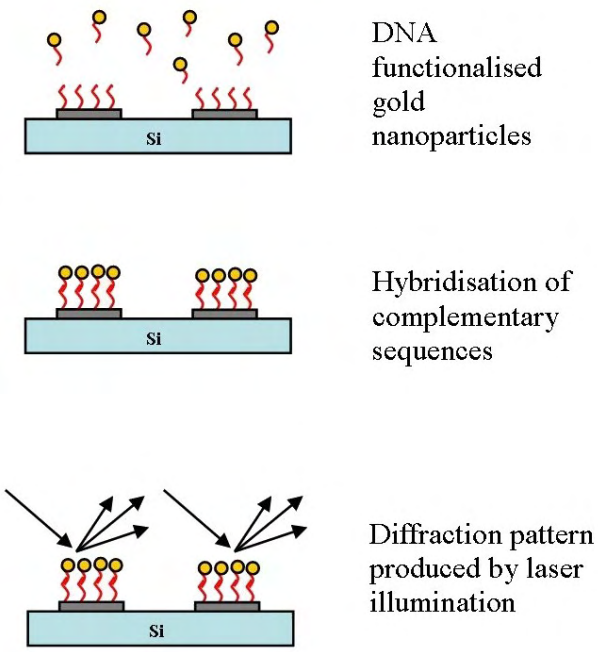

Figure 3.17: Schematic diagram of the detection experiment. Gold nanoparticles featuring oligonucleotide sequences complementary to those immobilised on the silicon surface were hybridised to test diffraction from DNA gratings.

3.7 Preparation of Gold Nanoparticles Functionalised with DNA

Gold nanoparticles functionalised with DNA oligonucleotides for use in hybridisation experiments were prepared in-house. Mono-maleimide functionalised gold probes of 1.4 nm diameter were supplied by Nanoprobe Inc. Gold colloids of 10 nm diameter were sourced from British Biocell International Ltd. Thiol-terminated oligonucleotides were produced by reduction of disulfide oligonucleotides with dithiothreitol (DTT). This involved dissolving freeze-dried disulfide oligonucleotides in 0.1 M $NaHCO_3$ 0.01 M DTT solution and incubating at room temperature for one hour. Ethyl acetate was added to extract DTT from the solution and repeated 3 times. The solution was then put through a Nap-10 column (GE Healthcare) with de-ionised water to remove salt. The collected fractions were then freeze dried.

The freeze-dried thiol-terminated oligonucleotides were re-dissolved in de-ionised water and added to a gold nanoprobe solution in 150 mM NaCl, 1.0 mM ethylenediamine tetra-acetic acid (EDTA), 20 mM NaH_2PO_4 (sodium dihydrogen phosphate) pH 6.5 buffer. This solution was then shaken for 24 hours at 4^oC. The solution was then adjusted to 0.1 M NaCl 10 mM

phosphate buffer pH 7.0 and shaken for another 40 hours. The solution was then washed by centrifuging for 10 minutes at 13 000 rpm, taking the supernatant and centrifuging that for 45 minutes at 45 000 rpm. The supernatant was disposed of and the sediment re-dispersed in fresh 10mM phosphate buffer 0.1 M NaCl pH 7.0. This was repeated 3 times and after the final wash the solution was adjusted to hybridisation buffer conditions, 0.3 M NaCl 10 mM phosphate buffer pH 7.0. Gold nanoparticles were then ready for hybridisation to complementary DNA sequences immobilised on silicon substrates (as shown in Figure 3.16).

3.8 Fabrication Development

Fabrication of DNA samples on silicon produces very good patterns for successful samples, but is often a low yield process in comparison to fabricating planar metal structures due to the large number of processing steps involved and the fragility of biological samples. There are several stages where slight variations of the conditions can prevent patterning from being successful.

To reduce the rate of re-oxidisation of the silicon surface and to avoid exposure of the alkene to light samples were kept in a dark nitrogen environment prior to the UV illumination patterning. Samples were also patterned in a nitrogen environment because of the long exposure time. This was found to successfully increase the yield of fabrication.

Water or moisture absorption by the alkene prior to patterning greatly reduced its functionality. A number of methods were used to minimise exposure to moisture whilst defrosting the alkene by drying it out with nitrogen, and absorbing condensation that formed around the glass vial. It was also flushed through with nitrogen and sealed prior to re-freezing. The alkene powder was weighed and added to the DCM solvent and sealed in a glass vial as quickly as possible, whilst the silicon substrates were being cleaned in fuming nitric acid. The UANHS alkene solution was then spun on to the samples immediately after removal of the oxide layer with HF acid. The alkene solution worked best when used within 2 hours. If another batch of samples was attempted using an alkene solution older than this, the patterning tended to fail or have a lower yield.

Some problems were identified with the UV illumination of the alkene and this was resolved using the following method. Initial patterning for the first diffraction gratings fabricated had used an Excimer laser (248 nm wavelength). Whilst illumination times were very short

(due to the high intensity of laser light), the beam quality was poor and diffraction grating lines appeared quite "grainy". The early gratings had a 10 micron line width, and 20 micron period. This was resolved by placing the mask directly on top of the sample, with gravity providing adequate force to ensure close, parallel contact between the mask face and the alkene coated silicon surface. Initial masks had been fabricated from chrome on fused silica, but in order to ensure an inert surface gold was used for direct contact masks. Masks were cleaned with isopropanol between batches to keep them clean. These steps removed the diffraction fringes from the DNA grating patterns, but the laser-speckle effect remained due to the coherent nature of the laser beam with poor spatial beam quality.

It was desirable to be able to use a UV lamp for patterning for several reasons. Firstly, to improve the line quality of the DNA grating by allowing homogeneous illumination with an incoherent UV source. An Oriel Instruments 500 W mercury xenon Hg(Xe) lamp was used for UV illumination of the UANHS alkene. The exposure time and lamp intensity were varied to find the optimum conditions for patterning.

When illumination conditions had been optimised fabrication was proving to be inconsistent with the UV lamp. If the grating pattern was faint but visible, it indicated alkene attachment (otherwise there would be no pattern), but no DNA conjugation. Since patterning was more consistent with the monochromatic laser emission at 248 nm, a filter was tried to cut out the high energy, short wavelength emission from the HgXe lamp, which could have been causing damage to the functional group of the alkene and preventing DNA conjugation. The lamp spectrum was very broad from $\sim 180 - 2500$ nm. An interference filter centred on 253.7 nm wavelength with a 10 nm FWHM transmission was used to limit the wavelength range to that required to initiate the photoreaction (around 250 nm). The illumination intensity and time were then optimised for the new illumination conditions. Optimum fabrication was achieved when an intensity of 1.0 mW/cm^2 was incident on the mask at 254 nm wavelength (measured with a UV power meter set to 250 nm), for a time of 6 minutes. This improved the fabrication yield and consistency of patterning using the UV lamp and therefore these conditions were adopted for the UV patterning of the alkene as diffraction gratings on silicon.

Early grating patterns had used a 20 μm period design with a 50 : 50 linewidth:separation ratio. It was observed that bubbles often formed under the glass coverslip during DNA conjugation, which created areas of the grating where DNA did not attach. This problem was resolved by altering the linewidth:separation ratio to 1 : 3 and using a larger period, enabling gas to escape and not build up. The design of the new grating structure which was adopted is described in detail in Chapter 4.

3.9 Silver-Enhanced Gold Nanoparticle Detection

The small size of gold nanoparticles is well beyond the resolution limit of conventional microscopes and makes them very difficult to detect with AFM. However, the gold nanoparticles can act as a useful reduction centre for silver enhancement [216], enlarging the particle size and enabling easier detection. The gold nanoparticles act as a catalyst causing the growth of a silver shell around the nanoparticles; without the gold present silver growth will not be initiated. By altering the silver enhancement time the size of the silver shell can be controlled until the particles become large enough to be detected by methods such as SEM. Further silver growth by precipitation of metallic silver gives a high contrast signal visible under a light microscope. Figure 3.18 shows a schematic of the silver-shell growth on gold nanoparticles hybridised to DNA immobilised on silicon.

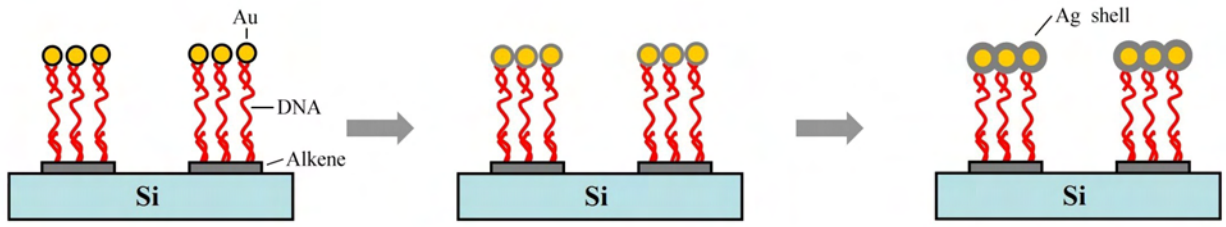

Figure 3.18: Silver enhancement causes the growth of a silver shell around the gold nanoparticles, making their detection possible under a visible light microscope.

3.9.1 Silver Enhancement Procedures

DNA samples were fabricated as described previously (see Section 3.5). Gold nanoparticles used for hybridisation to DNA patterns were either 1.4 *nm* or 10 *nm* in diameter. According to the protocol developed by Bao *et al*, after hybridisation of gold nanoparticles to samples the buffer needed to be exchanged for a sodium nitrate based buffer rather than sodium chloride [127]. A Sigma Silver Enhancer kit was used for the silver growth. A silver salt solution and initiator solution were mixed in a 1 : 1 ratio immediately before use and applied to the samples with gold nanoparticle-labelled DNA regions. A silver salt solution, such as silver nitrate, is formed when silver reacts with a base and is dissolved in solution. Upon addition of an initiator e.g. hydroquinone, the silver ions are displaced by the quinone and then will condense around heavy metals or reduction nuclei. The solution is metastable and spontaneous metal deposition is very slow without condensation nuclei present to catalyse and significantly accelerate the process [74].

After the desired enhancement time the samples were rinsed with de-ionised water and then fixed for 2 minutes in a sodium thiosulfate solution, and rinsed again. Samples were examined under a light microscope and then by SEM with topography profiles determined using a KLA-Tencor surface profiler.

3.9.2 Results of Silver Enhancement

Initial silver growth experiments were carried out on one-dimensional DNA diffraction gratings on silicon. Samples were tested without DNA conjugation (the alkene patterned sample was exposed to buffer only conditions), with DNA only, and with DNA and hybridised gold nanoparticles. Figure 3.19 shows a conventional light microscope image of a sample where only conjugation buffer (0.1 M $NaHCO_3$ 10 % DMF) was applied to the sample before silvering i.e. no DNA or gold was present on the sample. This sample shows little contrast after silver growth for 7 minutes, showing that silver reduction did not occur.

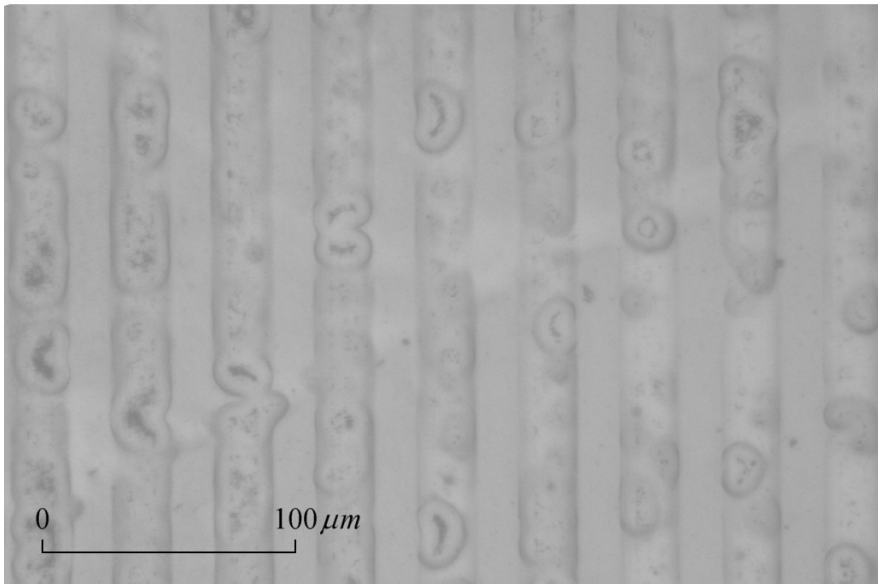

Figure 3.19: Without conjugated DNA or the presence of gold nanoparticles, silver growth was not observed using an optical microscope.

Figure 3.20 shows a DNA grating which was silvered under the same conditions but without hybridised gold. Some silver precipitation is visible on this sample due to the presence of DNA, but the rate of silvering was much slower than for samples with hybridised gold nanoparticles of 1.4 nm diameter (such as the sample shown in Figure 3.21). The samples with hybridised gold nanoparticles showed a much greater light/dark contrast between regions with DNA and hybridised gold (where silver growth was high) and the silicon background (where silver precipitation was low) when imaged on a reflecting optical microscope.

All samples in the initial experiment were silvered for 7 minutes, but some silver growth is visible between grating lines where there should be no DNA or attached gold nanoparticles, indicating that the enhancement time could be reduced.

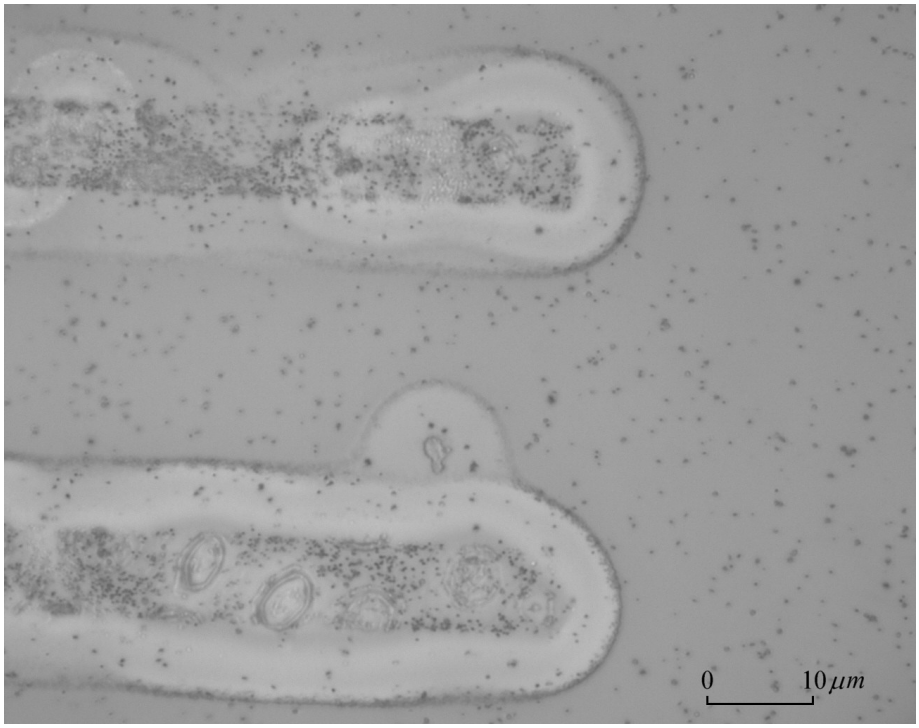

Figure 3.20: On DNA gratings without gold colloids, minor silver precipitation was evident, observed at 100× magnification using a reflecting optical microscope.

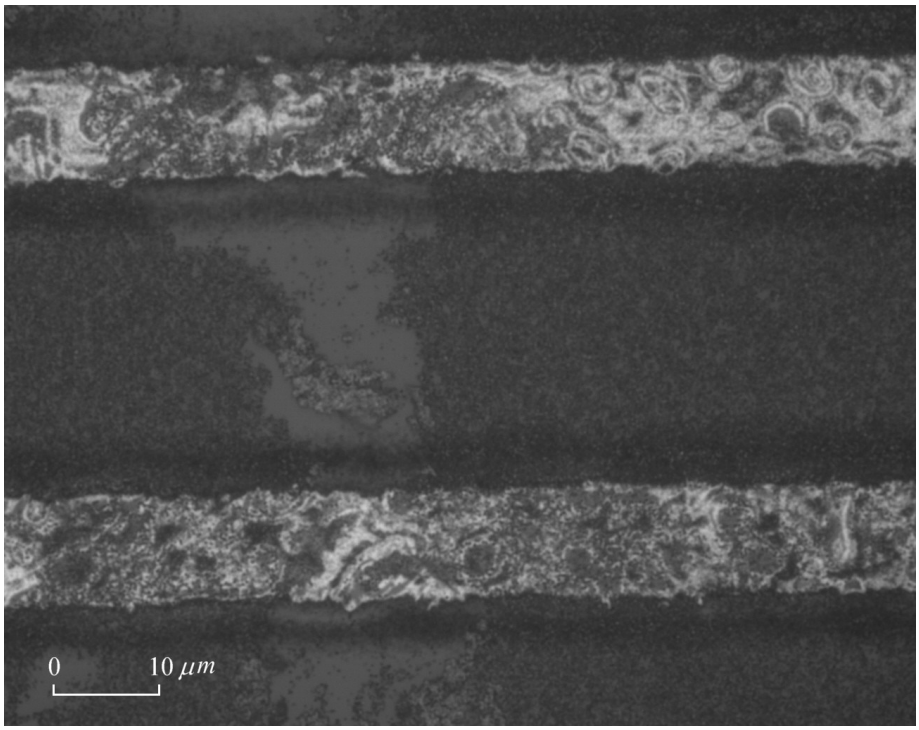

Figure 3.21: Samples with hybridised gold nanoparticles showed significant silver growth on DNA regions and a much higher optical contrast (100× magnification).

Work on silver growth conditions was optimised on two-dimensional DNA patterns of 100 μm diameter dots on the silicon substrate with hybridised 10 nm diameter gold colloids. The optical contrast between a gold labelled DNA region compared to the bare silicon was measured after silver enhancement for varying times. The optical contrast was determined by measuring the maximum pixel brightness of a DNA spot compared to a bare silicon region of the sample. An almost linear relationship was found between the length of time a sample was immersed in the silver enhancement solution compared to the change in optical contrast observed within the first 4 minutes, as shown in Figure 3.22. Microscope images of the samples used for the reflected light intensity measurements are shown in Figure 3.23 before and after silver enhancement procedures.

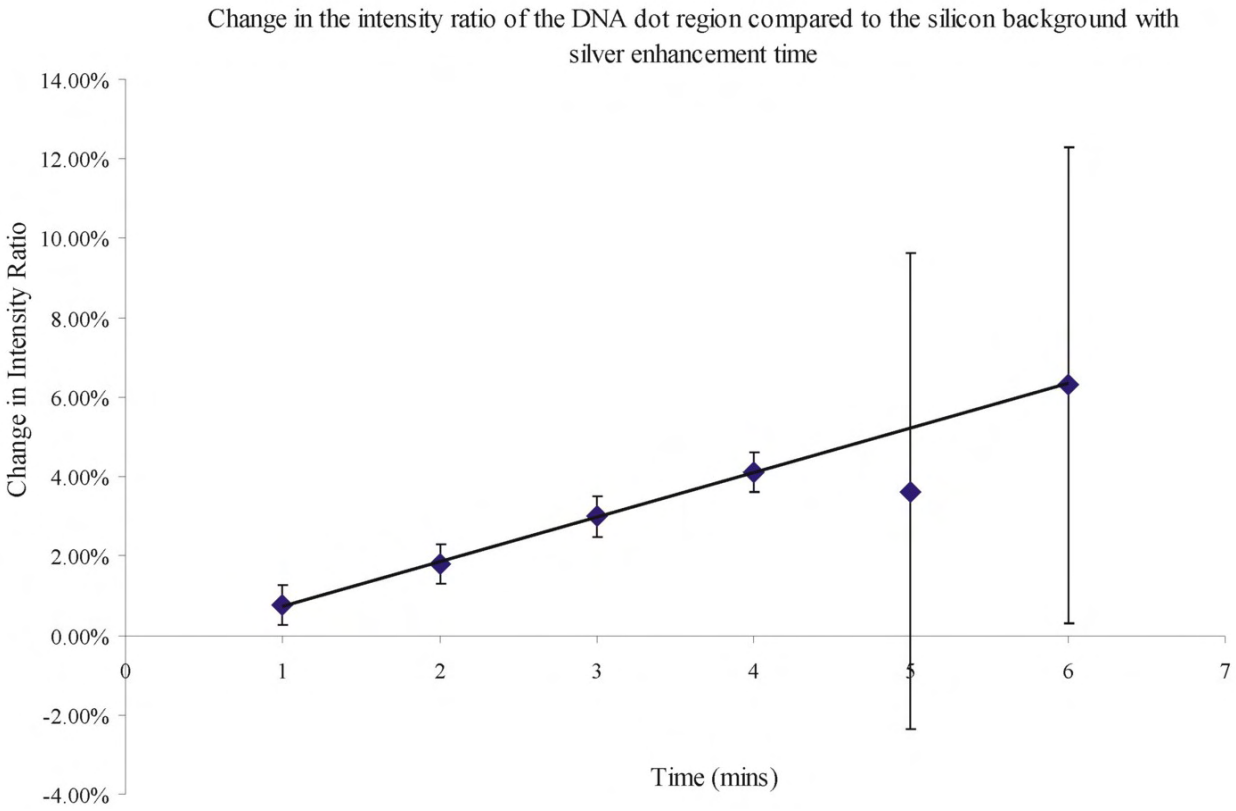

Figure 3.22: A linear relationship was observed between the change in optical contrast of a DNA region with hybridised gold nanoparticles over an unpatterned silicon region, with the duration of time immersed in the silver enhancement solution.

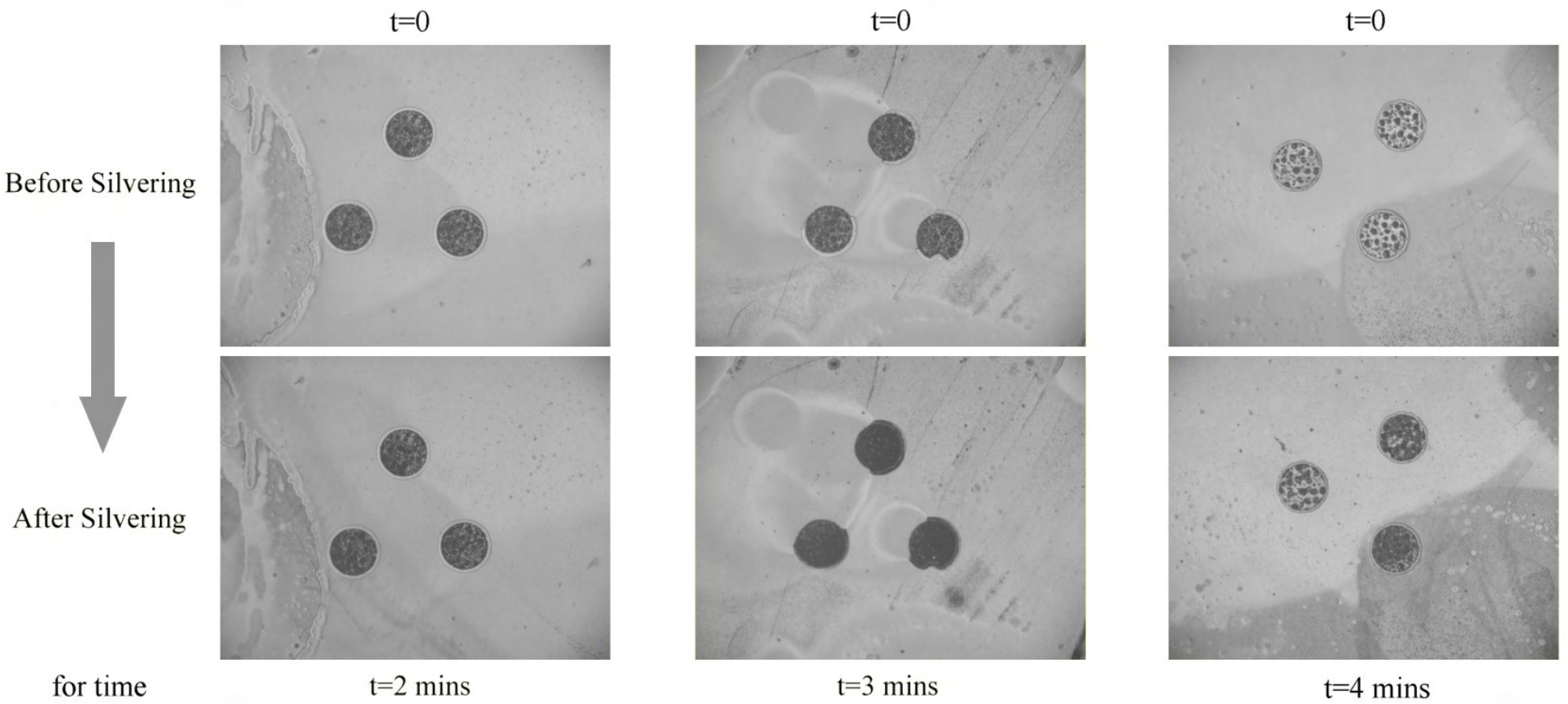

Figure 3.23: Silvered dot-pattern reflection microscope images used for measuring the dependence of the change in optical contrast with silver enhancement time. The DNA dots have a diameter of 100 μm and were hybridised with 10 nm gold nanoparticles prior to silver enhancement.

No difference in optical contrast was observed for the DNA patterns upon hybridisation of 10 *nm* gold colloids alone, but a decrease in the reflectivity of the DNA region compared to the silicon background was observed following silver enhancement of the samples. After silver enhancement times of greater than 4 minutes the homogeneity of the surface becomes much less consistent and the contrast measured was much more variable.

A Scanning Electron Microscope (Oxford Instruments, LEO 430 SEM) was used to examine the DNA-spot patterns to determine the extent of silver enhancement. Figures 3.24, 3.25 and 3.26 show the extent of silver coverage after gold nanoparticle labels (hybridised to the DNA regions) were treated with a silver enhancement solution for various times from 1 minute through to 8 minutes. After only 1 minute of silver reduction very little contrast is visible between the gold-labelled DNA spot and the background silicon in either the SEM or optical microscope images. After 2 minutes the DNA spots appear slightly darker in an optical microscope image (due to more scattering caused by growth of the silver particles) than before silver enhancement. The contrast was even more significant when observed using the SEM.

After 3 minutes the optical contrast between images captured before and after silver enhancement is readily visible by eye in conventional microscope images, as can be seen in Figure 3.25. The DNA spots (with silver enhanced gold nanoparticles) also appear a lot brighter on an SEM image than for samples subjected to shorter silver growth times.

After 4 minutes immersion in the silver enhancement solution silver growth started to saturate over the DNA regions. Further silver enhancement (from $5 - 8$ minutes) led to silver precipitation and a layer forming over the whole sample surface, as visible in Figure 3.26. The microscope image after 8 minutes clearly shows the brightness of the whole surface after extensive silver growth on top of the silicon, increasing the reflectivity. From these experiments it was determined that the optimum time for silver enhancement was 3 minutes. This provides significant silver enhancement of the gold nanoparticles, enabling a change in contrast to be observed on an optical microscope (therefore verifying the presence of the gold nanoparticles by silver growth), without over-developing the sample and causing precipitation to form on the whole surface.

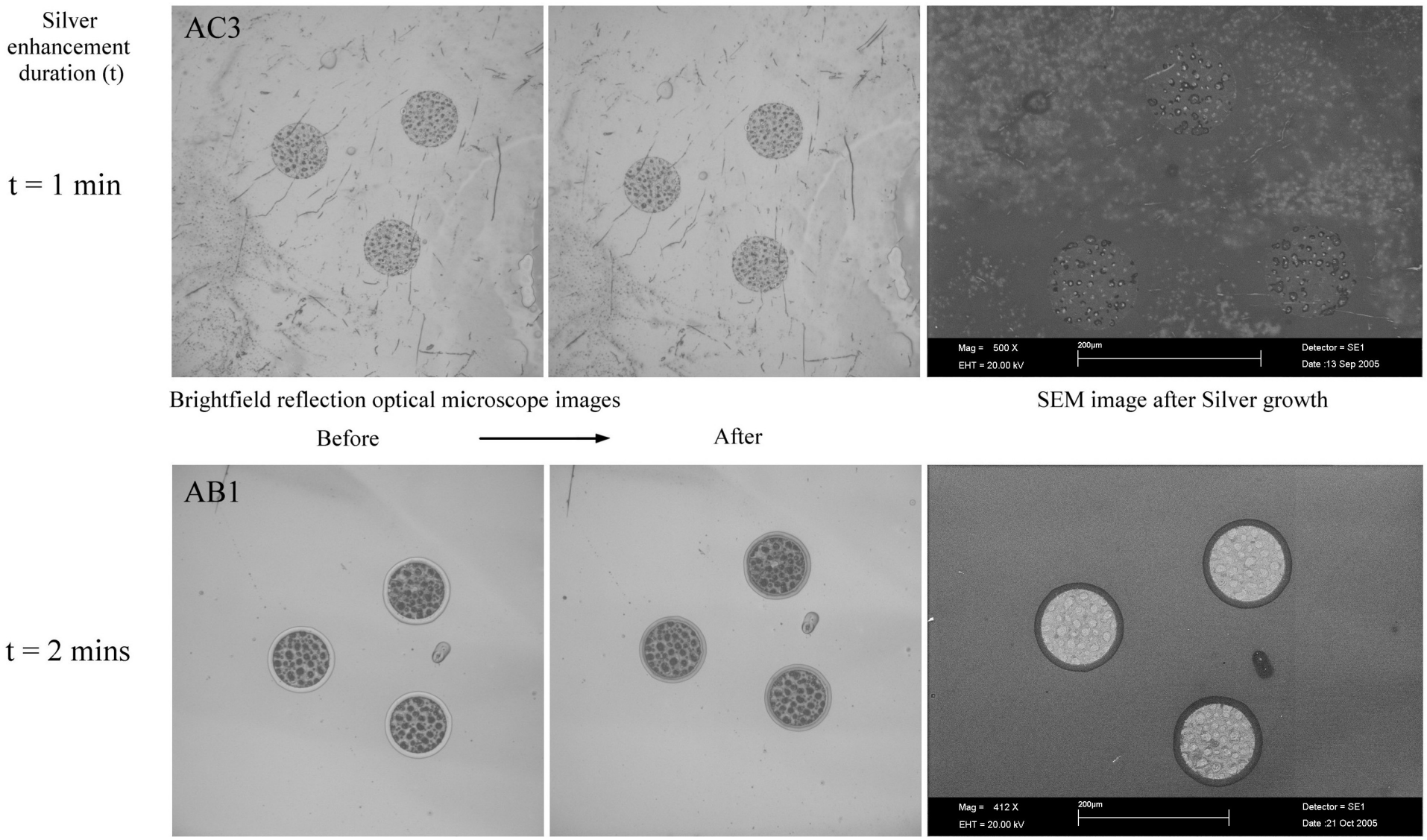

Figure 3.24: Left-hand column: Optical microscope images of the DNA on silicon samples. Centre column: Images after silver enhancement. Right-hand column: SEM images after silver growth. Top row: Sample silvered for 1 minute. Bottom row: Sample silvered for 2 minutes.

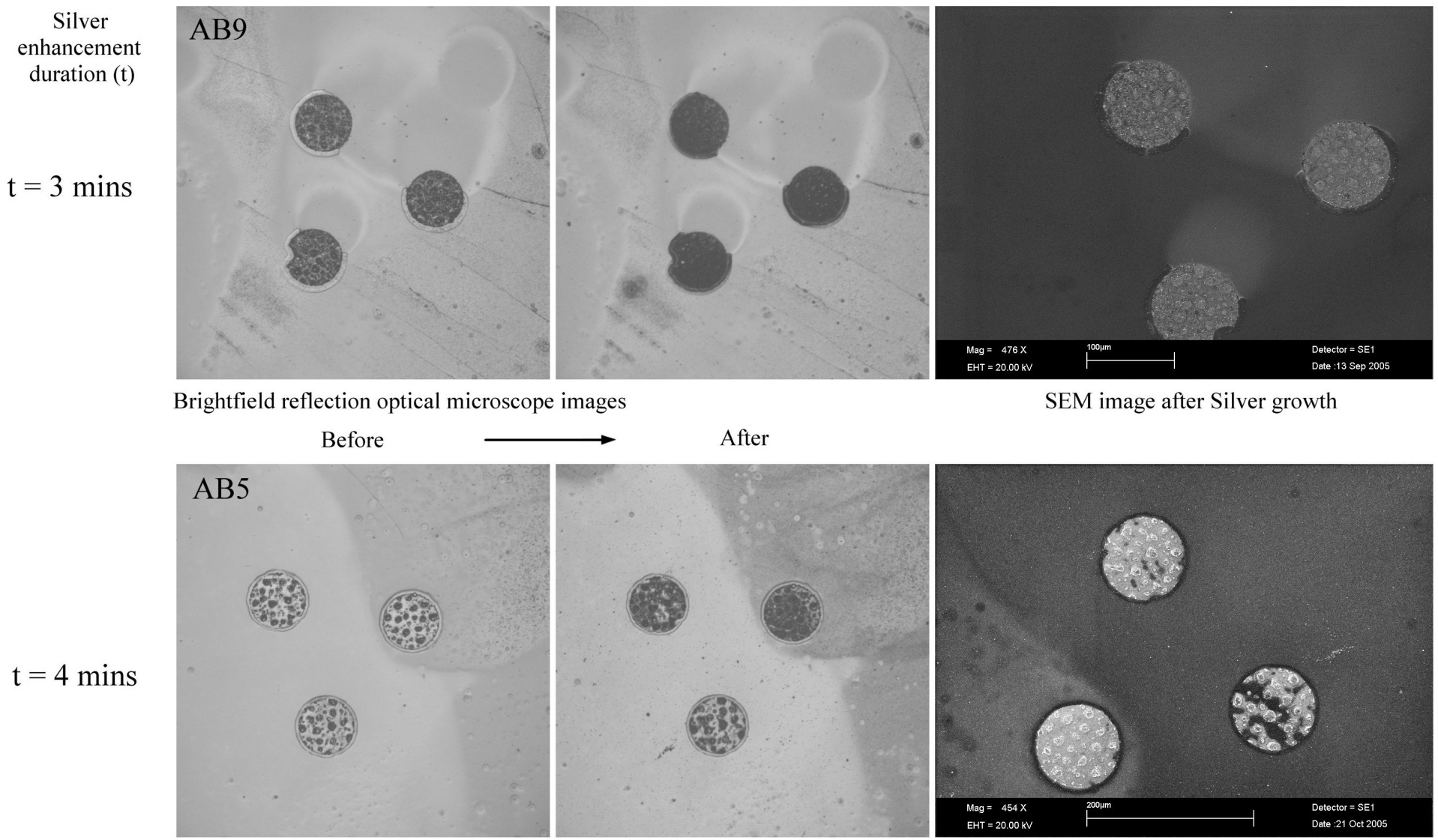

Figure 3.25: Left-hand column: Optical microscope images of the DNA on silicon samples. Centre column: Images after silver enhancement. Right-hand column: SEM images after silver growth. Top row: Sample silvered for 3 minutes. Bottom row: Sample silvered for 4 minutes.

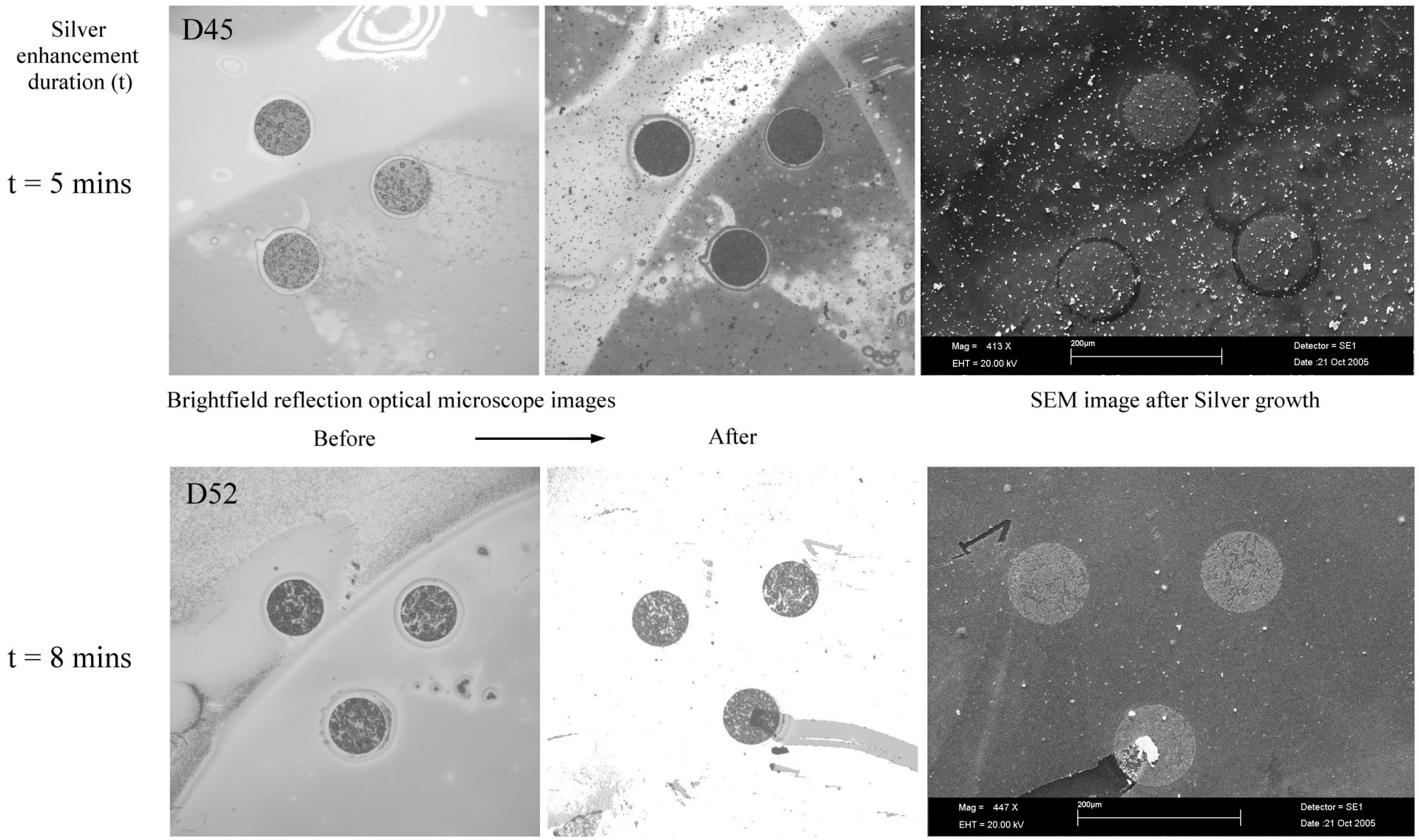

Figure 3.26: Left-hand column: Optical microscope images of the DNA on silicon samples. Centre column: Images after silver enhancement. Right-hand column: SEM images after silver growth. Top row: Sample silvered for 5 minutes. Bottom row: Sample silvered for 8 minutes.

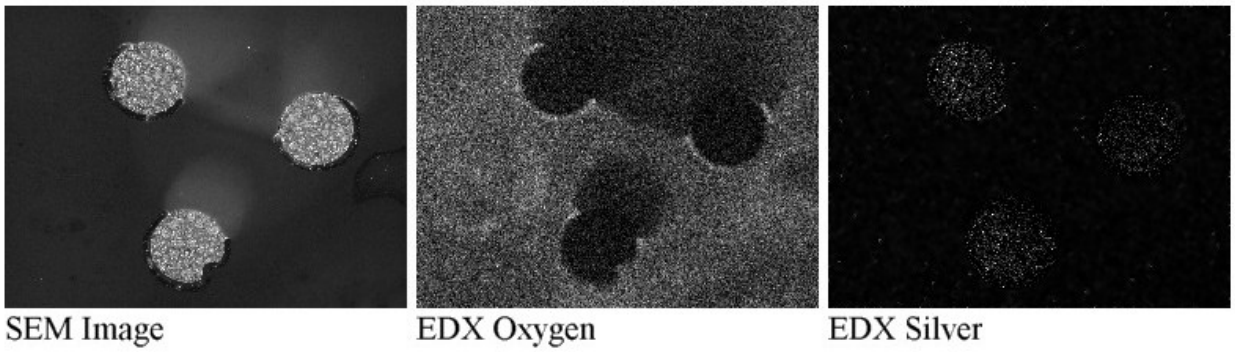

Figure 3.27: EDX analysis of DNA spots on silicon with gold nanolabels, silver enhanced for 3 minutes.

Silver presence can be determined by energy dispersive X-ray analysis (EDX) of the samples on the SEM, and the DNA spots appeared to have a significant change in contrast when imaged on an optical microscope. In this technique the energy spectrum of X-rays produced from the interaction of the electron beam with elements in the sample is measured, with different energy X-rays being emitted by different elements. The electron beam is scanned across the sample and the spectrum analysed at each point to build up an image of where different materials are located [217].

The EDX images of the silicon sample in Figure 3.27 show where the native oxide layer regenerated on the silicon, and how the alkene and DNA coverage prevented oxide growth. The silver component EDX image indicates that the brightness of the spots on the SEM image is due to the presence of silver. The trace is weak due to the thinness of the silver layer. At higher magnifications (nearly 30 000×) the individual silver coated gold particles are resolved by the SEM, with sizes in the range of $200 - 700\ nm$ following a silver enhancement duration of 3 minutes, as shown in Figure 3.28.

These results indicate that the presence of hybridised gold nanoparticles (too small to be detected easily with conventional microscopy techniques) can be readily verified by using silver enhancement. Using the optimised development time of 3 minutes, particle growth of up to 700 nm diameter generated resolvable features on an SEM and caused significant scattering to change the contrast of optical microscope images by ~ 3 %.

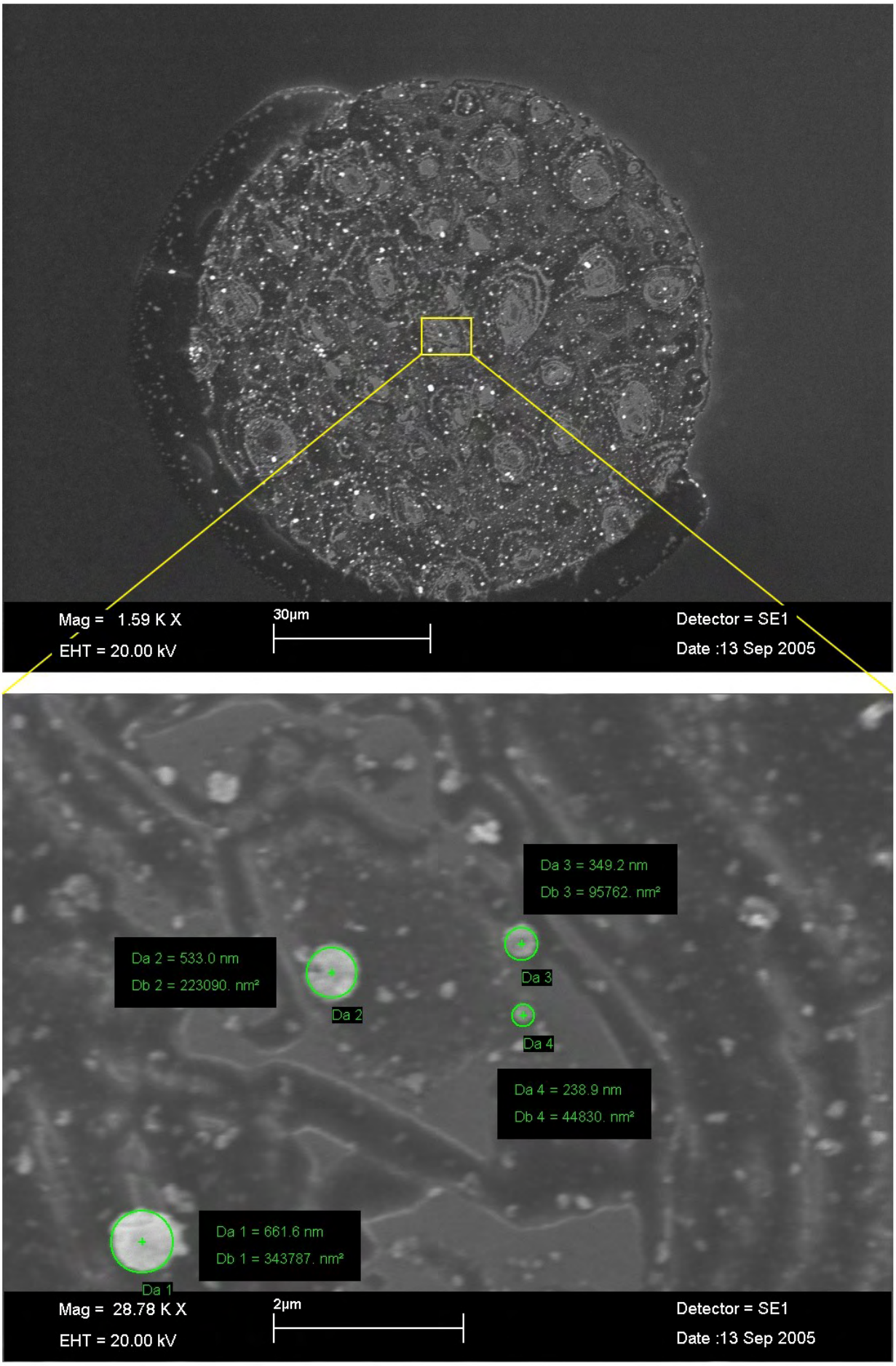

Figure 3.28: SEM images of a DNA spot on silicon with hybridised 10 *nm* diameter gold nanoparticles silver enhanced for 3 minutes, at 1 600 × and 29 000 × magnifications.

3.10 Summary

In summary, DNA patterns have been successfully fabricated on silicon (100) substrates via UV light initiated covalent attachment of the alkene UANHS, modified with functional groups for the conjugation of oligonucleotides. Patterns were designed and masks were produced to meet both the biological and optical requirements for fabrication and functionality. DNA patterns were then successfully created on silicon substrates for use in diffraction experiments. The patterns were neat and well-defined, with an absence of non-specific attachment and high density of DNA attachment, with a fluorescent probe hybridisation density of 1.2×10^{13} molecules/cm^2 representing a major achievement. Oligonucleotides were attached to gold nanoparticle labels complementary to sequences immobilised on the silicon surface. The gold nanoparticles were then successfully hybridised to DNA immobilised on the planar silicon substrate for use in diffraction experiments.

Silver enhancement (of gold nanoparticles) enabled the presence of hybridised gold nanoparticles to be detected using optical microscope reflection images to observe the change in contrast between silvered-DNA regions and the silicon substrate. The silver enhancement was verified, and individual particles with sizes in the range of $200 - 700$ nm were observed, by using SEM. The silver enhancement of gold colloids should increase the sensitivity of the DNA grating sensor compared to using gold alone by increasing the size of particles, causing a larger change in the reflectivity contrast between the DNA and silicon regions and generating more diffraction.

The physical and biochemical fabrication processes have been successfully established and optimised so that biological diffraction gratings could be prepared to enable the sensor performance to be evaluated.

Chapter 4

Modelling 1-D Diffraction Gratings

4.1 Principles of Diffraction Analysis

The first DNA analysis sensor investigated in this project was based on a one-dimensional reflecting diffraction grating. This consists of an array of parallel lines with periodic repetition. This chapter outlines the basic principles of how reflecting diffraction gratings work.

In order to develop the optimum diffraction grating pattern design for a DNA grating on silicon, diffraction theory had to be extended and modelled to cover an interlaced diffraction grating. In this situation both the DNA lines and the silicon substrate between the lines form reflecting diffraction gratings, which combine to contribute to the final diffraction pattern. The aim was to develop a grating structure which would maximise the sensitivity of diffraction order intensities to an increase in reflectivity of the DNA region (associated with hybridisation of gold nanoparticle probes).

The results of modelling interlaced reflecting diffraction gratings are used to design the optimum grating for fabricating with DNA on silicon. The surface coverage of gold nanoparticles is related to the change in reflectivity of the DNA lines and used to predict the change in diffraction. The effects of variations of diffraction grating parameters are also considered later in the chapter.

4.1.1 The Causes of Diffraction

Diffraction is a wave phenomena property of electromagnetic radiation. Diffraction may be defined as the departure from rectilinear propagation that cannot be interpreted as reflection or refraction. It is an effect resulting from interference of electromagnetic waves encountering obstacles, being scattered off surfaces, or passing through apertures. Diffraction is a useful technique to analyse the spacing between layers or rows of particles. For example, X-ray diffraction has been used to determine the orientation of single crystal grains, to determine the crystalline structure of materials, and to measure the size, shape and internal stress of small crystalline regions.

When light scatters off an atom the photon interacts with the atom and the resultant re-radiated photon has an equal probability of travelling in any direction. In scattering from regular arrays (for example in crystalline materials), constructive interference occurs in certain directions due to the geometry. This occurs when probability density waves of scattered photons interfere in-phase, adding constructively in superposition [218].

Electromagnetic waves may be described by the solution of Maxwell's wave equation, $\underline{\mathbf{E}} = \underline{\mathbf{E}}_o e^{i(\underline{\mathbf{k}}.\underline{\mathbf{r}}-\omega t+\phi)}$, where $\underline{\mathbf{E}}$ is the electric field intensity, $\underline{\mathbf{E}}_o$ the maximum intensity, ω is the angular frequency of propagation and ϕ is the phase shift, $\underline{\mathbf{k}}$ the propagation constant and $\underline{\mathbf{r}}$ the point of observation at time t [219]. For the waves to be in phase and add constructively then $\phi = 2m\pi$, where m is an integer. The intensity of scattered waves is the square of the total amplitude, which is given by the summation of the amplitudes of the electromagnetic fields from all points in space (by the principle of superposition). When the phase of scattered waves at a point is exactly out of phase ($\phi = \pi$), then complete cancellation occurs (destructive interference).

4.1.2 The Diffraction Grating Equation

Diffraction effects are easily observed by examining the transmission of light through multiple slits. By considering the interference of light propagating from each slit using ray optics the diffraction grating equation may be derived. An equivalent situation is to consider the interference of light reflected from a periodic array of reflectors, such as depicted in Figure 4.1. The diffraction grating equation describes the angle of an intensity maximum of the light diffracted from the scattering aperture (or surface), related to the order of the interference

pattern, the regular spacing of the contributing sources in the array and the wavelength of light used.

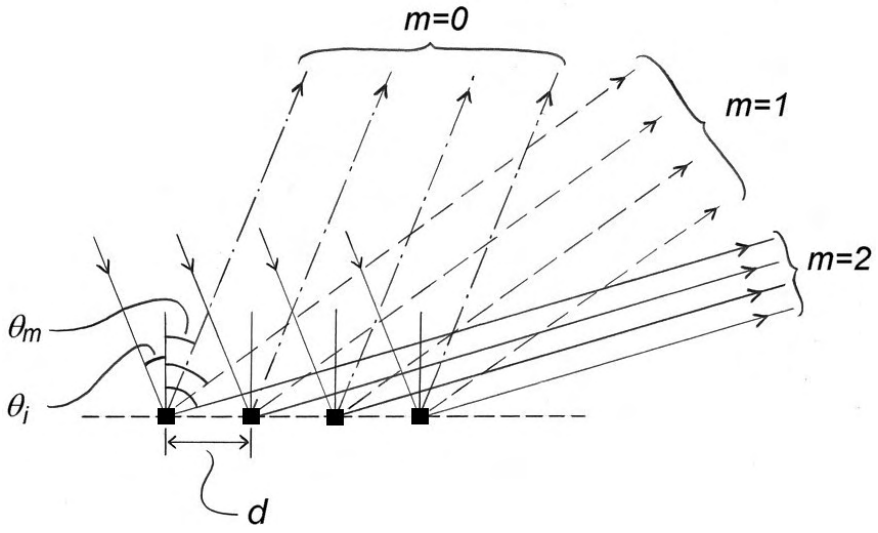

Figure 4.1: Rays scattered parallel with respect to each other are of the same diffraction order of wavelength path difference.

Parallel coherent light rays (for example, from a laser), are incident at an angle θ_i on the plane of adjacent lines of a diffraction grating which are separated by a distance d. Rays that scatter in a parallel direction belong to the same diffraction order (see Figure 4.1). The parallel scattered rays are aligned at an angle θ_m to the normal of the plane. At the point of observation any difference in the optical path length travelled between interfering rays, is a consequence of their diffraction being from different lines.

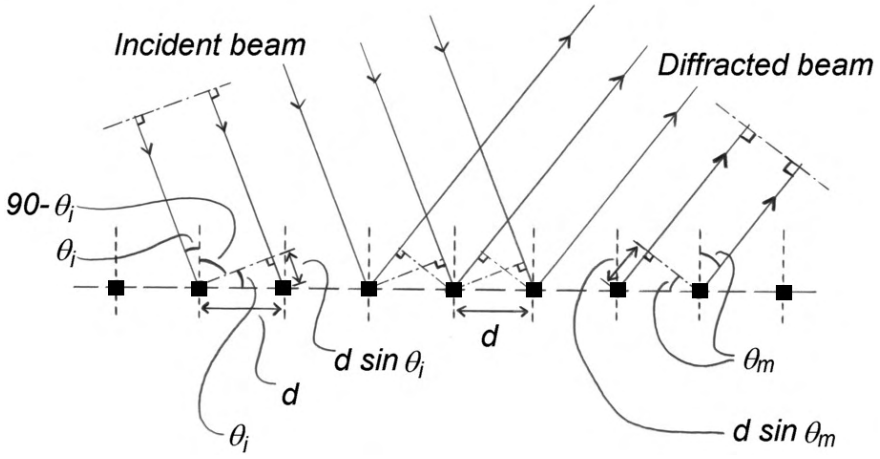

Figure 4.2: There is an optical path length difference introduced between incident and diffracted beams.

The optical path length difference on incidence (Δ_i) between two light rays incident on adjacent lines separated by a distance d is $\Delta_i = d \sin \theta_i$ (see Figure 4.2). The difference in optical path length for scattered rays (Δ_m) is given by $\Delta_m = d \sin \theta_m$.

To form an intensity maximum all the rays of the same order (i.e. rays that have scattered parallel to each other) must interfere constructively. Hence the total path difference $\Delta = m\lambda$, where m is an integer, so that all the waves are in phase and their path difference is a whole number of wavelengths.

The total optical path length difference (Δ) between incident and scattered rays necessary for constructive interference is $\Delta = \Delta_m - \Delta_i = m\lambda$:

$$d(\sin\theta_m - \sin\theta_i) = m\lambda \tag{4.1}$$

This is called the diffraction grating equation [220]. The diffraction grating equation specifies the angular location of the principal maximum of the m^{th} diffraction order [221]. The equation relates the angle θ_m of diffraction order m to the grating period d, for a given wavelength λ of light incident upon the grating at an angle of θ_i [222]. Under the condition of an infinite array of diffracting slits, or scattering points, then the superposition of light rays will cancel everywhere except where the path difference is exactly $m\lambda$. This leads to a diffraction pattern of sharply defined points; intensity maxima. When there is a finite number of scattering points in the array there will not be exact cancellation at all points in between maxima, and the points will be 'blurred' or broadened. In this case, the grating equation specifies the location of the centres of the intensity maxima relative to one another.

A pattern that has small features in real space, of the same order of magnitude as the wavelength of light, will produce a diffraction pattern that is broad in reciprocal space compared to features which are several orders of magnitude larger than the wavelength, which will produce narrow features in a diffraction pattern. The greater the number of scattering points involved in generating the diffraction pattern, the narrower the angular width of the intensity maxima will be in reciprocal space.

4.2 Fourier Theory of 1-D Diffraction Gratings

The diffraction theory presented here is based on a classical treatment of the wave nature of light. The measured intensity of light (I) is proportional to the square of the total amplitude (R_{total}) at the point of observation:

$$I \propto {R_{total}}^2$$

When features on a reflecting surface are of a size greater than the wavelength of light illuminating them, diffraction effects are observable. The diffracted wave amplitude R is proportional to the Fourier Transform of the transmission function $T(x, y)$.

$$R(\theta) \propto \mathcal{F}\{T(x, y)\}$$

The same is true for reflection from a surface, with $T(x, y)$ being the surface reflectivity rather than transmission as a function of position.

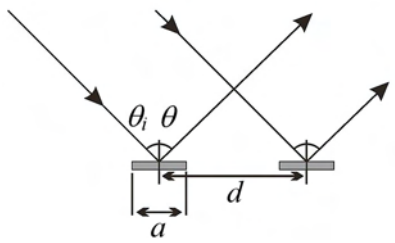

Figure 4.3: There is an optical path length difference introduced between light reflected from adjacent lines.

For the case of a reflecting diffraction grating (see Figure 4.3), the reflection function $T(x, y)$ is that of a rectangle of width a, repeated N times with a periodic displacement of d. $T(x, y)$ is the convolution of the reflecting surface shape (the line of width a) with its distribution function (N lines with a periodic separation of d). Since the amplitude of the diffraction pattern observed is proportional to the Fourier Transform of the transmission function, the diffraction pattern corresponds to the diffraction pattern of a single line multiplied by the Fourier Transform (FT) of the distribution function. These well-known results are:

$$\mathcal{F}\{distribution\} \propto \frac{\sin(N\delta/2)}{\sin(\delta/2)} \quad \text{and} \quad \mathcal{F}\{line\} \propto \frac{\sin(\beta)}{\beta}$$

where

$$\delta = 2\pi d(\sin\theta - \sin\theta_i)/\lambda \quad \text{and} \quad \beta = \pi a(\sin\theta - \sin\theta_i)/\lambda$$

Note that the fixed angle of incidence θ_i is taken into consideration in the δ and β terms. θ represents the angular position co-ordinate over which the diffracted intensity distribution is being calculated.

Subsequently the expression obtained for the resultant amplitude of the diffraction pattern is

$$R(\theta) = \mathcal{F}\{T(x, y)\} \propto \frac{\sin(N\delta/2)}{\sin(\delta/2)} \times \frac{\sin(\beta)}{\beta}$$

or

$$R(\theta) = A\frac{\sin(N\delta/2)}{\sin(\delta/2)}\frac{\sin(\beta)}{\beta}$$

Since $I \propto {R_{total}}^2$ then the resultant intensity observed is determined by

$$I(\theta) = I(0)\frac{\sin^2(N\delta/2)}{\sin^2(\delta/2)}\left(\frac{\sin(\beta)}{\beta}\right)^2$$

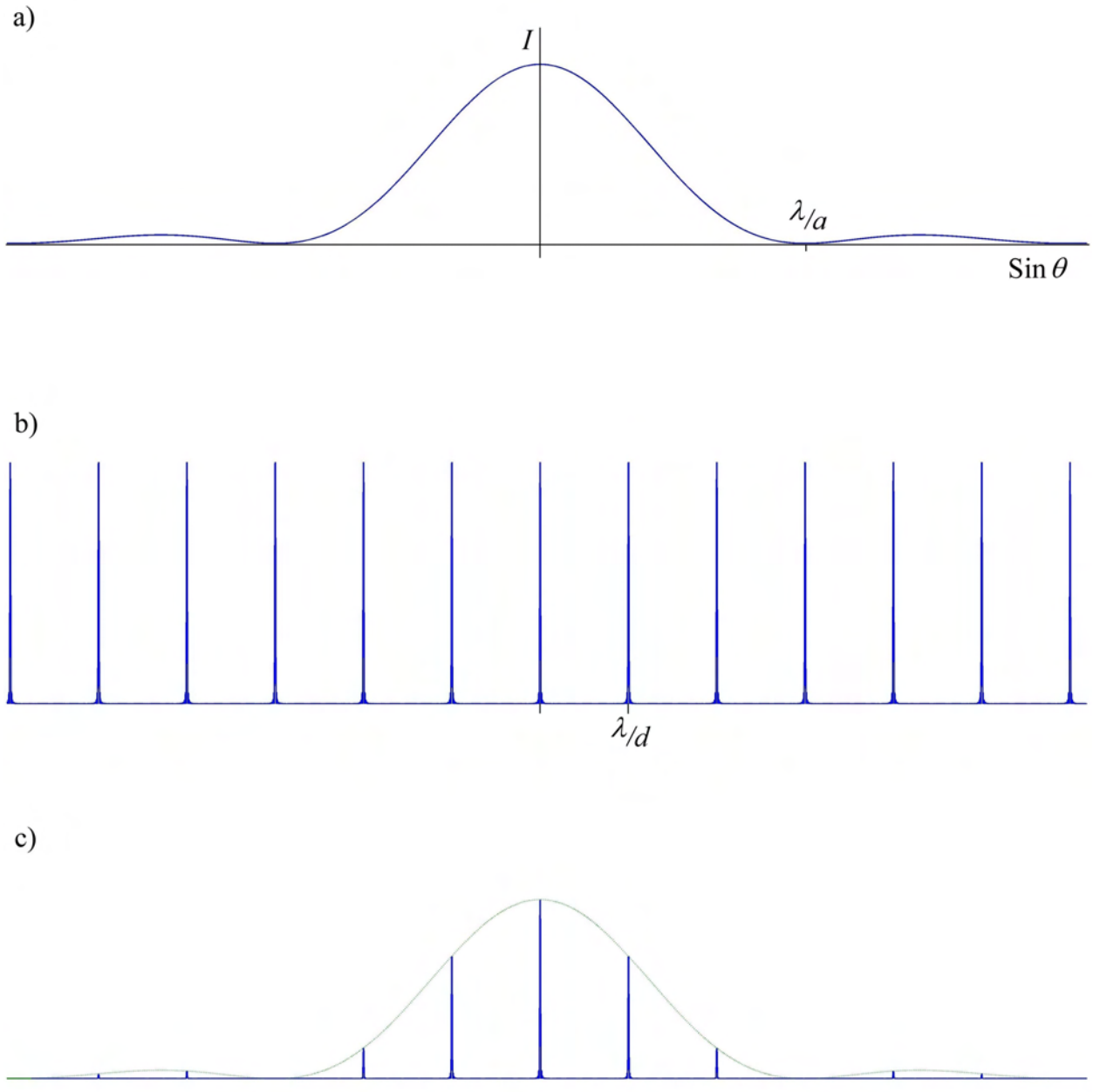

Figure 4.4: a) Envelope function due to the shape of the lines within the grating. b) Modulation due to distribution of lines. c) Resultant diffraction intensity pattern.

The width of the line a (as shown in Figure 4.3) is the smallest dimension involved with the diffraction and so diffracts light over the widest angular range, producing an 'envelope

function' centred with I_{max} at $\theta = \theta_i$. This governs the overall intensity maxima of the diffraction pattern (as shown in Figure 4.4) and is a $\text{sinc}^2\beta$ function, where $\text{sinc}\beta = (\sin\beta)/\beta$. The envelope is modulated by the square of the FT of the distribution function

$$\frac{\sin^2(N\delta/2)}{\sin^2(\delta/2)}$$

This gives the position of the diffraction orders and the angular width of the orders decreases reciprocally with more lines N contributing to the diffraction pattern:

$$\text{width} \propto \frac{1}{N}$$

4.2.1 Interlaced Diffraction Gratings

The situation described above assumes that only light from the line of width a contributes to the diffraction pattern. To accurately model the situation of having a reflecting diffraction grating that is also on a reflective substrate, consider two interlaced diffraction gratings.

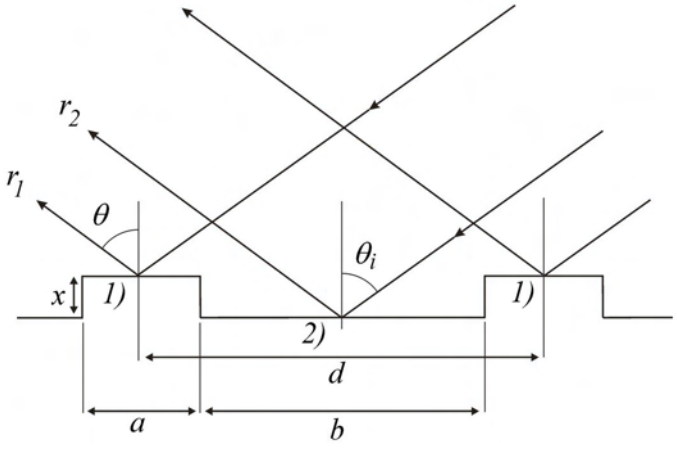

Figure 4.5: Two interlaced diffraction gratings with a fixed period. Amplitude contributions come from both regions (1) & (2).

Now there are two different β functions, β_a and β_b, corresponding to lines of width a and b, giving different envelope shapes. Both gratings have the same period (d) since a is the width of the grating line and b is the line separation, such that $a+b = d$. Both diffraction envelopes will therefore share the same modulation due to δ. When $a \neq b$, they will contribute different amounts of energy to the diffraction pattern due to having different areas. The interlaced gratings have different surface reflectivities (r_1, r_2) and there may also be a step height (x)

between them (see Figure 4.5). The vertical step height x will introduce a phase difference between the two gratings, as will their horizontal offset relative to each other of $d/2$. All of these factors must be taken into consideration to derive an expression to predict the diffraction pattern produced.

With reference to Figure 4.5, the contribution to the diffracted amplitude due to region (1), the grating line on the substrate, is given by:

$$R_1 = r_1 \left(\frac{a}{d}\right) \left(\frac{\sin\beta_a}{\beta_a}\right) \frac{\sin(N\delta/2)}{\sin(\delta/2)}$$

The contribution due to reflection from the substrate, region (2) of width b is:

$$R_2 = r_2 \left(\frac{b}{d}\right) \left(\frac{\sin\beta_b}{\beta_b}\right) \frac{\sin(N\delta/2)}{\sin(\delta/2)}$$

where

$$\beta_a = \frac{\pi}{\lambda} a(\sin\theta - \sin\theta_i) \quad \text{and} \quad \beta_b = \frac{\pi}{\lambda} b(\sin\theta - \sin\theta_i)$$

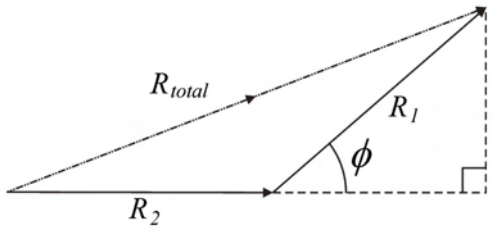

Figure 4.6: Phasor diagram showing the resultant amplitude R_{total} when accounting for the phase difference ϕ between amplitudes R_1 and R_2.

When adding amplitudes the phase difference ϕ due to the horizontal offset and vertical step height between the interlaced gratings must be taken into account. This can be calculated using the Pythagoras theorem via a phasor diagram (see Figure 4.6).

$$R_{total}{}^2 = R_1{}^2 + R_2{}^2 + 2R_1R_2\cos\phi$$

The resultant intensity is therefore

$$I(\theta) = I_0 \left[r_1^2 \left(\frac{a}{d}\right)^2 \left(\frac{\sin\beta_a}{\beta_a}\right)^2 \frac{\sin^2(N\delta/2)}{\sin^2(\delta/2)} + r_2^2 \left(\frac{b}{d}\right)^2 \left(\frac{\sin\beta_b}{\beta_b}\right)^2 \frac{\sin^2(N\delta/2)}{\sin^2(\delta/2)} \right.$$
$$\left. + 2r_1 \left(\frac{a}{d}\right) \left(\frac{\sin\beta_a}{\beta_a}\right) r_2 \left(\frac{b}{d}\right) \left(\frac{\sin\beta_b}{\beta_b}\right) \frac{\sin^2(N\delta/2)}{\sin^2(\delta/2)} \cos\phi \right]$$

or

$$I(\theta) = I_0 \frac{\sin^2(N\delta/2)}{\sin^2(\delta/2)} \left[r_1^2 \left(\frac{a}{d}\right)^2 \left(\frac{\sin\beta_a}{\beta_a}\right)^2 + r_2^2 \left(\frac{b}{d}\right)^2 \left(\frac{\sin\beta_b}{\beta_b}\right)^2 + 2r_1 r_2 \left(\frac{a}{d}\right)\left(\frac{b}{d}\right)\left(\frac{\sin\beta_a}{\beta_a}\right)\left(\frac{\sin\beta_b}{\beta_b}\right)\cos\phi \right]$$

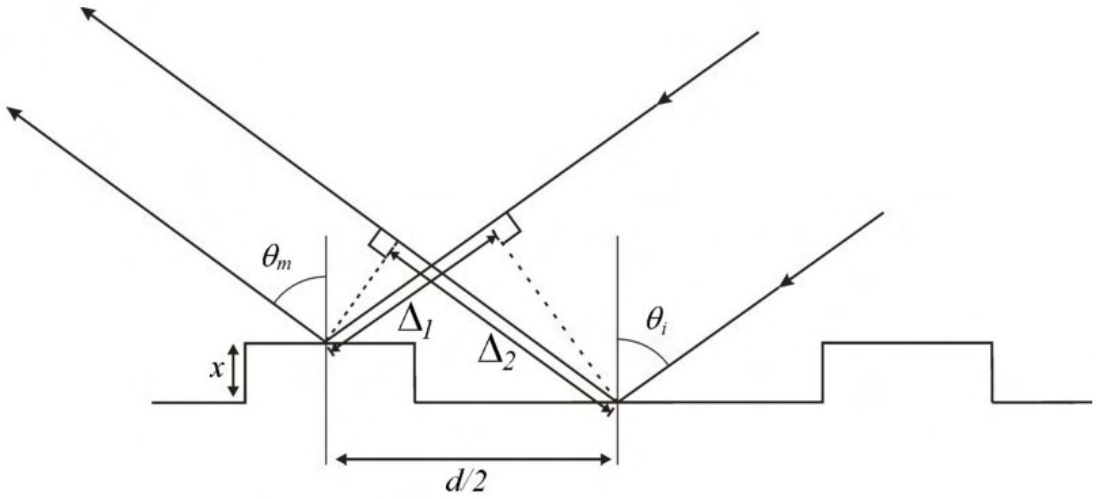

Figure 4.7: The origin of the optical path difference between the two interlaced diffraction gratings is due to lateral separation of half a period ($d/2$) and the vertical height difference (x) between the grating lines and the substrate. The path difference is given by $\Delta_2 - \Delta_1$.

Now consider the phase difference between light diffracting from region (1) compared to region (2). The phase difference is dependent upon the optical path difference between light reflecting off region (1) compared to adjacent region (2), as shown in Figure 4.7.

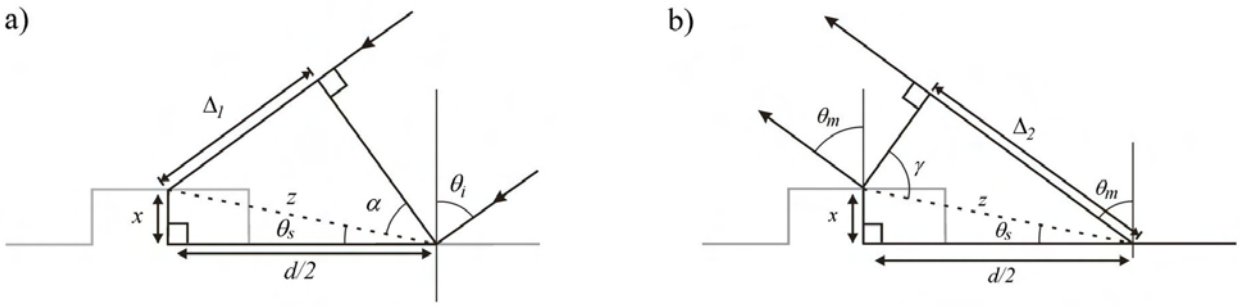

Figure 4.8: The optical path difference between light diffracted from the grating line and the substrate region may be calculated geometrically. a) The optical path difference on incidence is given by Δ_1. b) The path difference on diffraction is given by Δ_2.

The path difference on incidence (indicated in Figure 4.8 a), $\Delta_1 = z \sin\alpha$, where $z =$

$(x^2 + (d/2)^2)^{1/2}$, $\alpha = \theta_i - \theta_s$ and $\theta_s = \tan^{-1}(2x/d)$. Hence $\Delta_1 = z\sin(\theta_i - \theta_s)$. Similarly, it can be seen from Figure 4.8 (b) that $\Delta_2 = z\sin(\gamma) = z\sin(\theta_m + \theta_s)$. The total path difference is then given by:

$$\Delta_2 - \Delta_1 = z\left[\sin(\theta_m + \theta_s) - \sin(\theta_i - \theta_s)\right]$$

The phase difference is then $\phi = \frac{2\pi}{\lambda}(\Delta_2 - \Delta_1)$

$$\Rightarrow \phi = \frac{2\pi}{\lambda}\left(x^2 + \frac{d^2}{4}\right)^{1/2}\left[\sin(\theta_m + \theta_s) - \sin(\theta_i - \theta_s)\right]$$

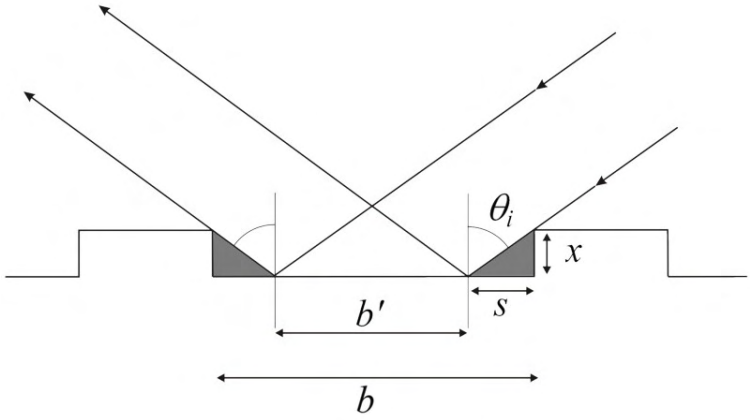

Figure 4.9: Two shadow regions are created due to the step height x and angle of incidence θ_i. Consequently, the illuminated region contributing to diffraction from the bottom surface is reduced. This has the effect of the size of the feature being reduce from b to b'.

Another point to consider is the effect of shadow regions (s) generated by the step height x and angle of incidence θ_i, as shown in grey in Figure 4.9. This reduces the effective contribution of the bottom surface, since one shadow region is not illuminated and light from the second shadow region is blocked by the vertical step. The size of the reflecting feature is reduced from b to b' where $b' = b - 2s$ and $s = x\tan\theta_i$. For DNA gratings on silicon the step is likely to be non-vertical, the semi-transparent nature of the surface coverage and the fact that the feature size b is over 300 times larger than the step height (30 μm versus < 100 nm), the shadow correction may be neglected.

Using the derived expression for combining the amplitudes from two interlaced diffraction gratings several programs were written in MATLAB^{TM} to examine the dependence of the diffraction order intensities with changes in the reflectivity ratio (r_1/r_2), the line:space ratio ($a : b$), and the height difference (x) between the two regions.

To verify the validity of the equation several test cases were examined. Firstly, when the

reflectivity from either one of the regions is zero the diffraction pattern should simply correspond to the diffraction pattern from a grating with lines of the width of the reflecting region. This was verified for normal incidence and for light incident at an angle θ_i. When $r_2 = 0$, the diffraction envelope corresponds to a linewidth of a. When $r_1 = 0$, the diffraction envelope is due to a linewidth of b. When the reflectivities are equal, $r_1 = r_2$ with no step height difference ($x = 0$), then the surface is effectively a plane mirror and there is only reflection, independent of the values of a and b. When a step height was introduced, the diffraction pattern corresponded to that of a single material with a relief grating.

With these limiting cases behaving as expected for individual diffraction situations, the program was also tested with values approaching the limiting situations to check that the predicted diffraction intensities were tending towards the expected values. When there was only a small difference in reflectivity and no step height, or a small step height and no difference in reflectivity, there were only very low intensity diffraction orders for $m \neq 0$, with most light being reflected in the $m = 0$ component, approaching the case of a plane reflecting surface. A similar situation was obtained for substantially different reflectivities, or a substantial step height ($x \approx \lambda/4$) as the value of $a/d \rightarrow 0$. This is also a mirror-like situation as light from a makes little contribution to the total amplitude when a is very small.

The expected height of the DNA gratings on the silicon substrate is approximately 10 nm. However, when samples were measured using AFM and a surface profiler, this height was found to range from approximately $80 - 120$ nm (as shown in Figure 4.10). This may be because the silicon is etched (where there is no alkene layer) during the DNA conjugation step, which uses an alkali buffer of pH 8.5, or may be a result of polymerization of the alkene during illumination, but an in-depth investigation of this was precluded by a loss of facilities.

The surface reflectivities of silicon samples that had been through the processing stages necessary to fabricate a DNA grating have previously been measured. The reflected intensity from a processed silicon region was found to be 7.97 ± 0.8 % of the incident power, with 4.27 ± 0.9 % reflectivity from a DNA covered region when illuminated at $57 \pm 1^\circ$ with a red (633 nm) laser. These values were used in the calculations to determine the optimum diffraction grating design for detecting a change in reflectivity.

There are three variables that affect the diffraction pattern shape, and hence diffraction order intensities; reflectivity ratio, line-width ratio and height difference. To highlight the inter-dependence of each diffraction order on particular variables 2−D contour plots have

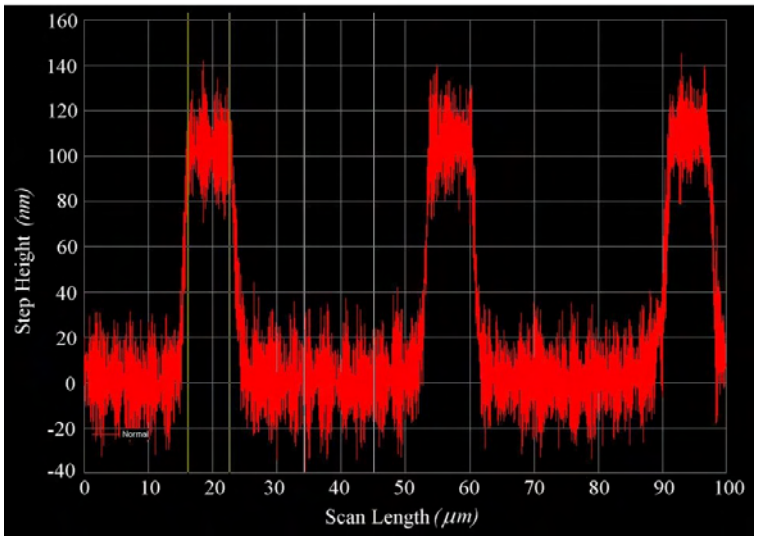

Figure 4.10: The step height x for DNA gratings on silicon was measured at $\sim 100\ nm$ on a surface profiler.

been produced. These show the intensity dependence of individual diffraction orders (from $m = 0 - 5$) on any two of the variables, with the other variable held constant. Consequently there are three sets of plots. In studying the change in diffraction order intensity with a varying reflectivity ratio (r_1/r_2), r_2 was fixed at the measured reflectivity of fabrication processed silicon ($r_2 = \sqrt{0.0797} \approx 0.282$). The values of r_1 began at $r_1 = \sqrt{0.0427} \approx 0.207$, the reflectivity of DNA on silicon and were then increased as would occur when gold nanoparticles hybridise with complementary DNA sequences. The step height used for calculations was varied from $0 - 633\ nm$. The ratio of $a : b$ was also varied using a small step height x held constant at $100\ nm$. These results are shown in Figure 4.11.

The behaviour of the intensity of each diffraction order was examined with varying reflectivity and line-width fraction when $x = 0$ (see Figure 4.12). For the zeroth order, corresponding to the reflected component, the intensity increases with an increase in the ratio of r_1/r_2. For non-zero orders the intensities decrease to zero as r_1/r_2 increases from 0 to 1.0. At this point, the reflectivities are equal so there is no diffraction (independent of the ratio of $a : b$). As r_1 becomes larger than r_2, the intensity of the diffraction orders increases with increasing reflectivity. Certain values of the line-width ratio $a : b$ introduce zero intensities for particular orders. For example, when $a : b = 1 : 1$, then $a/d = 1/2$ and all even orders ($m = 2, 4, 6, \ldots$) have zero intensity. When $a : b = 1 : 2$, then $a/d = 1/3$ and the 3^{rd} order has a zero in intensity. The 4^{th} order has intensity zeros when $a : b = 1 : 1$ and $1 : 3$. The 5^{th} order has zeros when $a : b = 1 : 4$ or $a/d = 1/5$ and $a/d = 2/5$. This may be seen more clearly in Table 4.1.

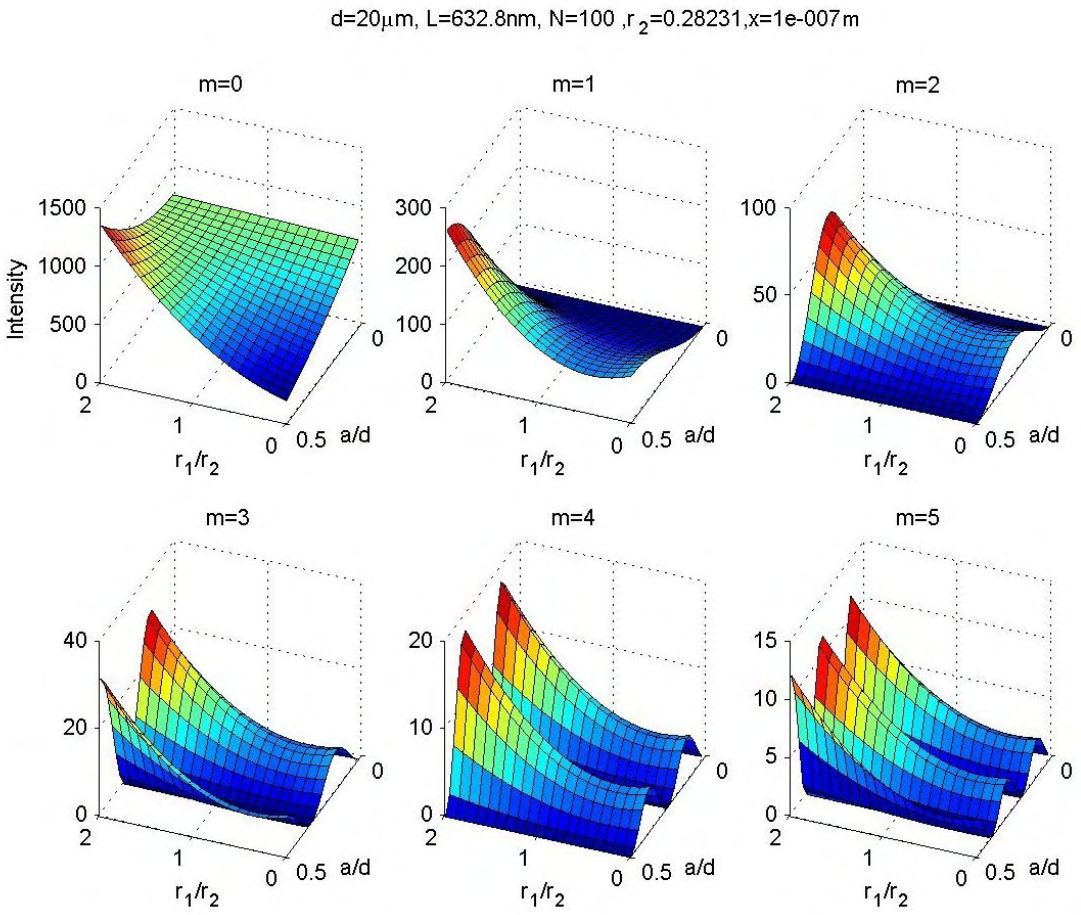

Figure 4.11: Intensities of individual diffraction orders $m = 0 - 5$ as a function of reflectivity r_1/r_2 and line-width a/d. Top Left: $m = 0$, zeroth order corresponding to the main reflection. Calculations used the values indicated in the top left corner of the figure, with $d = 20$ μm, $\lambda = 632.8$ nm, $N = 100$ lines illuminated, $r_2 = \sqrt{0.0797}$ and step height $x = 100$ nm, $\theta_i = 57°$.

$a : b$	Order					
	$m = 1$	$m = 2$	$m = 3$	$m = 4$	$m = 5$	$m = 6$
1 : 1		0		0		0
1 : 2			0			0
1 : 3				0		
1 : 4					0	
1 : 5						0

Table 4.1: This table shows the ratios for $a : b$ which causes cancellation of certain orders, giving them an intensity of 0.

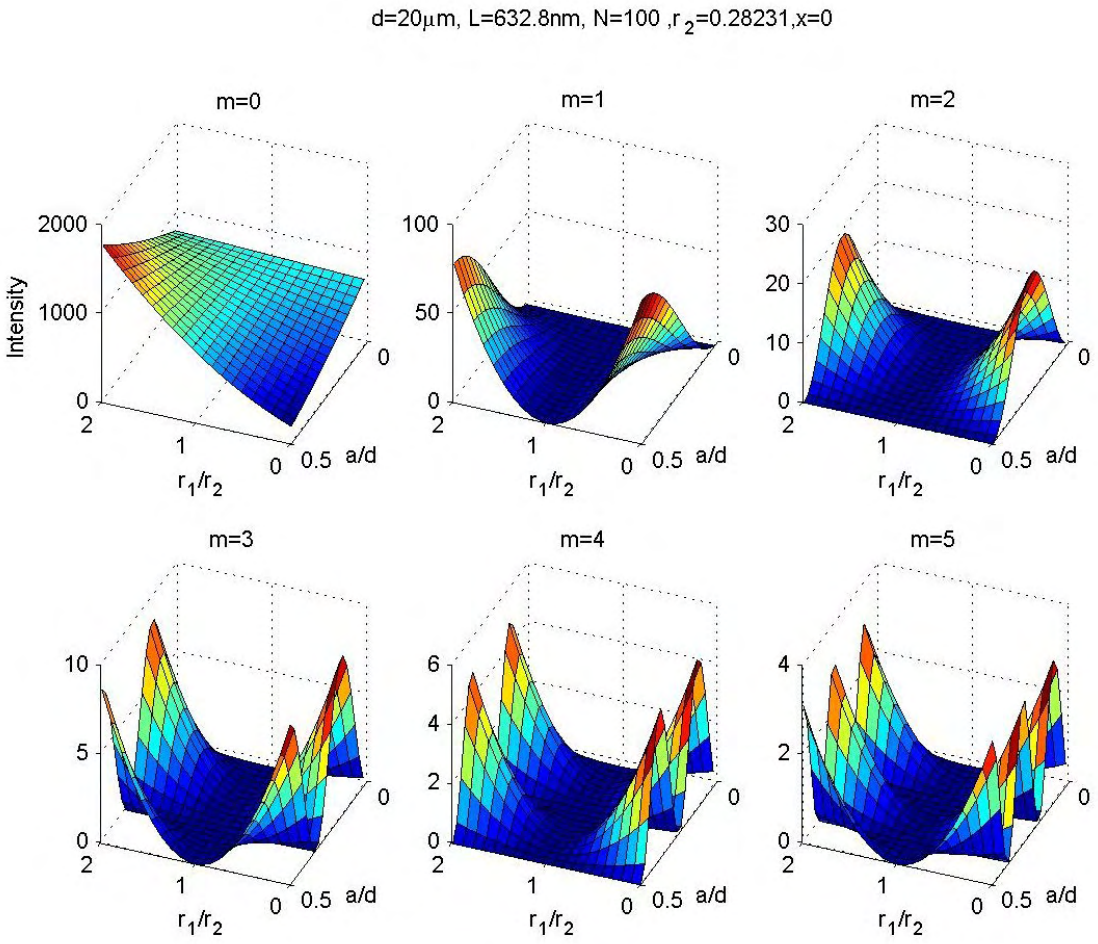

Figure 4.12: Intensities of individual diffraction orders $m = 0 - 5$ as a function of reflectivity r_1/r_2 and line-width a/d, with no height difference ($x = 0$).

The effects of changing reflectivity, and variation of the step height, on diffraction order intensities were calculated for a fixed linewidth ratio. The results for $a : b = 1 : 3$ are shown in Figure 4.13. When $x \approx 300\ nm$ the phase difference due to the step height generates destructive interference for the zeroth order reflection, but the non-zero orders are present and have maximum values with respect to x. Consequently a step height of approximately 300 nm would give the optimum sensitivity to a difference in reflectivity. Note that since $a : b = 1 : 3$, then $a/d = 1/4$ and hence the 4^{th} order coincides with the first minimum of the $\text{sinc}^2(\beta_a)$ envelope function and $I(m = 4) \approx 0$.

Figure 4.14 shows the intensity dependence for diffraction orders $m = 0 - 5$ on the linewidth ratio and step height for fixed reflectivities. r_1 is the square root of the measured reflectivity for DNA on silicon at 633 nm incident at 57°, and r_2 corresponds to processed silicon. Altering the difference in reflectivity only has a scaling effect on the intensity graphs and did not alter the shape.

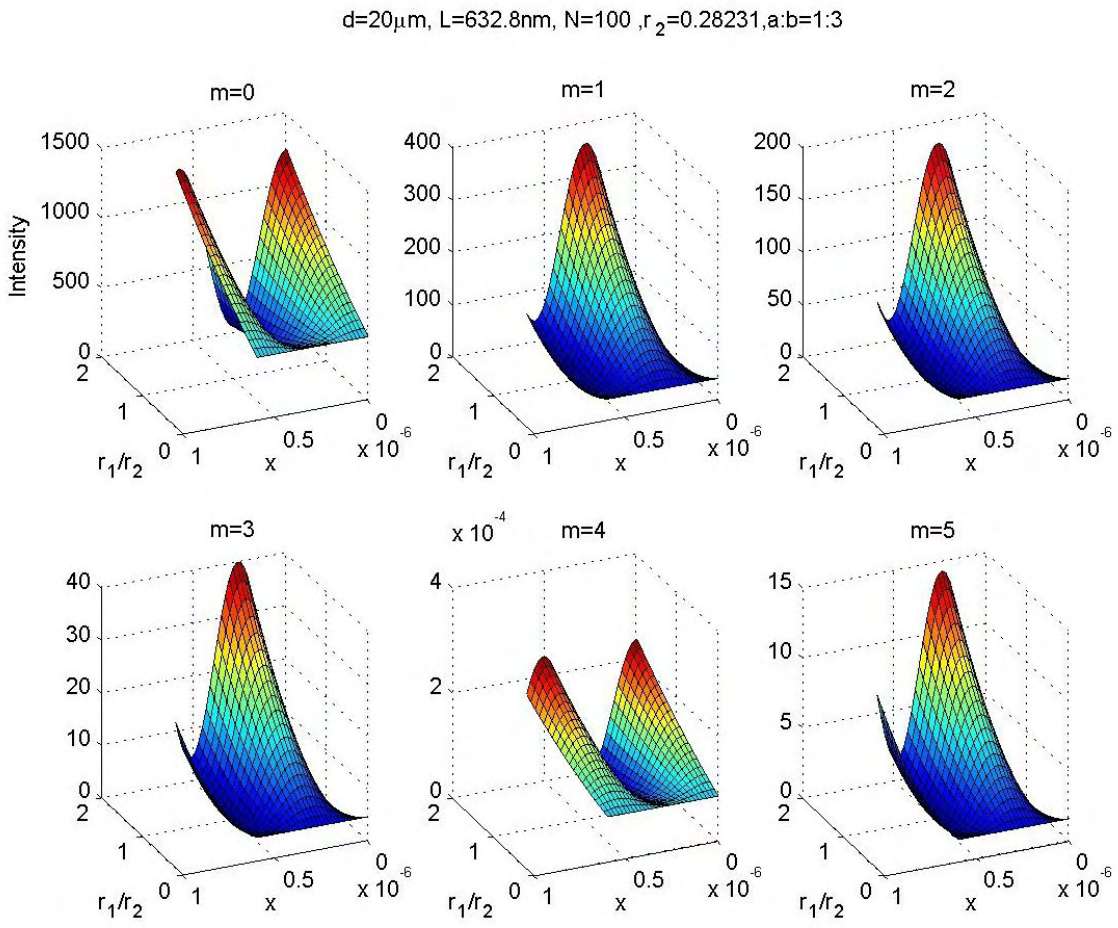

Figure 4.13: Intensities of individual diffraction orders $m = 0 - 5$ as a function of reflectivity r_1/r_2 and height difference x, with constant linewidth ratio $a : b = 1 : 3$ or $a/d = 1/4$.

4.3 Optimum Grating Design

From these calculations several conclusions can be made. Diffraction order intensities are very sensitive to changes in the value of a/d. Individual orders can be very sensitive to a small change in the linewidth. The larger the ratio of $a : b$, the less effect a small change in the linewidth will have. The smaller the linewidth a is in relation to the period d, the wider the $\text{sinc}^2(\beta_a)$ envelope function, and the less sensitive low order diffraction intensities are to variations of the linewidth. This is helpful when considering the design of a practical sensor that is difficult to fabricate with very precise linewidths. The diffraction pattern is very dependent on the step height x of the DNA relative to the silicon substrate. A step height of $\approx 300\ nm$ would give the best sensitivity to a change in reflectivity. A step height of $\sim 100\ nm$ would be sufficient to reduce the trough effect on the non-zero diffraction orders and shift the intensity minima to a lower value of r_1/r_2 as the reflectivity of the DNA line increases with hybridisation of gold. Using experimentally measured values the minimum

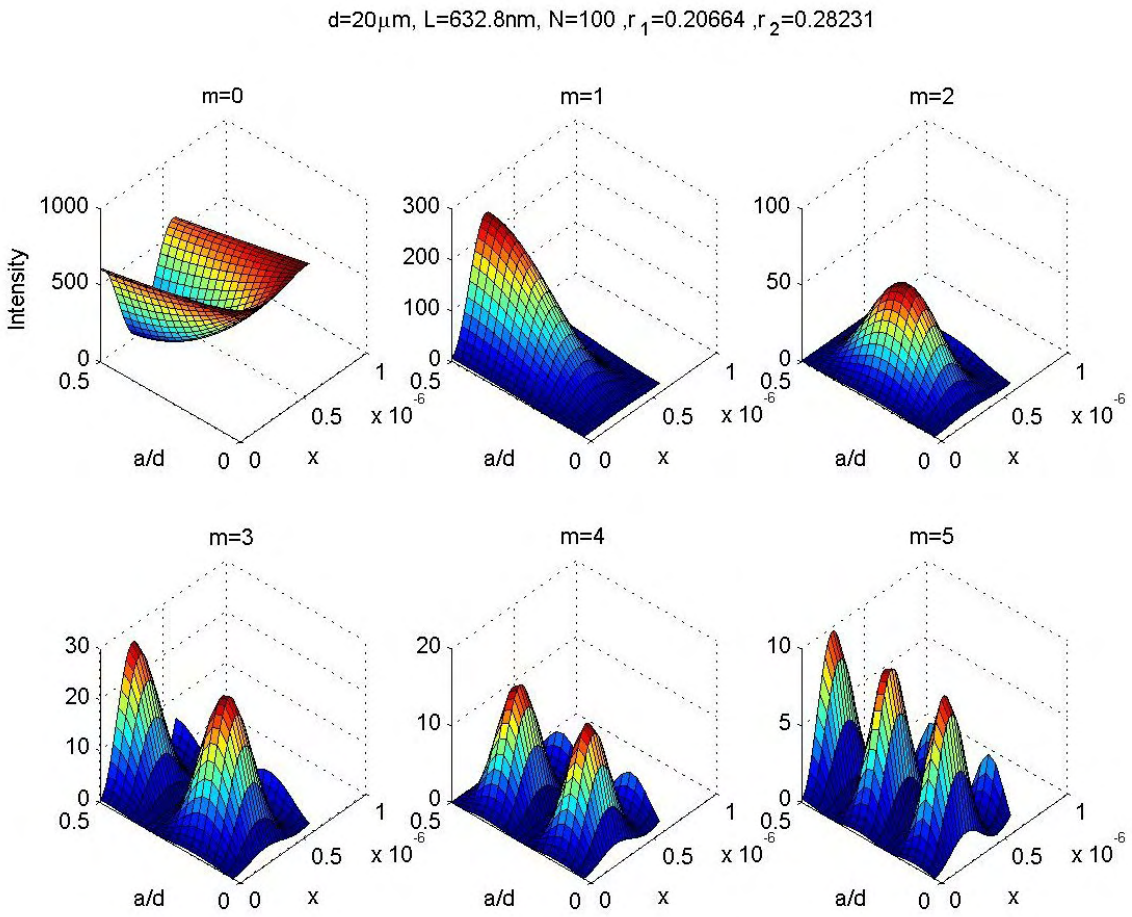

Figure 4.14: Intensities of individual diffraction orders $m = 0 - 5$ as a function of linewidth ratio a/d and height difference x, with constant reflectivity r_1/r_2.

of $r_1/r_2 \approx 0.7$, so any increase in reflectivity of the DNA grating line will only lead to an increase in diffraction order intensities, rather than passing through a minimum (see Figure 4.16). This means that the diffraction intensity measured for all orders will be proportional to the difference in reflectivity enabling quantification of the amount of hybridised gold nanoparticles from the reflectivity that generates the measured diffraction intensities.

A step height of less than $\sim 100\ nm$ would not change the optimum design of the grating, but would alter the diffraction response for a given reflectivity ratio change. When x is less than 70 nm, the non-zero diffraction orders ($m \geq 1$) will initially decrease through a minimum before then increasing with increasing reflectivity ratio. The zeroth order ($m = 0$) will still only ever increase with an increase in the reflectivity ratio, enabling detection of the reflectivity change.

For this project therefore a diffraction grating that is most sensitive to changing reflectivity,

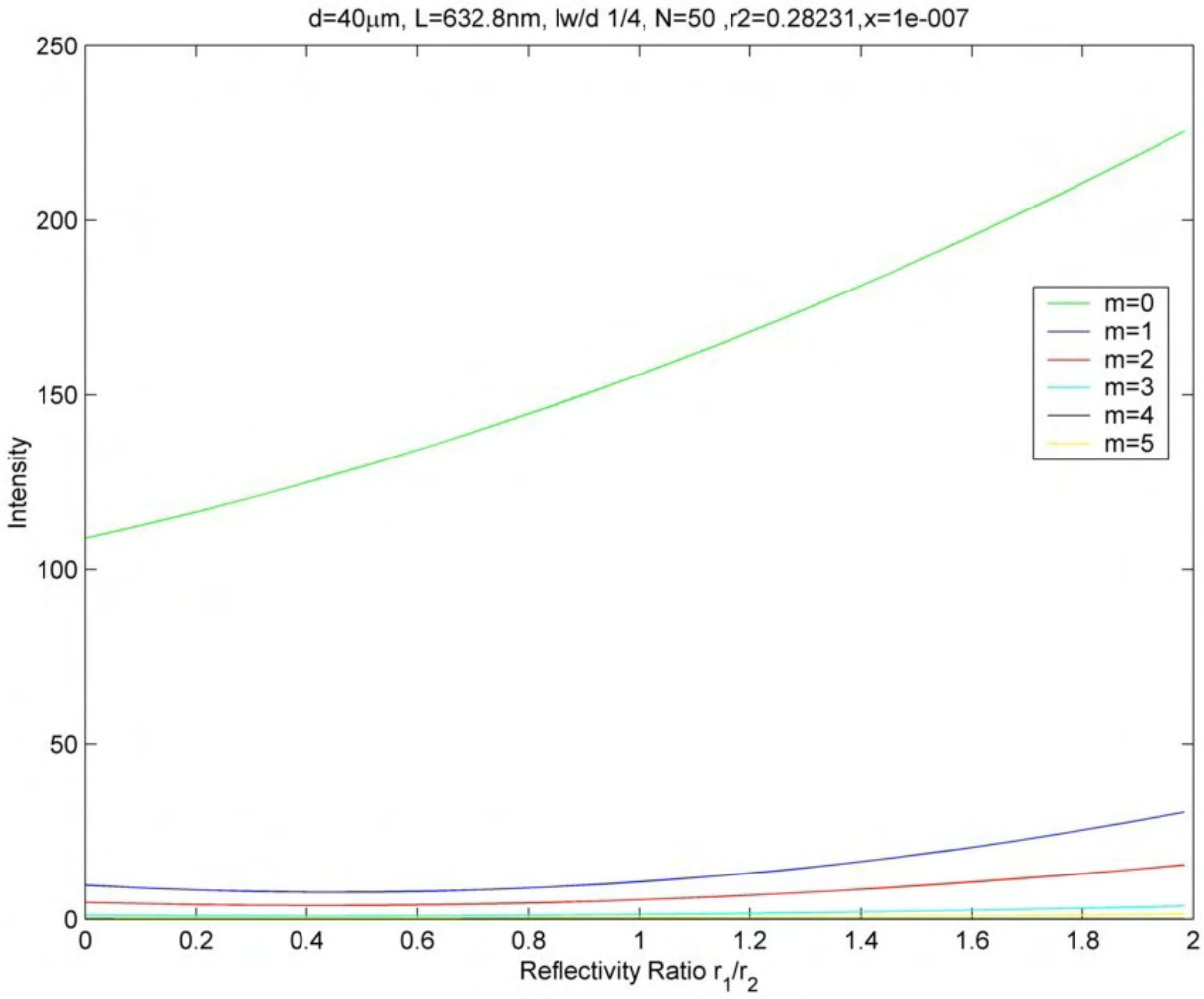

Figure 4.15: Intensities of individual diffraction orders $m = 0 - 5$ as a function of reflectivity r_1/r_2, with a linewidth ratio $a : b = 1 : 3$, period $d = 40\ \mu m$ and step height $x = 100\ nm$. Note that order $m = 4$ intensity ≈ 0.

and less dependent on variations of linewidth has been designed. The design also had to take into account fabrication and measurement constraints. For fabrication of homogeneous DNA lines the grating lines needed to be at least 10 μm wide, with a larger line separation being better for the escape of gas to prevent the build up of bubbles during DNA attachment (discussed in Section 3.8). For optical detection purposes the larger the separation of the lines, the less the sensor lines contribute to the diffraction pattern, and hence the less sensitive the sensor will be. Also the larger the period, the closer the diffraction orders become, and fewer lines are illuminated tending to blur and merge the diffraction orders. However, the larger the line separation, the lower the sensitivity to variations of linewidth, so there is a compromise to be made. With a minimum linewidth of 10 μm, the period is dictated by the ratio of $a : b$. A ratio of 1 : 3 has been chosen for the diffraction grating, as the period of the grating is small enough for good angular separation of the diffraction orders,

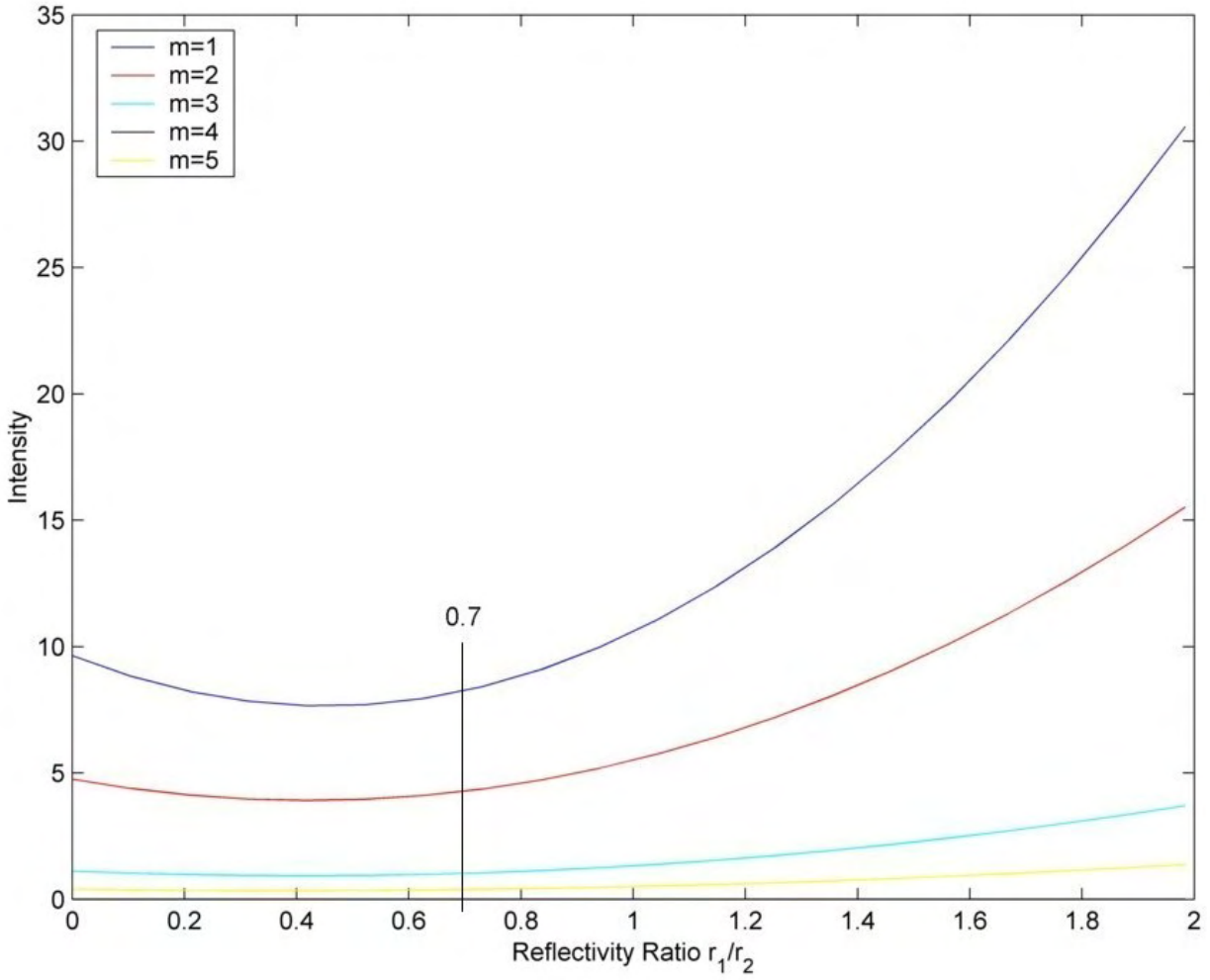

Figure 4.16: Close up of the intensities of individual diffraction orders $m = 1 - 5$ as a function of reflectivity r_1/r_2, with a linewidth ratio $a : b = 1 : 3$, period $d = 40\ \mu m$ and step height $x = 100\ nm$, as detailed in Figure 4.15. Note that order $m = 4$ intensity ≈ 0.

but the separation is large enough to reduce intensity variations due to differing linewidth. The line separation is also sufficient to improve the fabrication process by reducing gas build up. The intensity of diffraction orders above $m = 5$ is usually very low and disappears into background noise of a few nanowatts. Using a $3 : 1$ ratio, light in the orders $m = 0, 1, 2, 3$ will be relatively high intensity as they occur before the first minimum of the $\text{sinc}^2\,\beta_a$ envelope function. Order $m = 4$ will be zero for a perfect $3 : 1$ ratio and $m = 5$ will be present, but low intensity. The step height of the grating being around $100\ nm$ is beneficial, since any increase in reflectivity of the DNA line as gold is hybridised will generate increased diffraction, and not decrease through a minimum (which could cause ambiguity in the reflectivity value). The reflectivity will simply be proportional to the diffraction order intensities, with $m = 1$ being the most sensitive to a change in reflectivity (other than $m = 0$).

4.4 Gold Nanoparticle Surface Coverage

The intensity of the diffraction pattern observed depends on the ratio of r_1/r_2; the amplitude reflectivity coefficients of the two surfaces. For the diffraction sensor r_2 is fixed and equals the reflectivity of silicon that has been through the processing stages necessary for the DNA grating fabrication. The reflectivity r_1 corresponds to the reflectivity of processed silicon with a layer of DNA oligonucleotides that is modified by hybridisation of a variable number of gold nanoparticles. By measuring the diffraction order intensities with all other variables constant the pattern observed can be correlated to a specific value of r_1/r_2. Since r_2 is fixed, r_1 may be calculated. Variation in the value of r_1 is related to the number of hybridised Au nanoparticles per unit area. Consequently, it is possible to quantify the number of hybridised gold nanoparticles from the diffraction order intensity distribution.

A given number of particles per cm^2 corresponds to a certain fractional area coverage of the surface, dependent on the particle size. The surface coverage calculations detailed below are based on a hexagonal packing structure, giving the maximum fractional area coverage by spherical particles. Figure 4.17 shows the hexagonal packing method used for calculations.

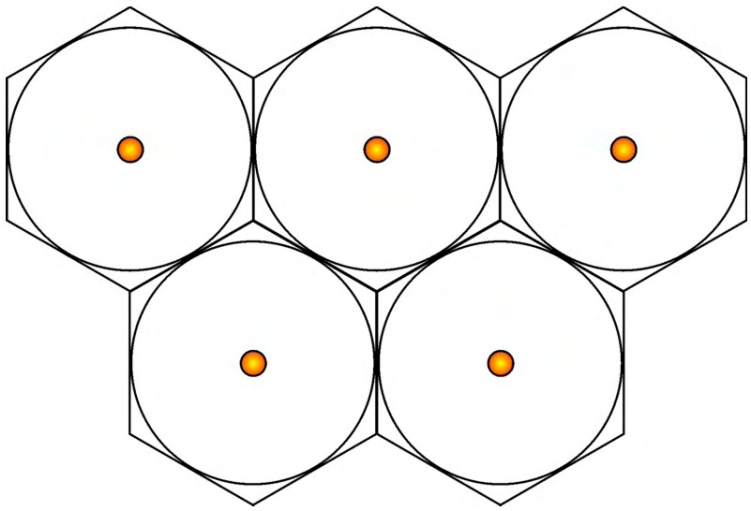

Figure 4.17: Area of surface coverage based on hexagonal packing of nanoparticles.

One nanoparticle of diameter ϕ is located within a hexagon, bounding a circle of radius R. As can be seen from Figure 4.17, the particles are separated by a centre to centre distance of $2R$. The fractional area coverage of the surface depends on the radius of the particle ($r = \phi/2$) compared to the hexagonal area specified by R (see Figure 4.18).

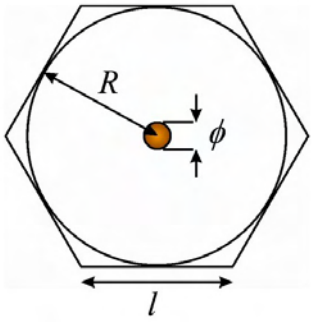

Figure 4.18: The maximum hexagonal area occupied by a nanoparticle of diameter ϕ is determined by R.

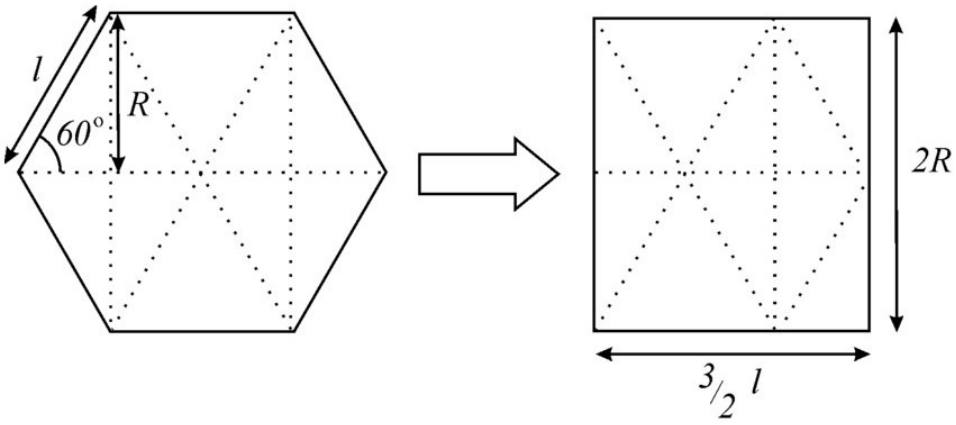

Figure 4.19: Geometrical calculation of area of hexagonal region.

The area of a particle is $\frac{1}{4}\pi\phi^2$, with the area of the hexagon given by $\frac{3}{2}l \times 2R$. From Figure 4.19 it can be seen that $R = l \sin 60 \;\Rightarrow\; l = \frac{2R}{\sqrt{3}}$. Hence the hexagonal area can be written as $2\sqrt{3}\ R^2$. The fractional area coverage (ρ) is then:

$$\rho = \frac{\pi\phi^2/4}{2\sqrt{3}R^2} = \frac{\pi}{8\sqrt{3}}\left(\frac{\phi}{R}\right)^2$$

Thus the maximum fractional area coverage when $\phi = 2R$ is $\rho = 90.67$ %. Knowing the number of particles per unit area (N/cm^2) and the particle diameter, the fractional area coverage ρ can be calculated along with an estimate of the average particle separation ($2R$). The maximum fractional area coverage of a close packed hexagonal arrangement of 10 nm diameter particles would correspond to $1.15 \times 10^{12}\ cm^{-2}$.

Inductively coupled plasma-mass spectroscopy (ICP-MS) was used by Dr H Yin (working with Dr J A Milton from the National Oceanography Centre, University of Southampton)

for analysis of DNA-gold nanoparticle conjugates dehybridised from DNA gratings on silicon [223]. Samples were dehybridised in 800 μl of water at 90°C for 15 minutes. The silicon sample was removed, washed twice with 100 μl of water and added to the collected solution, giving 1 ml total. The gold nanoparticles in the solution were dissolved by adding 50 μl of 0.1 M KCN and 1 mM $K_3Fe(CN)_6$ and were then diluted with 9 ml of 5 % HCl. ICP-MS was used to determine the mass of gold in the solution, using the method developed by Pitcairn *et al* [224]. This was compared to the average particle mass for 1.4 nm and 10 nm gold nanoparticles to quantify the number of particles dehybridised from the samples. It was determined that 'good' hybridisation yields approximately 6.4×10^9 gold nanoparticles per cm^2 (or 64 particles per square micron) for 10 nm diameter colloids and $2.15 \times 10^{12} cm^{-2}$ for 1.4 nm diameter particles. Fluorescent molecules were found to hybridise with a higher area density of 1.2×10^{13} cm^{-2}. For 10 nm diameter gold nanoparticles, this hybridisation density corresponds to a fractional area coverage of the surface of $\rho \approx 0.5$ % with an average separation of 134 nm (assuming an even distribution).

An area coverage of 0.5 % corresponds to a reflectivity ratio change of 2.4 % in the reflectivity of a DNA line compared to the silicon substrate. The diffraction intensity changes were predicted for a fractional area coverage of gold particles of 0.5 %, on a 40 micron period grating, with 3 : 1 mark-space ratio and a step height of 100 nm. The intensity changes predicted for each diffraction order are shown in Table 4.2.

Order	$\Delta\ I_m/I_{input}$
$m = 0$	+0.65 %
$m = 1$	+1.17 %
$m = 2$	+1.18 %
$m = 3$	+1.25 %
$m = 4$	+0.65 %
$m = 5$	+1.28 %

Table 4.2: Change in diffraction intensities predicted for a 40 μm period DNA grating hybridised with 10 nm diameter gold colloids.

In order to produce an approximate 10 % change in the intensities of the majority of the diffraction orders it was calculated that the surface area coverage needed would be $\rho \approx 2.6$ %. This required 3.3×10^{10} particles/cm^2, approximately 5 times higher particle hybridisation density than achieved in practice for the 10 nm diameter gold.

Order	$\Delta\ I_m/I_{input}$	
	$\rho = 2.6$ %	$\rho = 3.3$ %
$m = 0$	+ 4.01 %	+ 5.15 %
$m = 1$	+10.42 %	+13.37 %
$m = 2$	+10.22 %	+13.12 %
$m = 3$	+10.03 %	+12.87 %
$m = 4$	+ 3.54 %	+ 4.55 %
$m = 5$	+10.56 %	+13.55 %

Table 4.3: Change in diffraction intensities predicted for a 40 μm period DNA grating hybridised with gold colloids. The centre column shows that an approximate 10 % change in diffraction values is predicted for a fractional area coverage of $\rho = 2.6$ %. The right hand column indicates the predicted change in diffraction with hybridisation of 1.4 nm diameter particles at the highest measured density of $2.15 \times 10^{12} cm^{-2}$, giving $\rho = 3.3$ %.

The equivalent number for 1.4 nm gold colloids was calculated to be 1.3×10^{11} particles $/cm^2$. The diameter of the smaller gold colloids was just over 7 times smaller, so that at the same hybridisation density they would cover 51 times less surface area. However, the smaller particles were able to hybridise at a greater density, with the maximum measured value of $2.15 \times 10^{12} cm^{-2}$ being 336 times higher for 1.4 nm particles than for 10 nm diameter colloids. This corresponded to a fractional area coverage of $\rho = 3.3$ %, which was 6.6 times higher than for the 10 nm gold. The predicted change in diffraction associated with this level of fractional area coverage is shown in Table 4.3.

In genomic DNA samples, hybridisation is less likely to be as high as determined above for complementary, short oligonucleotide sequences. It is desirable to be able to empirically correlate the reflectivity ratio r_1/r_2, to the number of particles per cm^2, by measuring the diffraction patterns associated with different fractional area coverage of gold nanoparticles.

4.5 The Effects of Grating Variability

Whilst every effort was made to fabricate uniform diffraction grating structures, in practice there are variations in the linewidth, step height and reflectivity of the grating from point to point. Using the diffraction intensity model developed here the grating parameters were varied to calculate the predicted effect on the diffraction pattern.

The optimum grating design chosen featured a 10 μm linewidth, 40 μm period and 100 nm step height. The reflectivity ratio was set at 0.7 as measured for DNA on silicon. The line:space ratio, step height and reflectivity parameters were altered one at a time whilst holding the other variables constant. The change in diffraction intensities predicted for a 10 % variation of each parameter are shown in Table 4.4.

Order	$\Delta\ I_m/I_{input}$		
	$\Delta a = 10$ %	$\Delta x = 10$ %	$\Delta r_1/r_2 = 10$ %
$m = 0$	− 2.98 %	+ 3.17 %	+ 2.97 %
$m = 1$	+15.62 %	−17.87 %	+ 5.81 %
$m = 2$	− 2.51 %	−17.73 %	+ 5.87 %
$m = 3$	−45.17 %	−17.85 %	+ 6.14 %
$m = 4$	+31971.91 %	−17.80 %	+ 2.97 %
$m = 5$	+70.63 %	+ 3.69 %	+ 6.23 %

Table 4.4: Changes in diffraction intensities predicted for a 40 μm period DNA grating on silicon when the linewidth a, step height x and reflectivity ratio r_1/r_2 are varied by 10 %.

The magnitude of the change in intensity for the zeroth order by varying each parameter by 10 % is ≈ 3 %. However, the predicted changes for other diffraction orders vary significantly depending on which parameters are altered. These calculations show that variations in the linewidth can have a very large impact on the intensity of the 3^{rd}, 4^{th} and 5^{th} diffraction orders. The 4^{th} order shows an extremely large increase due to the near-cancellation of that order associated with a $1:3$ line to space ratio.

The effect of a 10 % increase in step height x produces an almost uniform change of ≈ -18 % for orders $m = 1 - 4$, whilst the 5^{th} order changes by almost the same amount as the zeroth order.

The change in diffraction order intensities associated with a change in the reflectivity ratio gives the most uniform change between orders. However, the change in diffraction for a 10 % variation in reflectivity is also less significant than a 10 % change in linewidth or step height.

4.6 Theory versus Experimental Data

Test pattern diffraction gratings, fabricated from evaporated gold on silicon, were created for the comparison of experimental diffraction data with theory, and evaluation of the measurement apparatus (as discussed later in Chapter 5). A surface profiler was used to characterise the parameters of the fabricated gratings so that the theoretical diffraction could be predicted as accurately as possible for that grating to enable a fair comparison. Figure 4.20 shows the experimental diffraction order intensities compared to the theory for a gold grating on silicon. The sample featured a linewidth of $8.05 \pm 0.17\ \mu m$ and a step height of $106.9 \pm 1.6\ nm$ with a 40 μm period. The theoretical values agree very well with the experimental data for diffraction orders $m = 0 - 2$, being within 3.5 % of the predicted values. However, using a linewidth of 8.05 μm for calculations makes the 5^{th} order almost cancel out in theory, where experimentally a low intensity was measured, producing a very large difference (over 7000 %).

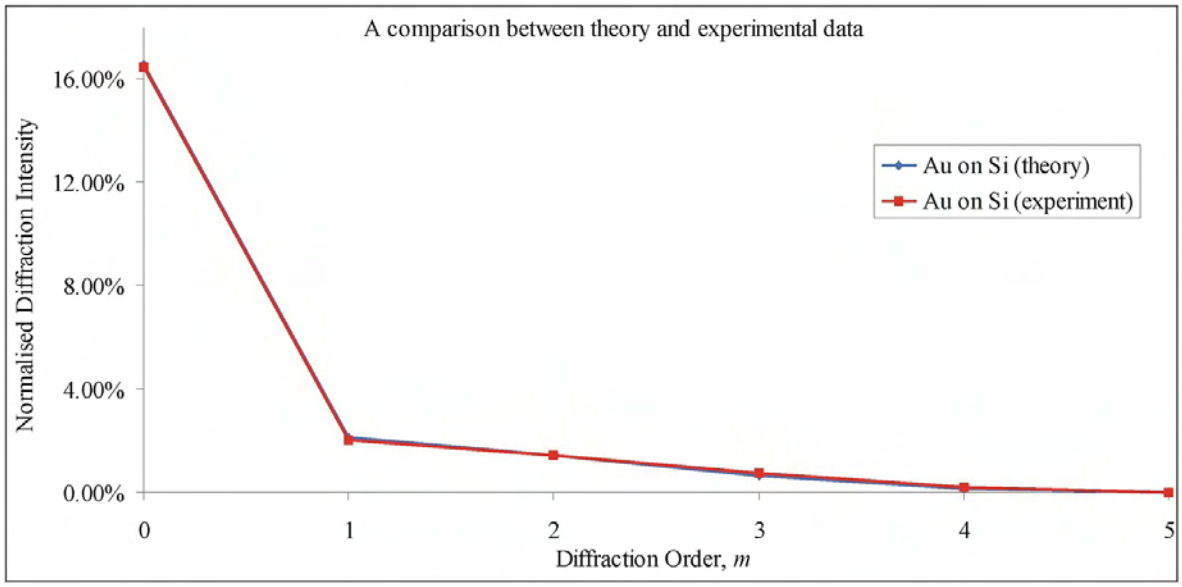

Figure 4.20: A comparison of the theoretical and experimentally measured diffraction intensities for evaporated gold diffraction gratings on silicon.

4.7 Conclusions

Conventional diffraction theory was extended to consider the additional complexity of an interlaced diffraction grating featuring different reflectivities, different line-widths and a step height between them. Using the theory developed an optimal grating design was chosen for

the fabrication of DNA gratings on silicon region. The grating design featured a 40 μm period with a 1 : 3 ratio of the DNA linewidth to the silicon separation. Following earlier measurements of DNA gratings on silicon a 100 nm step height was used for calculations.

The change in the reflectivity ratio of the DNA line to silicon substrate was related to the surface area coverage of gold nanoparticles. The amount of gold nanoparticles hybridised to samples was quantified and used to predict the change in diffraction intensities expected. This predicted a 1 % change in diffraction order intensities for 10 nm diameter nanoparticles and a 13 % change for 1.4 nm particles.

Variation of the grating parameters was evaluated to predict the changes in diffraction associated with a 10 % change in linewidth, step height or reflectivity ratio. This showed that the zeroth order was equally sensitive to each parameter. The step height x had the largest impact for orders $m = 1,\ 2$. Variation in the reflectivity ratio generally produced the smallest change in intensity, but most uniform change across the orders. Variation of the linewidth predicts the largest effect on the distribution of light in each order.

Chapter 5

DNA Gratings and Instrumentation

5.1 Introduction

The aim of the project was to develop diffraction measurement apparatus for the analysis of DNA diffraction gratings on silicon. The sensor realised in this project was a one-dimensional diffraction grating structure; an array of parallel lines with a periodic repetition in one direction. A test diffraction system was designed and developed, and then DNA gratings were realised on a silicon substrate and characterised by diffraction. The DNA strands (covalently attached to the silicon in a grating pattern) were then hybridised with complementary DNA strands labelled with gold nanoparticles (at the $3'$ end, see Section 3.6) and characterised by diffraction again. Any change in diffraction associated with the hybridised gold nanoparticles would indicate that complementary sequences were present.

The fabrication techniques described in Chapter 3 were developed for the creation of a silicon-based diffraction sensor for DNA analysis. This chapter outlines the evolution of the experimental optical apparatus used to develop a diffraction grating sensor and the results achieved for model test patterns, DNA gratings, and DNA gratings with hybridised gold nanoparticles.

5.2 Initial Diffraction Experiments

Several methods were evaluated for the measurement of diffraction data. Initial setups used a CCD camera positioned at a fixed observation distance to simultaneously capture several diffraction orders. As the experimental technique evolved, later measurements were made using photodiode detectors to measure the light intensity in each diffraction order individually. This enabled the accuracy of measurement to be improved and the detection limits reduced.

5.2.1 Diffraction Data Collection on Trial Gratings

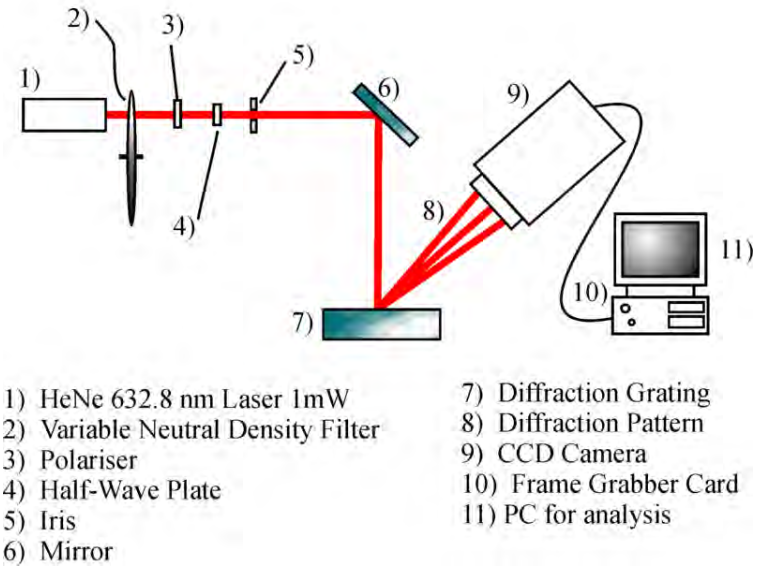

Figure 5.1: Initial optical apparatus for 1−D diffraction grating.

An initial basic configuration, for diffraction analysis and for testing the image capturing possibilities (along with software and programming development), was set up using a commercially available diffraction grating with a period of 1.67 μm. The optical setup was designed to capture as much of the diffraction pattern as possible on the CCD detector chip in a digital camera, without unnecessary additional optics that could introduce errors to the image. To enable capture of the higher orders, and not the zeroth (corresponding simply to reflection from the surface), the laser beam was incident at an angle of 0° to the normal of the diffraction grating. Whilst the configuration, shown in Figure 5.1, worked well for small grating periods ($< 20\ \mu m$), the setup and image analysis had to be modified for larger periods to capture the diffraction patterns. Due to the smaller angular separation of diffraction

orders with larger periods, the CCD camera housing obscured measurement of the first few diffraction orders when light was incident normal to the grating (see Figure 5.2).

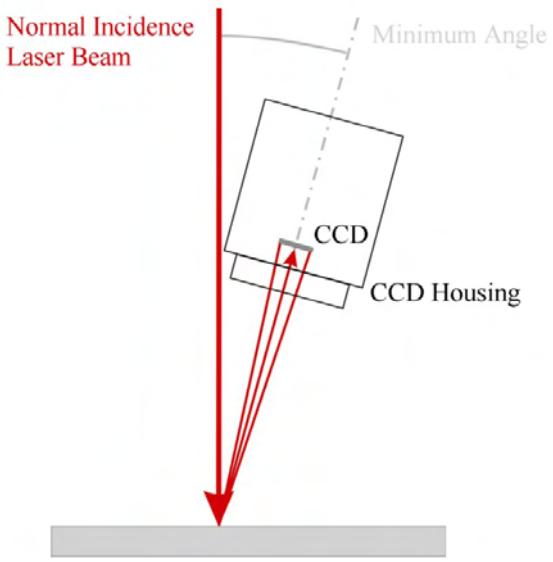

Figure 5.2: CCD Housing limits the minimum angle of capture to the surface normal.

The experimental methodology was adapted for testing sample reflection gratings. A series of trial grating designs was fabricated on a chrome on silica glass mask plate by direct beam writing (fabrication was carried out by either Innos^{TM}or RAL). The principle of operation of these gratings was the same as that for the biological gratings for which the setup was being developed. The contrast in reflection between the chrome lines and the silica substrate formed reflecting diffraction gratings. When the diffraction gratings were first tested, it became apparent that reflection from the surface of the silica was significant compared to the reflection by the chrome. This problem caused the captured diffraction pattern images to feature additional complexity due to multiple reflections between the top and bottom surfaces of the mask plate.

A solution to the problem of reflection of the incident laser beam from the surface of the silica, was to utilise the fact that the laser beam was polarised, and align the incident beam at the Brewster angle for glass. The Brewster angle θ_B, is the angle of incidence at which the reflected intensity for p-polarised light travelling from medium 1 to medium 2 is zero (see Figure 5.3), since the transmitted beam is orthogonal to the reflected beam [218]. The Brewster angle θ_B is related to the refractive indices of the two media (n_1 and n_2) and is specified by the relationship:

$$\tan \theta_B = n_2/n_1 \tag{5.1}$$

This means that p-polarised radiation incident on the silica surface at the Brewster angle is not reflected, and does not interfere with the diffraction pattern produced by the chrome. Light that is transmitted through the mask plate then encounters another refractive index change, leaving the silica mask plate and resuming propagation in air. Since the beam was incident on the top surface at the Brewster angle for air to silica ($n_1 \rightarrow n_2$), the refracted beam is also at the Brewster angle for the bottom surface, exiting the silica into air ($n_2 \rightarrow n_1$).

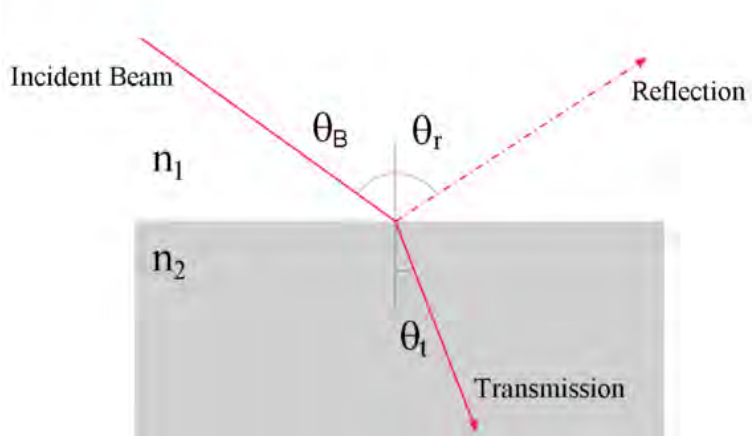

Figure 5.3: When p-polarised light is incident on a surface at the Brewster angle, the reflected intensity drops to zero and all light is transmitted.

The optical apparatus was developed as shown in Figure 5.4. Using two mirrors in this configuration, it was possible to finely control the exact incident angle of the laser beam. The 632.8 nm wavelength beam produced by the HeNe laser (Melles-Griot) provided around 1.0 mW of power output; this was sufficient to saturate the CCD detector (Pulnix TM−1020) when reflected from the solid chrome lines. The beam intensity was attenuated by using a variable neutral density filter. The laser beam then passed through a polariser to maximise the degree of linear polarisation of the laser beam. A half-wave plate was used to rotate the polarisation of the beam to ensure that p-polarised light was incident upon the mask plate. An adjustable mirror was used to align the angle of incidence to the Brewster angle giving the minimum reflected intensity. The diffraction pattern was subsequently captured on the camera's CCD detector chip directly. The CCD camera was moved in an arc with a fixed observation distance by mounting an extension arm to a rotation stage centred in line with the point of incidence of the laser beam.

Alignment at the Brewster angle virtually eliminated top and bottom surface reflections for unpatterned regions of silica. However, this was not the case when the diffraction grating patterns were translated into the path of the laser beam. A secondary 'ghost' image was superimposed onto the original diffraction pattern as follows. Light was not reflected from the top surface of the mask (except that desired from the chrome reflection grating), but

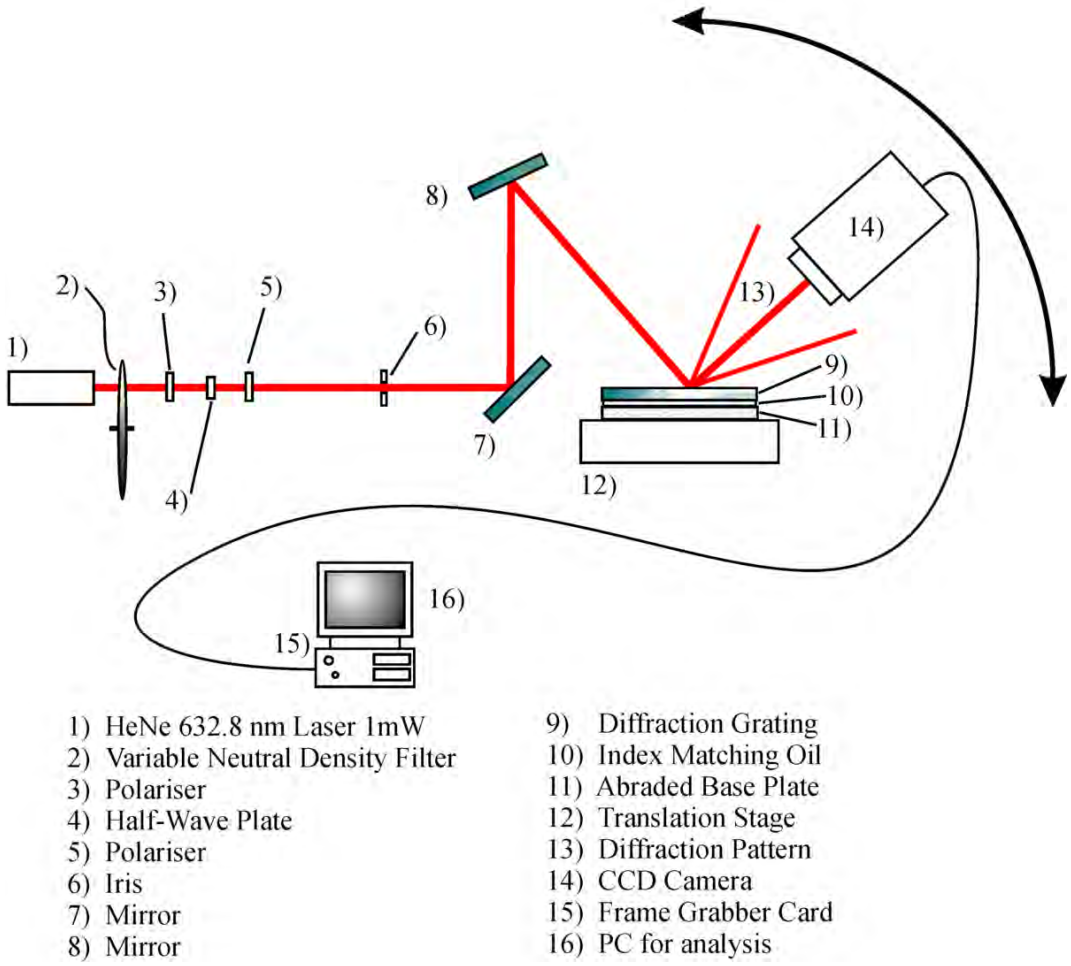

Figure 5.4: Experimental layout developed for testing 1−D diffraction gratings. The CCD camera was moved in an arc to capture the whole diffraction pattern in multiple images.

transmitted light was also diffracted by passing through the chrome grating into the silica. Some of the transmitted light was, therefore, no longer incident on the bottom mask plate surface at the Brewster angle and was consequently reflected back. The image quality was further degraded by multiple reflections, and by the fact that light was diffracted again through the chrome grating as it leaves the silica. Also, due to the close spacing of different diffraction gratings on the mask, some of the diffracted light exited through 'different period' adjacent grating patterns. The net effect of all this interference was resulting diffraction images with little correlation to the expected diffraction pattern for the diffraction grating on the surface.

A method was tested to reduce light reflection from the back surface of the mask plate. Light was coupled from the mask plate to a second silica plate via refractive index matching oil. The bottom surface of the second plate had been abraded (by sand blasting) to create an uneven surface to diffusely scatter the transmitted light rather than reflect it (shown schematically in Figure 5.5). This successfully prevented the 'ghost' images in the observed

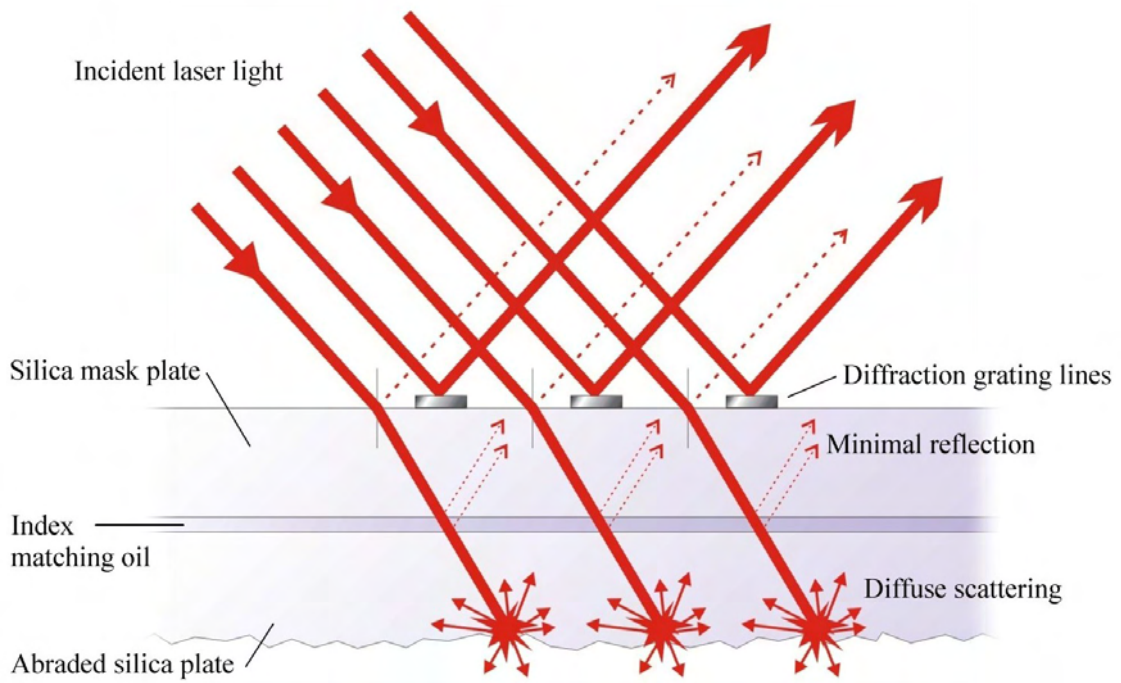

Figure 5.5: To prevent reflections from the back surface of the silica mask plate from diffracted transmission light, a silica mask plate was abraded by sand blasting to provide a diffuse scattering surface.

diffraction image from the chrome grating, but added to the background radiation noise by scattering more light randomly in all directions. The background noise level was significantly lower compared to the high intensity of the reflected light for solid chrome lines, but was more of a problem for grating patterns with lower chrome surface area coverage.

The mask plate used was a silica substrate with a thin chrome layer ($\sim$ 150 nm) on the top surface. In order to create a reference library of Fourier transform patterns relating to specific types of diffraction gratings, the mask plate was patterned with 46 different designs. These different patterns covered a range of periods from $1.0 - 20.0$ μm. The aim was to use the trial designs to determine the optimum grating period for the optical system. Additional grating patterns were created to analyse the impact upon the diffraction pattern of the ratio of line width to line spacing, or the effect of missing lines (1 in 3 to 1 in 10 lines missing). Some patterns were also generated that could test the effect of having fragmented lines made from dots rather than solid reflecting lines. Some sample images of these patterns (in photoresist prior to etching) are shown in Figure 5.6. The patterns were designed using a specialised mask design program, L-Edit^{TM}.

It was found experimentally that the effect of missing lines within the grating reduced the amount of interference and cancellation that is present in a normal grating. Consequently, if,

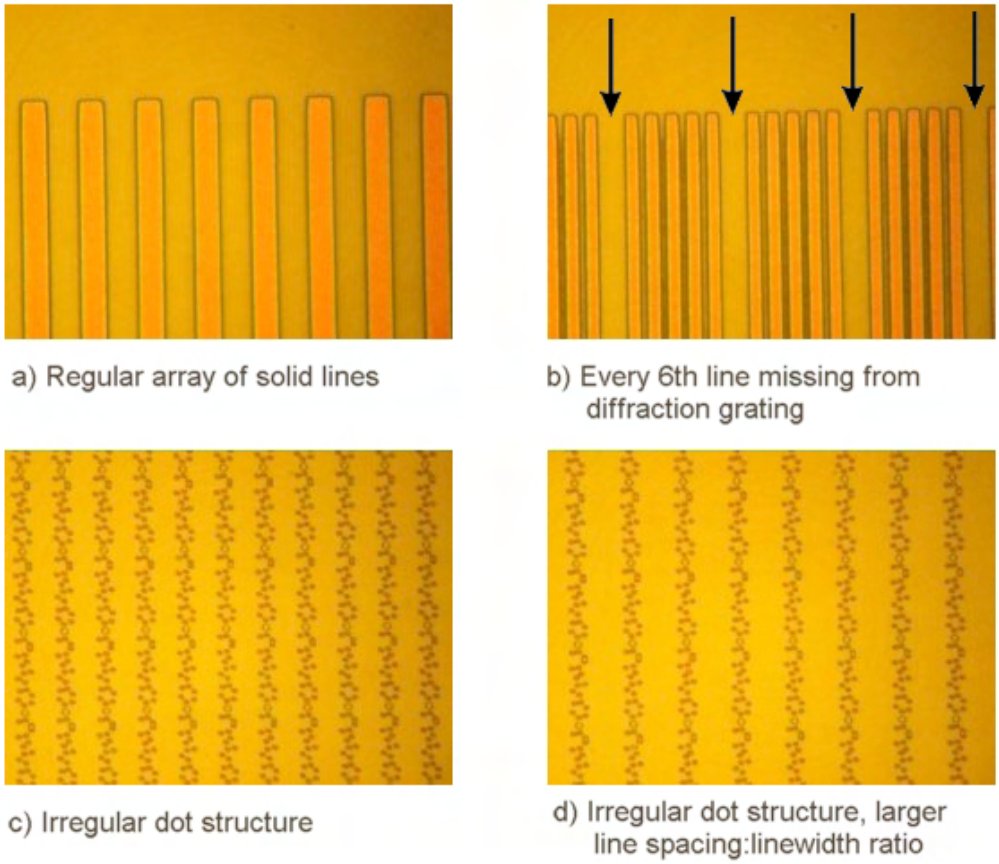

Figure 5.6: Example diffraction grating patterns created on a silica mask plate.

for example, 1 out of 3 lines was missing in a 10 μm grating, then 2 'sub-orders' became visible in between the 'normal' orders of the original period. The periodicity of the missing feature was reducing cancellation and introducing diffraction orders corresponding to a periodicity of 30 μm in the diffraction pattern. This was the case for other ratios of missing lines too. In general, if 1 out of n lines is missing from a grating of period d, then the diffraction pattern will feature the normal grating orders corresponding to the period d, with $(n-1)$ additional sub-orders in between main diffraction orders, relating to a period of $n \times d$. Figure 5.7 illustrates this effect diagrammatically, with the missing line indicated in the left hand column and the corresponding schematic diffraction pattern on the right-hand side, with sub-orders appearing in between the main diffraction orders of a regular grating.

5.2.2 Image Analysis

After capturing the diffraction images, subsequent analysis was required. A program was written in MATLAB^{TM} to calculate the inverse Fourier transform (IFT) of the images. This

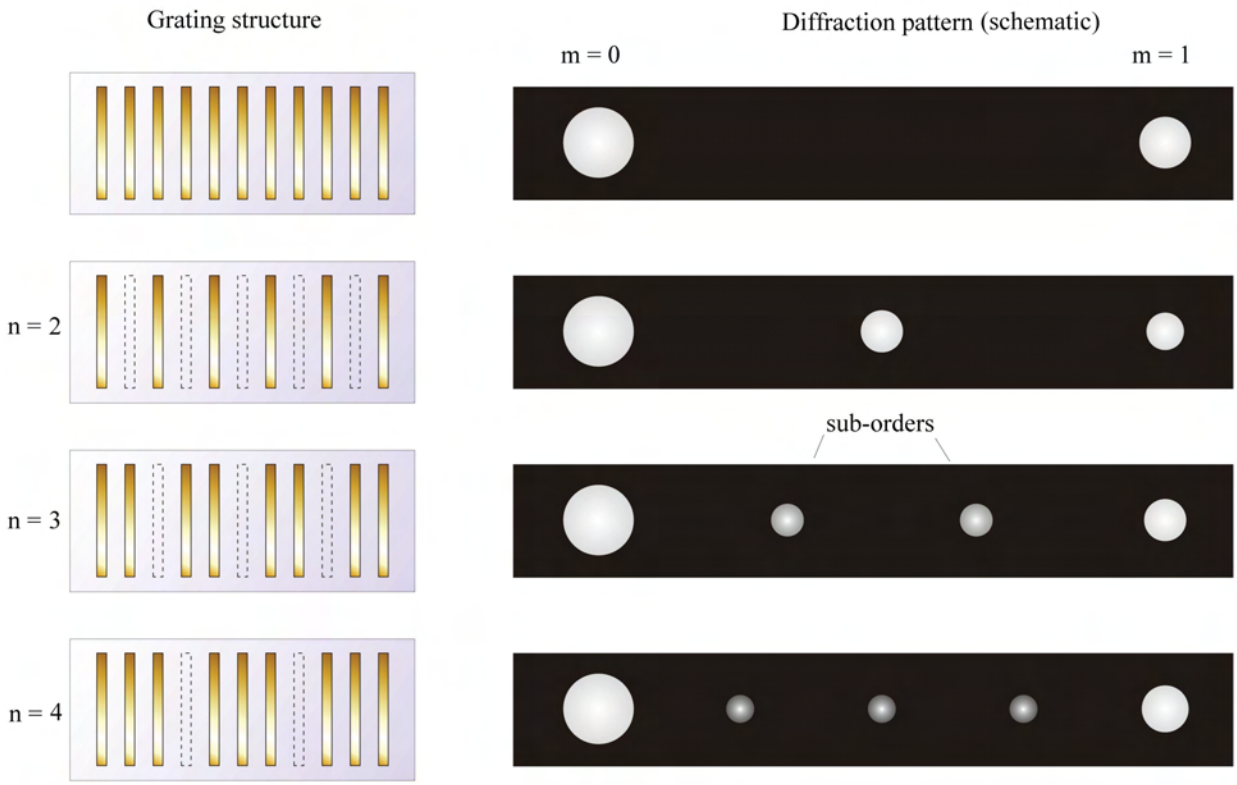

Figure 5.7: The effect of missing every n^{th} line within a diffraction grating structure on the diffraction pattern is to introduce $(n-1)$ sub-orders between the main diffraction orders of the complete grating.

displayed the periodicities (and their directions) detected in the input image. Some examples of the captured images and their corresponding IFT plots are shown in Figure 5.8. When large features in the captured image were Fourier transformed they represented small periods in the IFT. The small features in the IFT plot were not visible until the magnification of the plot was increased and centred on the origin ('zooming in' on the detail). These results showed some periodicity from within the image, but did not agree with the actual grating periods as designed. The program needed to be adjusted to ensure that small period features could be displayed properly in the IFT plot.

After initial analysis of the trial mask plate, areas for systematic improvements were identified. The software analysis of the images needed to be further refined in order to bring out the best results from the images obtained. What shall be referred to as 'zero-padding' is the process of increasing the size of the input image matrix by creating a larger, empty two-dimensional matrix full of zeros, and then adding the image data to the centre of the matrix. This is the equivalent of adding a large black border surrounding the original image. Zero-padding of the image matrix (after having been 'read-in' by the program) improved the display of the IFT plot.

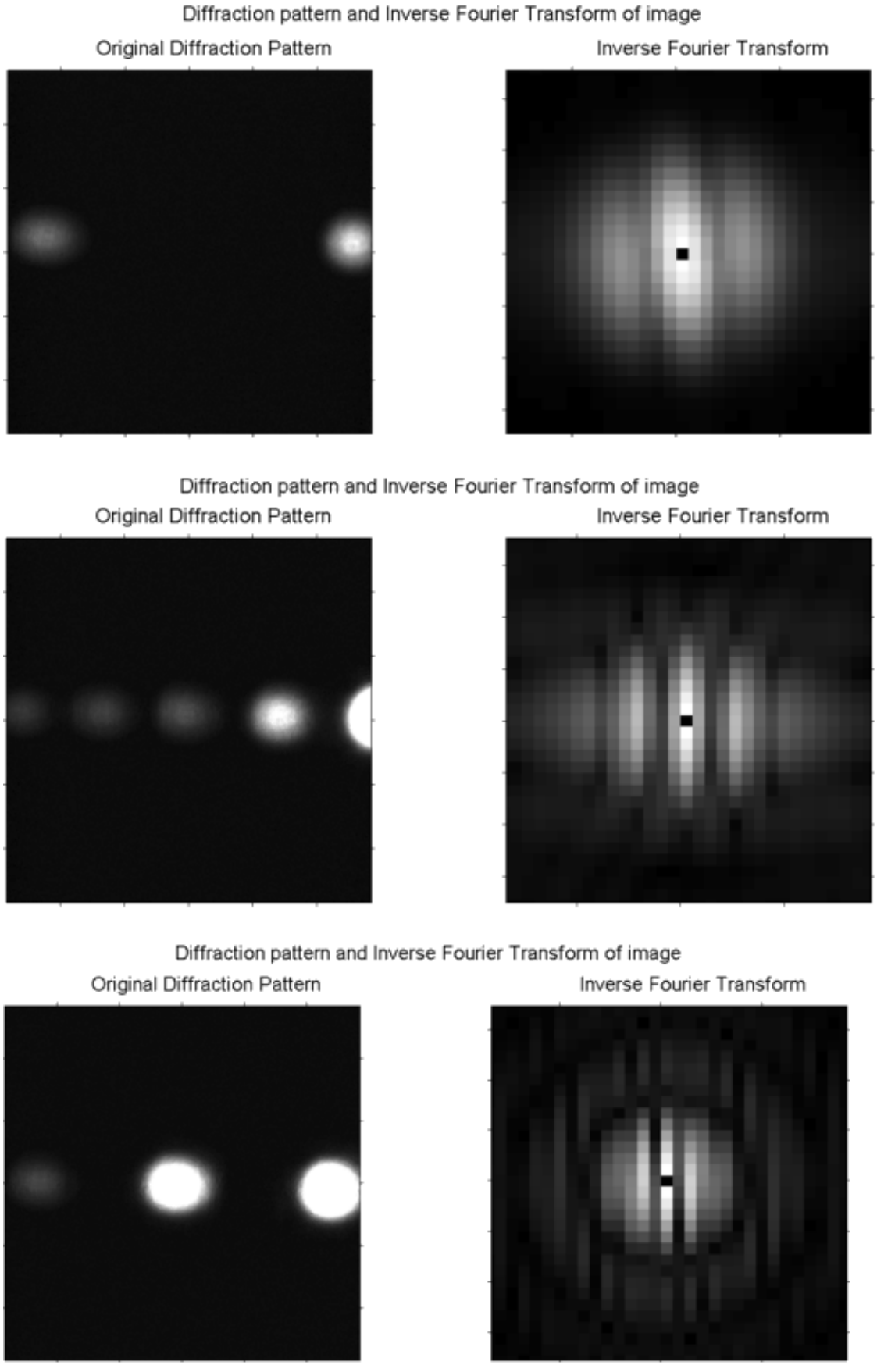

Figure 5.8: Example results from the Inverse Fourier Transform of captured images.

The larger the zero-padding of the input image, the better the resolution of the IFT. There is no more information contained within the input image, but more information becomes possible to display in the Fourier Transform plot. This is because of the reciprocal relationship between feature sizes in the input image to the corresponding feature sizes in the transform (see Figure 5.9). For example, with an image width of 1000 pixels, a feature that is 1000 pixels in size in the image is represented by 1 pixel in the IFT plot. A feature that is 500 pixels is transformed to a feature size of 2 pixels in the IFT plot.

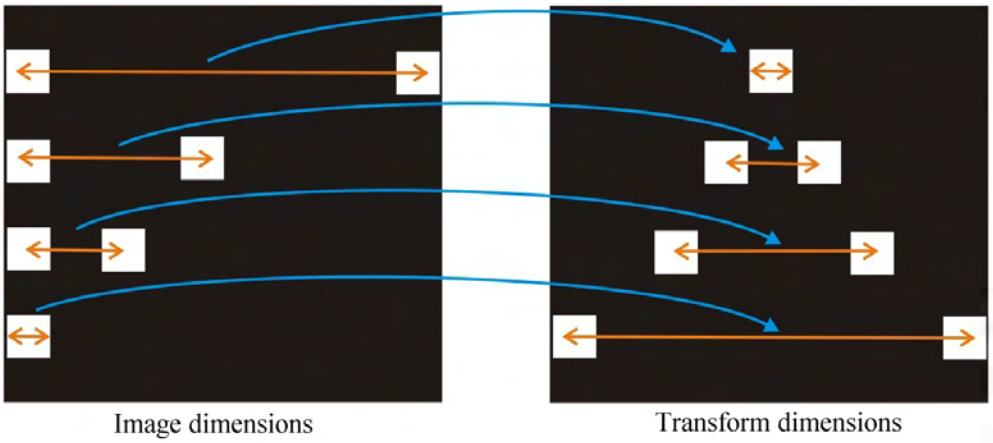

Figure 5.9: A reciprocal relationship exists between the dimensions in the image and the Fourier transform plot.

Most feature separation distances (the diffraction order separation) imaged on the CCD were in the region of $250 - 1000$ pixels, but the distinction is lost in the IFT since this range was only represented by $1 - 4$ pixels. The difference between 400 pixels and 450 pixels separation was clearly visible in the diffraction pattern image, corresponding to different diffraction grating periods, but this detail could not be displayed in the transform, which had a resolution limited by the relative size of the feature in the image to the image size. By increasing the border (zero-padding) around the image, the feature sizes in the image were relatively smaller in relation to the matrix size and were consequently represented by larger features in the IFT. When the image size was zero-padded to larger than 2048×2048 pixels (image sizes were zero-padded to powers of 2 for convenience and faster processing with MATLAB^{TM}) the file became too large to be processed. Zero padding of images to the next higher power of 2 than the original size gave sufficient resolution for transforming most images.

There were two main approaches to capturing the diffraction image, which had an impact upon the best pattern for the grating. One option was to have the CCD detector close to the slide to capture as much of the diffraction pattern as possible in a single image (example images are shown in Figure 5.8). Since even the biggest detector chips were fairly small

($\sim 8.0\ mm$) and the camera could not be mounted closer than 25 mm because of the casing and also the angle of the diffracted beam the capture angle was limited (as shown earlier in Figure 5.2). The period of the grating therefore needed to be fairly large (around 20 μm) to capture more than one diffraction order on the chip, even at close range ($\sim 30 - 40\ mm$). In this situation, the maximum angular range of capture was $\sim 10°$.

The alternative image capture method was to mount the detector further away and to scan across the large area of the diverging diffraction pattern (as shown in Figure 5.4), capturing several images and then 'stitching' them together. This setup had the advantage of at least a 90° capture angle range, and also a high resolution detail of the diffraction pattern obtained by joining together all the images. However, the resulting image had a large file size and created very lengthy processing times to calculate the IFT. The distance of the detector from the slide could be adjusted to work out the distance for the best trade-off between image resolution and file size. Also, it was only necessary to take a $1-$D cross-section through the diffraction orders for IFT analysis. This $1-$D matrix could easily be zero-padded to give the necessary resolution in the inverse transform plot.

The position of the CCD camera was accurately controlled by mounting it on a mechanical arm attached to a motorised rotation stage. Knowing the constant distance of the CCD from the centre of rotation, where the sample was located, and the size of the CCD chip, enabled calculation of the angular size of the image captured at any given point. From this point the rotation stage was moved to the next image capture point, with 0.001° accuracy in the angular position. The images were then stitched together, using a program written with MATLAB ™, and stretched out to the equivalent image as would be observed on a flat screen perpendicular to the zeroth diffraction order (see Figure 5.10) and then subsequently Fourier transformed. The image had to be stretched out to the flat-screen equivalent since the FT simply searches for common periodicities, but in the curved image captured, orders appear progressively closer together at larger angles from the zeroth order.

The best method to confirm the periodicity of the test gratings was to record the angular position of the centre of each diffraction order. The rotation stage was moved until the diffraction order was aligned with its centre over a cross-hair marked on the monitor. The angular position was read from the digital read-out of the motorised stage, an image captured and then the stage was moved on to the next diffraction order. Knowing the angular position of the diffraction orders, together with the angle of incidence, the period was directly calculated using the diffraction equation.

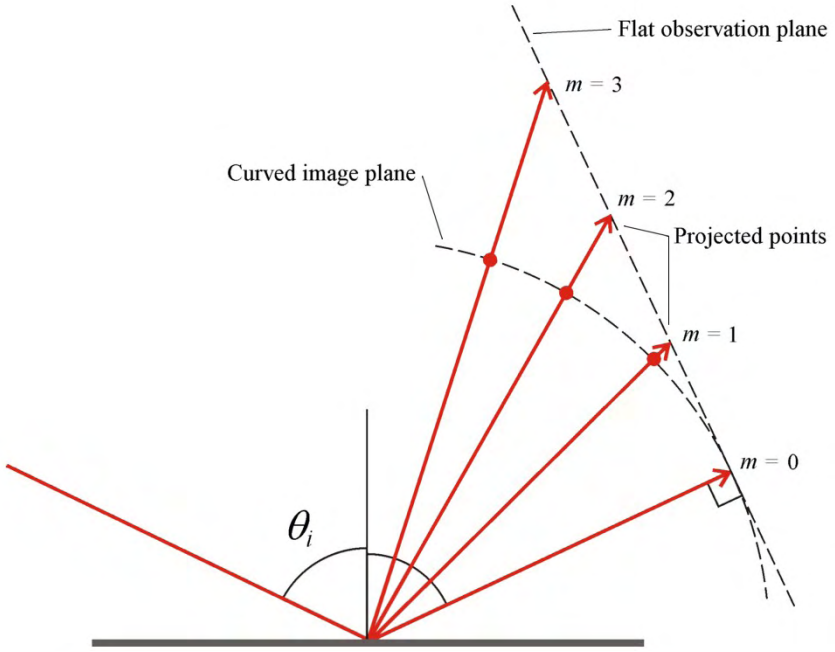

Figure 5.10: Diffraction images captured in a curved plane were stretched out to the equivalent as would be imaged on a flat screen perpendicular to the zeroth diffraction order.

The diffraction pattern for a 20 μm period chrome grating on silica is shown in Figure 5.11. The stitched image shows the relative angular spacing of the diffraction orders. The zeroth order was located at 55.9°, with the angular range of the image continuing to the $m = -13$ order located at 23.6°. This image represents a curved observation surface, with a constant observation distance. The image shown was deliberately saturated to make the detail of all the diffraction orders visible; these were not the images used to calculate the relative intensities of the diffraction orders. To calculate the relative intensities of the diffraction orders the illumination power was adjusted by rotating the variable neutral density filter to ensure that the CCD camera was not saturated and within a linear response range. When the incident power was adjusted two images were collected. The first was taken at the original power (at this stage the intensity was too low to be visible by eye on the monitor). The power was then increased towards the upper limit of the linear response region of the CCD camera, and a second image of the same diffraction order captured. Without adjusting the power from the lowest level (to avoid saturation at the zeroth and first orders), it was not possible to distinguish the higher orders from background light levels in a dark room. Taking two images of the same order when the power was adjusted enabled normalisation of the diffraction order intensities.

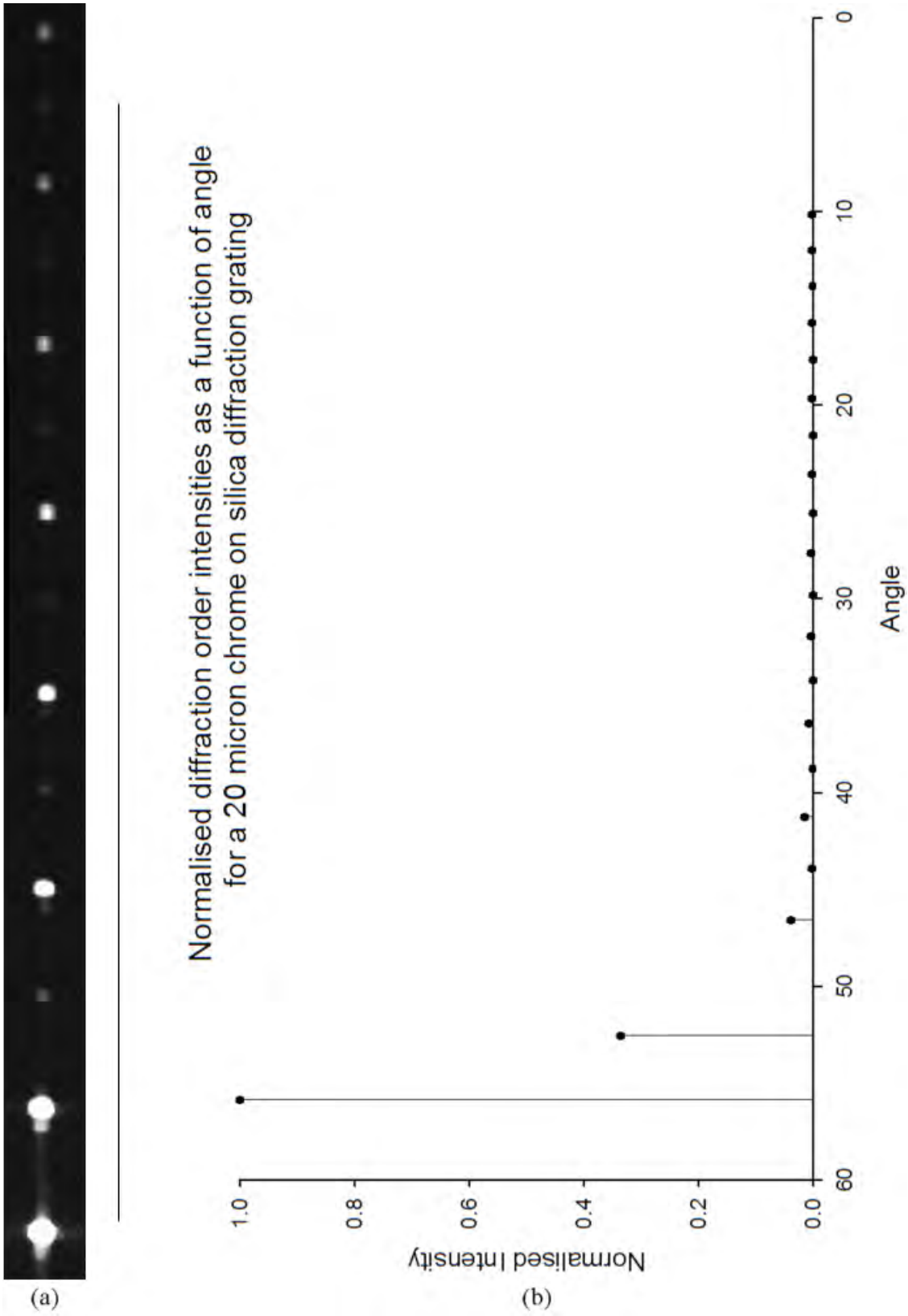

Figure 5.11: (a) Diffraction image produced by a 20 μm period, 10 μm linewidth chrome grating on silica illuminated with a 632.8 nm wavelength laser. (b) Normalised intensity graph of the diffraction orders.

5.2.3 DNA Diffraction Gratings and Gold Nanoparticles

The chosen diffraction grating pattern from the trial designs outlined in Section 5.2.1 featured a period of 20 microns with an equal line:space ratio. As detailed in Chapter 3, the grating design on the mask plate was replicated for use in DNA grating fabrication by creating a dark field mask on a fused silica substrate by etching a transmission grating through a 300 nm thick gold film (on a 20 nm chrome seed layer). This mask was then used (by Dr H Yin) to develop the DNA attachment chemistry and pattern the silicon substrate with DNA, as described in Section 3.5. Diffraction gratings consisting of DNA functionalised lines were prepared on silicon, with a period of 20 μm and a 10 μm linewidth. For initial experiments the oligonucleotides on the surface were capture sequences directly complementary to the oligonucleotide functionalised gold nanoparticles (1.4 nm, 10 nm and 50 nm diameters), with no sample DNA necessary to link them together (Figure 5.12).

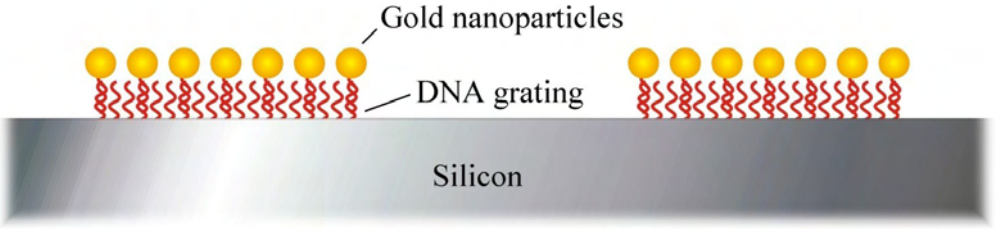

Figure 5.12: DNA grating on silicon with hybridised complementary oligonucleotide functionalised gold nanoparticles.

It was decided to investigate the relationship between structure within the lines of the diffraction grating, surface area coverage and the effect on the intensities of the diffraction orders. By looking at the different diffraction order intensities formed by the DNA diffraction gratings, information would be extracted about the hybridisation density. The diffraction efficiencies, the ratio between the reflected power in the zeroth order to the intensities of the other orders, should relate to the surface area coverage.

Owing to the biological nature of the diffraction sensor, the sample needed to be kept in a liquid buffer environment for experiments to retain the functionality of the DNA grating. Once gold nanoparticles had been attached, the buffer was also necessary to prevent dehybridisation. Consequently all experiments were carried out in hybridisation buffer; 0.3 M NaCl 10 mM phosphate pH 7.0.

The silicon surface was patterned with 20 μm period DNA lines, as shown in Figures 5.13 and 5.14, although the linewidth:separation ratio did not come out as 50 : 50, instead

featuring linewidths of around $3 - 5\ \mu m$. The grating was then tested for diffraction with a red wavelength HeNe laser. The DNA patterned silicon sample was placed in a shallow container and covered with buffer solution. There was a very high reflectivity of the incident laser beam from the silicon surface. The Brewster angle was calculated to be 69° for silicon in water. To align the optics a silicon wafer was immersed in buffer to locate the Brewster angle and minimize the reflected signal. When the angle of incidence was varied from 0° to 80° the intensity of the reflected beam did not appear to diminish significantly at any angle for p-polarised light, unlike for silica where reflection drops to zero at the Brewster angle. This is because silicon is not a dielectric like silica and so, although there is a minimum in the reflectivity, a substantial value of 13.8 % was still measured. Consequently, the angle of incidence for silicon was kept at the Brewster angle for glass to enable direct comparisons of the diffraction patterns.

Figure 5.13: Microscope image of a 20.0 μm period DNA grating on silicon.

When the DNA patterned sample was illuminated it produced a diffraction pattern visible by eye. This was related to the height difference between the DNA and silicon surface, and differing reflectivities. Since the DNA was patterned in a periodic fashion, this itself produced a diffraction grating without the addition of the gold nanoparticles, because the exposed silicon reflects much more strongly than DNA covered regions. The diffraction order intensities (I_m) were measured by scanning through the angular range of the first six diffraction orders with a power meter at an observation distance of 20.0 cm. The experimental layout was as shown earlier in Figure 5.4; a CCD camera was used to capture images of the diffraction pattern and was then replaced with a power meter detector head to measure the

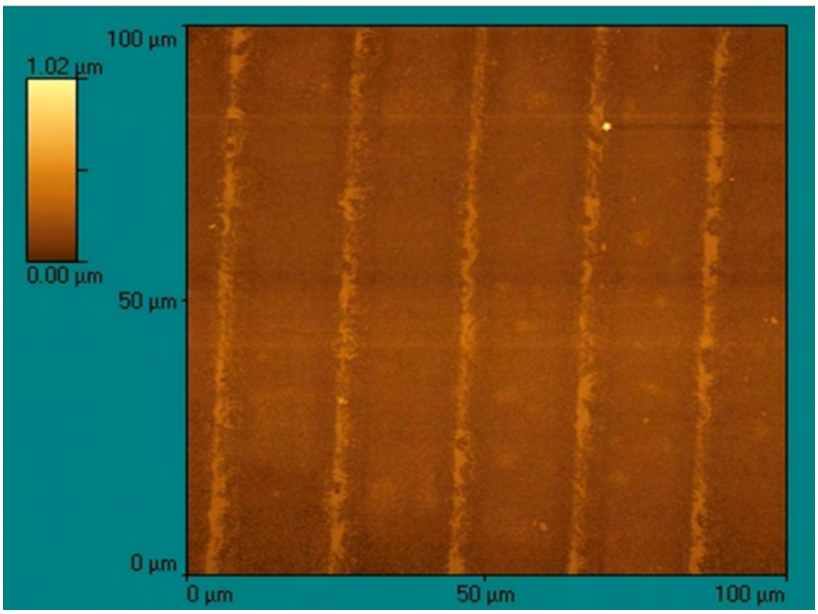

Figure 5.14: AFM image of a DNA diffraction grating on silicon with a 20 μm period.

intensities.

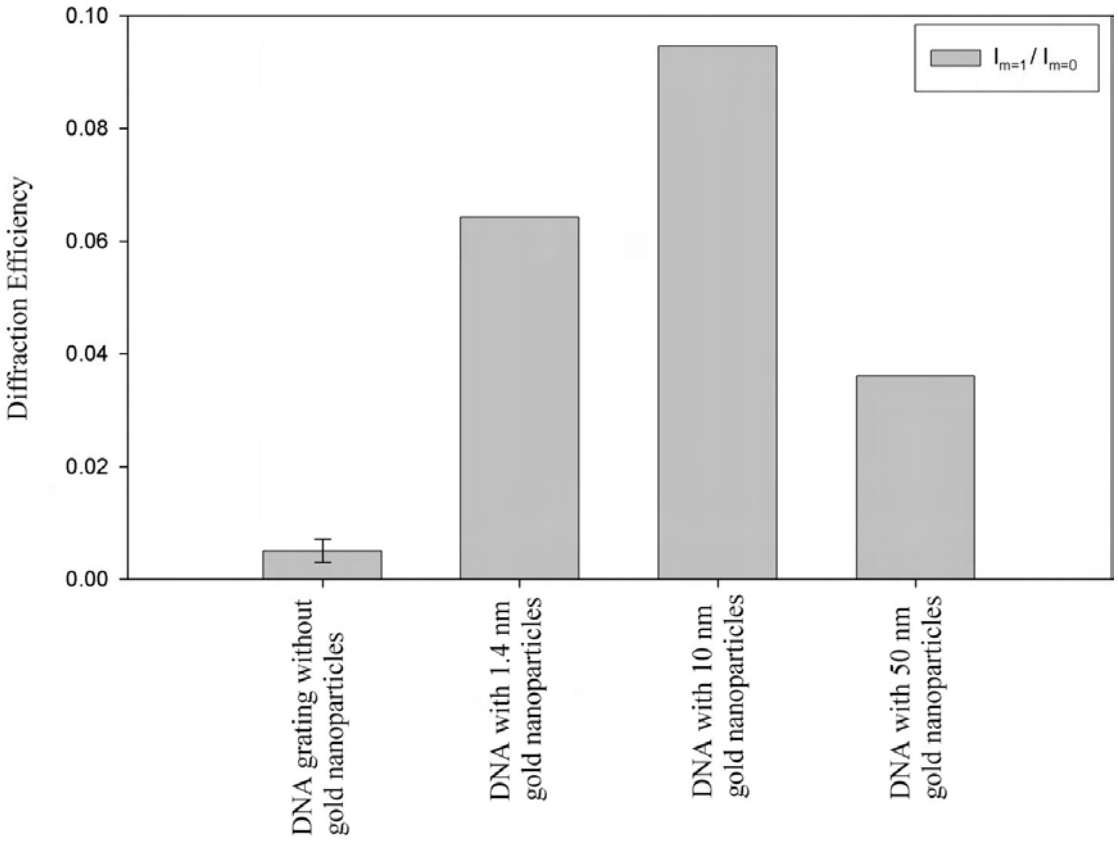

Figure 5.15: First-order diffraction efficiencies ($I_{m=1}/I_{m=0}$) for DNA gratings on silicon (10 μm linewidth, 20 μm period) hybridised with different sized diameter gold nanoparticles.

The diffraction efficiency of a grating is commonly referred to, in the literature, as the ratio of the first order to the zeroth reflection intensity ($I_{m=1}/I_{m=0}$) [14, 143]. The first-order diffraction efficiency is usually the highest and therefore the best indicator of the amount of diffraction being generated by a grating. The diffraction efficiency was measured as 0.5 % for several samples with DNA only lines. Samples were prepared with gold nanoparticles of 1.4 nm, 10 nm and 50 nm diameters. Upon hybridisation with the gold nanoparticles the first order diffraction efficiencies were found to be 6.4 %, 9.5 % and 3.6 %, for 1.4 nm, 10 nm and 50 nm diameter particles respectively (see Figure 5.15). The intensities of the diffraction orders were at least seven times higher for samples with gold nanoparticles hybridised to the gratings, enabling detection of the DNA sequences attached to the nanoparticle probes.

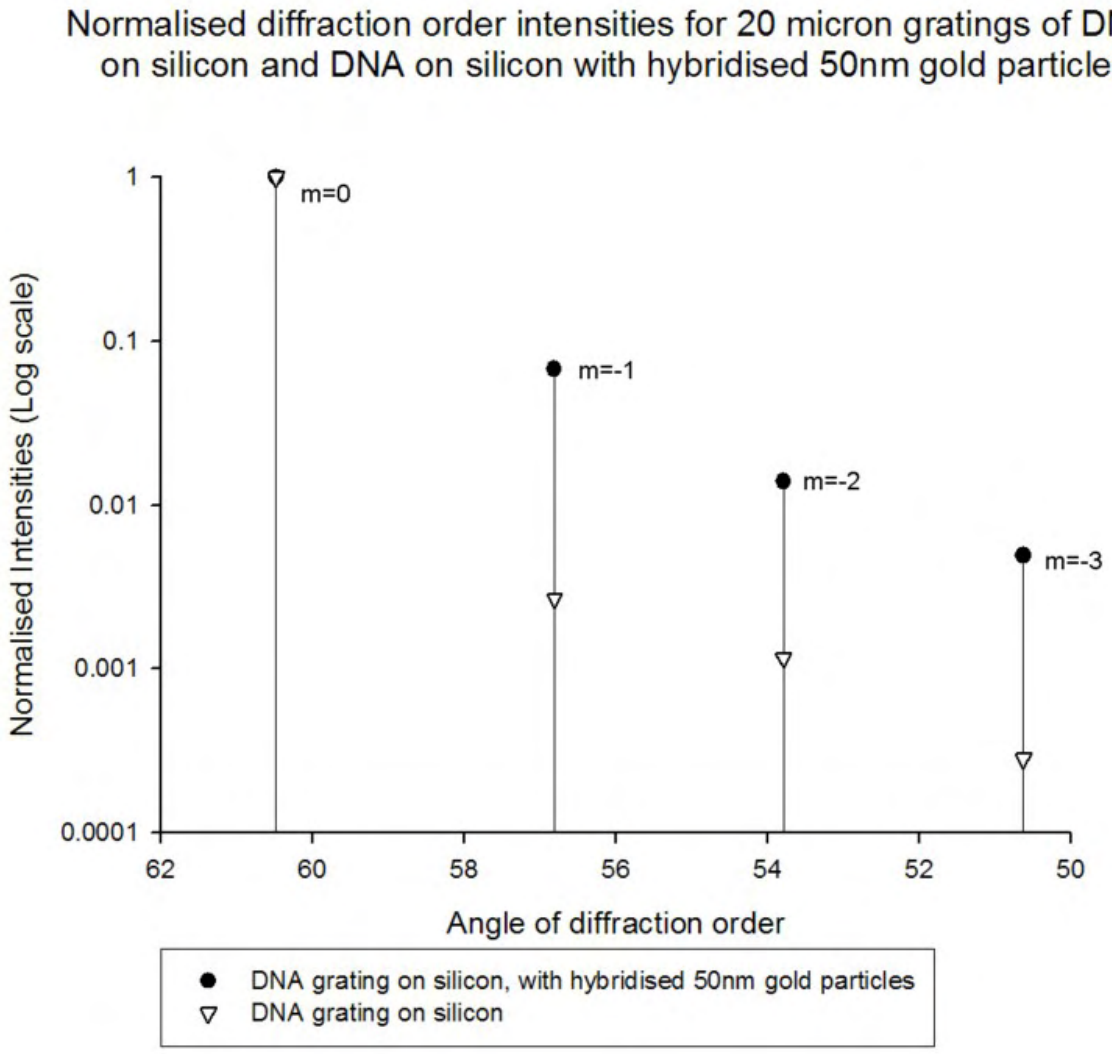

Figure 5.16: Normalised diffraction order intensities for a 20 μm period DNA grating on silicon, with and without hybridised 50 nm diameter gold nanoparticles.

A sample from another batch was prepared and tested with 50 nm diameter gold nanoparticles hybridised, and the diffraction efficiency was measured as 6.7 %, over thirteen times higher than for DNA alone. The difference in diffraction efficiency between a DNA grating

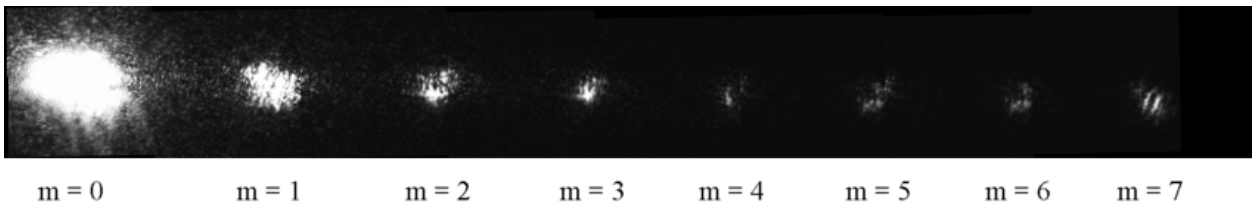

Figure 5.17: Diffraction pattern (stitched images) of 20 μm DNA grating with hybridised 50 nm gold particles.

and a sample with hybridised 50 nm gold nanoparticles, can be seen most clearly on a logarithmic scale of the normalised diffraction order intensities, as a function of angle for the DNA grating and the DNA grating with gold (see Figure 5.16). The period was calculated to be 20.0 μm from the angular position of the diffraction orders, as can be seen in Figure 5.17.

5.3 Diffraction Intensity Data Collection

Although 5 DNA samples had been tested and all produced only a weak diffraction grating (diffraction efficiency $I_{m=1}/I_{m=0} \approx 0.5$ %, see Figure 5.15) and then another 3 samples this time hybridised with gold nanoparticles for measurement all showed much higher diffraction efficiency ratios; similar results were not obtained for subsequent fabrication batches. After image-based diffraction measurement was used in initial proof-of-concept experiments, a more complex diffraction experiment was developed to more accurately measure the intensity of diffraction orders.

The initial experiments had measured the diffraction order intensities at a fixed point within a grating using a power meter. The diffraction pattern was measured in a region of the grating where the diffraction pattern was most intense prior to the hybridisation of gold nanoparticles. The sample was then aligned to approximately the same region and the position was adjusted to maximise the diffraction pattern intensity, obtained with gold nanoparticles attached to the grating.

As more diffraction experiments were carried out it became evident that there was a large change in diffraction order intensities as a function of position within the grating; something that had not been characteristic of the solid chrome on silica test patterns. This variation originated from the variation in surface profile, linewidth, step height and density of DNA

coverage (modifying the reflectivity of the surface). Another source of variation was that the DNA samples had to be measured in a liquid buffer environment to preserve their functionality and ensure that gold nanoparticles remained hybridised to the grating. The next development steps implemented were to improve the DNA grating consistency, optimise the grating design and improve the data capture methodology.

Sample fabrication was improved to give a more consistent surface coverage, linewidth and step height, as detailed in Chapter 3. Bubble formation had been a problem during DNA conjugation, leaving regions of the grating with limited or no DNA coverage. To improve the surface coverage it was desirable to alter the design of the grating to reduce gas build up and allow the gas to escape by increasing the separation of the DNA lines compared to their width. At the same time it was necessary to develop a diffraction grating structure that would produce a diffraction pattern with order intensities less sensitive to variations in linewidth.

It was possible to calculate theoretical intensities for diffraction orders produced by a grating with a linewidth of a and separation b. However, the equations that govern these calculations were derived for normal incidence. The derivation needed to be extended to modify the equation to produce correct values for the angular positions of the diffraction orders and their intensities. This was done as described in Chapter 4, additionally taking in to account the fact that both the grating lines and the intermediate regions contribute to the diffraction pattern. A new diffraction grating structure was chosen with a 40 μm period and a 10 μm linewidth, giving a $1:3$ ratio of $a:b$. This grating structure (with overall dimensions of $3\ mm \times 6\ mm$) is referred to from here onwards.

A new approach to characterising the sample and measuring diffraction patterns was developed to yield more consistent results. Scanning of the sample and averaging of the diffraction order intensities over the whole grating was achieved by translating the sample in the path of the laser beam and recording the power measurement at each point within a scan matrix (see Figure 5.18). Motorised translation stages were computer controlled using a program written using the National Instruments^{TM} software LabVIEW^{TM}. The sample was mounted in a trough containing a liquid buffer mounted on a small rotation stage on top of the $x-y$ translation stages. The sample was rotated to ensure that the translation scan was parallel with the edges of the sample. The sample was translated so that the centre of the scan region and the centre of the grating were co-aligned.

The detector was changed to a photodiode instead of a power meter and a multimeter was

used to record voltages and communicate with the computer. The detector was aligned to the position of the zeroth order ($m = 0$) and a scan was executed. The program translated the sample in the path of the laser beam, and at each point in the scan, the diffraction intensity was averaged over 500 consecutive readings, recorded to an array and then moved to the next position. At the end of the scan the detector was aligned to the next diffraction order, the sample returned to the origin and a new scan commenced. This was repeated for diffraction orders $m = 0$ to $m = 5$.

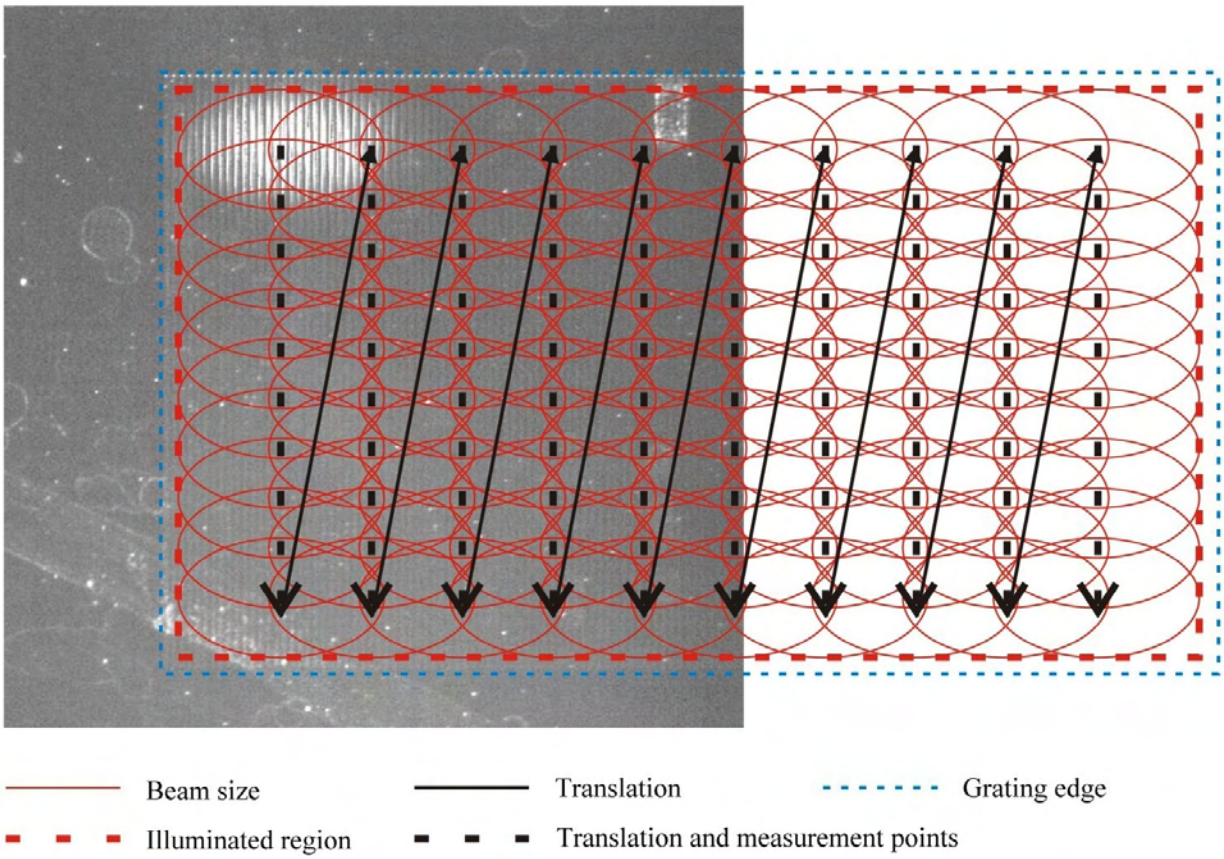

Figure 5.18: Automated scan and intensity measurement used to translate the grating in the path of the beam and collect data for the whole grating, illustrated schematically over a sample image.

After the grating had been characterised for the inherent diffraction intensities (for orders $m = 0 - 5$) from the DNA lines on the silicon, gold nanoparticles were hybridised featuring complementary oligonucleotide sequences to those immobilised on the grating. The protocols for hybridisation are described in Chapter 3. The samples were rinsed to remove any un-hybridised gold and then re-tested to characterise diffraction with the hybridised gold nanoparticles. For many samples tested the average change in diffraction with the addition of gold nanoparticles yielded less change than that caused by positional variations. Even a point-by-point comparison yielded inconsistent changes.

Initial results from attaching gold nanoparticles to DNA diffraction gratings on silicon proved

promising and a substantial change in diffraction intensities had been expected. However, in contrast to photolithographically fabricated metal patterns, DNA gratings were inherently more variable. Measuring the diffraction pattern was unexpectedly sensitive to positional changes. The initial assumption, that gratings which had been successful in DNA conjugation would exhibit very similar diffraction patterns, proved false.

5.4 Diffraction Experiment Development

To improve the diffraction intensity measurement and accuracy the repeatability of measurements was examined. Measures introduced to improve diffraction measurement repeatability included:

1. Monitoring the laser output power simultaneously to each measurement and normalising the intensity variations.
2. Development of the best sample holder for the liquid buffer environment needed for the DNA.
3. Using more points in the diffraction scan to reduce the positional variation.
4. Incorporation of alignment marks at the edge of the grating and use of a CCD camera with a zoom lens to aid alignment.

5.4.1 Laser Output Power Monitoring

Although the diffraction patterns were being averaged over 500 readings at each point, and over the whole sample at up to 1500 points, the diffraction measurements took approximately 30 minutes per order, during which time the laser output power or alignment could drift. Subsequently the system power output was monitored over time (see Figure 5.19) using a mirror at the sample location and aligning the diffraction detector to the reflected beam. During the start-up period, the laser power fluctuated by up to 20 % between maximum and minimum power. Although, after 30 minutes warm-up time, the laser became stable (maximum-minimum range 1.2 %, standard deviation of 0.23 %) over the time frame of a diffraction scan, the overall system power could still fluctuate by up to 6.3 % (power drift region indicated in Figure 5.19), which could overlap with measurements. To minimise this

error in measurement the laser output power was monitored simultaneously to recording the diffraction intensity.

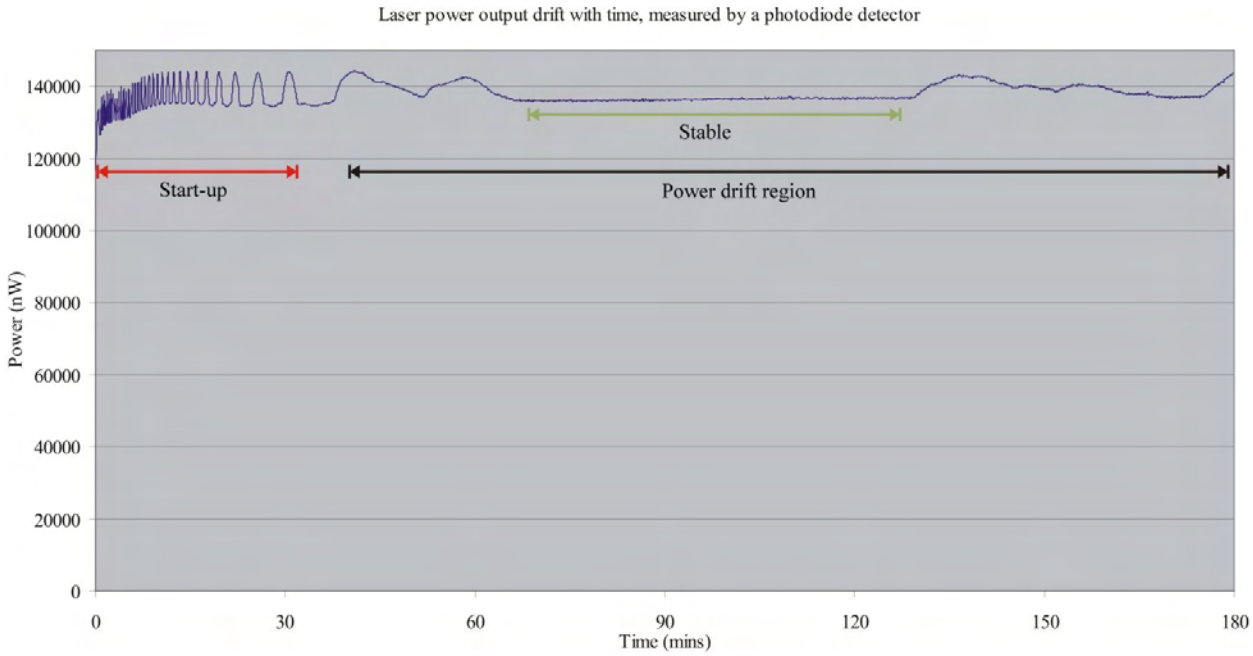

Figure 5.19: Laser power fluctuations were monitored over a 3 hour period from start-up.

In order to record two input powers through LabVIEW^{TM} it was necessary to install an analogue data acquisition card (National Instruments DAQ card), rather than use a multimeter and RS-232 connection. A second amplified photo-detector was built and calibrated to measure the laser output power, sampled by using a wedge prism to reflect $\sim$ 1 % of the incident beam to the photodiode (shown in Figure 5.20). The rest of the beam was transmitted and used to illuminate the sample. To reduce the impact of alignment changes of, for example, the pinhole in the spatial filter, the beam-splitter was placed after the precisely aligned optics. The analogue voltages output from the photodetectors were input to a National Instruments DAQ input block, connected to the data acquisition card, so that both measurements could be captured by the computer program. Using this method the incident power onto the sample was measured, thus power fluctuations and alignment drift were taken into account.

To configure the apparatus for the dual measurement, the sample was replaced with a plane mirror in air. For each point within a scan, the diffraction detector power (I_{D_1}) and the incident laser power detector intensity (I_{D_2}) would be averaged over 500 simultaneous readings, and then the two average values recorded to be normalised to each other. The incident power monitoring detector received $\approx$ 1 % of the beam reflected from the beam-splitter. When bare silicon was used at the sample location to reflect the beam, the ratio of the two detector power measurements was 79.9.

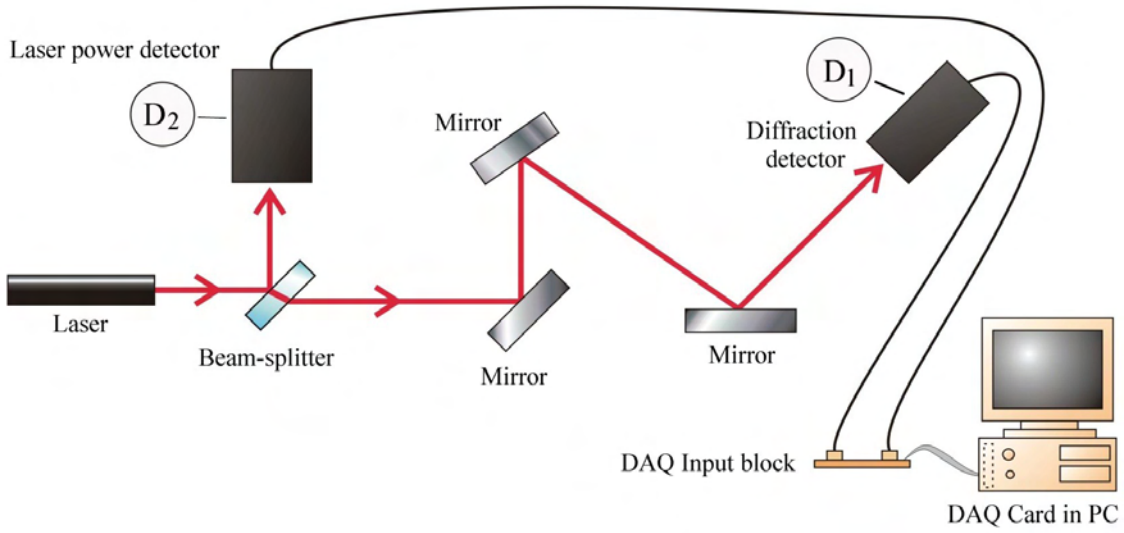

Figure 5.20: Laser power fluctuations were monitored using two photo-detectors. The diffraction detector (D_1) intensity was normalised to the incident power monitoring detector (D_2).

Figure 5.21 (i) shows the power measurements from each detector, unscaled. The laser power clearly varies by ± 3.2 % for the individual traces. However, when the power monitoring detector intensity measurement is scaled, it almost identically matches the measurement made by the diffraction detector, as shown in Figure 5.21 (ii) scaled to view the power range of interest. The ratio of the scaled values produces an almost constant value of 1.00, with a standard deviation of the ratio between the two measurements of 0.034 % (shown with a highly zoomed-in vertical scale around 1.0 in Figure 5.21 iii). Thus nearly a 100 fold reduction in the error of measurements was achieved.

5.4.2 Sample Holder for DNA Functionalised Gratings

As mentioned earlier in the chapter, for experiments to retain the functionality of the DNA grating and to prevent dehybridisation, the sample had to be kept in a liquid buffer environment . Consequently all experiments were carried out in a liquid buffer environment of 0.3 M NaCl 10 mM phosphate, pH 7.0.

There are several problems associated with accurately measuring diffraction from a sample in a liquid environment. It was found that by simply using a coverslip on top of a sample with a drop of liquid, it dried out too quickly, forming bubbles and moving the position of the diffraction order off the detector within one or two minutes. To reduce evaporation effects samples were placed in a trough of buffer. However, this meant that there was potential for the sample to move within the trough (although weighted down with pieces of glass). It

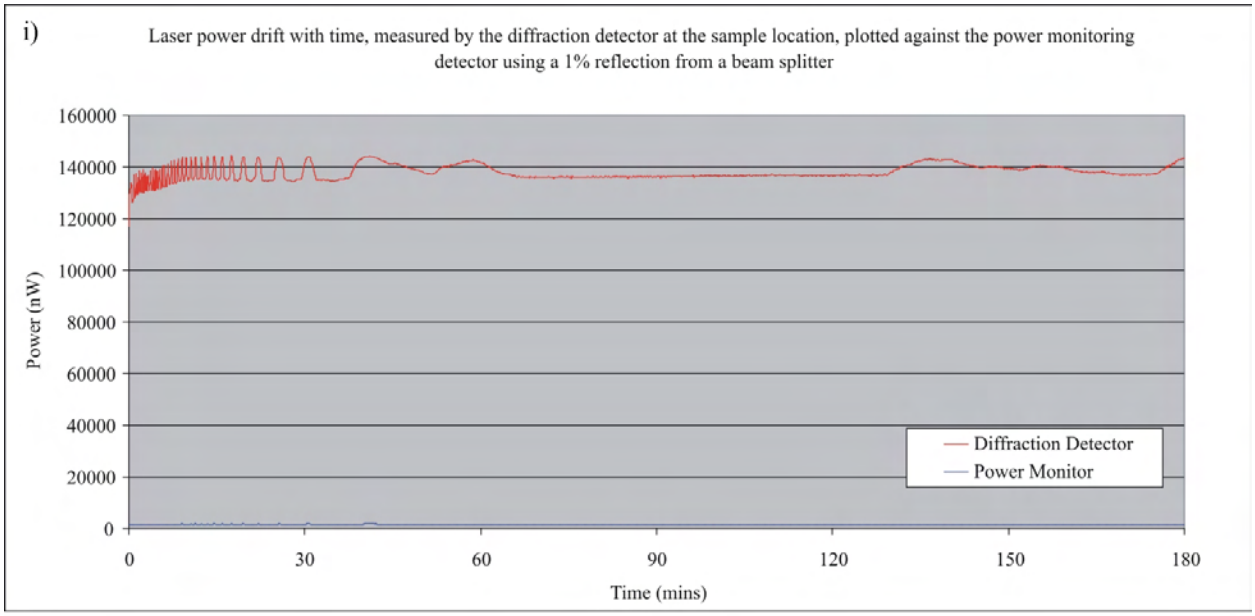

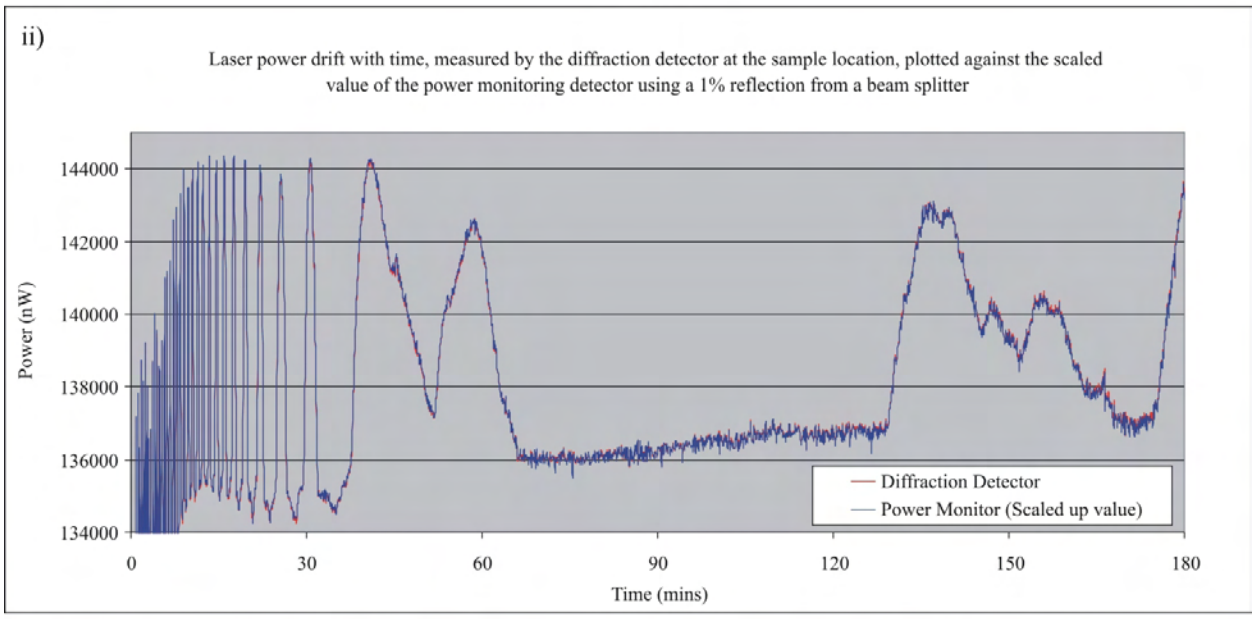

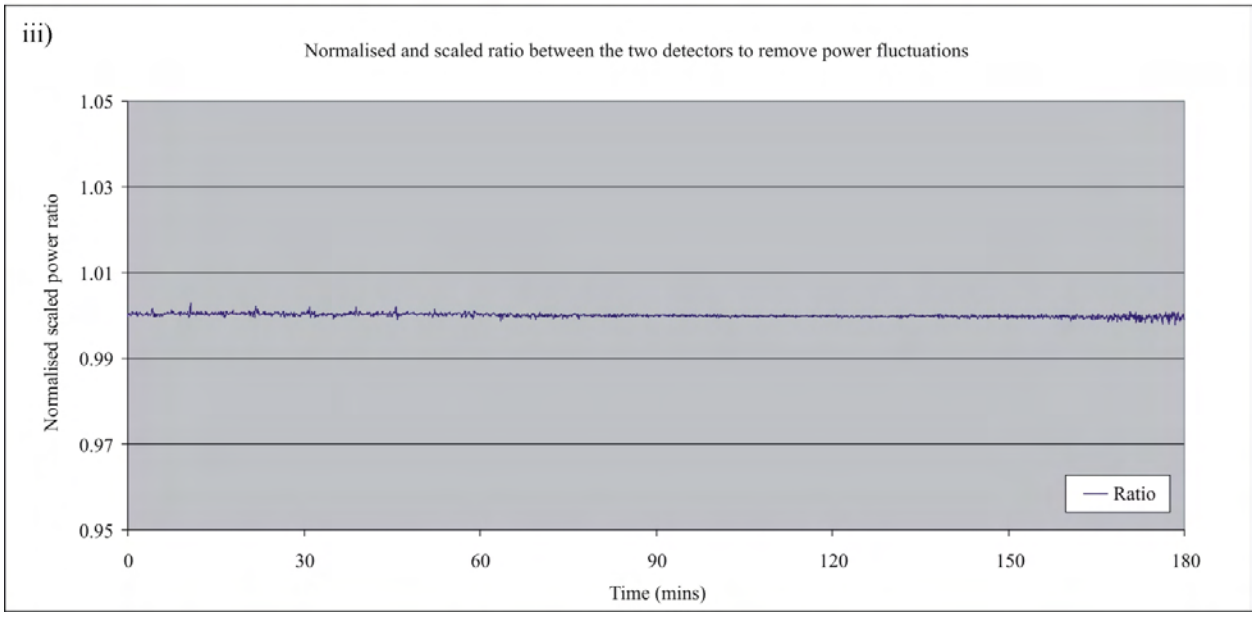

Figure 5.21: Laser power fluctuations were monitored using two photo-detectors. The diffraction detector intensity was normalised to the scaled-up incident power monitoring detector.

also meant that readings had to be delayed after each translation of the sample (with the motorised stages) to allow the induced surface perturbations of the liquid surface to stabilise.

A sample holder was fabricated to hold the sample in place using microscope slides and Parafilm, so that it could not move as the sample was translated in a diffraction experiment. Experiments were carried out to improve the sample alignment in diffraction experiments and minimise this source of error. During these trials, it became apparent that the volume occupied by the sample holder, in the water trough previously used, meant that the buffer in the trough evaporated faster. This changed the surface level and profile of the liquid thus altering the refraction and causing a 'lensing' effect on the diffraction pattern. This affected the sharpness of an order, its angular position, and vertical plane of propagation. Consequently, although the detector was aligned at the start of each measurement scan, the position of the order could move partially or wholly off the detector.

Measurements were taken on the variation with time of the zeroth diffraction order intensity, using a photodiode, and normalised to laser power variations as described above. When the grating was in the sample holder with water on top, up to the edges of the holder, it evaporated too quickly to remain constant during a diffraction experiment. The readings slowly increased and then dropped off after $10 - 15$ minutes. The experiment was repeated again with a coverslip on top of the trough to see if this reduced the evaporation rate. The reading dropped to $\sim$ 90 % of the initial value within 2 minutes, then dropped rapidly to $\sim$ 10 % within the next 5 minutes. It appeared that a loose coverslip over the sample compartment alters the position of the diffraction orders more than without a coverslip. The repeatability of measurements is crucial to be able to determine a small change in diffraction intensities, so several other options were trialled.

The graph in Figure 5.22 shows the drop in intensity measured for the zeroth order over a 1 hour period for a DNA on silicon diffraction grating sample. The grating was placed in a sample holder in the centre of a Petri dish half-filled with water. The bottom left graph is the power measured by the diffraction detector. Results showed that as the water evaporated and the water level changed, the diffraction order position moved off the detector, causing the measured intensity to drop. The bottom-right graph shows how the laser power fluctuates during the experiment and the top graph is normalised to this. The intensity reading was fairly stable for the first $10 - 15$ minutes, but this was not long enough for a full scan of the sample to be completed. During diffraction experiments, it was found that as the sample was translated, each move agitated the liquid. This meant that approximately 10 seconds had to be left before each reading could be taken and the next move made. When averaging

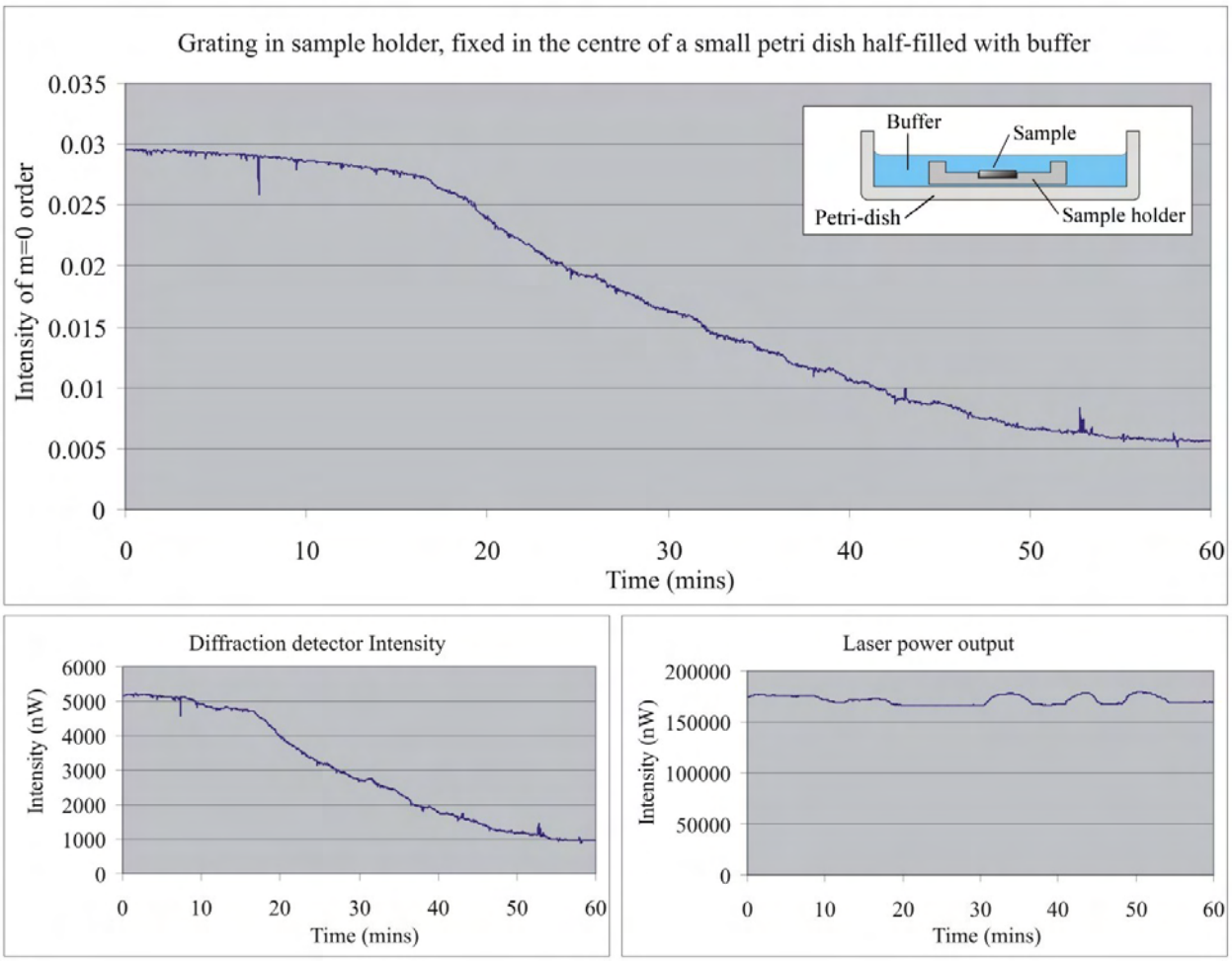

Figure 5.22: The intensities of the first-order diffraction (bottom left) and laser output power (bottom right) were monitored over time. The first-order diffraction normalised to power fluctuations (top) was used to study alignment drift for the sample holder shown (inset).

over a large number of points this took a long time (about 1 hour per order).

To resolve this a variety of alternative sample holder trials were evaluated to reduce evaporation. For example using a large volume of liquid, sealing the sample holder with Parafilm using a coverslip-window, using a Peltier stage to cool down the sample, and using a Peltier stage with a loose coverslip on top.

The consistency of readings over time was vastly improved when a Parafilm-sealed coverslip was used to seal the sample holder (without requiring a Peltier stage), the formation of bubbles under the glass over time was reduced by placing the sealed sample holder in a Petri dish and covering the edges of the film in water. As can be seen in Figure 5.23.

Although many of the methods tested worked well, the best option was found to be using a sample holder constructed by machining a solid piece of PTFE (polytetrafluoroethylene)

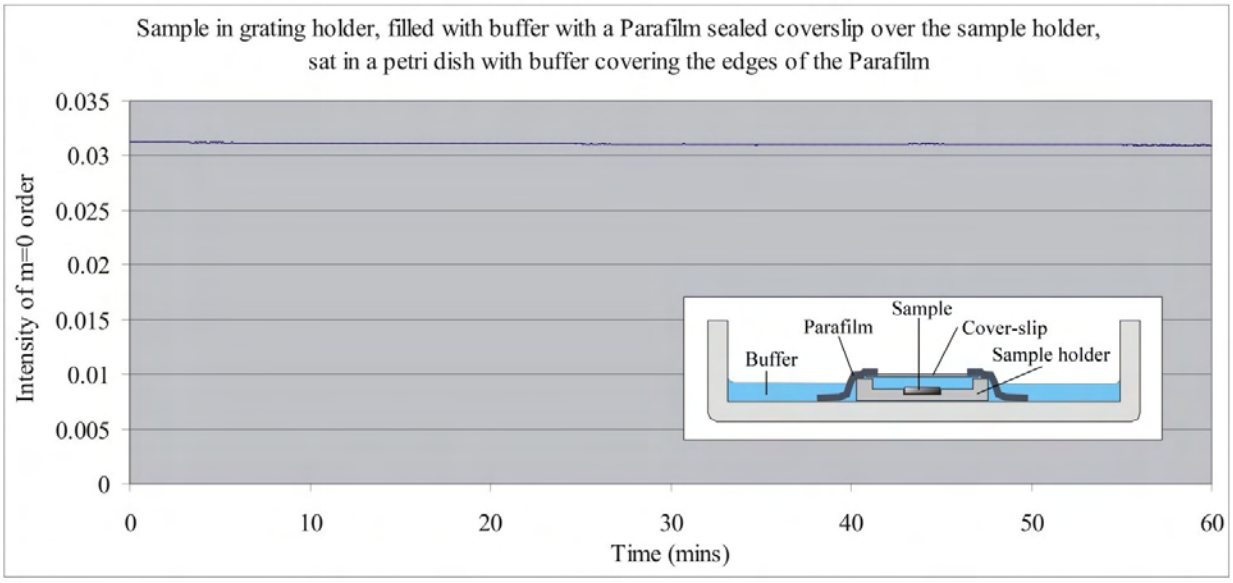

Figure 5.23: Alignment drift using a sealed sample holder in a buffer reservoir.

Figure 5.24: The final sample-holder used for experiments was machined from PTFE, with a recess to accommodate the sample and a buffer reservoir. The holder was then sealed using Parafilm tape with a coverslip window in the centre.

material, so that liquid could not leak out of the bottom. The final sample holder design is shown in Figure 5.24. The sample was placed in the centre recess and then buffer was added on top to fill the whole cavity. A window was cut out of the centre of a piece of Parafilm and heat sealed on to a glass coverslip (0.2 mm thick). This was placed over the top of the sample holder (ensuring that no bubbles were present) to seal in the buffer and prevent evaporation.

This solved the problem of alignment drifts and enabled consistent readings to be taken over lengthy periods ($\sim$ 3 hours). Due to its constant plane the glass top surface prevented measurement fluctuations (on sample translation), meaning that the sample could be translated and readings taken at the maximum rate; taking approximately one second to move to the next position and take a reading. This was determined to be the optimum setup for minimising intensity measurement errors without the need for extra equipment.

5.4.3 Diffraction Pattern Averaging

To improve the characterisation of diffraction from the DNA gratings on silicon, the number of points within a scan (see Figure 5.18) was increased from an initial value of 36 points to 100, to 1000, 1458, and finally 1540.

The laser beam size was measured using a beam profiler and the beam waist size was determined to be 0.33 mm in radius at an intensity of $1/e^2$ of the maximum intensity and an observation distance of 50 mm from the sample (see Figure 5.25). Due to the angle of incidence of the laser beam, the spot radius on the sample was elongated to ~ 0.6 mm. The step size was initially chosen so that each spot just overlapped to cover the whole surface in a scan region. The first scan-based methods scanned the central region within the grating so that edge effects would not be taken into account.

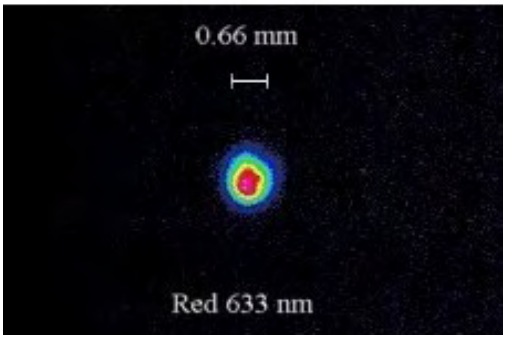

Figure 5.25: A beam profiler was used to measure the laser beam radius at the point of incidence on the sample.

The final measurement and analysis methodology adopted was to average the intensity over the scan area. The diffraction intensity measurements were normalised to the input laser power at each scan point over the grating surface. The mean intensity of the normalised diffraction data was calculated for each diffraction order, averaging the data recorded over the scan area. The absolute error was calculated as follows; the relative error of the average normalised intensity (I_m/I_{input}) was taken as the standard deviation of the normalised intensity readings (σ); the relative standard error (ϵ_{rel}) of the average was then $\epsilon_{rel} = \sigma/\sqrt{N}$, where N was the number of data points. The absolute standard error was then $[I_m/I_{input}] \times [\sigma/\sqrt{N}]$.

To calculate the relative difference between two diffraction pattern measurements i and ii, the fractional ratio was taken between them for each diffraction order:

$$\Delta\ I_m/I_{input} = \left[\frac{[I_m/I_{input}]_{ii}}{[I_m/I_{input}]_i} - 1\right] \times 100\%$$

The absolute error was calculated by adding the relative error of each average value in quadrature and multiplying by the change in diffraction intensity:

$$\epsilon_{abs} = \sqrt{(\epsilon_{rel\ i})^2 + (\epsilon_{rel\ ii})^2} \ \times \ \Delta\ I_m/I_{input}$$

5.4.4 Sample Alignment

After monitoring the laser power output to normalise the diffraction measurement against incident power variations; improving the sample holder environment to minimise alignment changes; and increasing the number of points and averaging in a diffraction scan, it was apparent that the key error in repeatability of measurements was sample alignment.

To further increase the accuracy and repeatability of diffraction grating characterisation alignment marks were incorporated into the gold on fused silica masks used for DNA sample fabrication. A cross-hair was added, offset to the top and side of the grating. A CCD camera was fitted with a zoom lens and placed directly above the grating (item 15 in Figure 5.27) to focus on the alignment marks. The sample was orientated to the correct angle to remain parallel with the translation path. The sample was then translated to the cross-hair to centre the beam and ensure that each scan started aligned with the same reference point. Example images taken from the alignment camera are shown in Figure 5.26, showing the accuracy of realignment after the sample was removed from the sample holder and then replaced and aligned to the laser beam again. The final experimental set-up developed is shown in Figure 5.27.

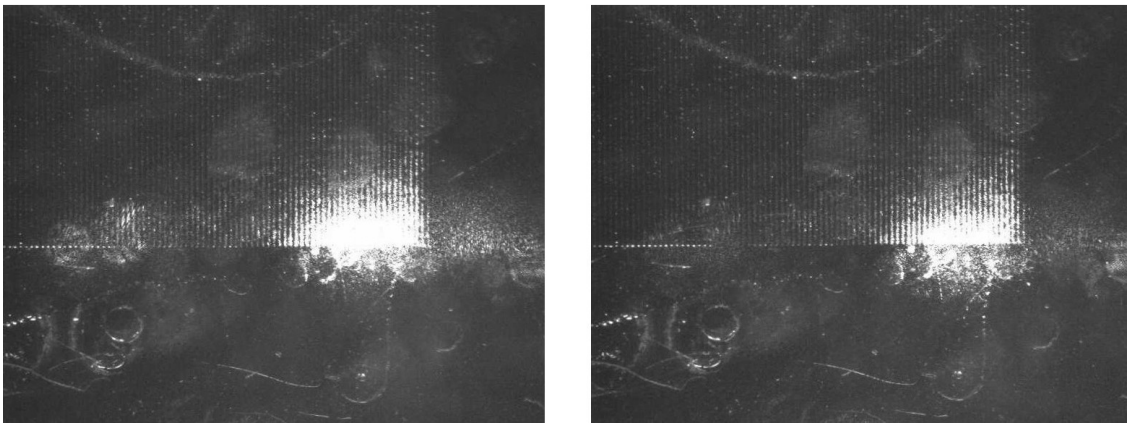

Figure 5.26: Sample alignment was improved using a CCD camera with a zoom lens to observe and image the position of the laser beam on the sample. These two images show the repeatability of repositioning of the sample after being removed and replaced in the sample holder and realigned.

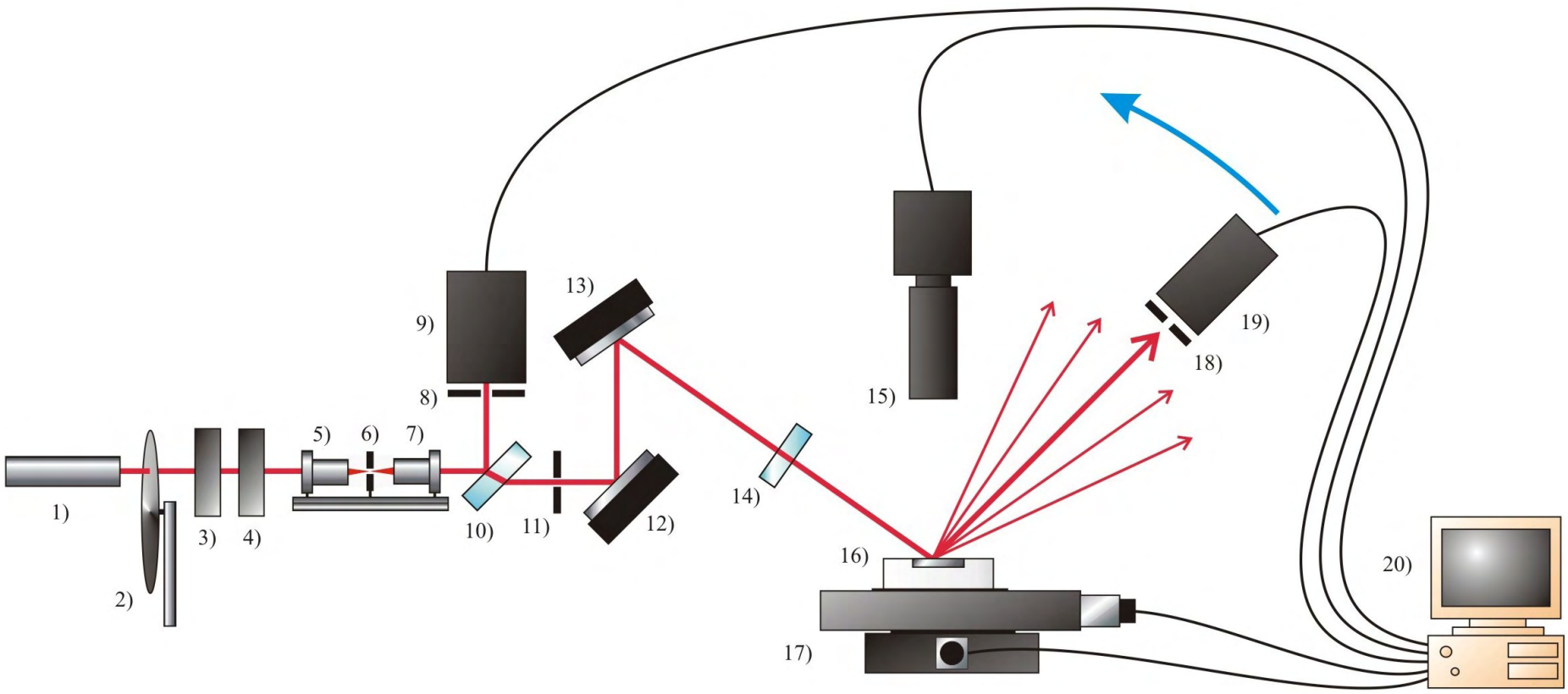

1) HeNe Laser
2) Variable Neutral Density Filter
3) Polariser
4) Polariser

Spatial Filter Assembly
5) Objective Lens 10x
6) Pinhole (30 micron)
7) Objective lens 10x

8) Iris
9) Photodiode Detector
(For Laser Power measurement)

10) Beam Splitter
11) Iris
12) Mirror

13) Mirror

14) Half-Wave plate

15) CCD Camera with Zoom Lens

16) Sample holder and Sample

17) X-Y Translation Stages

18) Iris

19) Photodiode Detector
(For Diffraction Intensity measurement)

20) Control Computer
(For sample translation and data acquisition)

Figure 5.27: Schematic illustration of diffraction experiment setup for diffraction grating analysis, incorporating input power monitoring and a CCD camera for sample alignment.

5.5 Results and Discussion

5.5.1 Gold Test Gratings on Silicon

To establish the performance of the diffraction set-up developed, replica diffraction gratings of solid gold lines were fabricated on silicon. This involved photolithographically patterning a 200 nm thick gold film with the 40 μm period, 10 μm linewidth diffraction grating.

The repeatability of measurement of the diffraction from a gold-line grating on silicon was measured in the same way as for the biological samples (in a sealed liquid buffer environment). The sample was removed, replaced and the diffraction pattern was measured again. The repeatability of measurement is shown in Table 5.1, next to the change in the measured diffraction intensity value, for each diffraction order ($\Delta\ I_m/I_{input}$). The calculated absolute standard error (ϵ_{abs}) is shown for comparison with the measured change.

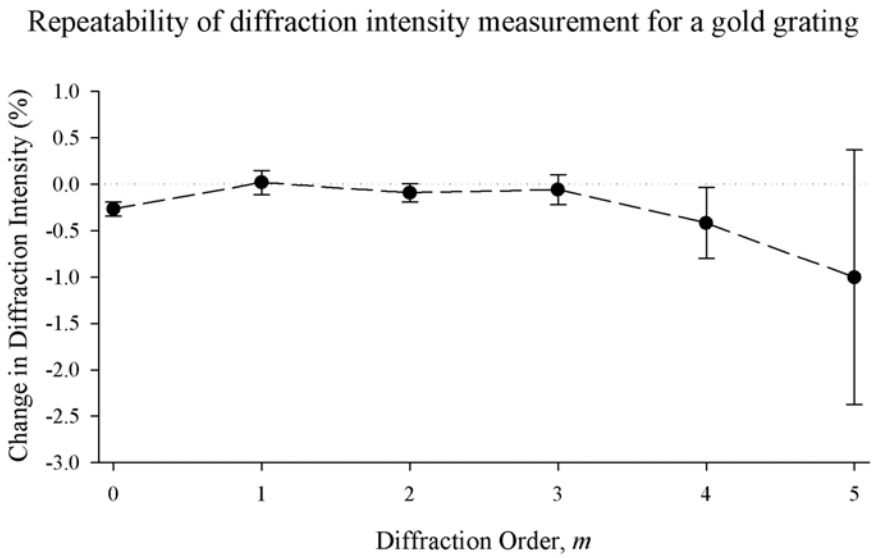

Figure 5.28: Change in diffraction intensities normalised to input laser power averaged over the scan ($\Delta\ I_m/I_{input}$) for orders $m = 0 - 5$ for a gold grating on silicon (10 μm linewidth, 40 μm period). Error bars plot the absolute standard error of each average intensity.

The uniformity of the metal gratings was indicated by the low absolute standard error (ϵ_{abs}) values calculated for each diffraction order. The standard deviation of intensity readings over a gold grating for the zeroth ($m = 0$) order was only 1.5 %. The standard deviation of readings was also low for orders $m = 1 - 3$, being 2.5 %, 1.9 % and 3.6 % respectively. The standard deviation of orders $m = 4$ and $m = 5$ were higher (at 7.7 % and 27.8 %) over the scan area due to the design of the grating.

Order	$\Delta\ I_m/I_{input}$	Abs. Error (ϵ_{abs})
$m = 0$	-0.27 %	± 0.08 %
$m = 1$	$+0.02$ %	± 0.13 %
$m = 2$	-0.09 %	± 0.10 %
$m = 3$	-0.06 %	± 0.16 %
$m = 4$	-0.42 %	± 0.38 %
$m = 5$	-1.00 %	± 1.37 %

Table 5.1: Repeatability of diffraction intensity measurements for a grating (10 μm linewidth, 40 μm period) consisting of solid Au lines photolithographically patterned on Si.

The minimum intensity of the $\text{sinc}^2\beta$ envelope function occurs at $\sin\theta = \lambda/a$, corresponding to $m = 4$ for a perfect 3 : 1 ratio of line-separation to linewidth (see Chapter 4). However, the fabricated grating had an average linewidth of 8.0 $\pm$ 0.2 μm (measured on a surface profiler, see Appendix A), shifting the position of the intensity minimum towards the $m = 5$ order. The intensity minimum was very sensitive to a change in linewidth, and consequently the intensity of the $m = 5$ diffraction order was significantly more variable from point to point than the other orders.

5.5.2 DNA Gratings on Silicon

The repeatability of measurement for a DNA grating on silicon was measured using the same methodology. A DNA-only grating was characterised for diffraction, removed and then re-tested the following day under the same conditions. The results obtained are shown in Table 5.2. The repeatability of measuring diffraction orders $m = 0 - 3$ was lower than that for the metal grating pattern, indicated by a larger change in the average intensity measurement ($\Delta\ I_m/I_{input}$) and a much larger absolute standard error (ϵ_{abs}). The standard deviation of measurements over the scan area was much larger than for the metal pattern. The standard deviation of the zeroth order was 43.5 % compared to only 1.5 % for the gold test gratings. The standard deviation of readings for $m = 1 - 5$ was 34.9 %, 86.5 %, 64.9 %, 68.1 % and 53.3 %. The large variations in diffraction intensity (for all orders) from point to point of measurement for a DNA grating on silicon originates not just from a variation in linewidth, but also step height and surface coverage of DNA. This inherent variation manifests itself in the larger absolute standard error values (ϵ_{abs}). The repeatability variation for each order

was within these error limits.

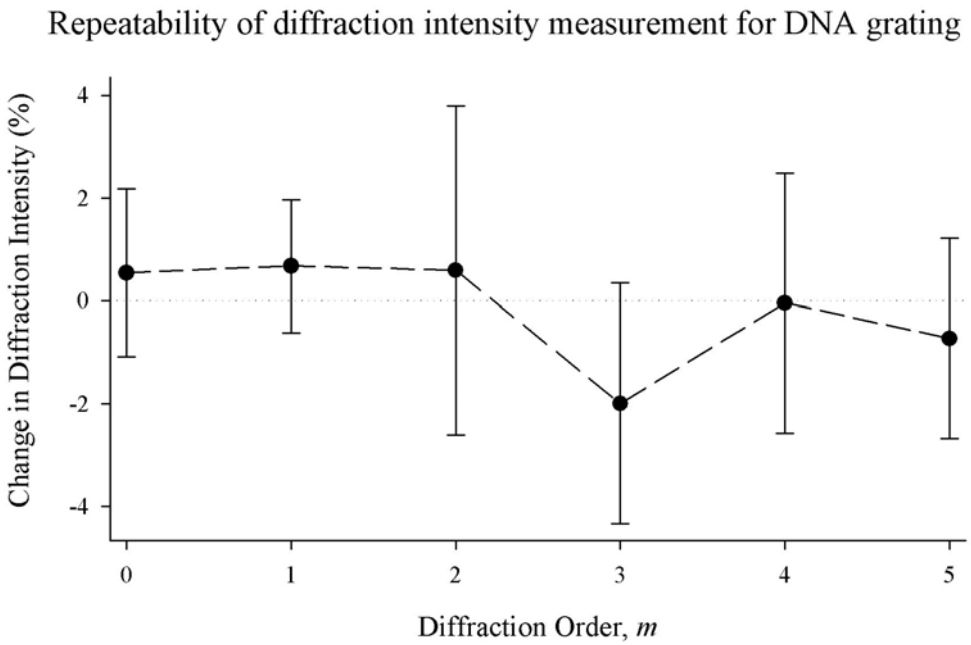

Figure 5.29: Change in diffraction intensities normalised to input laser power ($\Delta\ I_m/I_{input}$) of diffraction orders $m = 0 - 5$ for a DNA grating on silicon (10 μm linewidth, 40 μm period). Error bars plot the absolute standard error of each average intensity.

Order	$\Delta\ I_m/I_{input}$	Abs. Error (ϵ_{abs})
$m = 0$	+0.54 %	±1.63 %
$m = 1$	+0.67 %	±1.29 %
$m = 2$	+0.59 %	±3.20 %
$m = 3$	−2.00 %	±2.34 %
$m = 4$	−0.04 %	±2.53 %
$m = 5$	−0.74 %	±1.95 %

Table 5.2: Repeatability of diffraction intensity measurements for a grating consisting of DNA lines on silicon (10 μm linewidth, 40 μm period).

5.5.3 Gold versus DNA Grating Comparison

A comparison between diffraction from a typical DNA grating and a thin gold film grating with the same design (10 μm linewidth, 40 μm period) highlights the variations within a DNA grating. Although the fabrication of DNA gratings on silicon was a significant achievement, and the biological patterning achieved was remarkably uniform, it was not possible to achieve

as precise a standard of uniformity as photolithographically fabricated metal gratings (see images in Figure 5.30). It was important to establish where experimental variations came from in order to determine the limiting factors in detecting changes in diffraction.

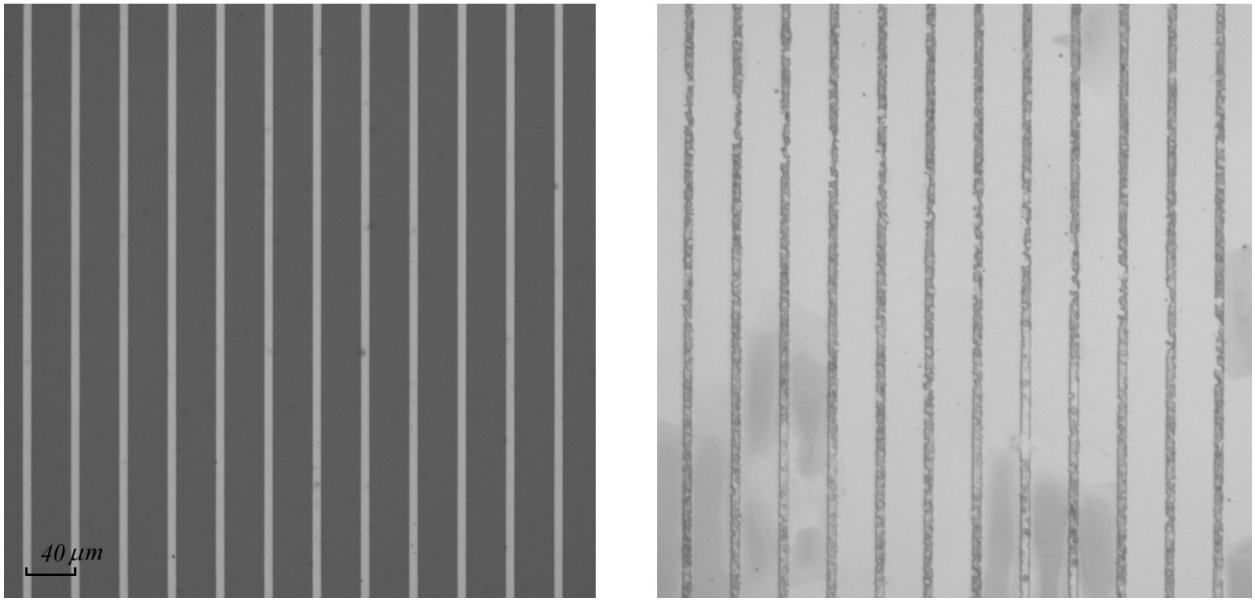

Figure 5.30: Reflection optical microscope images (10× magnification) of a gold grating on silicon (left) and DNA grating on silicon (right), both with a 10 μm linewidth and 40 μm period.

A scan matrix was used to take measurements with the laser beam incident just off the grating to give a border around the diffraction pattern. Figures 5.31 and 5.32 show the diffraction order intensities (for orders $m = 0 - 2$ and $m = 3 - 5$ respectively) plotted as a function of scan position on the grating surface. The left-hand column in each figure shows the data measured for a photolithographically fabricated gold metal grating on silicon. The right-hand column in each figure shows the data recorded for a typical DNA grating on silicon.

The zeroth diffraction order, $m = 0$, shows that the reflectivity of the gold grating was highly uniform over the grating surface (Figure 5.31). The central zone of the scan area (highlighted in yellow in Figure 5.33) corresponds to the laser beam being entirely within the grating area. For the metal grating there was not a large change in the reflected intensity as the beam moved onto the grating region. This was because although the reflectivity was increased (due to the higher reflectivity of the gold lines compared to the silicon), light was being diffracted into other orders.

In contrast, for the DNA grating, the reflectivity of the DNA covered region was lower, and the reflected intensity was observed to drop over the grating area. The uniformity of the central region (highlighted in yellow in Figure 5.33) was much lower than for the

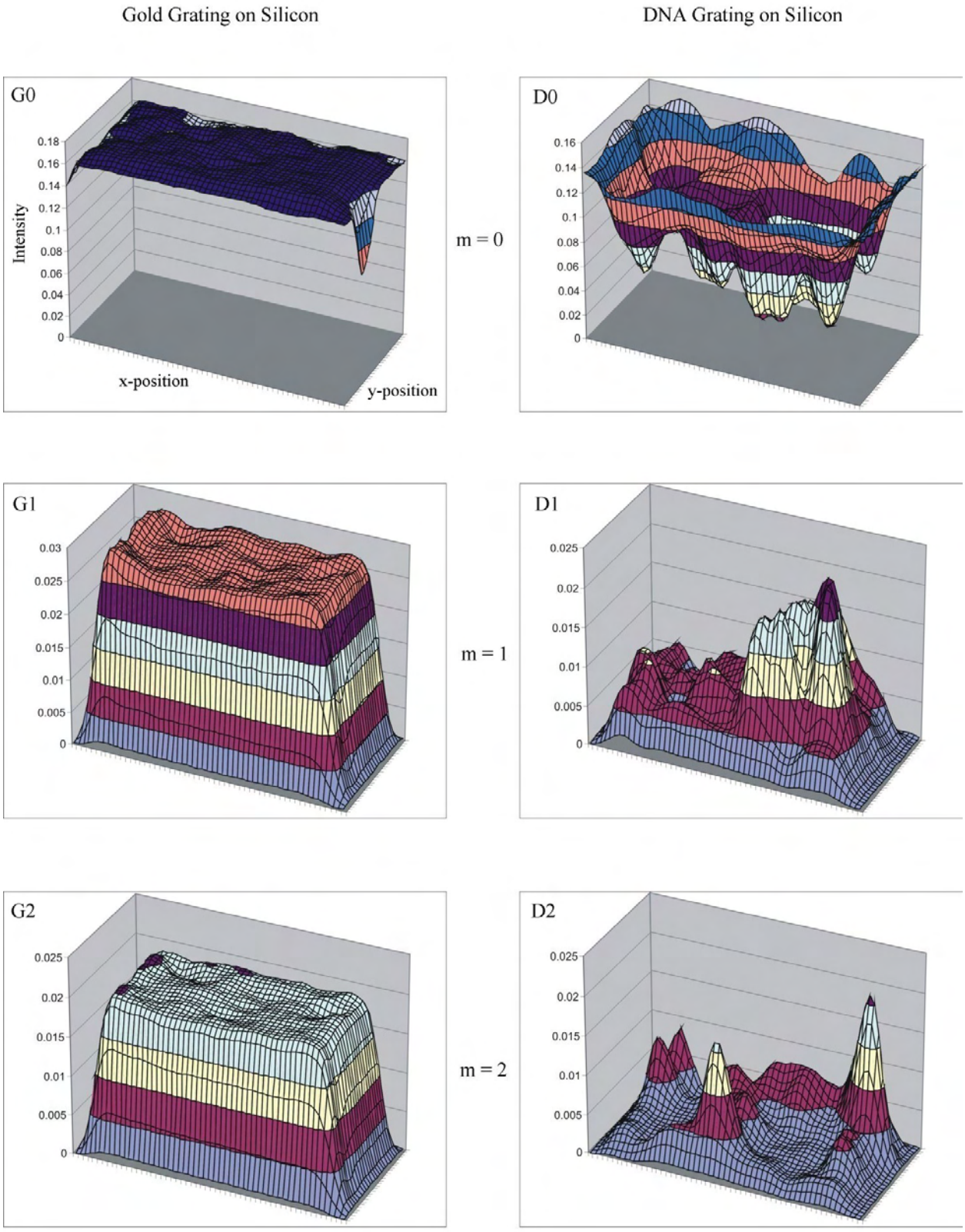

Figure 5.31: Graphs showing diffraction data (normalised to input power fluctuations) for diffraction orders $m = 0 - 2$ for solid gold line test gratings on silicon (left-hand column, G0−G2) and a DNA grating on silicon (right-hand column, D0−D2), both with a 10 μm linewidth and 40 μm period.

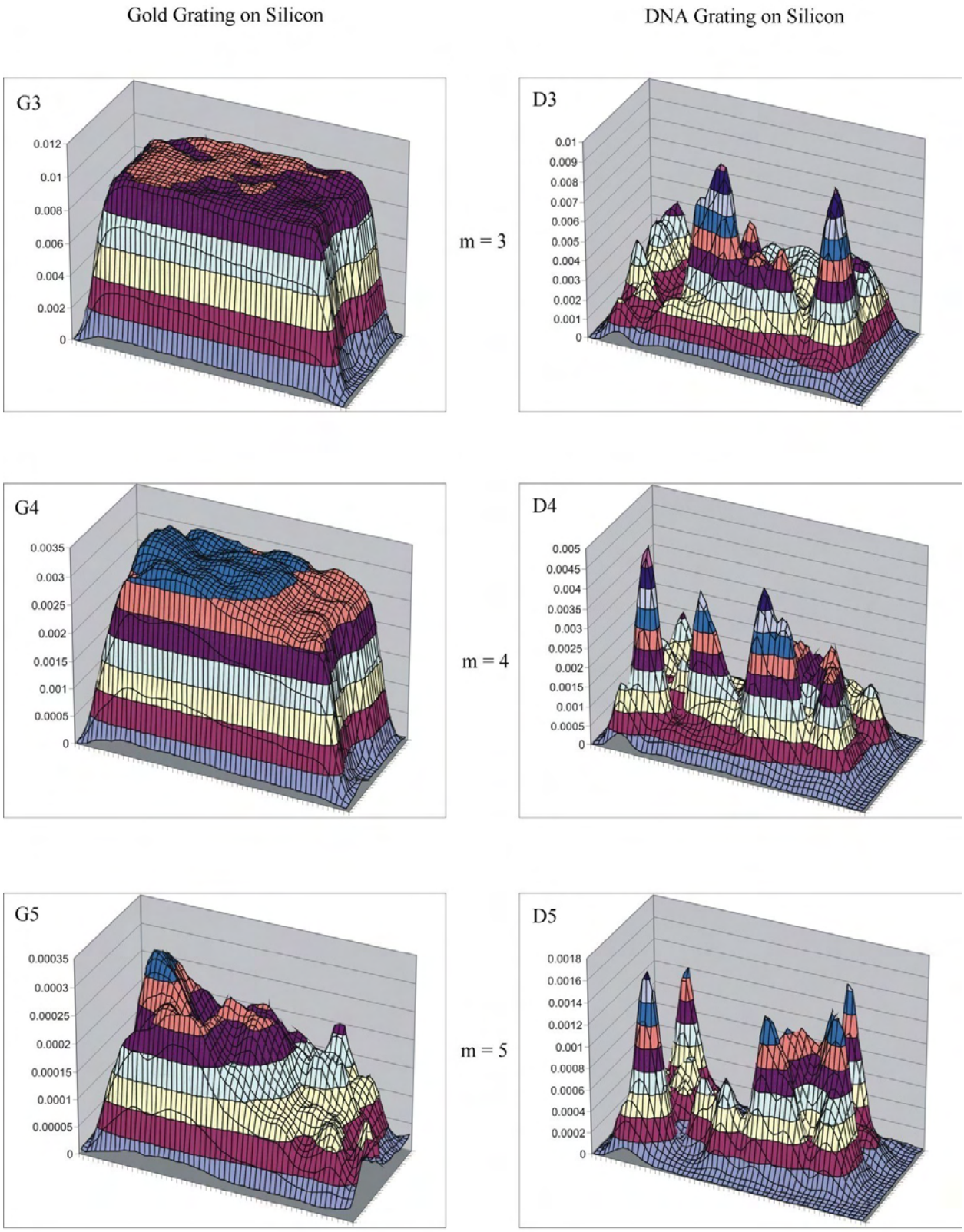

Figure 5.32: Graphs showing diffraction data (normalised to input power fluctuations) for diffraction orders $m = 3 - 5$ for solid gold line test gratings on silicon (left-hand column, G3−G5) and a DNA grating on silicon (right-hand column, D3−D5), both with a 10 μm linewidth and 40 μm period.

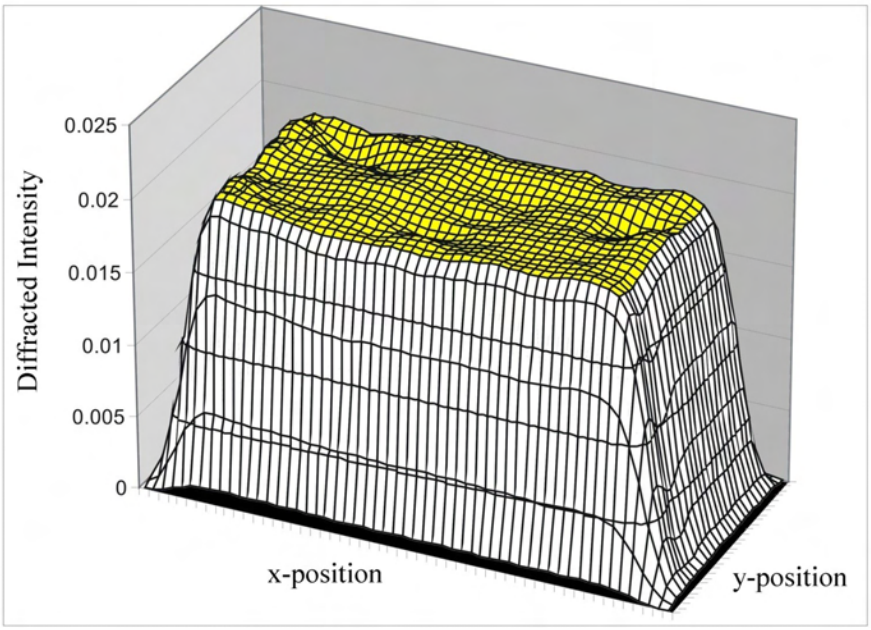

Figure 5.33: Diffraction intensity of non-zero order (e.g. $m = 2$) plotted as a function of position on the sample surface. The central zone (high-lighted in yellow) corresponds to the laser beam being wholly on the grating. The diffracted intensity drops to zero at the outer limits of the scan area as the laser beam moved off the edge of the grating.

lithographically patterned gold gratings. Regions within the grating area showing the largest drop in reflected intensity corresponded to higher surface area coverage of DNA and/or more diffraction of light into higher orders.

Order	Au on Si			DNA on Si		
	I_m/I_{input}	σ_{frac}	ϵ_{abs}	I_m/I_{input}	σ_{frac}	ϵ_{abs}
$m = 0$	16.6853 %	1.51 %	±0.0088 %	7.7470 %	29.67 %	±0.0803 %
$m = 1$	2.7355 %	2.49 %	±0.0024 %	0.9493 %	52.50 %	±0.0174 %
$m = 2$	1.9399 %	1.87 %	±0.0013 %	0.4216 %	54.45 %	±0.0080 %
$m = 3$	0.9911 %	3.55 %	±0.0012 %	0.2917 %	51.50 %	±0.0052 %
$m = 4$	0.3022 %	7.66 %	±0.0008 %	0.1411 %	57.25 %	±0.0028 %
$m = 5$	0.0202 %	27.85 %	±0.0002 %	0.0470 %	72.16 %	±0.0012 %

Table 5.3: Repeatability of diffraction intensity measurements for a grating consisting of 10 μm DNA lines on silicon with a 40 μm period.

The diffraction data was averaged over the central region of the scan for the comparison of a DNA grating with a gold-line grating on silicon. Figure 5.34 shows the diffraction intensities of orders $m = 0 - 5$ for each grating, with error bars given by the absolute standard error of the scan data for each measurement. The intensity data is shown in Table 5.3 together

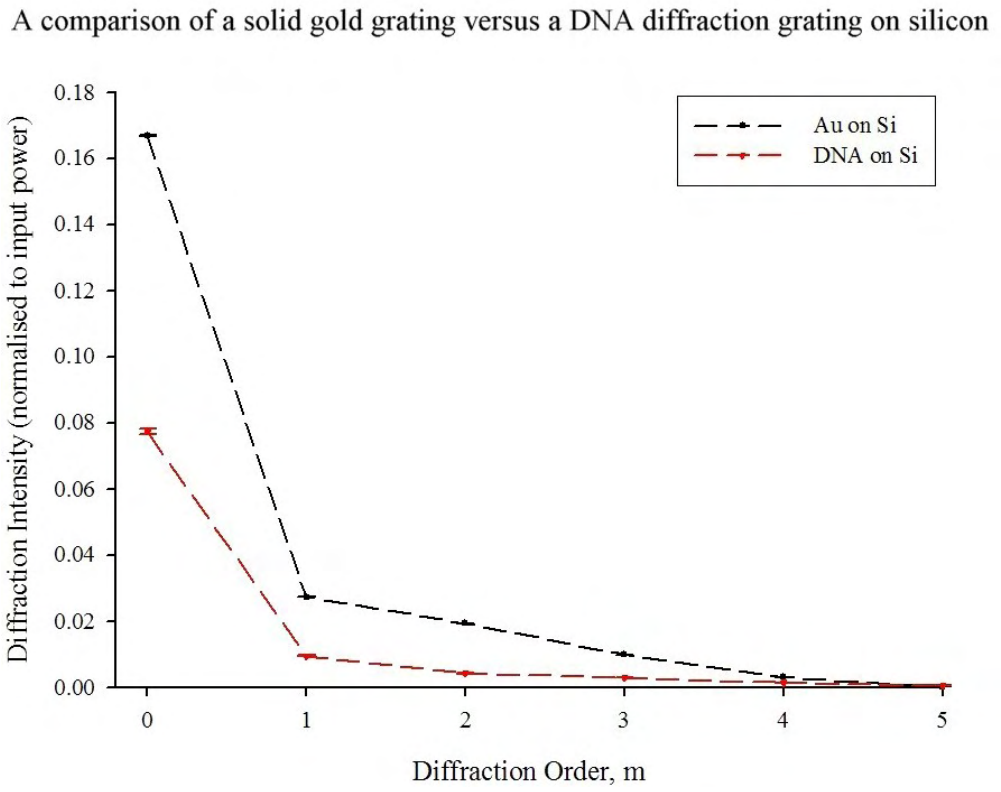

Figure 5.34: Averaged intensities (normalised to input laser power) of diffraction orders $m = 0 - 5$ for a gold grating on silicon and a DNA grating on silicon (both with a 10 μm linewidth and 40 μm period).

with the fractional standard deviation of readings in a scan and the absolute standard error in the averaged intensity values calculated for the error bars. The diffraction intensities for the DNA grating were at least 50 % lower than those measured for the photolithographically prepared gold grating for orders $m = 0 - 4$. The exception was the intensity of the $m = 5$ diffraction order, where the intensity was 133 % higher than for the metal grating. This originated from the very low intensity of the 5^{th} order of the fabricated grating, which had an average linewidth of 8.0 $\pm$ 0.2 μm causing the position of the intensity minimum to be around the $m = 5$ order.

The repeatability of a diffraction experiment for a metal grating pattern was found to be within $\pm$ 0.50 % for diffraction orders $m = 0 - 4$, with the repeatability error (the observed difference in measurements, $\Delta\ I_m/I_{input}$) being approximately the same as the absolute standard error (ϵ_{abs}) calculated from the standard deviation of readings (see Table 5.1). The repeatability of diffraction measurements for a DNA grating was found to be within $\pm$ 2.0 % for all measured diffraction orders, which was slightly below the calculated absolute standard error values, ϵ_{abs} (see Table 5.2). Following on from these and numerous other similar experimental results it was concluded that ϵ_{abs} was a good measure of the repeatability of a diffraction measurement.

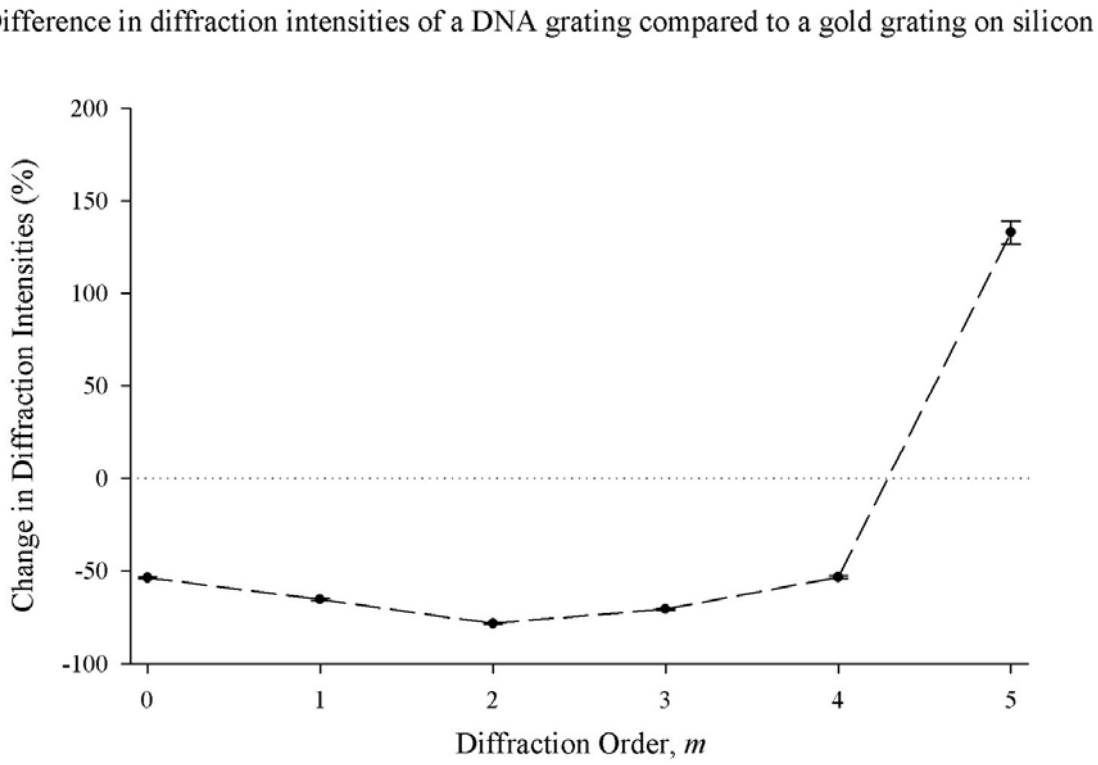

Figure 5.35: Change in diffraction intensities normalised to input laser power ($\Delta\ I_m/I_{input}$) of diffraction orders $m = 0 - 5$ for a DNA grating compared to a gold-line grating on silicon, both with a 10 μm linewidth and 40 μm period. Error bars plot the absolute standard error of each average intensity.

Aside from the difference in diffraction intensities, recorded between a gold grating and a DNA grating on silicon substrates, there was an instantly observable visible difference. When aligning the 'diffraction detector', the difference in diffraction patterns was visible on a screen (such as a piece of white card). The diffraction pattern produced by the lithographically patterned grating featured much 'sharper' diffraction orders, with light being confined over smaller spatial regions. The diffraction patterns measured also better matched the theoretical diffraction patterns predicted from the mathematical modelling. The DNA grating diffraction orders were less well spatially confined and more scattering was evident. The metal grating diffraction pattern observed was much more consistent under translation of the sample. When the DNA samples were translated the appearance of the diffraction orders could diminish significantly with a lot of scattering being evident at certain points of the grating. Figure 5.36 shows example images of the diffraction patterns produced when illuminated with a red HeNe laser, imaged on a screen and captured with a digital camera. The image of the DNA grating diffraction shows that the diffraction pattern can approach the quality of the metal grating, with neat well-defined diffraction orders visible.

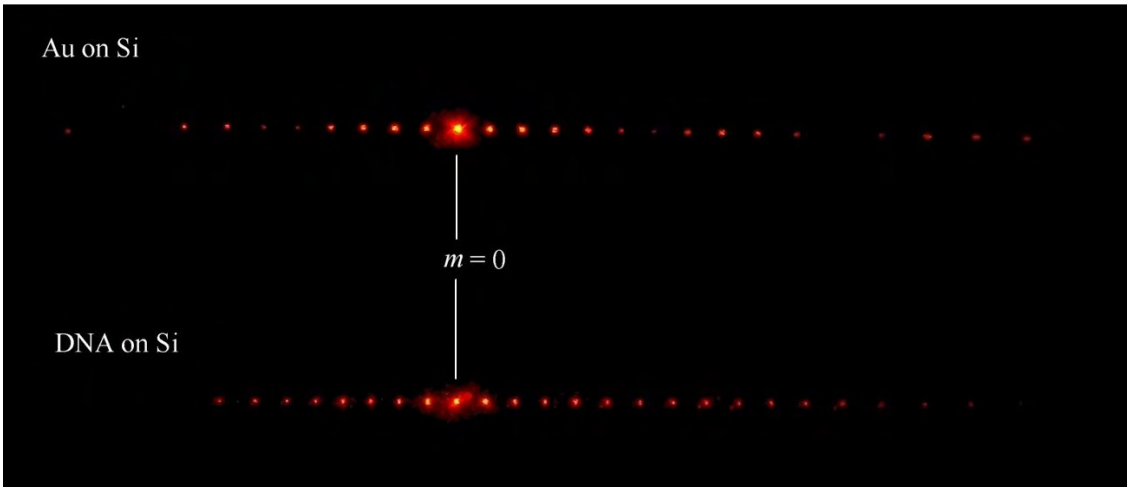

Figure 5.36: Diffraction pattern images captured by imaging the diffraction pattern on a screen and taking a photograph on a digital camera, both gold and DNA gratings feature a 10 μm linewidth and 40 μm period.

5.6 DNA Gratings with Gold Nanoparticles

Following on from the earlier trials of hybridising DNA-functionalised gold nanoparticles to DNA diffraction gratings with the original 20 μm period, gold colloids were added to the new-design 40 μm period gratings. Samples were characterised to measure the inherent diffraction intensities and were then tested again after hybridisation with 1.4 nm and/or 10 nm diameter gold nanoparticles. The changes measured for various samples are examined and discussed individually in this section.

An example of a DNA grating on silicon (featuring a 10 μm linewidth and 40 μm period), referred to as 'sample A', showed a significant change in diffraction upon hybridisation with 10 nm diameter gold colloids, averaged over a scan containing 100 data points. Diffraction orders $m = 0, 1$, and 2 only showed a small, but positive change of the order of the absolute standard error of readings (see Figure 5.37). Greater changes were measured for higher diffraction orders; $\Delta\ I_{m=3}/I_{input} = +\ 9.1\ \pm\ 5.2\ \%$; $\Delta\ I_{m=4}/I_{input} = +\ 29.5\ \pm\ 8.8\ \%$; $\Delta\ I_{m=5}/I_{input} = +\ 23.3\ \pm\ 6.3\ \%$.

An assessment of the amount of gold that hybridised to the grating was achieved by Dr H Yin by dehybridising the gold particles in a small volume of water at $90°C$ and using inductively coupled plasma-mass spectroscopy (ICP-MS) analysis (as described earlier in Section 4.4, page 113). The density of 10 nm diameter gold particle binding was quantified as $6.4 \times\ 10^9$ particles/cm^2, or 64 particles per square micron. The increase in intensity of diffraction orders $m = 4$ and 5 was significant, primarily because these orders are the most sensitive

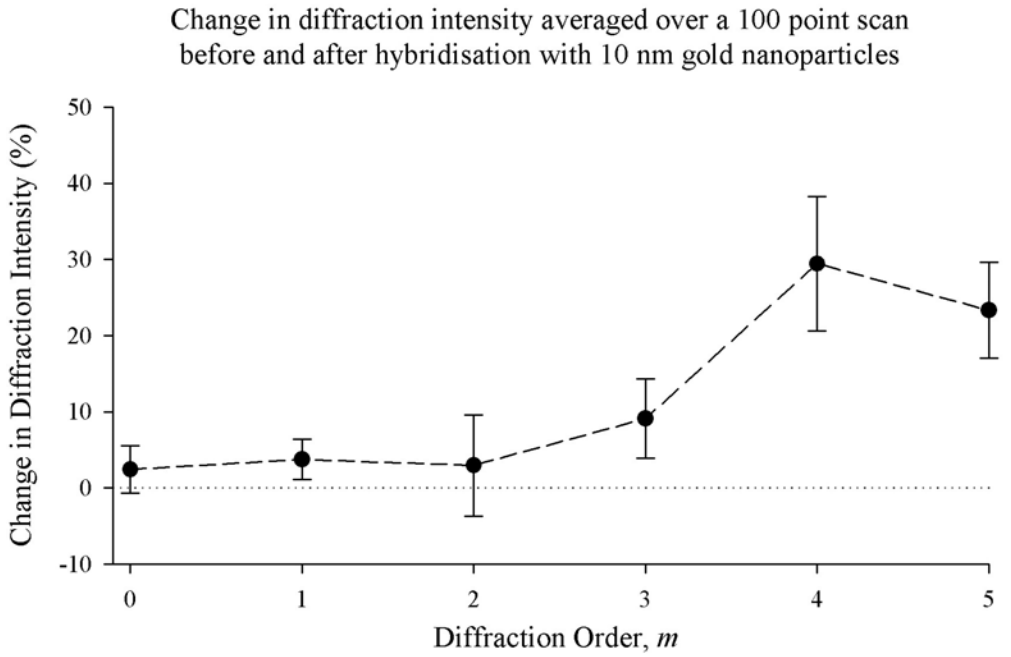

Figure 5.37: Change in diffraction intensities normalised to the input laser power ($\Delta\ I_m/I_{input}$) of diffraction orders $m = 0-5$ for DNA grating 'sample A' following hybridisation of 10 nm diameter gold nanoparticles. Error bars plot the absolute standard error of each average intensity.

to variations of the grating from the 'ideal' structure. Analysis of a fluorescent microscope image of sample A showed that the DNA was concentrated at the edge of the grating lines (see Figure 5.38), which had an average linewidth of 13.4 μm with a standard deviation of 5.1 μm or 38.2 % . The reason for this two-line structure originated from the use of a spacer (125 μm) between the mask and substrate during fabrication using laser illumination, giving a near field diffraction pattern producing lines which appear out of focus. Since the grating period was 40 μm, the 4^{th} order lay at the point where light was diffracted from 10 μm periods, and the 5^{th} order lay at the point where light would be diffracted from 8 μm periods. It is therefore probable that the increase in intensity of the 4^{th} and 5^{th} orders was due to particles hybridising mainly along the edge of grating lines.

Whilst this sample showed a substantial change in diffraction, the absolute standard errors were quite high as the sample was only averaged over 100 data points. The repeatability of measurement was approximately $\pm$ 5 % for each order when the sample was removed, replaced and measurements repeated. In other samples measured in the same way, changes were not significantly larger than the measurement errors.

Figure 5.39 shows atomic force microscope (AFM) images of sample A, which reveals that some of the dark regions in the centre of the lines showing no fluorescence in Figure 5.38 correspond to regions which appear to have been slightly etched in processing (by up to 1.9 μm).

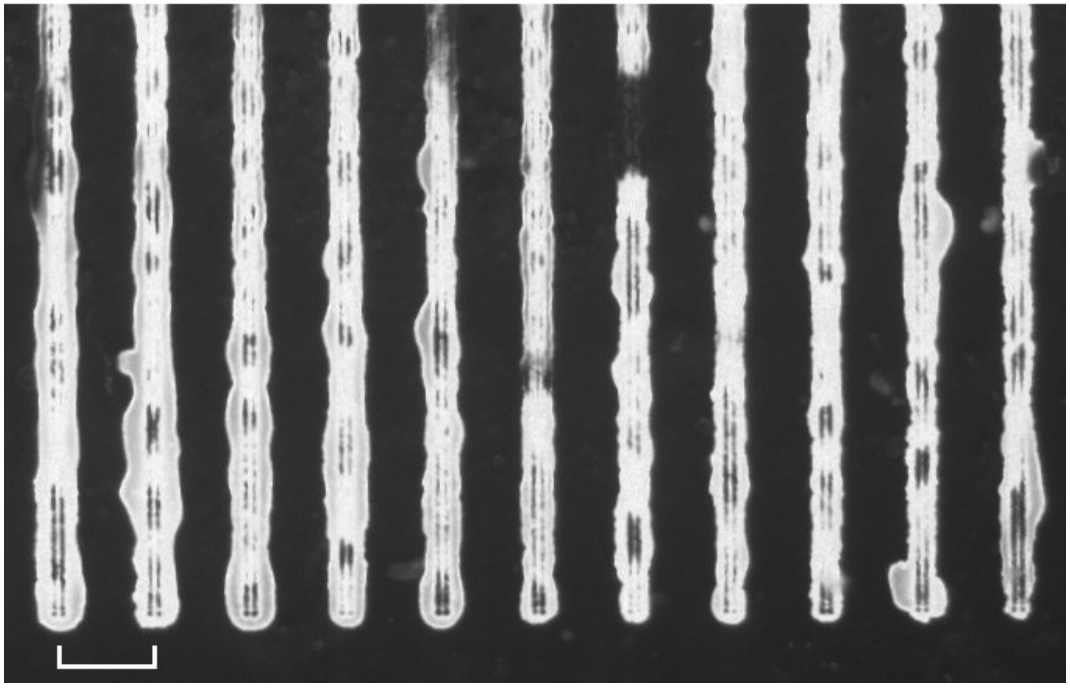

Figure 5.38: Fluorescence image of sample A hybridised with fluorescein-labelled complementary DNA (the scale bar is 40 μm).

Areas such as this greatly influence the diffraction intensity at a point of measurement and make repeatability of alignment difficult.

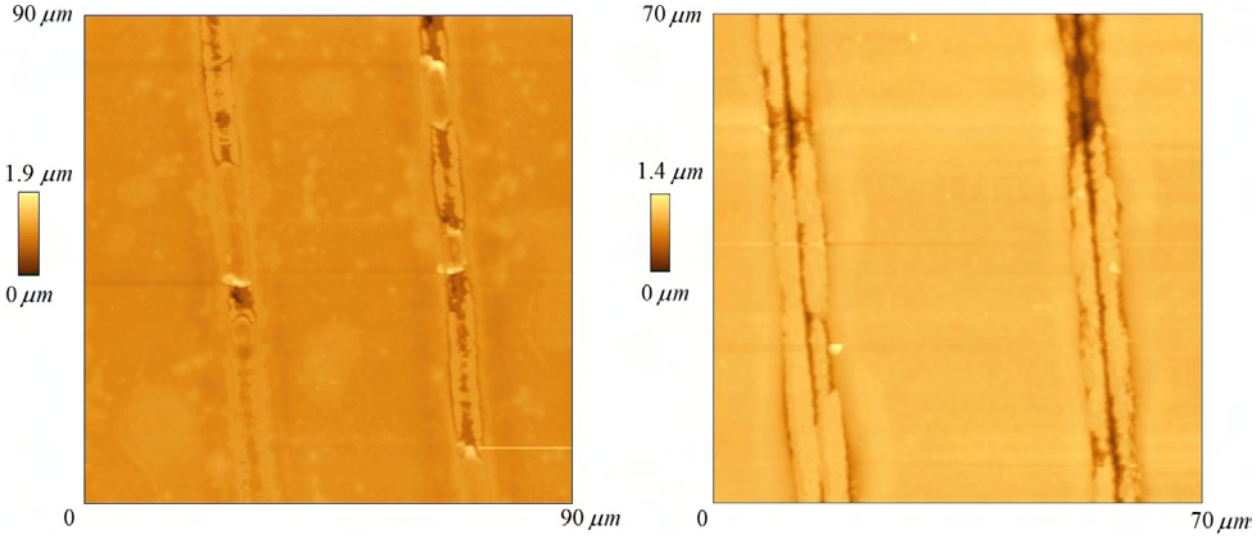

Figure 5.39: AFM images of sample A DNA grating on Silicon.

Along with the experimental improvements detailed earlier (see Section 5.4) to reduce the errors in characterisation, the number of data points was increased from 100 to over 1400 for subsequent samples. The fabrication technique of samples had used a KrF excimer laser (248 nm) to provide UV illumination of the silicon. This was changed to a UV lamp to

reduce surface damage (which appeared to be a consequence of the laser illumination), and to improve patterning uniformity.

Another grating, sample B, was characterised for diffraction after fabrication, using a scan consisting of 1404 data points, and was then measured again after hybridising 1.4 nm diameter gold colloids tagged with a complementary DNA sequence to that immobilised on the silicon substrate. A comparison of the diffraction intensities, measured for each diffraction order, before and after the addition of gold, is shown in Figures 5.40, 5.41 and 5.42. The left-hand column of each figure shows the diffraction intensities measured for the DNA grating during a scan over the sample surface, plotted as a function of position. The central column shows the measurements made after hybridisation with 1.4 nm gold. The right-hand column shows the change in diffraction with position on a point-by-point comparison.

For diffraction orders $m = 0, 1, 2, 4$ and 5, it can be seen that over the majority of the surface the ratio of diffraction intensity measured after the addition of gold colloids divided by the value before, is close to 1.0, indicating no change in diffraction. For the third order ($m = 3$) however, there was a change in the diffraction intensity measured over the majority of the surface with an average increase of 125.3 % when compared before and after the addition of gold on a point-by-point basis. When a smaller region within the scan was examined (5×10 points around the largest peak for $m = 3$ in Figure 5.41), the change in diffraction was over four times higher (+ 334.33 $\pm$ 2.47 %) than the original levels for the $m = 3$ order averaged over the 50-points. The diffraction intensity changes (and errors), of all the orders measured, are shown in Table 5.4.

Order	Averaged over scan (1404 points)		Averaged over peak (50 points)	
	$\Delta I_m/I_{input}$	ϵ_{abs}	$\Delta I_m/I_{input}$	ϵ_{abs}
$m = 0$	− 3.392 %	±0.018 %	− 11.318 %	±0.359 %
$m = 1$	− 7.536 %	±0.010 %	+ 10.929 %	±0.969 %
$m = 2$	− 10.332 %	±0.013 %	+ 26.076 %	±1.267 %
$m = 3$	+125.265 %	±0.046 %	+334.333 %	±2.470 %
$m = 4$	− 19.359 %	±0.009 %	− 3.811 %	±0.548 %
$m = 5$	− 16.369 %	±0.013 %	− 1.304 %	±0.899 %

Table 5.4: The change in diffraction order intensities after hybridisation with 1.4 nm diameter gold colloids compared on a point-by-point basis and then averaged over the whole scan area (central column) and region of peak change (right-hand column).

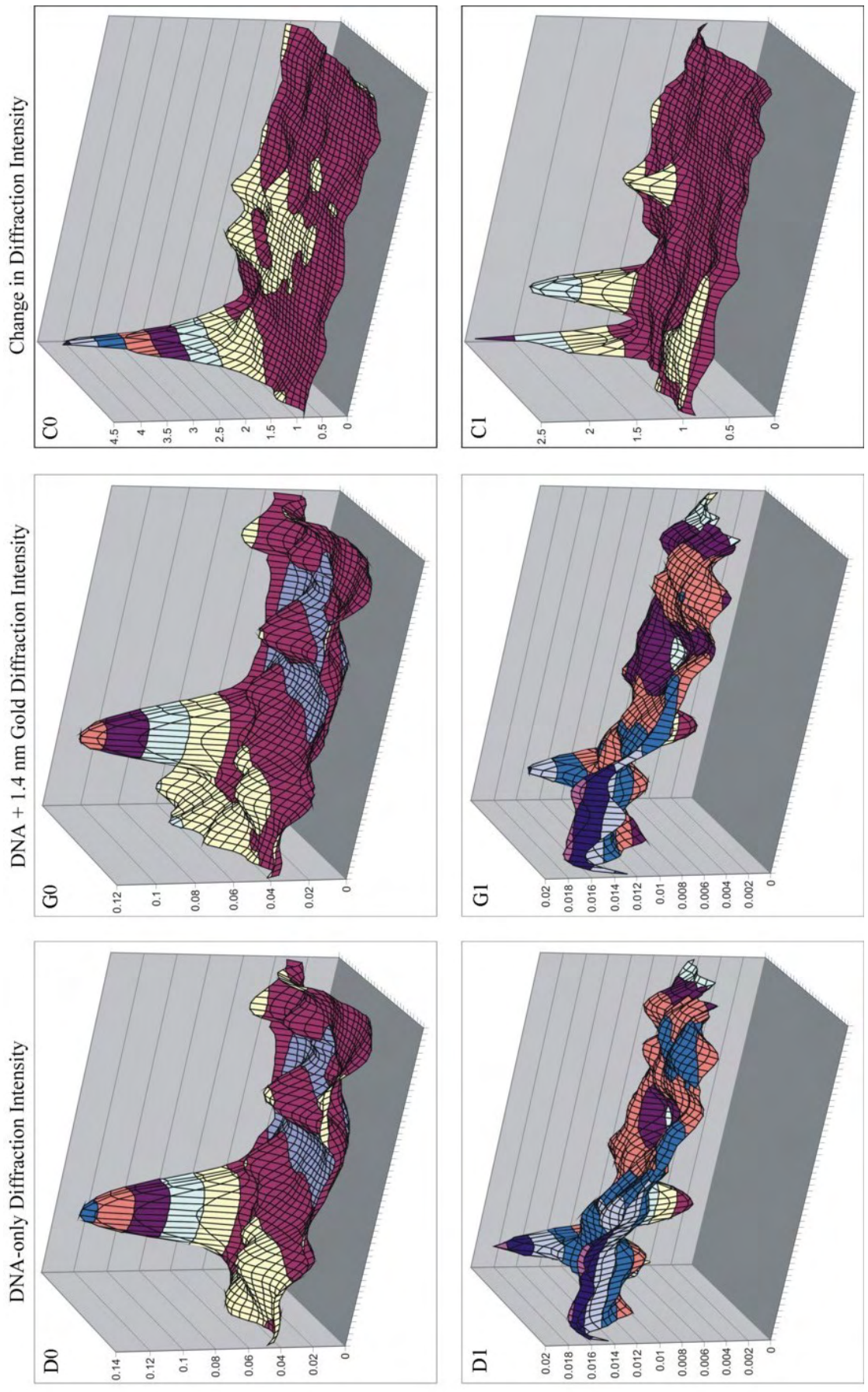

Figure 5.40: Diffraction intensity plots as a function of scan position. Left-hand column: Characterised diffraction intensity measured for the DNA grating on silicon with a 10 μm linewidth and 40 μm period (D0 for $m = 0$, D1 for $m = 1$). Centre: Diffraction intensity when hybridised with 1.4 nm gold nanoparticles (G0 for $m = 0$, G1 for $m = 1$). Right-hand column: Change in diffraction with position on a point-by-point comparison (C0 for $m = 0$, C1 for $m = 1$).

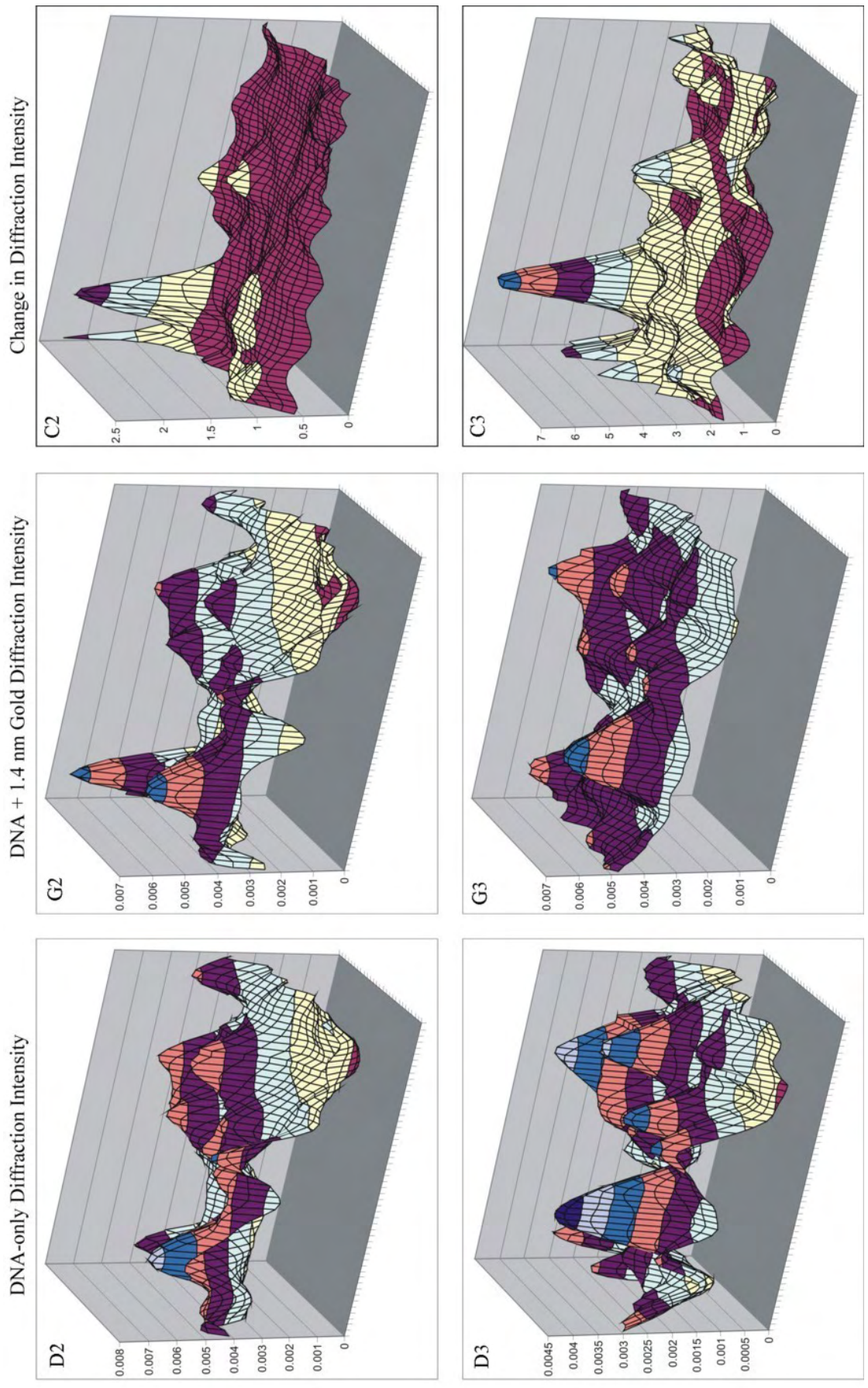

Figure 5.41: Diffraction intensity plots as a function of scan position. Left-hand column: Characterised diffraction intensity measured for the DNA grating (D2 for $m = 2$, D3 for $m = 3$). Centre: Diffraction intensity when hybridised with 1.4 nm gold nanoparticles (G2 for $m = 2$, G3 for $m = 3$). Right-hand column: Change in diffraction with position on a point-by-point comparison (C2 for $m = 2$, C3 for $m = 3$).

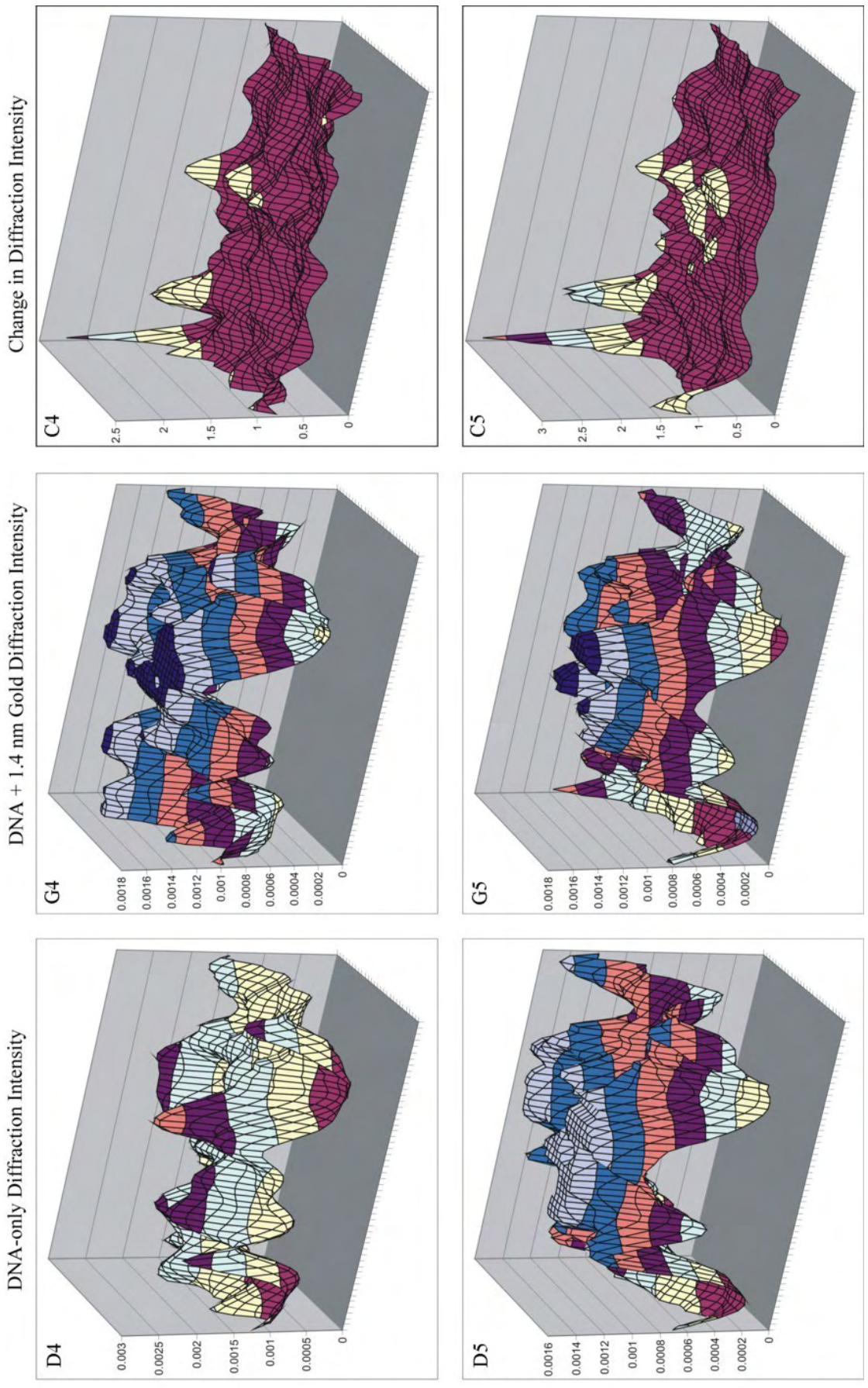

Figure 5.42: Diffraction intensity plots as a function of scan position. Left-hand column: Characterised diffraction intensity measured for the DNA grating (D4 for $m = 4$, D5 for $m = 5$). Centre: Diffraction intensity when hybridised with 1.4 nm gold nanoparticles (G4 for $m = 4$, G5 for $m = 5$). Right-hand column: Change in diffraction with position on a point-by-point comparison (C4 for $m = 4$, C5 for $m = 5$).

Even when the diffraction intensities were averaged over the whole surface and then compared, there was an average increase of 108.79 $\pm$ 1.98 % for the third order. The diffraction intensity was more than double what it had been prior to gold particle hybridisation. The changes measured for diffraction orders $m = 0 - 5$ are shown in Table 5.5 and displayed in Figure 5.43.

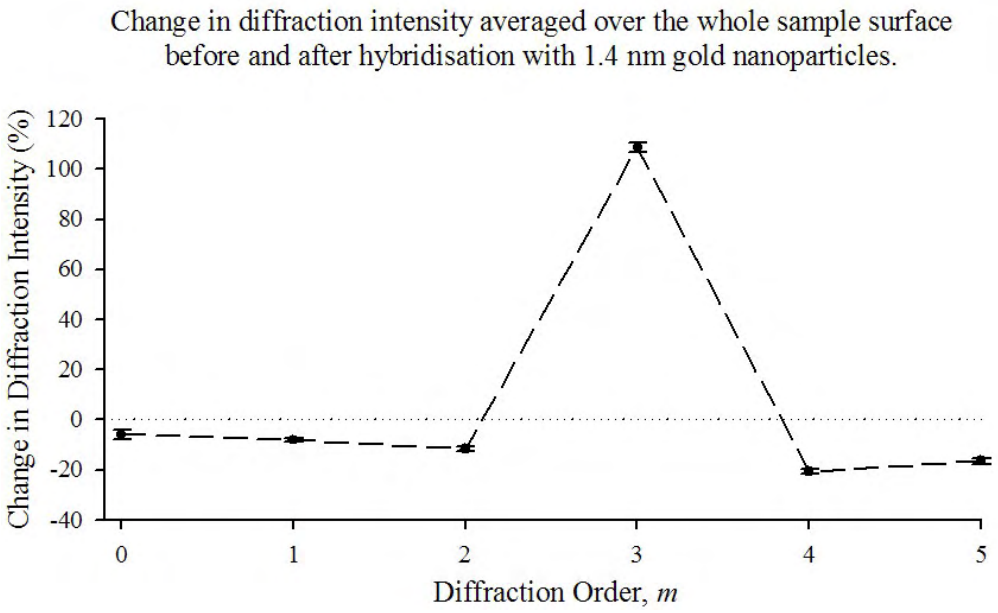

Figure 5.43: Change in diffraction intensities normalised to the input laser power ($\Delta\ I_m/I_{input}$) of diffraction orders $m = 0 - 5$ for DNA grating on silicon with a 10 μm linewidth and 40 μm period (sample B) following hybridisation of 1.4 nm diameter gold nanoparticles. Error bars plot the absolute standard error of each average intensity.

Order	$\Delta\ I_m/I_{input}$	Abs. Error (ϵ_{abs})
$m = 0$	$-$ 5.86 %	$\pm$1.86 %
$m = 1$	$-$ 8.13 %	$\pm$0.84 %
$m = 2$	$-$ 11.75 %	$\pm$1.02 %
$m = 3$	+108.79 %	$\pm$1.98 %
$m = 4$	$-$ 20.69 %	$\pm$0.85 %
$m = 5$	$-$ 16.46 %	$\pm$1.20 %

Table 5.5: Change in diffraction intensity measurements for a grating consisting of 10 μm DNA lines on silicon (with a 40 μm period) when hybridised with 1.4 nm diameter Au nanoparticles. The data was averaged before and after addition of gold nanoparticles, and then compared.

Averaged over the whole sample, the diffraction intensities were lower for diffraction orders $m = 0, 1, 2, 4$ and 5, whilst more light was diffracted in to the third order, $m = 3$, with 1.4 nm diameter gold particles hybridised to the DNA grating. This result was different to that expected from theory, where an increase in the reflectivity of the DNA lines due to the

presence of gold particles should increase the diffraction intensity of each order. The fact that only the $m = 3$ order showed a very large increase implied that the addition of gold added additional complexity to the grating structure; such as the gold particles hybridising along the edges of the DNA lines rather than being uniformly distributed over the area of a grating line. Assessment of the amount of gold that hybridised to the grating (as described earlier, page 113), showed that the binding density was 4.40×10^{11} particles/cm^2 for this particular sample (with the highest density measured being 2.15×10^{12} particles/cm^2 for another sample).

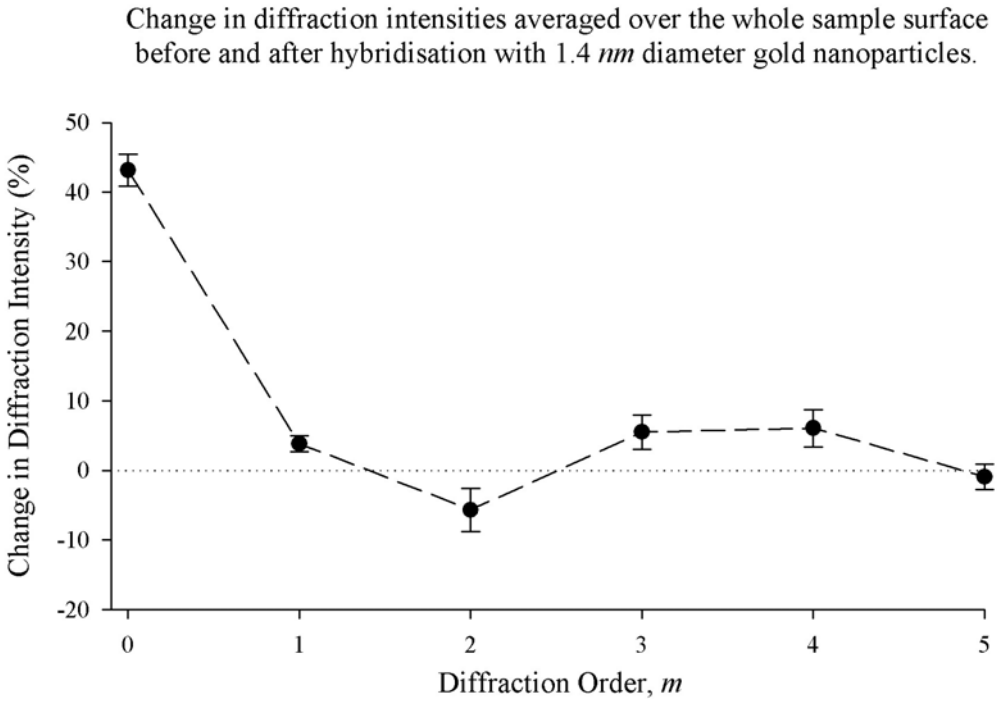

Figure 5.44: Change in diffraction intensities normalised to the input laser power ($\Delta\ I_m/I_{input}$) of diffraction orders $m = 0-5$ for DNA grating 'sample C', following hybridisation of 1.4 nm diameter gold nanoparticles. Error bars plot the absolute standard error of each average intensity.

Another DNA grating, sample C (still featuring a 10 μm linewidth and 40 μm period), was averaged over a 1458 data points scan and hybridised with 1.4 nm diameter gold colloids. In this case, the intensity of the zeroth order ($m = 0$) was observed to increase by $+43.11 \pm 2.30$ %. The diffraction orders $m = 1 - 4$ showed smaller changes of ≈ 5 % – around double the standard errors (see Table 5.6 and Figure 5.44).

The amount of gold hybridised to the grating was quantified at 1.49×10^{11} cm^{-2}, corresponding to a surface coverage of $\rho = 0.23$ %. Using the model developed in Chapter 4 the theoretical diffraction order intensities could be calculated. The predicted change in diffraction for such coverage was less than the measurement errors achievable in practice, and a factor of 123 times less than the experimental change measured for the zeroth order.

Order	$\Delta\ I_m/I_{input}$	Abs. Error (ϵ_{abs})
$m = 0$	+43.11 %	±2.30 %
$m = 1$	+ 3.83 %	±1.13 %
$m = 2$	− 5.67 %	±3.11 %
$m = 3$	+ 5.52 %	±2.49 %
$m = 4$	+ 6.08 %	±2.68 %
$m = 5$	− 0.91 %	±1.87 %

Table 5.6: Change in diffraction intensity measurements for a grating consisting of DNA lines on silicon (sample C) when hybridised with 1.4 nm diameter Au nanoparticles. The data was averaged before and after addition of gold nanoparticles, and then compared.

The predicted results were closer for the non-zero orders, as can be seen in Table 5.7.

Order	$\Delta\ I_m/I_{input}$		Factor of
	Predicted for $\rho = 0.23$ %	Measured	Difference
$m = 0$	+0.35 %	+43.11 %	123.4
$m = 1$	+0.89 %	+ 3.83 %	4.3
$m = 2$	+0.87 %	− 5.67 %	6.5
$m = 3$	+0.85 %	+ 5.52 %	6.5
$m = 4$	+0.31 %	+ 6.08 %	19.8
$m = 5$	+0.91 %	− 0.91 %	1.0

Table 5.7: The change in diffraction predicted for a DNA grating with $\rho = 0.23$ % (1.49×10^{11} particles $/cm^2$ of 1.4 nm diameter) compared to the measured change in diffraction. The factor of increase of the magnitude of the actual diffraction intensity changes measured over the predicted level is shown in the right-hand column.

5.7 Conclusions

A diffraction apparatus was successfully established for accurate characterisation of diffraction order intensities. Excellent performance of the system was demonstrated for non-biological model structures fabricated from gold on silicon.

The accuracy of the optical intensity measurement of the system was ±0.034 %. When testing diffraction samples the effects of line width, step height and reflectivity variations caused the intensity measured to vary from point to point within the grating. Consequently, the accuracy of the diffraction intensity characterisation was calculated from the standard deviation and the number of readings. For the case of evaporated gold lines on silicon, the accuracy of measurement was found to be within ±0.1 % for diffraction orders $m = 0 - 2$ and less than ±1 % for orders $m = 3 - 5$.

The standard deviation of the intensity values over the surface was found to be in very close agreement with the repeatability of measurement error. For the case of evaporated gold lines on silicon, the accuracy of repeatability was found to be within ±0.5 %, for all but the 5^{th} order (±1.4 %). The variability of the sample limits the accuracy of the repeatability of the diffraction characterisation.

The fabrication of one-dimensional DNA diffraction gratings on silicon was achieved. An optical characterisation methodology was developed and automated to measure diffraction accurately from DNA gratings. Changes in the diffraction intensity of up to +108.79 ± 1.98 %, averaged over the entire grating surface, were observed upon hybridisation of 1.4 nm diameter gold nanoparticles to the DNA gratings. Due to the biological nature of the DNA gratings on silicon the changes in diffraction observed were both very different from point to point within the grating and between different samples. The inherent surface variations associated with the biological gratings limited the minimum change in diffraction that could be detected.

Whilst the DNA patterning of silicon is a major achievement and the patterns achieved are very neat and uniform for biomolecule attachment [16], the relatively high background reflectivity from the silicon substrate required an extremely high uniformity from the DNA patterning. The strong existing diffraction levels generated from a DNA-only grating meant that the signal increase associated with hybridised gold nanoparticles can be drowned-out by background variations.

Comparison between the changes in diffraction measured and the theoretical changes predicted are difficult due to the variations in linewidth, DNA coverage and step height or surface damage over the grating. Further complications probably arose from the non-uniform distribution of hybridised gold particles on the grating, causing some regions to have much larger changes in diffraction than others, altering the grating line structure differently at different locations.

Despite the lack of a definite trend between samples of which diffraction orders changed in intensity upon hybridisation of gold nanoparticles, or by how large a change was observed, many samples did show substantial changes greater than the absolute standard error of measurements.

In order to improve the performance of the silicon diffraction sensor, there are several avenues of exploration. Further development of the biological procedures for attaching the DNA to the silicon substrate may lead to improved uniformity of attachment and result in a smoother surface. The combination of these improvements would generate a more uniform grating structure. Better surface coverage would also generate more sites for successful hybridisation of complementary DNA labelled gold nanoparticles and increase the change in diffraction intensities. An alternative measurement system could be developed in which the gold nanoparticles are hybridised in-situ. Without removing and replacing the sample, the diffraction from the area illuminated by the laser beam could be studied for a change in diffraction intensities monitored in real-time (using one photo-detector per order) without the need to realign the sample.

Chapter 6

Two-Dimensional Diffractive Structures

The one dimensional DNA diffraction grating system developed in Chapter 5, provides the potential to detect the presence of one DNA sequence variation per grating. If the gratings were fabricated with different DNA sequences on different lines of the grating, it would not be possible to detect which lines captured complementary DNA-gold nanoparticle probes, and which ones did not, from the diffraction pattern alone. In order to establish the presence of several DNA sequences simultaneously, two-dimensional patterns would be more suitable as distinguishable diffraction patterns are yielded if different motifs of different DNA sequences are used. This would obviously depend upon which features are contributing to the diffraction pattern. A two-dimensional array of different DNA patches would thus enable multiplexing of sequence detection. This is beneficial for several reasons:

- To increase the speed of DNA sample analysis
- To reduce the quantity of DNA required for each sequence (since multiple lines are required for a grating but not for $2-$D patterns, and less area is required)
- To produce visible diffraction pattern changes that indicate which sequences are present
- To incorporate reference test patches to verify correct hybridisation conditions

This chapter covers the principles of two-dimensional diffraction theory, surface pattern design and theoretical diffraction pattern prediction. The optical apparatus used in the experiments is described, along with the evaluation of diffraction images captured from test patterns produced on photolithographic mask plates, replicated with gold on silicon,

and DNA on silicon. The captured diffraction patterns from DNA arrays on silicon are tested with hybridised gold nanoparticles, and tested again following the silver enhancement procedures described in Chapter 3. The results are then analysed and discussed.

6.1 Two-Dimensional Diffraction Principles

The basic principles of diffraction were outlined earlier in Chapter 4, with particular attention focused on 1−D diffraction gratings consisting of regular periodic structures. A more general consideration of electromagnetic wave diffraction from arrays of arbitrary apertures may be used to derive the Kirchhoff diffraction integral by making the simplifying assumptions that the apertures are the only regions contributing to the amplitude at the observation point, and that edge effects and reflections from the apertures are zero. The diffraction pattern observed depends upon the distance of observation. Immediately after the aperture the diffraction pattern resembles the shape of the aperture with some fringing. Fresnel diffraction is known as near-field diffraction since it corresponds to the diffraction pattern close to the aperture. As the observation distance increases from the aperture, the fringes change towards those approximated by the Fraunhofer diffraction pattern. Once in the Fraunhofer regime of far-field observation the diffraction pattern does not change in shape other than in scaling, which changes linearly with distance. The Fraunhofer regime can be reasonably well approximated when the observation distance R, the Rayleigh length, is greater than a^2/λ, where a is the dimension of the aperture and λ the illumination wavelength. This means that the distance from the source and aperture is large enough that waves arriving at the observation point are essentially plane waves, even if the apertures are illuminated by a point source providing spherical waves. Consequently, the phase variation arising from the different path lengths travelled can be neglected, as would be the case for plane waves. At closer points of observation the curvature of the waves being observed is great enough for phase differences to affect the diffraction pattern depending on the distance.

In the Fraunhofer regime the electric field amplitude u_p of the wave at a point p is proportional to the Fourier transform of the transmission function:

$$u_p \propto \mathcal{F}\{T(x,y)\}$$

Therefore, when a diffraction pattern is observed at a distance greater than the Rayleigh length the image formed is approximately that of the reciprocal space Fourier transform.

If the structure of the object from which light was diffracted is unknown then it may be calculated by carrying out the inverse Fourier transform on the diffraction pattern obtained. This means that from the measured electromagnetic wave amplitude u_p at the point of observation p, the transmission function $T(x, y)$ is obtained by an inverse Fourier transform:

$$T(x, y) \propto \mathcal{F}^{-1}\{u_p\}$$

Note however, that the intensity I of an electromagnetic wave is proportional to the amplitude of the wave squared; $I \propto |u_p|^2$. Hence the amplitude of the wave is proportional to the square root of the intensities measured. Phase information is lost in the measurement of intensity due to squaring of the amplitude, losing the complex information.

If the diffracting surfaces are not rectangular in shape (as is traditional for a diffraction grating), but instead the target is an array of circular apertures then the transmission function needs to be modified. Instead of transmitting like a linear array of two-dimensional rectangular arrays the transmission function is a linear array of circular transmission functions. This may be extended to be a regular two-dimensional array, with $N \times M$ rows of circular apertures, the loci of which being described by a summation of delta-functions in both the x and y-directions. The Fourier transform of circular apertures is a lot more complex however, involving Bessel functions. The resulting Fraunhofer diffraction pattern for a single circular transmission function is the Airy pattern [225] (shown in Figure 6.1). The diffraction pattern for an array of circular apertures is a superposition of Airy patterns for each aperture.

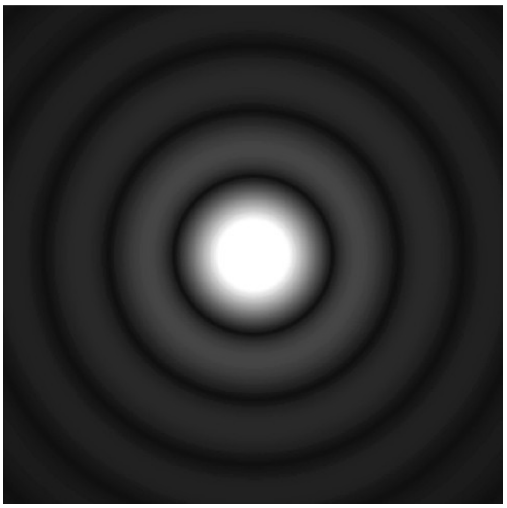

Figure 6.1: Airy diffraction pattern from a circular aperture.

6.2 Two-Dimensional Diffraction Sensor Surfaces

Due to the need for multiplexing of haplotype assays to increase the speed of analysis, two-dimensional diffraction arrays were investigated. Using the principles of Fourier optics, 2-dimensional diffraction sensor surfaces can be designed with distinguishable diffraction patterns. The aim of two-dimensional surface patterns is that the diffraction pattern captured on a CCD camera, can be directly interpreted to indicate the regions that are contributing to the diffraction pattern with hybridised gold being present. This theory was used to design trial arrays and the diffraction patterns captured are evaluated.

6.2.1 Sensor Surface Design

The assumption was made that the main cause of diffraction would be due to the presence of gold nanoparticles attached to patterned regions on the substrate; the scattering from these being expected to be much higher than that due to DNA alone. If substrates were patterned with different DNA sequences for each region then only the regions with hybridised complementary gold nanoparticles would contribute significantly to the diffraction pattern. Thus, a surface pattern could be designed where the diffraction pattern would be different depending upon which regions featured hybridised gold nanoparticles. The aim was to develop the best design to produce the maximal change in the observed diffraction pattern corresponding to the presence or absence of hybridisation at each region within the diffracting array.

The principles of Fourier optics mean that the spatial intensity of the optical diffraction pattern observed is proportional to the Fourier transform (FT) of the array of diffracting objects. This enabled theoretical testing of the surface array design by preparing images of the proposed designs and computing their two-dimensional Fourier transforms. Theoretical diffraction array pattern images were created for each pattern design. Images were created for each possible combination of different sequences being present (featuring complementary oligonucleotide functionalised gold nanoparticles). The series of possible surface region combinations for each array design were Fourier transformed using a program written in MATLAB (see Appendix C).

The aim was to design an array of test patches for different DNA sequences, incorporating a reference patch, that would have a unique diffraction pattern for each possible outcome of

the hybridisation assays. The reference would be a sequence that is definitely present. If the reference is detected, then the conditions for hybridisation are correct, and the determination of the presence or absence of other sequences is reliable. The array of diffracting objects had to be designed to give the maximum contrast in the Fourier transform, introducing features in the diffraction image when significant parts of the surface design are not present. This can be achieved by using angular design considerations (the direction in which a shape or array has a particular dimension or periodicity), to concentrate light in the diffraction pattern in areas away from the background diffraction features due to intrinsic periodicity. Other considerations were the periodicity and aperiodicity with certain features present or removed. Having different sized array patches could also be used to generate distinguishable features in the diffraction pattern, but this is better achieved with different shape array patches since it is desirable that each patch has the same area of DNA.

Although it was desirable to determine the outcome of as many assays as possible at once, it becomes more difficult to generate obviously unique diffraction patterns when there are more features involved. This is due to the number of diffraction patterns possible from a pattern containing n sequences following Pascal's triangle, giving 2^n combinations.

In reality, the most obvious change in the Fourier transform is created by the removal of objects within an array containing only a few objects. For example, one of the most obvious changes in diffraction patterns occurs for just two dots (see Figure 6.2 (a) and (b)). With only the reference circle present the diffraction pattern is an Airy disc. When another sample spot is present alongside the first spot the effect is similar to Young's slits, with modulation of the original Airy pattern occurring. The separation of the superimposed fringes is dependent on the dot separation, with a larger separation of the dots generating fringes that are closer together in the diffraction image. To make a sensor using two dots of the same size one would have to be a reference spot and the other a test spot, as if only one spot was causing diffraction it would be impossible to distinguish which one from the diffraction pattern alone. This is also the case more generally for any number of test sequences. If it is desired to detect n sample sequences, then $(n + 1)$ spots are needed to ensure that if only one of the sample sequences is present the diffraction pattern is distinguishable from the others by the presence of the reference spot.

The design chosen for the initial development of the sensor featured two test patches and one reference spot. This design has four unique FT diffraction patterns, depending on which patches contribute to the diffraction pattern. These can be seen in Figure 6.2, based on an equilateral triangle array of dots. The theoretical array pattern of dots is shown along with

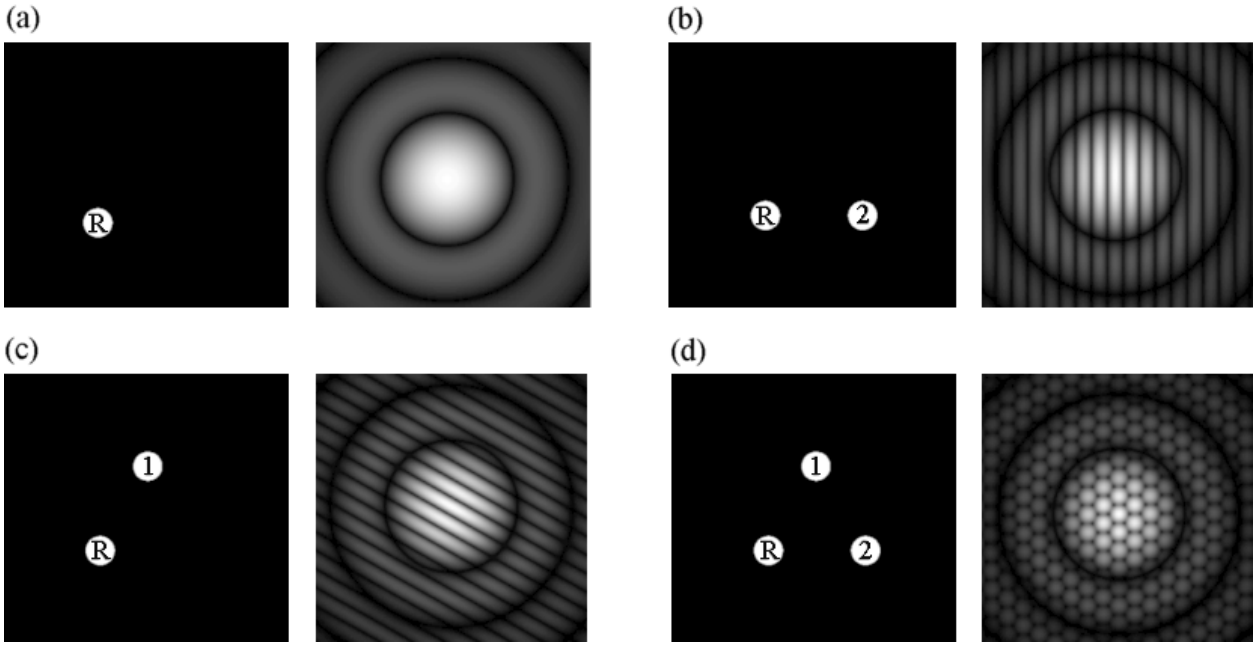

Figure 6.2: Theoretical diffraction patterns for an equilateral triangle array of three dots, consisting of a reference dot (R) and two sample patches (1 & 2), which could be used for different DNA sequences.

the corresponding theoretical two-dimensional Fourier Transform.

Circular test patches were chosen for the array features because the diffraction pattern corresponding to the reference signal is expected to be uniform in each direction. Modulation of the Airy diffraction pattern associated with circular features which is caused by the presence of test patches will feature equally strongly in each direction. Circular features were also chosen since it would be simple to pattern the substrate with DNA by spotting or micro-contact printing circular patterns in the future.

6.2.2 Image Capture

The experimental setup for the capture of 2−D diffraction patterns from the design templates (arrays of chrome dots on a glass photolithographic mask plate) was essentially the same as that developed for the 1−D gratings in Chapter 5. However, because Fourier optics based design was used, the sizes of the design structures on the surface were chosen so that the diffraction pattern would fit on to the area of the CCD camera. This meant that the CCD camera could be left at a fixed angle for image capture, the same angle as the incident laser beam. The experimental setup used is detailed in Figure 6.3.

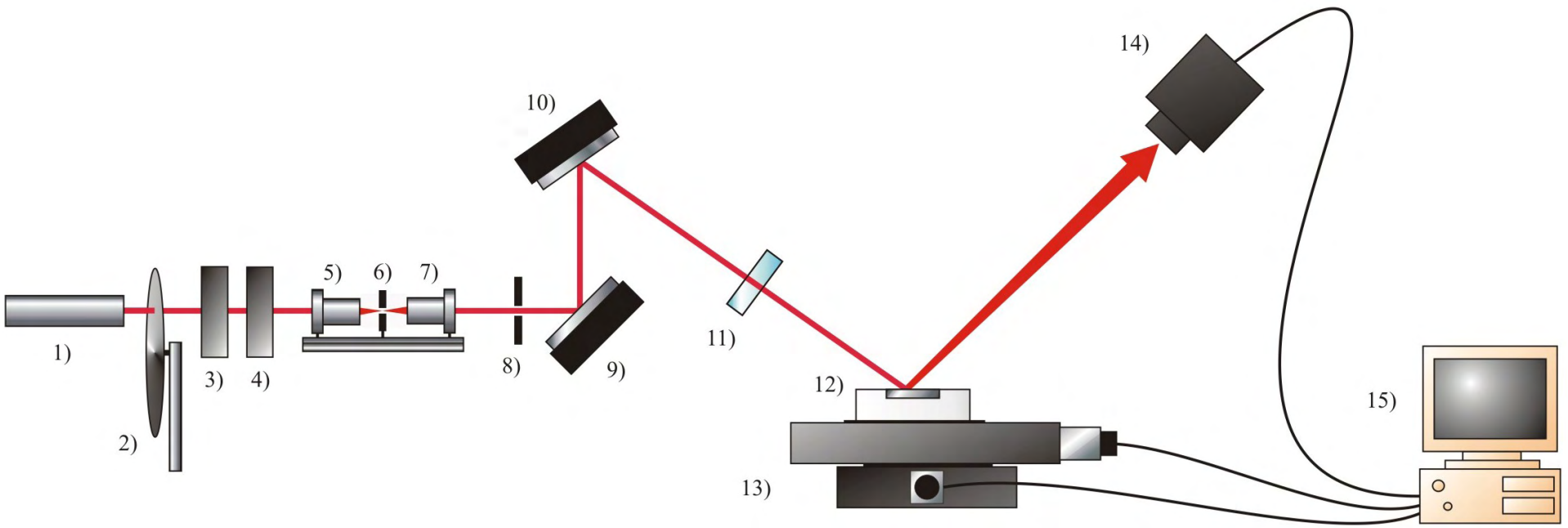

1) HeNe Laser
2) Variable Neutral Density Filter
3) Polariser
4) Polariser

Spatial Filter Assembly
5) Objective Lens 10x
6) Pinhole (30 micron)
7) Objective lens 10x

8) Iris
9) Mirror
10) Mirror

11) Half-Wave plate

12) Sample holder and Sample
13) X-Y Translation Stages

14) CCD Camera

15) Control Computer
(For sample translation and image capture)

Figure 6.3: Experimental layout for two-dimensional diffraction image capture.

The intensity of the incident laser light was attenuated using a variable neutral density filter to control the saturation level of the diffraction pattern images in order to best show the detail. A digital CCD camera (Pulnix TM1020−CL) was used with a large area detector chip (1" diagonal dimension) connected to a digital frame-grabber in the computer. The illumination intensity was adjusted whilst observing the CCD camera output live on the computer monitor.

The angle of incidence was set at the Brewster angle for glass, as detailed in Chapter 5. Translation stages were used to position samples in the path of the laser beam whilst observing the appearance of the diffraction pattern to centre the beam on the centre of the diffraction array. A rotation stage was mounted on top of the translation stages to ensure the correct angular orientation of the array patterns in the laser beam necessary due to the angle of incidence.

To determine the optimum feature sizes for the initial development of the sensor different sized versions of the three-dots test patterns were used. The diameter of the dots in the patterns used had the values; 20, 50, 100, 200, 400 μm. The dot separation in the equilateral layout was 60, 120, 240, 480, 960 μm, respectively. The horizontal separation of the 3^{rd} dot in the non-equilateral layout was 100, 200, 400, 800, 1600 μm for the corresponding spot sizes. Example diffraction images for the non-equilateral pattern are shown in Figure 6.4. The 20 μm (not shown) and 50 μm diameter spot sizes did not produce visible diffraction images. The 100 μm diameter spots produced enough diffracted light to be visible compared to the reflected light intensity. The images captured for the 2−D diffraction arrays showed that the optimum spot size to give the best diffraction images is 100 μm diameter.

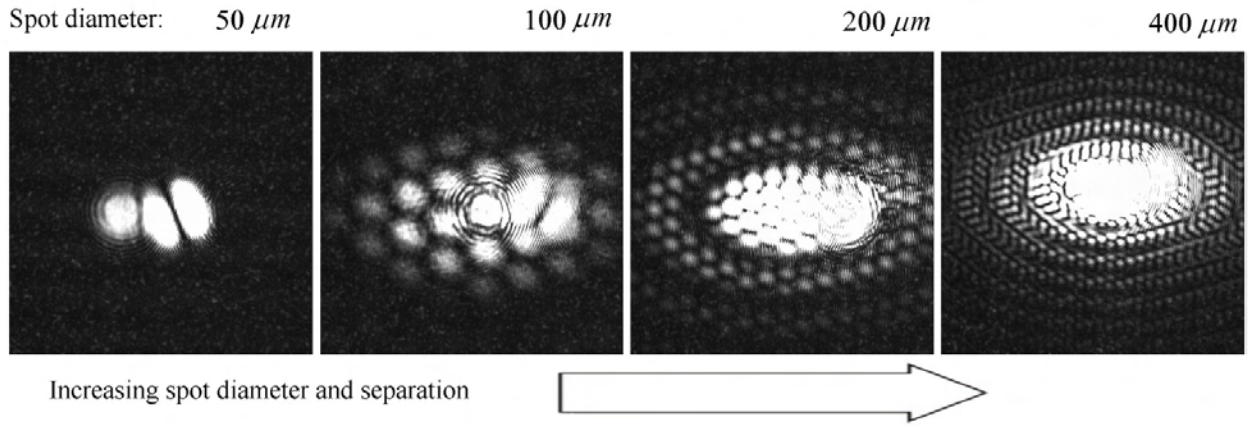

Figure 6.4: Captured diffraction pattern dependence on the size of the diffracting array. Note the reflected noise in the images is discussed in the next section.

The theoretical array pattern of dots is shown along with the corresponding theoretical

two-dimensional Fourier Transform, microscope image of the array and captured diffraction pattern from the chrome dots on the silica mask plate in Figure 6.5. The captured diffraction images show very good agreement with the theoretical patterns and are easily distinguishable from each other. This shows promising potential to be developed in to a DNA sensing technique.

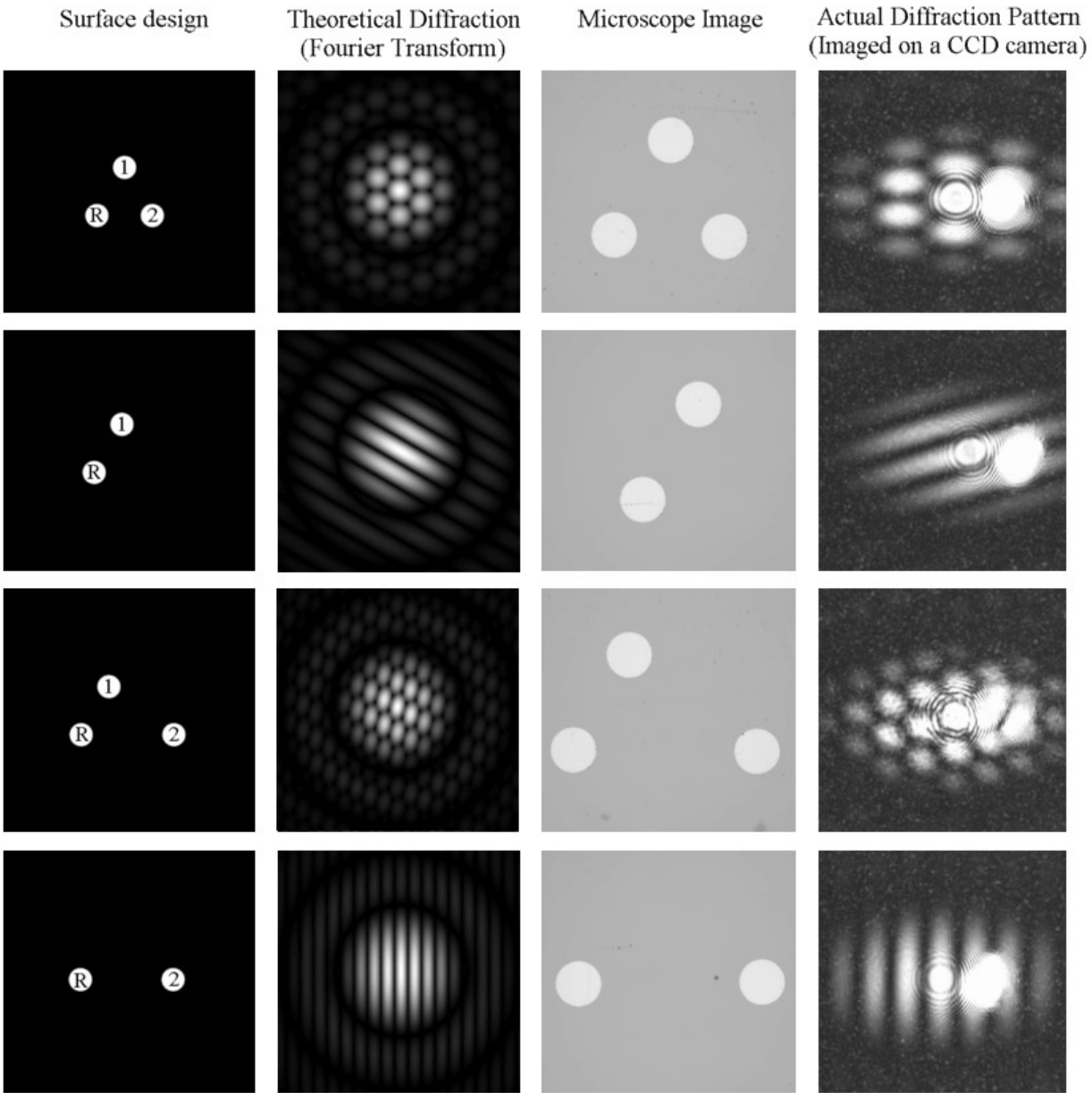

Figure 6.5: The left hand column shows the surface pattern design, with its corresponding FT pattern next to it. The 3^{rd} column shows a microscope image of the real patterns, with the diffraction pattern captured on the right. The noise, distortion and inversion of the images is discussed in the next section.

6.2.3 Image Analysis

Figure 6.6 shows that the diffraction pattern captured is in fact the mirror image of the Fourier Transform predicted for each pattern. This is because the diffraction is being observed in reflection. The images also show that the diffraction patterns do not have a circular 'envelope' but are ellipsoidal, due to the angle of incidence of the laser beam (see Figure 6.6). The size and scaling of the Airy pattern 'envelope' in the theoretical images relating to the spot size is dependent on the extent of zero-padding (described in section 5.2.2), hence is different in the real diffraction images.

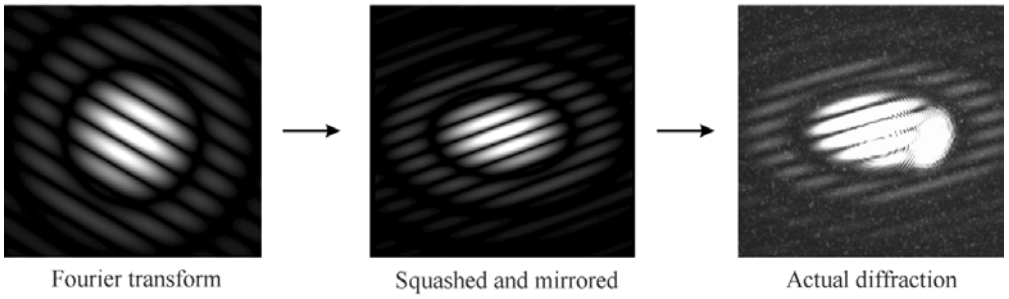

Figure 6.6: The predicted Fourier transform pattern agrees very well with the actual diffraction image when taking into account the angle of incidence and reflection.

Although the incident laser beam was aligned at the Brewster angle to eliminate surface reflection from the silica substrate, a reflection was still present in the image (as can be seen in Figure 6.7). It is very difficult to get complete cancellation of reflections. Firstly, the laser beam, although polarised with a ratio of approximately 100 : 1 (p-wave : s-wave), was not 100 % plane polarised. The laser was rotated to minimise reflection at the Brewster angle with no other components in place. Next, polarisers were added and aligned to improve the polarisation. This greatly improved the polarisation ratio. The angle of incidence was fine-tuned to remove reflection from the surface.

During alignment (and in diffraction) two reflections were visible using the trial designs on a silica mask plate (see Figure 6.7). The top reflection (1) corresponded to the diffracted beam, and could be virtually eliminated when no diffracting objects were present. The bottom reflection (2) was always present and corresponded to reflection from the bottom surface. The silica plate sat on top of a sand-blasted base plate, with index-matching oil at the interface. The index of the oil was close to that of silica, but not a perfect match, so this could have caused some reflection at the interface. The other reflecting surface was the abraded base plate. This produced the general background speckle of scattering which can be seen in the diffraction images in Figure 6.5. This is only visible in these images due to the

high intensity illumination required to show up the full diffraction pattern visible to the eye. This was reduced by smoothing out the abraded base plate with fine black powder mixed with vaseline. The background scattering and strong reflection in the images was also due to the illumination of a large surface area ($\sim 2\ mm^2$), with a relatively weak diffraction signal from a maximum of 0.006 mm^2 of chrome. The beam could be focused down to illuminate only the immediate area surrounding the array of dots, thus providing a much higher signal from the chrome compared to the silica.

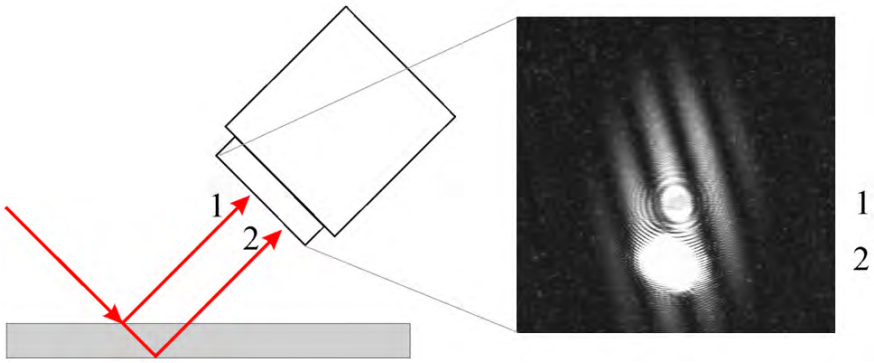

Figure 6.7: Offset of reflected beam from bottom surface (2) in the diffraction pattern (1).

Determination of which dots are contributing to the diffraction has to be identified by analysing the diffraction pattern. For test patterns which either feature a chrome dot at a particular location, or no dot, the diffraction pattern captured can be compared with the theoretical Fourier transform by eye. Quantitative analysis is required to allow for the fact that DNA patterns will not feature such high levels of contrast, to evaluate the 'quality' of a diffraction image and to identify in which directions periodicities are present. The information contained within the diffraction pattern may be extracted by Fourier transforming an image of the diffraction pattern. The extent to which periodicity exists in each direction may be quantified by examining the intensity peaks of the Fourier transform compared to the adjacent background noise, giving a signal-to-noise ratio (SNR) for diffraction in each direction.

Figure 6.8 shows the Fourier transform (centre) of a diffraction pattern (left) captured on a CCD camera. The periodic interference fringes in the diffraction pattern parallel to line a are represented by the peaks along the line a', circled in yellow in the Fourier transform, and correspond to interference between light reflected from dots 1 and 2 (see top row in Figure 6.5). The peaks along line b' correspond to interference between dots labelled R and 2 and along line c' due to R and 1. These directions will be referred to when discussing the SNR for diffraction patterns. The SNR measurements quoted are measured from cross-sections through the FT plots, with the peak intensity normalised to the adjacent noise level.

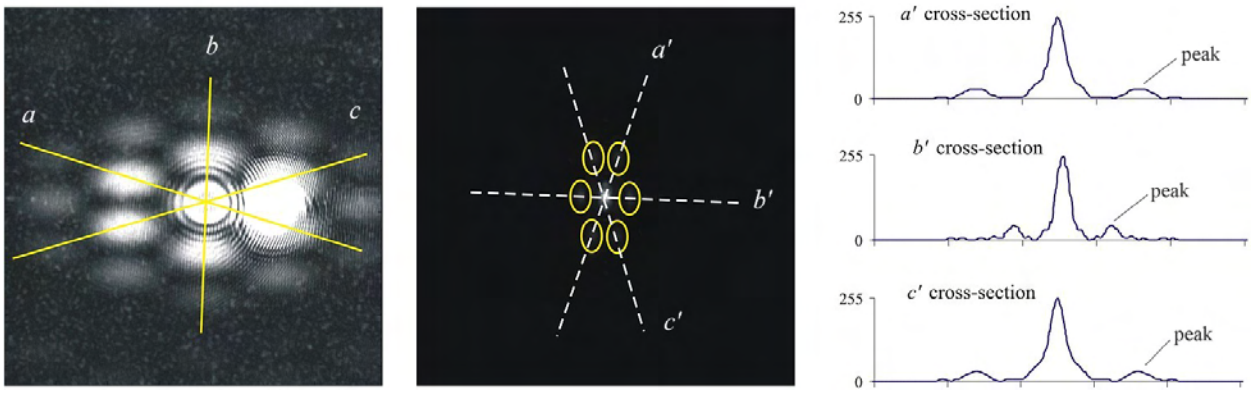

Figure 6.8: Fourier transform analysis of diffraction patterns captured on a CCD camera; Diffraction pattern image (left), 2−D Fourier transform plot (centre) and FT plot cross-sections (right).

6.2.4 Considerations for DNA Arrays on Silicon

For the test patterns captured from chrome on silica described above, the back reflection was separated from the zeroth diffraction order due to the thickness of the silica substrate and base plate (both 2.0 *mm*). Referring back to the 1−D grating experiments with DNA on silicon in Section 5.2.3, the reflection from the silicon substrate in a buffer solution will be much stronger than from silica. The reflection from the surface of the liquid could be reduced at the Brewster angle for the air/buffer interface, but would not be completely removed due to vibrations perturbing the surface of the liquid.

However, reflection from the surface of the liquid could be adjusted so that it lay in a different plane to that from the grating by tilting the grating plane slightly, and thus did not appear in the diffraction image, as was previously achieved with the DNA gratings on silicon. It was important for the diffraction gratings to reduce the difference in reflection from the silicon compared to the regions covered in DNA, since this was enough to form diffraction on its own. For 2−D arrays, the lack of reflection from the dots being covered with DNA should have a very small impact compared to the reflection from the surrounding surface and should not form a significant diffraction pattern. Upon hybridisation of gold nanoparticles, the signal from the array is expected to be detected, since it will diffract at an angle to a wider diameter size on the CCD than the beam reflection, regardless of the intensity of the central reflection.

The diffraction patterns obtained, and the predictions presented in Figure 6.5, are for the case of perfect surface coverage on all dots. In reality, even when the reference, test 1 and test 2 complementary sequences are all present in a sample, such that gold is hybridised to

all of the dots in the array, they will probably not have the same gold nanoparticle density on each spot due to differing hybridisation efficiencies. This would cause stronger diffraction from one spot than another. This has been modelled by altering the pixel values in the images, which represent reflected intensity values, to different values for each spot. White corresponds to a value of 255 and black to a value of 0, with different levels of grey in between. By changing the value of the spots to values such as 50 for one, 120 for another and keeping the reference signal strongest at 255, the impact upon the diffraction patterns can be seen.

The altered patterns representing different intensity spots and their Fourier transforms (the theoretical diffraction patterns) are shown in Figure 6.9. Where two spots appear much brighter than the other one, the diffraction pattern resembles that of only two dots, with a weak modulation from the other spot on the diffraction pattern. There is no longer complete cancellation to give a hexagonal pattern because the diffracted light from the spots has different intensities. The SNR values extracted for these theoretical images show that when the reflectivity of two dots is much less than one of the three, the interference in the direction between the low reflectivity dots only adds a weak modulation of the Airy pattern that corresponds to the high reflectivity single dot.

For the 2^{nd} row example in Figure 6.9, the SNR in the Fourier transform in direction c' is 1.00, and for the bottom row is 0. If a logarithmic ($\log_{10}$) intensity plot of the Fourier transform is used for analysis, the low-level signal is emphasised giving a SNR of 1.16 and 0.95, respectively. The log-intensity plot enables low-intensity peaks in the Fourier transform to be visible by eye and provides increased sensitivity in the detection of features. The threshold SNR value is approximately 1.15 for identification of the peaks by eye in a log-intensity plot, which would not be visible in a normal FT plot.

6.2.5 Optics Development

Improvements made to the optical apparatus enabled better imaging of the diffraction from the chrome dot patterns on the silica mask plate without the need for a sandblasted back-plate. The improved images are shown along with the theoretical images and initial images captured in Figure 6.10. Improvements included the use of a 50 μm diameter pinhole at the centre of a spatial filter and blocking the back-surface reflection close to the sample. Without requiring the diffusing back-plate, the background scattering was removed from the diffraction images. The theoretical diffraction images were generated by taking the Fourier

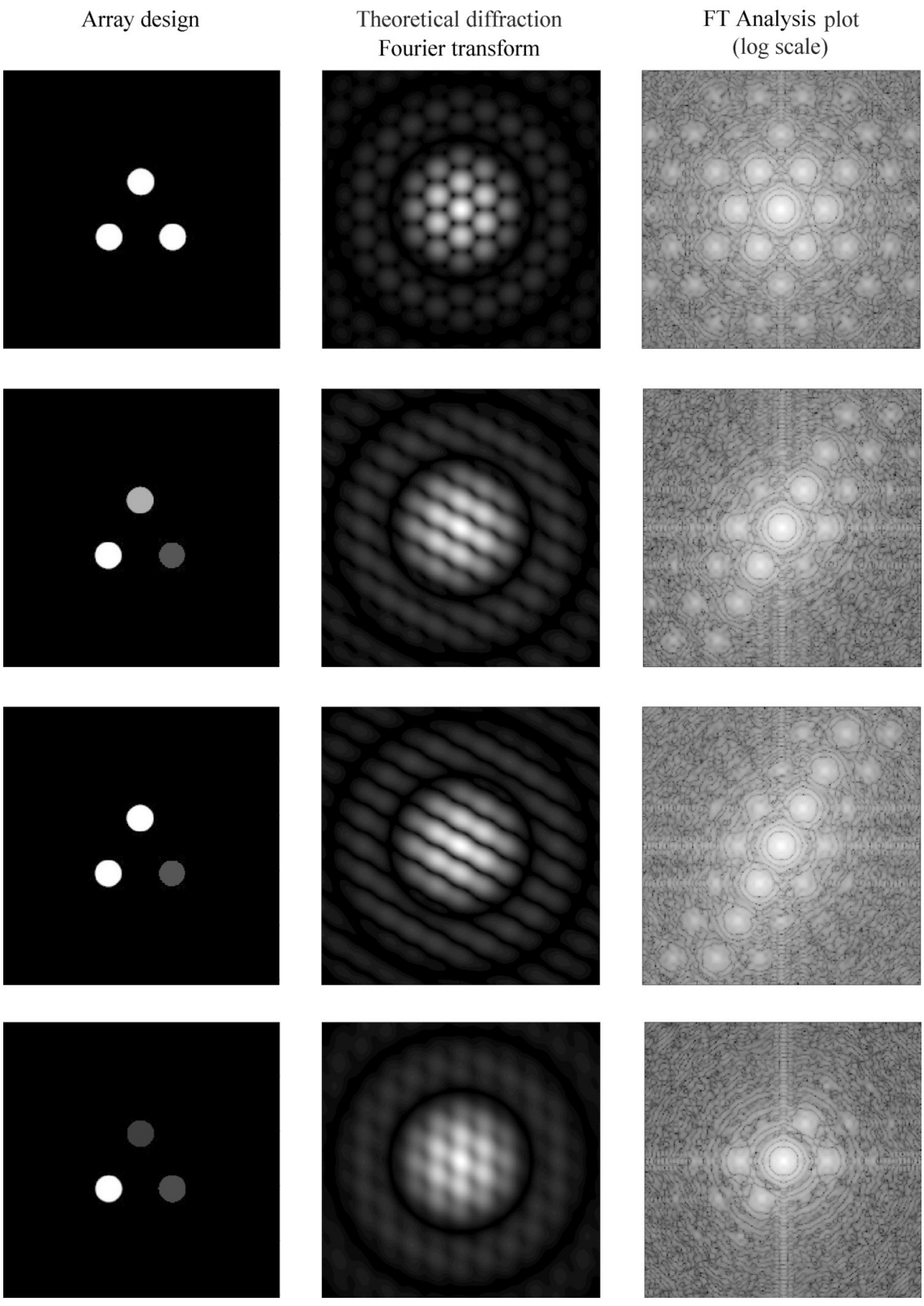

Figure 6.9: Different intensity values for different elements of the array (left-hand column), their theoretical diffraction patterns from Fourier transforms (centre) and Fourier transform analysis plots (shown on a logarithmic-scale) of the theoretical diffraction (right-hand column).

transform of the surface design, squashing the image to account for the angle of incidence and taking the mirror image to account for the reflection geometry. These are almost identical to the real diffraction images captured on a CCD camera. The improvements made to the optics

meant that the averaged SNR for the images in Figure 6.10 column (v) were 43.6 ± 1.0 % higher than for column (iv).

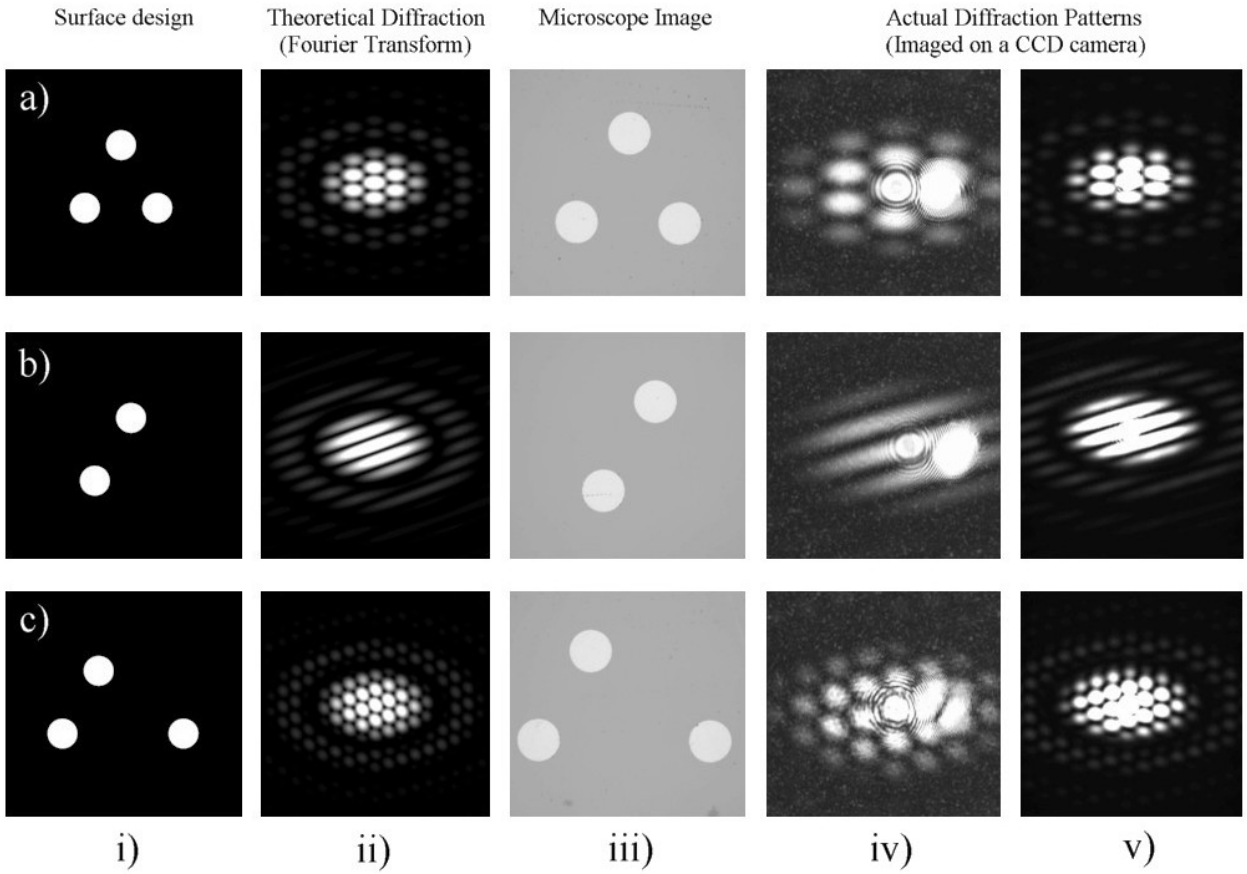

Figure 6.10: Improved imaging of two-dimensional diffraction patterns from chrome dots on silica by using a spatial filter, blocking the bottom surface reflection and using a longer observation distance.

The top row of Figure 6.11 shows the difference between using a spatial filter and not using one on the diffraction pattern for chrome dots on silica. The average SNR over the 3 directions was improved by 17.8 ± 0.6 % using the spatial filter. Diffraction patterns were also imaged from the same design reproduced with gold dots evaporated on to a silicon substrate with the improved image capture quality. The bottom-left diffraction pattern in Figure 6.11 shows that there was a much larger reflection from the silicon substrate, before using a spatial filter, than seen from the same pattern on a glass substrate, which was expected. The diffraction pattern was still recognisable, but had much lower contrast between the diffraction intensity and the reflected beam compared to the diffraction pattern imaged using a glass substrate. When a spatial filter was used, the average SNR was improved by 349.5 ± 59.0 % as can be seen by the much improved diffraction pattern image (bottom-right in Figure 6.11). The average SNR value of 4.49 ± 0.76 compares well with the 5.89 ± 0.20 optimum contrast achieved for chrome on silica, being only 23.8 % lower.

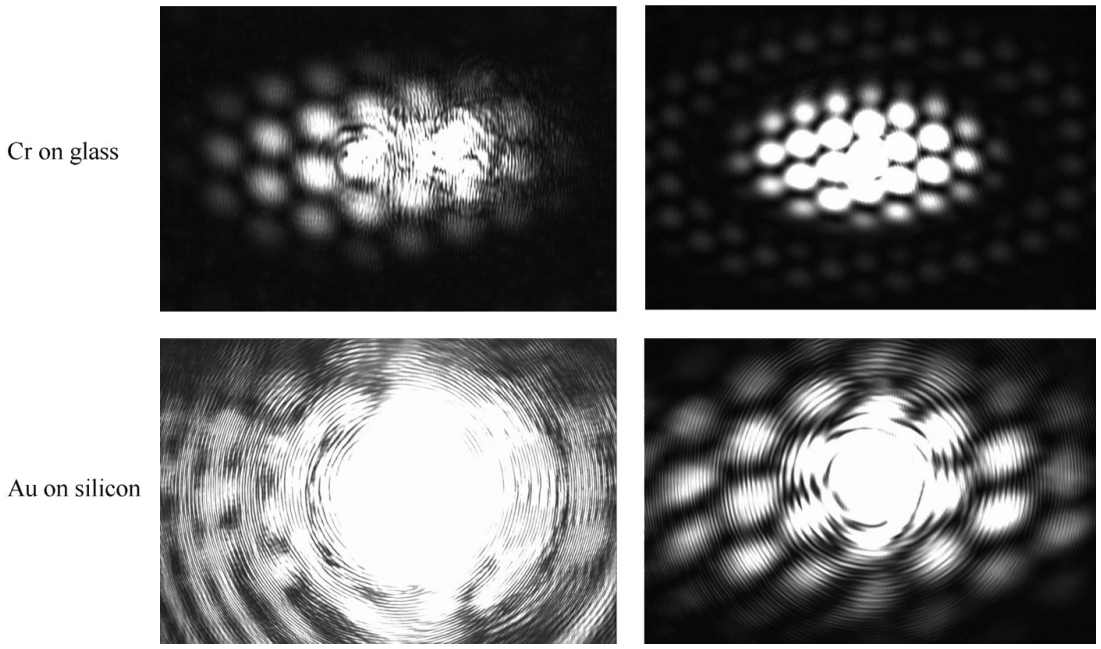

Figure 6.11: Diffraction pattern images with (right) and without (left) a spatial filter for chrome dots on silica (top row) and gold dots on a silicon substrate (bottom row).

6.3 DNA Diffraction Arrays on Silicon

Figure 6.12 shows the diffraction pattern obtained for examining a 'tri-dot' DNA pattern photolithographically generated (as detailed in Chapter 3) on a silicon substrate featuring silver enhanced gold nanoparticles. The diffraction pattern was imaged in reflection on a CCD camera as described above. A second CCD camera with a zoom lens was positioned above the sample to aid alignment. These images (left hand side of Figure 6.12) show the rough and scattering nature of the surface being illuminated with the 1.0 mW 632.8 nm HeNe laser beam. A Fourier transform of the diffraction pattern gave weak diffraction peaks indicating the presence of 3 dots with SNR values of 4.00, 1.00 and 3.00 in directions a', b' and c' respectively, giving an average SNR of 2.67. Note that although the FT shown in Figure 6.12 is shown on a log-intensity scale, this is only to make the peaks more visible and the SNR was measured on the normal FT plot.

Figure 6.13 shows the diffraction patterns obtained for another tri-dot DNA array on silicon. A diffraction pattern was recorded from the sample after DNA conjugation (left-hand image). Another diffraction pattern was recorded after hybridisation with 10 nm diameter gold colloids (centre image) and a final image was taken after silver-enhancement of the hybridised gold particles on the DNA functionalised dots (right-hand image). In all three images, the expected diffraction pattern, which should resemble the image in Figure 6.10 (a)

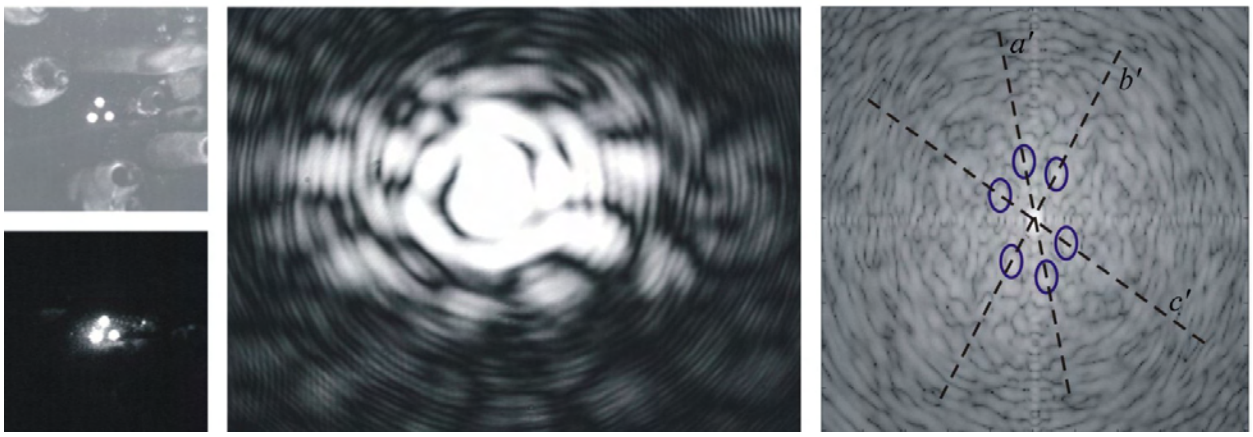

Figure 6.12: Top left: Above view of illuminated sample. Bottom left: above view of sample illuminated with laser in the dark. Centre: Diffraction image from DNA spots on silicon with silver-enhanced gold nanoparticles hybridised to the DNA. Right: FT of diffraction pattern shown on a log-intensity plot.

and (v) is not obviously visible. The images are dominated more by scattering and noise than a geometric diffraction pattern. However, the FT analysis of the diffraction patterns show that there are weak peaks in each image, which are more visible on a log-intensity plot. The SNR for DNA only is 2.00, 1.00 and 2.00 for directions a', b' and c'. With hybridised 10 nm gold nanoparticles the respective SNR values were 3.00, 1.33 and 2.00 and following silver enhancement were 3.00, 0.67 and 2.00. This gave average changes in the SNR values of $+26.7 \pm 3.7$ % with hybridised gold and $+13.3 \pm 0.2$ % compared to DNA only following silver enhancement, 13.4 % less than the change due to gold alone.

The problem of surface roughness resulting from sample fabrication (as found with 1−D gratings in Chapter 5), means that the optical path difference over the area of the dot array can vary by a large enough extent to prevent coherent interference from the periodic features. Figure 6.14 shows images of the reflected beams from silica and processed silicon. The beam reflected from the silica substrate is a lot more uniform than that reflected from silicon patterned with DNA, which generates a lot more scattering. The impact of the surface upon the beam quality generates a lot of noise in the diffraction patterns of the DNA dots on silicon, making detection of the diffraction pattern very difficult.

An alternative method of fabrication of a two-dimensional diffraction sensor could use DNA microarrays on glass as a lattice template. Different diffraction arrays could be designed by selecting which spots have a specific sequence. By using glass as a substrate, the diffraction images captured would offer more contrast in reflection than using silicon, and also offer the possibility of transmission imaging.

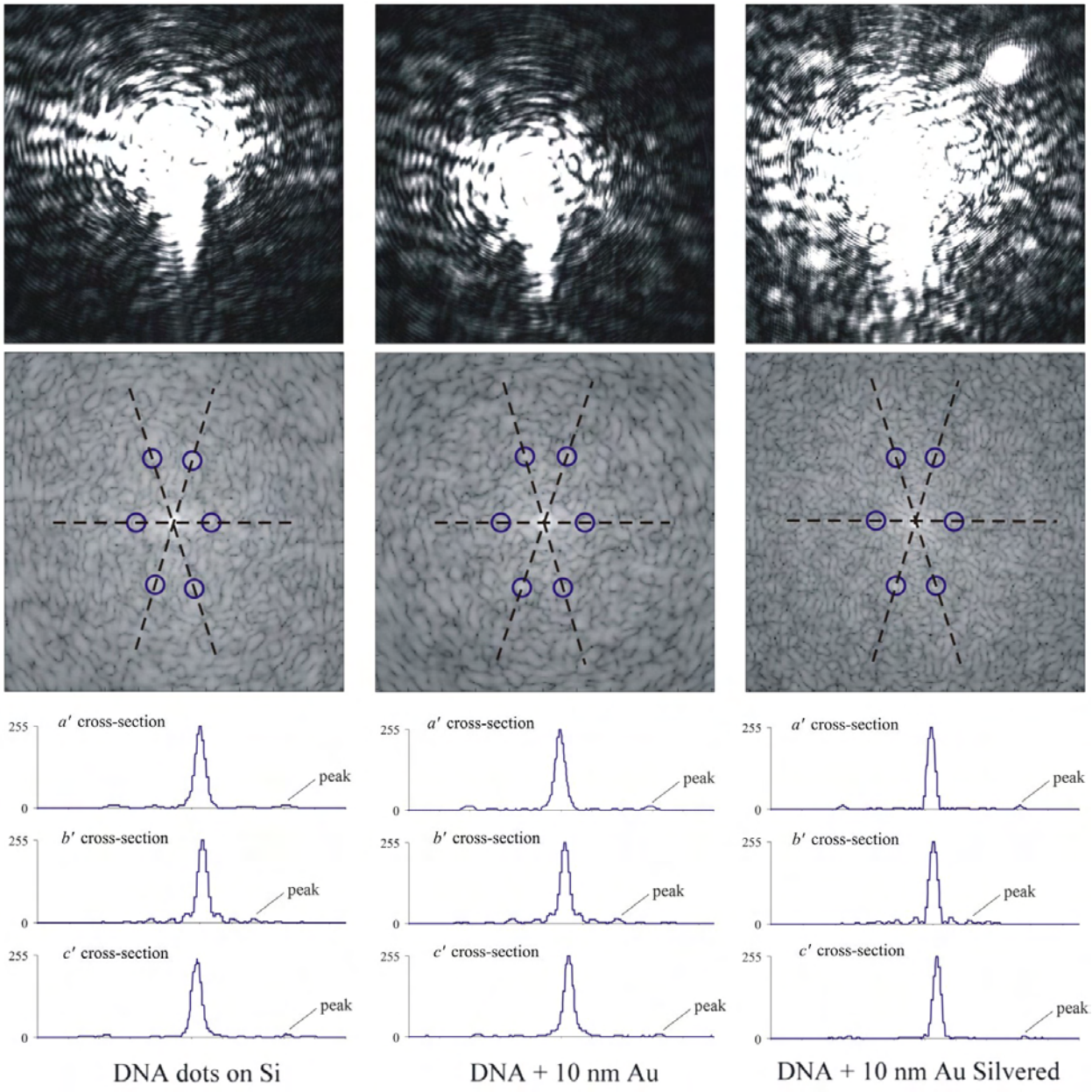

Figure 6.13: Diffraction images (top row), FTs (middle row, log-intensity scale) and FT cross-section plots for DNA spots on silicon. The left hand diffraction image was for DNA only, centre image DNA with gold nanoparticles and the right-hand image is for silver-enhanced gold nanoparticles hybridised to DNA.

Figure 6.15 shows an example of a 2−D array design for examining 4 DNA sequences simultaneously, with the array pattern based on an underlying square lattice of dots typical of DNA microarrays. The different coloured dots in Figure 6.15 represent where the different DNA sequences are spotted. Using multiple spots for each sequence adds some redundancy to the system against spots not hybridising as well as they should, which will improve the accuracy of detection.

Figure 6.16 shows the theoretical Fourier transform of the array sequences present and the actual diffraction pattern captured from chrome dots on silica. In order to capture diffraction

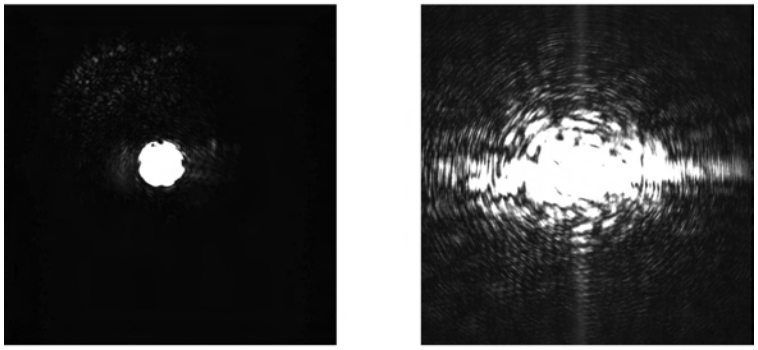

Figure 6.14: Reflected beams from silica substrate (left) and silicon which has been processed for DNA attachment (right).

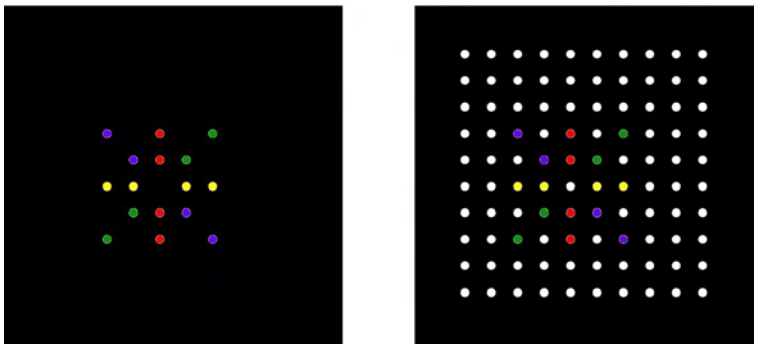

Figure 6.15: Array design pattern, with different DNA sequences shown using different colours, based on a microarray with a fundamental square lattice.

images from these patterns, the beam had to be expanded to illuminate the whole of the array. The design constraints of the commercial microarrays meant that the patterns were based on 100 μm diameter spots with a 300 μm separation (centre-to-centre), giving a total design size of 1300 μm $\times$ 1300 μm.

The diffraction patterns obtained for the optimum situation using photolithographically patterned arrays of chrome dots on a silica substrate show that the optical patterns do not agree with theory as well as for the three-dot design. The theoretical patterns are also much more complicated than for the 3 dot design and show less change for any one sequence not being present. Fourier transform analysis of the theoretical diffraction is also not as straight forward as it is for the 3 dot design. This is largely due to the design being based on a square lattice, so each design features integer multiples of the same period. Whilst it may be beneficial biologically to have several repeats of each sequence in one pattern, it increases the complexity of the diffraction pattern and also increases the size of the array that needs to be illuminated. This makes capturing a diffraction pattern more difficult and requires a greater accuracy and uniformity of sample patterning to generate distinguishable diffraction patterns. The most obvious changes in the optical diffraction pattern occurs for

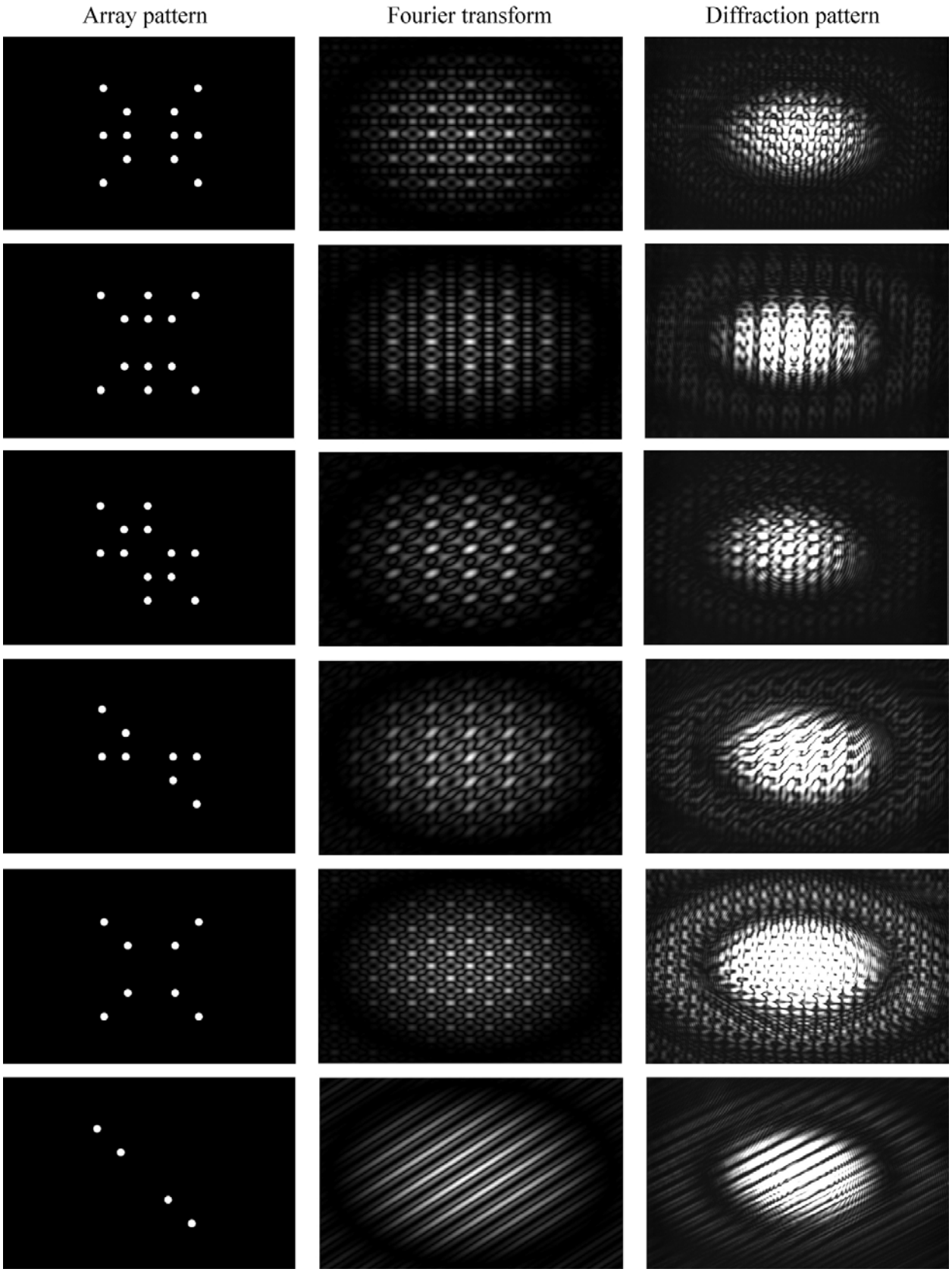

Figure 6.16: Theoretical and actual diffraction patterns for chrome dot array patterns on a silica substrate.

the simplest array designs, featuring a small number of features. Therefore, the optimum design to develop on a microarray layout would be based around a 3-dot design.

6.3.1 Summary of Diffraction Arrays

Two-dimensional diffraction structures were designed and fabricated from chrome on glass and gold on silicon substrates. The optimum diffraction results were obtained for glass substrates where the background reflection was minimised, giving a SNR of 5.89. The gold on silicon samples also gave good diffraction and the diffraction images all showed excellent agreement with the predicted Fourier transforms and had a SNR of 4.49.

DNA patterns were also produced on silicon substrates using the patterning methods developed in Chapter 3. The DNA samples showed excellent biological patterning with good DNA coverage on the patterned regions and no non-specific DNA attachment on the remainder of the silicon substrate. Diffraction from the DNA dot patterns with only DNA on the surface was not found to produce visually recognisable diffraction images, but there was some evidence of the diffraction pattern modulation in the Fourier transforms, with an average SNR of 1.67. There was some improvement in the diffraction images for hybridised gold giving a SNR of 2.11. Silver enhancement procedures produced a maximum SNR of 2.67. Whilst the technique offers the potential to enable multiplexing of DNA sequence detection, current fabrication procedures result in a rough surface which reduces coherence and reduces the amount of diffraction and causes more scattering. This suggests that it may be better to fabricate 2−D arrays on glass, as despite a lower density of DNA conjugation ($6.7 \times 10^{12}/cm^2$ [170] compared to 1.2×10^{13}), the background reflection can be minimised by illumination at the Brewster angle. The good results achieved with chrome on glass indicate that diffraction should be much better without a high intensity scattered reflected beam from a roughened silicon substrate.

6.4 2-D Diffraction-Based Self-Assembled Sensor

An alternative type of two-dimensional diffraction sensor was also investigated, aimed at a different application of DNA sensing. The methodology, based on diffraction in transmission through self-assembled microspheres, could be applied to studying DNA copying errors believed to be linked to types of cancer. When DNA replication occurs the strands can become switched over or translocated, meaning that the product features the sequences of part of one strand and part of the other (see Figure 6.17). This type of copying error is thought to play a role in causing certain cancers such as leukemia [226]. It is possible to determine whether a strand is intact and a replication of the original copy if the start and end sequences are

the same as the original. If the start and end sequences originally belonged to two separate strands, then it is a mutated copy. In addition to designing diffraction gratings and two-dimensional substrate patterns, a technique was established to create self-assembled arrays of polymer spheres for future work to address the application of identifying translocation errors.

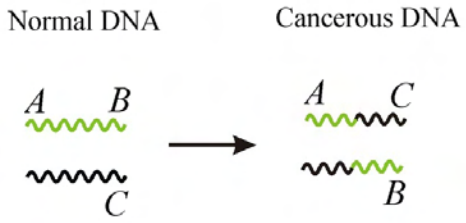

Figure 6.17: During DNA replication different strands may switch over creating a mutation.

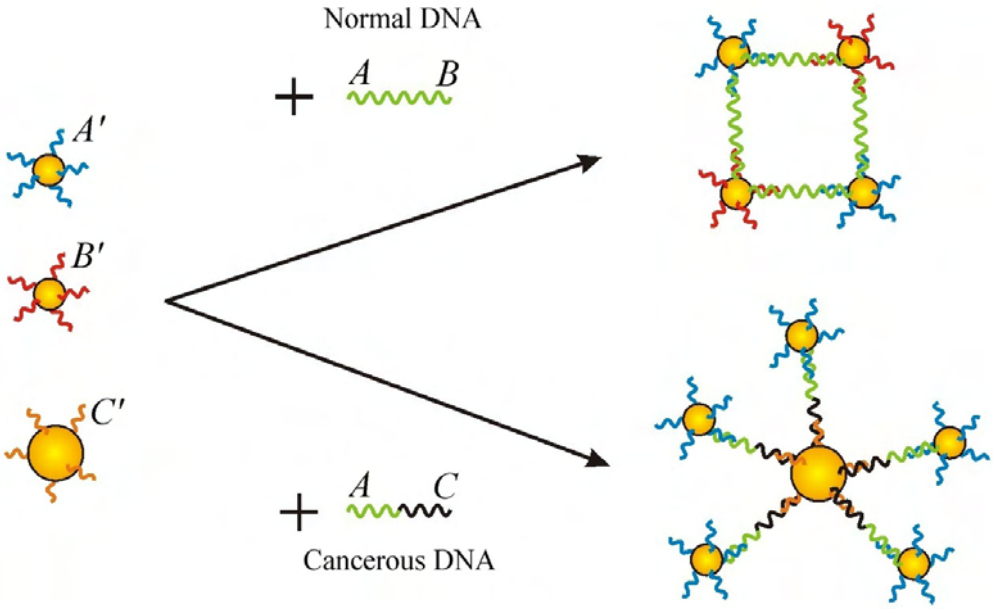

Figure 6.18: Different structure aggregates will form depending on the DNA sequence present in the sample.

If one size of sphere is functionalised with A', the complementary oligonucleotide sequence to the original start sequence A, and the same sized sphere labelled with B', the complementary sequence to the original end sequence B, and the sequence C' complementary to the mutated end sequence C attached to a different sized sphere, then depending on the sample DNA, different assemblies will be formed (as shown schematically in Figure 6.18). If the sample is not defective, an aggregate of $A-B$ particles will form. If the sample features mutated DNA, then $A-C$ aggregates will hybridise instead. Since C is a different size to A, this will have a different packing structure from that of $A-B$ where the particles are the same size, and as a consequence this would lead to different diffraction patterns. This methodology

can be employed to study any sequence mutation where the original sequence and mutated version are known.

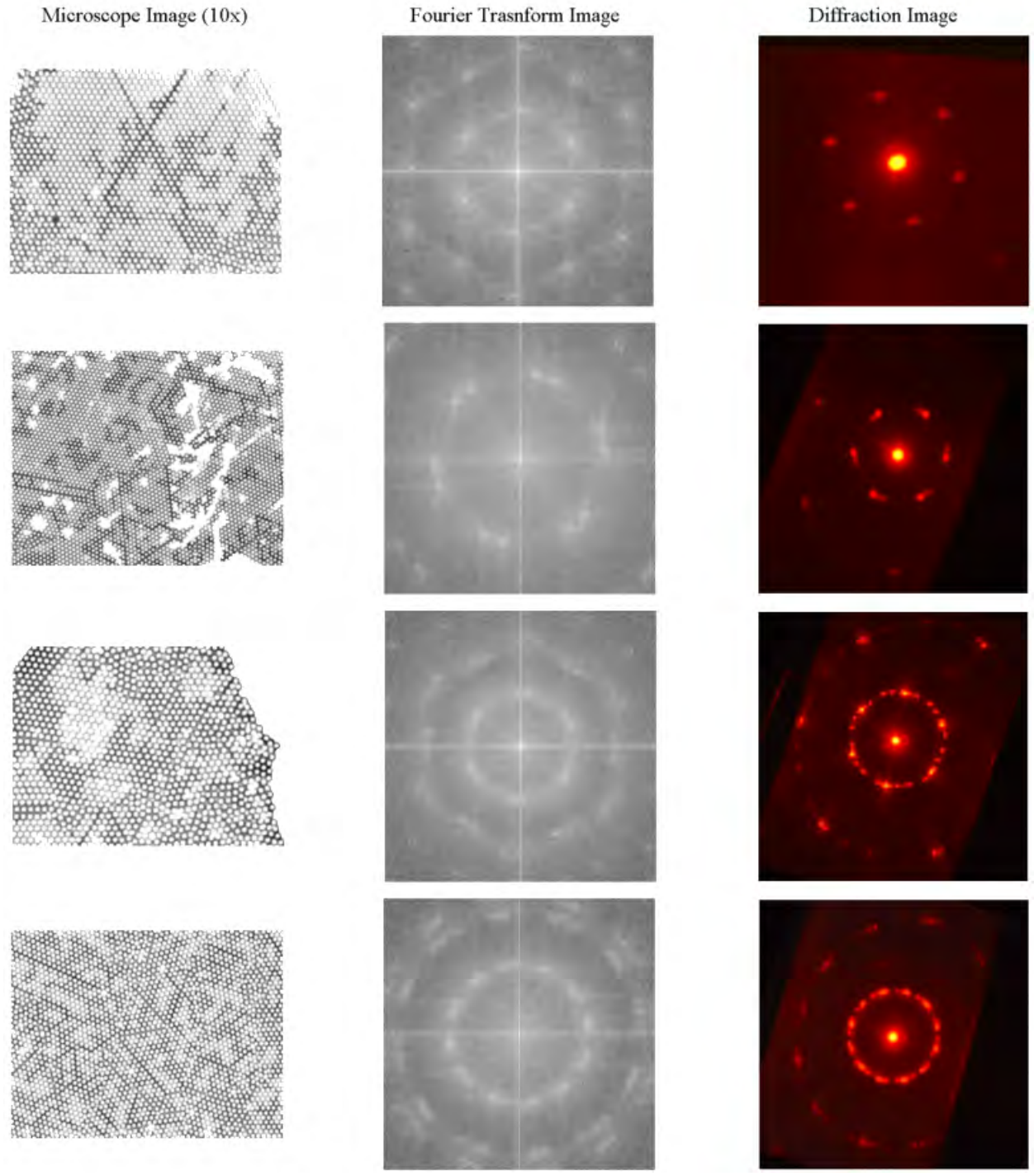

Figure 6.19: The microscope images of self-assembled 1.6 μm diameter latex particles are shown in the left-hand column, with the Fourier transforms in the centre. The right-hand column features the real diffraction patterns imaged on a screen and captured using a digital camera.

In order to establish the feasibility of developing a system to enable optical detection using such a scheme, some particle arrays were prepared and measured. Glass microscope slides were patterned with photoresist and then exposed to UV light via a phase mask. Exposed photoresist was removed with developer, leaving ridges formed of unexposed resist. A second

glass slide was attached using a Parafilm seal to form a small cavity between the slides. Then 1.6 μm polymer microspheres, held in suspension in fluid at a concentration of 1 % by weight, were added to the slide. As the solution evaporated, the fluid level dropped and the meniscus level forced the spheres to stack and self-assemble along the photoresist ledges. This can form a periodic array of regularly arranged particles under the right conditions.

The self-assembled structures were examined under a microscope and the captured images were Fourier transformed as described earlier. Due to the small size of the particles (1.6 μm diameter) the diffraction pattern was extremely divergent, and could not be imaged with a lens or the CCD camera. Instead, the geometry was altered from the reflection setup to observe diffraction in transmission. The diffraction pattern was too large to be imaged on the CCD camera at the closest possible location, and so the diffraction pattern was imaged on a paper screen and a photograph was taken on a digital camera. The real transmission diffraction images captured agree closely with those predicted (see Figure 6.19). Self-assembled microspheres structures have been successfully realised. Diffraction images captured were found to correlate well with the predicted diffraction from Fourier transforms of microscope images of the self-assembled structures. The sensitivity of this technique to changes in period and structure show that it has good potential to be developed into a biosensor.

6.5 Conclusions

Alternative approaches for a diffraction sensor for DNA analysis based on two-dimensional diffraction arrays were developed. Two-dimensional pattern design showed the potential for multiplexing DNA sequence analysis; in theory, these array patterns would provide unique diffraction patterns depending on which DNA sequences were present. Test array patterns were fabricated from chrome on glass, evaporated gold on silicon and DNA on silicon. An optical apparatus was developed to capture images of the optical diffraction patterns from the two dimensional arrays.

Test patterns of chrome on glass substrates were observed to have much greater clarity in the diffraction pattern than for those produced from gold on silicon, as background reflection was minimised by illumination at the Brewster angle for glass. The very distinct diffraction patterns observable depending on the combination of spots present suggests applying $2-D$ pattern designs to DNA microarrays as future work.

Chapter 7

Conclusions and Future Work

7.1 Introduction

In this thesis, silicon-based diffraction sensors for DNA analysis have been presented. The thesis documents the design, fabrication, characterisation and analysis of both 1−D and 2−D diffraction-based DNA sensors on silicon. The principle results obtained are summarised below in Section 7.2.

The progress-to-date for biosensors for DNA genetic analysis has been reviewed in Chapter 2 of the thesis. A wide variety of sensing strategies have been developed and exploited to enable the secrets held within our DNA code to be 'unlocked'. Significant innovation has yielded faster, more accurate and massively parallel sensors for DNA analysis. The gold nanoparticle labelling strategies proposed in this thesis were aimed to offer highly sensitive DNA haplotype analysis; the method involved diffraction analysis as a highly sensitive optical characterisation technique.

7.2 Diffraction Sensor Achievements

Fabrication techniques were based upon the work of H Yin [16, 179, 180],which enabled the successful covalent attachment of DNA oligonucleotides to the surface of silicon (100) substrates as described in Chapter 3. Patterning of the DNA was achieved by complete

removal of the native oxide layer on the silicon with HF acid and selective UV illumination of a photo-reactive alkene linker molecule using a mask. After conjugation of DNA to the attached alkene, a functional DNA sensor platform on silicon was realised.

In-situ silver enhancement of gold nanoparticles hybridised to DNA motifs on silicon was demonstrated in Chapter 3. This offers the possibility of enhancing the diffraction intensity for a given hybridisation density of gold nanoparticles by growing silver shells around the particles and increasing the amount of light diffracted. Gold nanoparticles were increased in size from 1.4 nm to $\sim$ 700 nm diameter, a factor of 500 times meaning a 250 000 times larger cross-sectional area.

Diffraction grating theory was comprehensively extended in Chapter 4 to cover inter-laced diffraction gratings illuminated at non-normal incidence and observed in reflection configuration. One-dimensional DNA diffraction gratings were modelled and the optimum design for the DNA sensing application was chosen and then fabricated on silicon substrates featuring a 40 μm period and 1 : 3 line:space ratio. Successful hybridisation of complementary DNA-labelled gold nanoparticles yielded densities of up to 6.4×10^9 particles $/cm^2$ for 10 nm diameter gold colloids and 2.15×10^{12} particles $/cm^2$ for 1.4 nm diameter nanoparticles.

An optical characterisation apparatus was developed to enable accurate measurement of diffraction order intensities (to an accuracy of ± 0.034 %) over the whole grating surface, and to measure the change in diffraction upon hybridisation of gold colloids, as detailed in Chapter 5. The accuracy of measuring changes in diffraction was determined to be ± 0.5 % for optimum test patterns. Examination of the diffraction patterns from DNA gratings on silicon revealed information about the variations in linewidth, topography and DNA coverage over the gratings. Upon hybridisation of 1.4 nm diameter gold nanoparticles to the DNA gratings changes in diffraction intensities of up to $+108.79 \pm 1.98$ % were measured averaged over the entire grating surface. Specific regions within gratings showed changes of up to $+ 334.33 \pm 2.47$ % in diffraction intensity, highlighting the potential sensitivity of detection possible if fabrication improvements enabled uniform dense coverage over the whole grating.

An alternative approach to a $1-D$ diffraction sensor based on two-dimensional diffraction arrays was developed, as described in Chapter 6. This sensor design showed the potential for multiplexing DNA sequence recognition tests, offering unique diffraction patterns depending on which sequences are present. Test patterns were fabricated from chrome on silica and gold on silicon and diffraction patterns were captured. The results obtained for chrome

on silica showed that the diffraction patterns agreed extremely well with the theoretical Fourier transforms. A comparison of the SNR values showed that using a glass substrate yielded a 23.8 % improvement. Array patterns of DNA were successfully reproduced on silicon, followed by DNA hybridisation and silver enhancement of the immobilised gold nanoparticles. Diffraction images were captured and the results showed that a SNR increase of $+26.7 \pm 3.7$ % was observed in the Fourier transform of diffraction patterns for DNA arrays on silicon when hybridised with 10 nm diameter gold colloids. The improved SNR values measured for metal patterns on glass substrates compared to silicon substrates suggests that detection sensitivity would be improved by fabricating the array patterns on a glass substrate.

The main aim of the project was to develop a DNA sensor on a silicon substrate, with the ultimate goal of applying the sensor to study DNA haplotypes. In this respect, the project has been partially successful. Two types of diffraction sensor were developed for detecting complementary DNA sequences with gold nanoparticle labels, but detection proved to be very difficult and varied a lot from sample to sample. This precluded applications to studying genomic DNA samples at this stage of development. However, successful fabrication techniques were developed for the attachment of DNA to silicon, with excellent discrimination between patterned and un-patterned regions with no visible non-specific attachment. The fabrication methodology could be applied to non-diffraction based sensors where DNA patterning on silicon is desired.

The optical apparatus developed for capturing $2-D$ diffraction pattern images on a CCD camera worked very well, with captured images from metal test patterns agreeing with the theoretical Fourier transforms. The $1-D$ diffraction grating characterisation system worked very well and could have alternative applications such as protein detection, where the large size of captured molecules generates a larger change in diffraction by an increase in step height.

Both $1-D$ and $2-D$ methods suggest that reliable DNA detection by diffraction should be possible if surface uniformity could be improved, but the optimum way to achieve this would be by using a non-reflective substrate. With proven reliable detection of directly complementary DNA-labelled gold colloids, the sensor could then be used for analysis of genomic DNA. The high reflectivity of silicon at optical wavelengths also creates a large background diffraction signal prior to the addition of gold colloids. To overcome the large inherent diffraction signal, the uniformity of surface coverage, line width and step height has to be more uniform to reduce the noise level compared to the signal change associated with

the gold colloids.

7.3 Future Work

7.3.1 Signal to Noise Improvements

One of the main drawbacks with using silicon as a substrate has been the high reflectivity of the surface. This causes a strong background reflection for the 2−D diffraction arrays. Additionally the surface can become roughened by the DNA attachment processing and this generates a significant level of scattering. For 1−D gratings, it means that there is strong diffraction prior to the addition of gold nanoparticles. A lower reflectivity surface would reduce the background diffraction and increase the reflectivity contrast between DNA regions and the substrate for the same quantity of gold nanoparticles. This would improve the signal to noise ratio and therefore the detection limit of the diffraction-sensor. A change of substrate material from silicon to glass would enable a very large reflectivity contrast to be achieved, since the background reflection may be greatly reduced by alignment of the incident linearly polarised light at the Brewster angle. This would offer a vastly improved signal to noise ratio and increase the detection sensitivity of the one-dimensional diffraction sensor. A similar approach would also improve the sensitivity for two-dimensional array diffraction too. Alternatively, an anti-reflection coating could be applied to the silicon and new attachment protocols developed to functionalise the anti-reflection surface.

Modelling of the diffraction gratings assumed gold nanoparticles effectively increased the reflectivity of the DNA lines. However, due to the small size of nanoparticles, they do not scatter equally in all directions [60]. Incorporation of Mie theory in to the modelling for diffraction gratings could improve the accuracy of diffraction predictions, taking account of the angular dependence of scattering. This may also explain some of the variability in which diffraction orders change in intensity by the largest amount, and some of the positional variability of diffraction from the gratings.

7.3.2 Application to Haplotyping

The DNA sensors tested so far have featured directly complementary gold-labelled DNA sequences to those immobilised on the silicon substrate. The next stage in development of the sensor would be to perform haplotype assays, where the gold nanoparticles would not be directly complementary to the surface oligonucleotides. Instead, the gold nanoparticles would be complementary to a particular sequence containing a SNP being screened for in a genomic DNA sample, and the oligonucleotide immobilised on the surface would be complementary to the other SNP of interest (see Figure 1.1, Section 1.4). If both sequences occur on the same DNA strand this would result in immobilisation of gold nanoparticles on the DNA patterned substrate. Detection would then be facilitated by the methodology developed in this thesis.

7.3.3 Alternative Approaches

Alternative approaches that could be investigated involve DNA spotting to create arrays on glass substrates. Different sequences can be positioned on different spots to produce distinguishable diffraction patterns which indicate which spot hybridise with complementary gold-labels. This could be carried in out in transmission rather than reflection, making the measurement setup more simplistic.

An alternative method for the fabrication of silicon devices for integration in micro electronics could be achieved using femto-second laser pulses to ablate the native oxide layer from the silicon. This selective oxide removal enables patterning of DNA on silicon since the alkene can only covalently bond where the oxide has been removed. The attachment can then be performed either thermally or by UV exposure with no need for a mask. This technique for attachment would enable a silicon microelectronic devices to be fabricated and then subsequently attach DNA, where as HF acid etching would attack the whole surface.

Another option which may enable multiplexing of assays is to use multiple wavelength illumination and to use different sized nanoparticles with different resonant wavelengths to monitor diffraction.

To conclude, this project has gone a long way towards creating a diffraction-based haplotype sensor with the development of an accurate diffraction grating characterisation apparatus.

Reduction of the background reflection from the substrate and improvements to the biochemical attachment would benefit both 1−D and 2−D sensor methodologies. The results obtained thus far highlight the exciting potential of future work.

Appendix A

Mask Fabrication

This section provides details on the stages involved in fabricating the diffraction grating masks, from the design of the original mask plate, through to the final replica gold mask on fused silica. Fabrication details are also provided for the fabrication of test patterns.

A.1 Mask Design and Preparation

Patterns fabricated for this project were devised theoretically for their diffraction properties and then a photolithographic mask design was produced using L-Edit^{TM} surface layout software (by Tanner EDA). The mask design was produced by either Innos^{TM} or RAL. Replica masks were made on fused silica (UV grade, UQG Ltd) for use in patterning silicon for DNA attachment and test patterns were created on glass and silicon substrates. Patterns were one-dimensional diffraction gratings and two-dimensional arrays.

To fabricate replica masks, samples were cleaned in acetone in an ultrasonic bath at $50°C$ for 20 minutes. Samples were rinsed in fresh acetone, isopropanol and blown dry with nitrogen gas. Samples were then cleaned in 'Piranha' solution (a mixture of hydrogen-peroxide and sulphuric acid in a $1:4$ ratio) for 20 minutes and then rinsed in de-ionised water. Samples were then finally cleaned in fuming nitric acid for 30 minutes to ensure all dirt had been removed and were rinsed again in de-ionised water and blown dry with nitrogen.

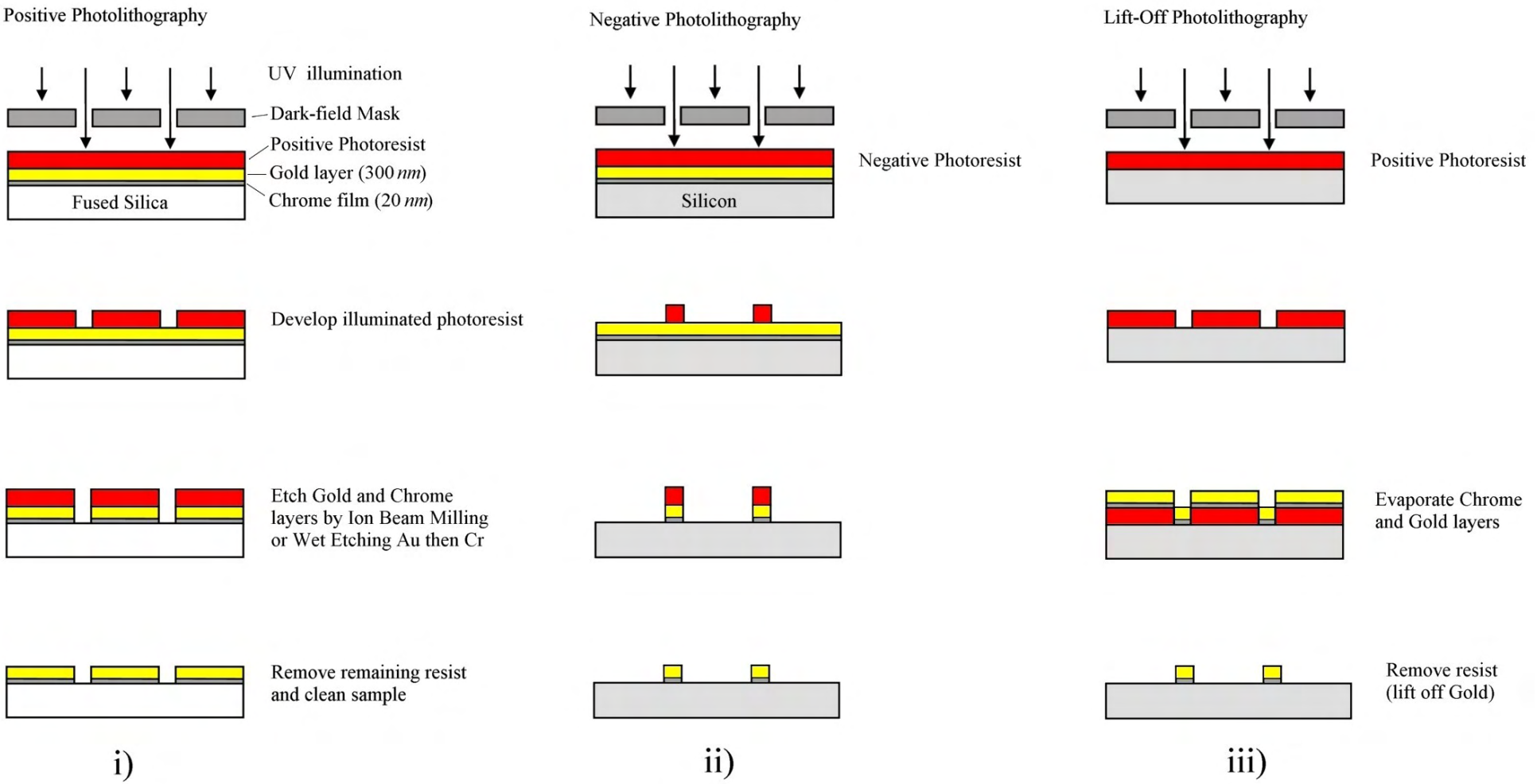

Figure A.1: Schematic illustration of photolithography processes used for the fabrication of replica masks and test patterns. i) Replica masks for DNA patterning were created using positive photolithography on fused silica. ii) Metal test patterns of the diffraction structures were created on silicon using negative photolithography, or iii) lift-off techniques.

Chrome-gold coating was used for producing replica masks on fused silica (for use in UV patterning of silicon with DNA) as described below. Positive photoresist was used to replicate the mask patterns and then samples were dry-etched using Ion-Beam Milling. An outline schematic of the steps involved in fabricating a dark-field replica mask from the original light-field design is detailed in Figure A.1 (i).

A.1.1 Chrome-Gold Coating

Cleaned samples were placed in an Edwards coater for evaporation of thin films in a vacuum chamber. A seed layer of chrome was used to ensure good adhesion of gold to the substrate. Current was passed through a chrome filament until it started to be evaporated (rates should be approximately 1 nm/s) and a 20 nm layer was deposited. A tungsten filament wound with gold wire was then heated until the desired thickness of gold was evaporatively coated (typically $250-300$ nm). The evaporative coating method was the same for silicon and glass test patterns and also for lift-off photolithography.

A.2 Photolithography Processes

After cleaning the samples, photoresist was applied through a 2.0 μm filter and then samples were spun at 6000 rpm for 60 seconds to produced a uniform thin film (≈ 1.0 μm in depth). Samples were soft-baked at $90°C$ for 30 minutes and were then ready for photo-patterning by UV light. A Karl Suss MA-6 mask-aligner was used to control the UV illumination (14 mW/cm^2 at 365 nm) and exposure time (typically 4.0 seconds), to ensure hard-contact between the mask and the sample and for alignment purposes.

Using Positive Resist

Positive photoresist (e.g. Shipley Microposit S1813) was used to directly replicate the original mask plate. When soft-baked for 30 minutes at $90°C$ positive photoresist attaches to the substrate. Upon illumination with UV light (365 nm), the bonding is photo-destroyed. Subsequently photoresist was removed by developer (Microposit MF-319) in the regions where it was illuminated, creating a direct replica of the original design in photoresist (see Figure A.1 i). After developing, samples were washed in de-ionised water and blown dry with nitrogen. Samples were then hard-baked at $120°C$ for 1 hour.

Using Negative Resist

Shipley Negative resist was used to fabricate test patterns with the opposite structure to that of the original mask plate (see Figure A.1 ii). Negative resist was used for fabricating test gratings of solid gold lines on silicon and glass. After illumination, samples were placed in Shipley negative resist developer for 30 seconds, followed by 10 seconds in a 50/50 mixture of developer and butyl acetate, another 10 seconds in butyl acetate and then rinsed with de-ionised water and blown dry.

Wet Etching

Photoresist patterned samples were placed in gold etchant for $10 - 20$ seconds. Unprotected regions of gold were dissolved. Samples were rinsed in de-ionised water and blown dry before adding to chrome etchant for 30 seconds to remove exposed regions. Regions protected on the surface by photoresist remain intact but care must be taken not to over-etch samples as undercutting may take place. Due to the nature of wet-etching the features produced will not have vertical walls. Wet etching was used for creating test gratings on silicon and glass, where the features were less critical than for the replica masks used for DNA patterning.

A.2.1 Reactive Ion-Beam Etching

Reactive Ion-Beam Etching or Ion-Beam Milling is a technique employed to transfer a photoresist pattern to samples with greater feature detail than achievable by using wet-etching. Argon gas was subjected to an acceleration voltage of 500 V and 125 mA current to generate a plasma and Ar^+ ions bombard the sample, eroding the surface. The photoresist covered region has a slower etch rate than the exposed gold and also has thickness of approximately 1 μm compared to 300 nm for the gold layer. This enables the exposed gold region to be totally eroded away whilst the photoresist protects the unpatterned areas. Ion-beam milling was used to fabricate masks because it generates patterns with vertical walls and more consistent feature sizes than wet-etching.

Masks were inspected in transmission on an optical microscope after milling to ensure there was a good optical contrast between the milled region compared to transmission through the gold. This enabled quality control of the masks, rejecting replicas where the gold featured pinholes or where windows were partially obscured. It was important to have an accurate replica mask as this limited the feature quality achievable by DNA patterning of silicon

with the fused silica mask. A KLA-Tencor P-16 Profiler was used to examine the surface topography of the replica masks. The profiler was fitted with a 100 nm radius tip, but was sensitive to 1 nm height resolution.

A.2.2 Lift-Off Procedures

Some test samples were created using the 'lift-off' technique (see Figure A.1 iii). Photoresist patterns were created directly on the substrate preceding evaporative coating of chrome-gold. Prior to developing S1813 photoresist, it was placed in dichlorobenzene for 5 minutes to toughen the top surface. When developed, this causes undercutting of the resist features. When subsequent evaporative coating takes place this generates a discontinuous film as the side walls of features are not coated. After coating, the gaps enable acetone to dissolve the photoresist and lift-off excess coating material with it.

Appendix B

Photodetectors

Photodetectors were built in-house specifically for measuring diffraction gratings used in this project. A 15 mm^2 area single element silicon photodiode (OSD15 − 5T) was supplied by RS components. An amplified detector circuit was built with the aid of Dr Stuart Russell. The circuit diagram is shown in Figure B.1. A TLO72 operational amplifier ('op-amp') was used to amplify the light-induced current from the photodiode. Four different resistors were used to increase the gain to the required amount depending on the diffraction order being measured, selectable by a switch located on the detector housing. The power scaling circuit used for the op-amp is shown in Figure B.2.

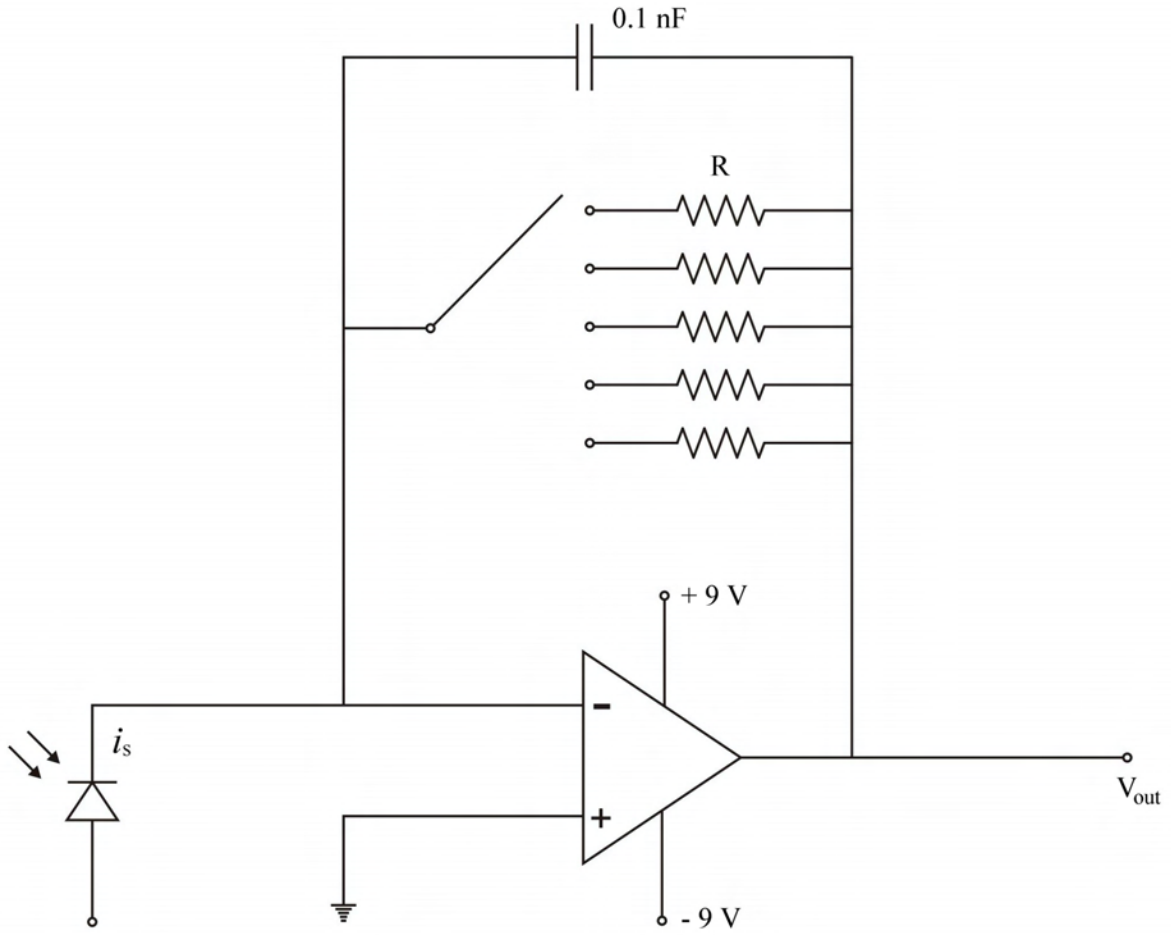

Figure B.1: Photo-detector circuit diagram, consisting of an operational amplifier with switchable gain.

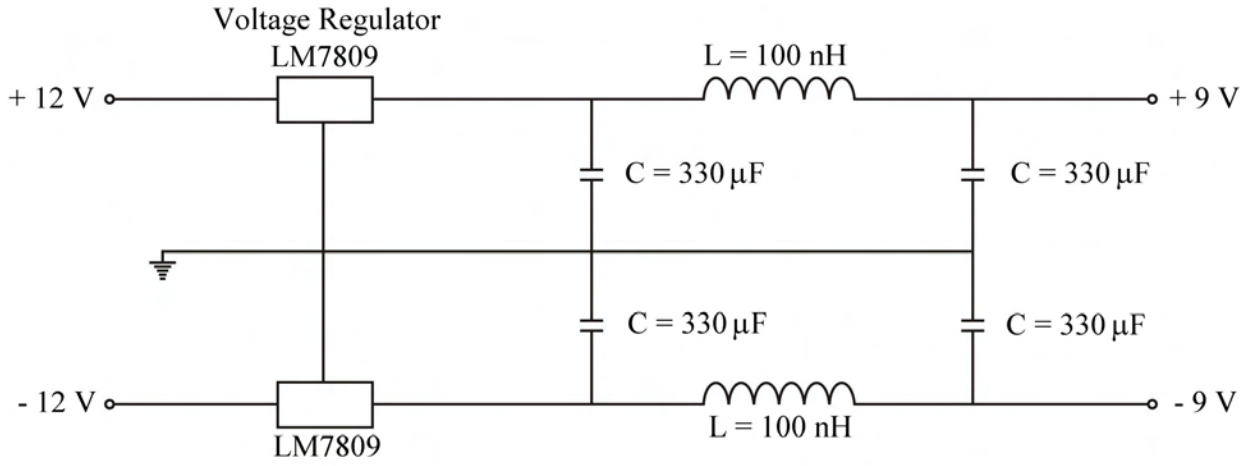

Figure B.2: Power-scaling and smoothing circuit for the op-amp.

Appendix C

Fourier Transform Program

A program was written in MATLAB^{TM}to compute the Fourier transform (FT) of an image (shown in Figures C.1 and C.2). The program used various in-built MATLAB^{TM}functions (shown in bold-type), including 'fft2', which calculates the fast Fourier transform of a two-dimensional matrix. Comments explaining parts of the program are shown in green and the remaining text consists of variables and active parts of the program.

Images were zero-padded to the next power of 2 to decrease processing time and to ensure accurate transforms due to the way MATLAB^{TM}works and calculates the Fourier transform using 'fft2'. The images needed to be zero-padded to enable the maximum detail from the input image to be visible in the FT image.

The program read-in the images from a file directory (or 'folder'), zero-padded the image size to 2048×2048 pixels and then computed the Fourier transform of each image. The original image was then plotted along side the FT image. The larger the zero-padding the larger the diffraction pattern in the FT plot, but in general the central region was 'zoomed-in' on to plot and visualise the most significant central detail of the Fourier transform. Depending on the contrast of the input image, the average value could be subtracted from the input image, or an intensity log-plot used to enable the detail to be displayed.

```
% PROGRAM 'imagefft001.m'                                    Andrew M Weld
%
% image fourier transform program - with zero-padding
%
clear
filedir='D:\Documents and settings\amw\My Documents\Matlab\dots01';
directory=pwd
tic
%%%%%%%%%%%%%%%%%%%%%%%%%%%%%% VARIABLES %%%%%%%%%%%%%%%%%%%%%%%%%%%%%%%%
cw2=201;            %  Central width (pixels) to zoom in on IFT plot (2D)

%%%%%%%%%%%%%%%%%%%%%%%%%%%%%% FUNCTIONS %%%%%%%%%%%%%%%%%%%%%%%%%%%%%%%%
files=dir(fullfile(filedir, '*.jpg'));
                           % List '*.x' files in directory DIR to matrix
n=size(files,1);           %     SIZE finds number of files in directory

for i=1:n,                 % Do loop to transform all files in directory
                           %                       Using the FOR function
  filen=files(i).name;     % Selects file .NAME from dir contents matrix
  filename=filen(:,1:size(filen,2)-4);    % Removes '.jpg' from filename
  dfp=imread([filedir,'/',filen]);        % IMREAD reads in image
                           %   IMREAD reads in diffraction pattern image
%%%%%%%%%%%%%%%%%%%%%%%%% 2-D DIFFRACTION GRATING %%%%%%%%%%%%%%%%%%%%%%%%%
dfg(:,:)=dfp(:,:,1);       %            as colour images have 3 channels

[h,w]=size(dfg);        % Measures the dimensions of the image using SIZE
if w<=h                 % Ensures smallest image length used for cropping
    h=w;
end
x=(w-h)/2;                      % x: size difference to crop off each side
crop=dfg;%(1:h, x:[w-x-1]);      %   Crops image to a square size to avoid
                                 %    distortion of the FFT image produced
dfg=double(crop);
%av2=dfg-mean(mean(dfg));        %   Subtract mean, incr relative contrast
av2=dfg;
npsz=nextpow2(size(dfg,2));
if npsz==7
    x2=4;
end
if npsz==8
    x2=3;
end
if npsz==9
    x2=2;
end
if npsz==10
    x2=1;
end
if npsz==11
    x2=0;
end
%x2=0;     %set x2=0 to prevent any extra zeropadding
v=mean(mean(dfg));
lrgmat=zeros(2^(nextpow2(size(dfg,1))+x2), ...
                                        2^((nextpow2(size(dfg,1))+x2)));
```

Figure C.1: Image Fourier transform program - part (i).

```
%lrgmat=av2;

ift2=ifft2(lrgmat);
absift2=abs(ift2);
shift2=fftshift(absift2);
%shift2=log(shift2);   % uncomment to take log of image
sx=round(size(shift2,1)/2);
sy=round(size(shift2,2)/2);
smallfft2=shift2(sx-cw2+1:sx+cw2+1, sy-cw2+1:sy+cw2+1);

fig1=figure(1);    % Generates a figure to show the following subplots
  subplot(1,2,1)
    set(gcf, 'PaperPositionMode', 'manual');
    set(gcf, 'PaperUnits', 'inches');
    set(gcf, 'PaperPosition', [1 1 14.6 6]);
    imagesc(lrgmat)
    colormap(gray);
    title('Diffraction Array and Fourier Transform of')
  subplot(1,2,2)
    imagesc(shift2);
    title(['pattern  ' filename ])
saveas(fig1,[filedir '/transform/',filename,'fig1.png'])

fig2=figure(2);
  subplot(1,2,1)
    set(gcf, 'PaperPositionMode', 'manual');
    set(gcf, 'PaperUnits', 'inches');
    set(gcf, 'PaperPosition', [1 1 14.6 6]);
    imagesc(av2)
    colormap(gray);
    title('Diffraction Array and Fourier Transform of')
  subplot(1,2,2)
    imagesc(smallfft2)
    title(['pattern  ' filename ])
saveas(fig2,[filedir '/transform/',filename,'fig2.png'])

fig3=figure(3);
    set(gcf, 'PaperPositionMode', 'manual');
    set(gcf, 'PaperUnits', 'inches');
    set(gcf, 'PaperPosition', [1 1 12.6 12]);
    imagesc(smallfft2)
    colormap(gray);
saveas(fig3,[filedir '/transform/',filename,'fig3.png'])

clear dfg shift2 av2 lrgmat ift2 absift2
end
toc
Program State='finished'
```

Figure C.2: Image Fourier transform program - part (ii).

References

[1] F. S. Collins, M. Morgan, and A. Patrinos, "The human genome project: Lessons from large-scale biology," *Science* **300**, pp. 286–290, 2003.

[2] A. Dove, "Sects, strangers, and drugs: Genotyping gets specific," *Genomics and Proteomics* **5**(7), pp. 19–22, 2005.

[3] E. T. Mollova, "Single-molecule fluorescence of nucleic acids," *Current Opinion in Chemical Biology* **6**, pp. 823–828, 2002.

[4] D. Tsuchiya and M. Taga, "Application of fibre-FISH (fluorescence *insitu* hybridisation) to filamentous fungi: visualisation of the rRNA gene cluster of the ascomycete *Cochliobolusheterostrophus*," *Microbiology* **147**, pp. 1183–1187, 2001.

[5] R. Jin, G. Wu, Z. Li, C. A. Mirkin, and G. C. Schatz, "What Controls the Melting Properties of DNA-Linked Gold Nanoparticle Assemblies?," *Journal of the American Chemical Society* **125**(6), pp. 1643–1654, 2003.

[6] J. J. Storhoff, S. S. Marla, P. Bao, S. Hagenow, H. Mehta, A. Lucas, V. Garimella, T. Patno, W. Buckingham, W. Cork, and U. R. Muller, "Gold nanoparticle-based detection of genomic DNA targets on microarrays using a novel optical detection system," *Biosensors and Bioelectronics* **19**(8), pp. 857–883, 2004.

[7] S.-J. Park, T. A. Taton, and C. A. Mirkin, "Array-based electrical detection of DNA with nanoparticle probes," *Science* **295**, pp. 1503–1506, 2002.

[8] A. J. Brookes, "The essence of SNPs," *Gene* **234**, pp. 177–186, 1999.

[9] R. Jenison, S. Yang, A. Haeberli, and B. Polisky, "Interference-based detection of nucleic acid targets on optically coated silicon," *Nature Biotechnology* **19**, pp. 62–65, 2001.

[10] F. Morhard, J. Pipper, R. Dahint, and M. Grunze, "Immobilization of antibodies in micropatterns for cell detection by optical diffraction," *Sensors and Actuators B* **70**, pp. 232–242, 2000.

[11] F. Yu, D. Yao, and W. Knoll, "Oligonucleotide hybridization studied by a surface plasmon diffraction sensor (SPDS)," *Nucleic Acids Reasearch* **32**(9), p. e75, 2004.

[12] P. P. Banada, S. Guo, B. Bayraktar, E. Bae, B. Rajwa, J. P. Robinson, E. D. Hirleman, and A. K. Bhunia, "Optical forward-scattering for detection of listeria monocytogenes and other listeria species," *Biosensors and Bioelectronics* **22**(8), pp. 1664–1671, 2007.

[13] R. B. Millington, A. G. Mayes, J. Blyth, and C. R. Lowe, "A holographic sensor for proteases," *Analytical Chemistry* **67**(23), pp. 4229–4233, 1995.

[14] R. C. Bailey, K. J. Stevenson, and J. T. Hupp, "Assembly of micropatterned colloidal gold thin films via microtransfer molding and electrophoretic deposition," *Advanced Materials* **12**(24), pp. 1930–1934, 2000.

[15] M. C. Pirrung, "How to Make a DNA Chip," *Angewandte Chemie International Edition* **41**, pp. 1276–1289, 2002.

[16] H. B. Yin, T. Brown, R. Greef, J. S. Wilkinson, and T. Melvin, "Chemical modification and micropatterning of Si(1 0 0) with oligonucleotides," *Microelectronic Engineering* **73**(74), pp. 830–836, 2004.

[17] B. Lewin, *Genes*, Oxford University Press, 7th ed., 2000.

[18] J. D. Watson and F. H. C. Crick, "A structure for deoxyribose nucleic acid," *Nature* **171**, pp. 737–738, 1953.

[19] W. Saenger, *Principles of Nucleic Acid Structure*, Springer-Verlag, 1984.

[20] Gene Center of the University of Munich, *Fluorescence in situ hybridisation (FISH).* Website: http://www.lmb.uni-muenchen.de/groups/Biostruc/chap-08/chap-08-slides.html.

[21] D. L. Hartl and E. W. Jones, *Genetics: Principles and Analysis*, Jones and Bartlett Publishers Inc., 4th ed., 1998.

[22] Ed Rybicki, Department of Molecular and Cell Biology, University of Cape Town, *PCR Primer Design and Reaction Optimisation.* Website: http://www.mcb.uct.ac.za/manual/pcroptim.htm.

[23] The International Human Genome Mapping Consortium, "Finishing the euchromatic sequence of the human genome," *Nature* **431**, pp. 932–945, 2004.

[24] B. Lewin, *Genes*, Oxford University Press, 8th ed., 2004.

[25] H. Lodish, A. Berk, S. L. Zipursky, P. Matsudaira, D. Baltimore, and J. E. Darnell, *Molecular Cell Biology*, W H Freeman and Company, 4th ed., 2001.

[26] N. C. Seeman, "DNA engineering and its application to nanotechnology," *Trends in Biotechnology* **17**(11), pp. 437–443, 1999.

[27] S. M. Waybright, C. P. Singleton, K. Wachter, C. J. Murphy, and U. H. F. Bunz, "Oligonucleotide-directed assembly of materials: Defined oligomers," *Journal of the American Chemical Society* **123**(9), pp. 1828–1833, 2001.

[28] E. Winfree, F. Liu, L. A. Wenzler, and N. C. Seeman, "Design and self-assembly of two-dimensional nanocrystals," *Nature* **394**, pp. 539–544, 1998.

[29] N. C. Seeman, "DNA nanotechnology: Novel DNA constructions," *Annual Review of Biophysics and Biomolecular Structure* **27**, pp. 225–248, 1998.

[30] J. J. Storhoff and C. A. Mirkin, "Programmed materials synthesis with DNA," *Chemical Reviews* **99**(7), pp. 1849–1862, 1999.

[31] W. S. Klug and M. R. Cummings, *Essentials of Genetics*, 3rd ed., 1999.

[32] H. M. Kingston, *ABC of Clinical Genetics*, BMJ Publishing Group, 2nd ed., 1997.

[33] L. W. Hillier *et al*, "Generation and annotation of the DNA sequences of human chromosomes 2 and 4," *Nature* **434**, pp. 724–731, 2005.

[34] D. Latchman, *Basic Molecular and Cell Biology*, BMJ Publishing Group, 3rd ed., 1997.

[35] M. Stoneking, "Single nucleotide polymorphisms: From the evolutionary past...," *Nature* **409**, pp. 821–822, 2001.

[36] W.-H. Li and L. A. Sadler, "Low Nucleotide Diversity in Man," *Genetics* **129**, pp. 513–523, 1991.

[37] The Chimpanzee Sequencing and Analysis Consortium, "Initial sequence of the chimpanzee genome and comparison with the human genome," *Nature* **437**, pp. 69–87, 2005.

[38] National Human Genome Research Institute, NIH News, *New Genome Comparison Finds Chimps, Humans Very Similar at the DNA Level*. Website: http://www.genome.gov/15515096.

[39] A. Chakravarti, "Single nucleotide polymorphisms: ... to a future of genetic medicine," *Nature* **409**, pp. 822–823, 2001.

[40] Human Genome Project Information website: http://www.ornl.gov/sci/techresources/Human_Genome/faq/snps.shtml.

[41] National Center for Biotechnology Information website: http://www.ncbi.nlm.nih.gov/About/primer/snps.html.

[42] S. Rodriguez, T. R. Gaunt, S. D. O'Dell, X. H. Chen, D. Gu, E. Hawe, G. J. Miller, S. E. Humphries, and I. N. Day, "Haplotypic analyses of the IGF2-INS-TH gene cluster in relation to cardiovascular risk traits," *Human Molecular Genetics* **13**(7), pp. 715–725, 2004.

[43] Applied Biosystems, *BloodPrep Chemistry*. Website: http://docs.appliedbiosystems.com/pebiodocs/00106734.pdf.

[44] W. M. Barnes, "PCR amplification of up to 35-kb DNA with high fidelity and high yield from λ bacteriophage templates," *Nature* **434**, pp. 724–731, 2005.

[45] C. Ding and C. R. Cantor, "Direct molecular haplotyping of long-range genomic DNA with M1-PCR," *Proceedings of the National Academy of Sciences of the United States of America* **100**(13), pp. 7449–7453, 2003.

[46] National Human Genome Research Institute, *Principles of FISH.* Website: http://www.genome.gov/Pages/Hyperion/DIR/VIP/Glossary/Illustration/Pdf/fish.pdf.

[47] Unistel Medical Laboratories, *Principles of FISH.* Website: http://admin.sun.ac.za/kie/unistel/medical _labs/fish.htm.

[48] J. A. Creighton, C. G. Blatchford, and M. G. Albrecht, "Plasma resonance enhancement of Raman scattering by pyridine absorbed on silver or gold sol particles of size comparable to the excitation wavelength," *Journal of the Chemical Society, Faraday Transactions II* **75**, pp. 790–798, 1979.

[49] S. R. Emory, W. E. Haskins, and S. Nie, "Direct Observation of Size-Dependent Optical Enhancement in Single Metal Nanoparticles," *Journal of the American Chemistry Society* **120**(31), pp. 8009–8010, 1998.

[50] K. Faulds, L. Stewart, W. E. Smith, and D. Graham, "Quantitative detection of dye labelled DNA using surface enhanced resonance Raman scattering SERRS from silver nanoparticles," *Talanta* **67**, pp. 667–671, 2005.

[51] L. Nirmal, M. Brus, "Luminescence Photophysics in Semiconductor Nanocrystals," *Accounts of Chemical Research* **32**(5), pp. 407–414, 1999.

[52] J. J. Storhoff, *DNA Linked Gold Nanoparticle Network Materials: Properties and Applications.* PhD thesis, 2000.

[53] R. G. Freeman, K. C. Grabar, K. J. Allison, R. M. Bright, J. A. Davis, A. P. Guthrie, M. B. Hommer, M. A. Jackson, P. C. Smith, D. G. Walter, and M. J. Natan, "Self-assembled metal colloid monolayers: An approach to SERS substrates," *Science* **267**, pp. 1629–1632, 1995.

[54] A. K. Boal, F. Ilhan, J. E. DeRouchey, T. Thurn-Albrecht, T. P. Russell, and V. M. Rotello, "Self-assembly of nanoparticles into structured spherical and network aggregates," *Nature* **404**, pp. 746–748, 2000.

[55] C. Kiely, J. Fink, M. Burst, D. Bethell, and D. Schiffrin, "Spontaneous ordering of bimodal ensembles of nanoscopic gold clusters," *Nature* **396**, pp. 444–446, 1998.

[56] K.-S. Lee and M. A. El-Sayed, "Dependence of the enhanced optical scattering efficiency relative to that of absorption for gold metal nanorods on aspect ratio, size, end-cap shape and medium refractive index," *Journal of Physical Chemistry B* **109**(43), pp. 20331–20338, 2005.

[57] S. Link and M. A. El-Sayed, "Size and temperature dependence of the plasmon absorption of colloidal gold nanoparticles," *Journal of Physical Chemistry B* **103**, pp. 4212–4217, 1999.

[58] C. R. Lawrence, N. J. Geddes, and D. N. Furlong, "Surface plasmon resonance studies of immunoreactions utilizing disposable diffraction gratings," *Biosensors & Bioelectronics* **11**(4), pp. 389–400, 1996.

[59] S. Empedocles and M. Bawendi, "Spectroscopy of single CdSe nanocrystallites," *Accounts of Chemical Research* **32**(5), pp. 389–396, 1999.

[60] C. F. Bohren and D. R. Huffman, *Absorption and Scattering of Light by Small Particles*, Wiley-VCH, 2004.

[61] S. J. Oldenburg, R. D. Averitt, S. L. Westcott, and N. J. Halas, "Nanoengineering of optical resonances," *Chemical Physics Letters* **288**, pp. 243–247, 1998.

[62] L. M. Liz-Marazan, M. Giersig, and P. Mulvaney, "Synthesis of nanosized gold-silica core-shell particles," *Langmuir* **12**(18), pp. 4329–4335, 1996.

[63] M. Quinten and U. Kreiberg *Surface Science* **172**, pp. 557–577, 1986.

[64] R. C. Mucic, *Synthetically Programmable Nanoparticle Assembly Using DNA*. PhD thesis, 1999.

[65] C. S. Weisbecker, M. V. Merritt, and G. M. Whitesides, "Molecular self-assembly of aliphatic thiols on gold colloids," *Langmuir* **12**(16), pp. 3763–3772, 1996.

[66] Z. Li, R. Jin, C. A. Mirkin, and R. L. Letsinger, "Multiple thiol-anchor capped DNA-gold nanoparticle conjugates," *Nucleic Acids Research* **30**(7), pp. 1558–1562, 2002.

[67] D. Murphy, R. Eritja, and G. Redmond, "Monitoring denaturation behaviour and comparative stability of DNA triple helices using oligonucleotide-gold nanoparticle conjugates," *Nucleic Acids Research* **32**(7), p. e65, 2004.

[68] Y. Cao, R. Jin, and C. A. Mirkin, "DNA-modified core-shell Ag/Au nanoparticles," *Journal of the American Chemical Society* **123**(32), pp. 7961–7962, 2001.

[69] Y. Maeda, H. Tabata, and T. Kawai, "Two-dimensional assembly of gold nanoparticles with a DNA network template," *Applied Physics Letters* **79**(8), pp. 1181–1183, 2001.

[70] J. Zhang, Y. Liu, Y. Ke, and H. Yan, "Periodic square-like gold nanoparticle arrays templated by self-assembled 2D DNA nanogrids on a surface," *Nano Letters* **6**(2), pp. 248–251, 2006.

[71] C. M. Niemeyer, B. Ceyhan, M. Noyong, and U. Simon, "Bifunctional DNA-gold nanoparticle conjugates as building blocks for the self-assembly of cross-linked particle layers," *Biochemical and Biophysical Research Communications* **311**, pp. 995–999, 2003.

[72] M. G. Warner and J. E. Hutchinson, "Linear assemblies of nanoparticles electrostatically organised on DNA scaffolds," *Nature Materials* **2**, pp. 272–277, 2003.

[73] H. Li, S. H. Park, J. H. Reif, T. H. LaBean, and H. Yan, "DNA-templated self-assembly of protein and nanoparticle linear arrays," *Journal of the American Chemical Society* **126**(2), pp. 418–419, 2004.

[74] E. Braun, Y. Eichen, U. Sivan, and G. Ben-Yoseph, "DNA-templated assembly and electrode attachment of a conducting silver wire," *Nature* **391**, pp. 775–778, 1998.

[75] M. S. Urdea, B. D. Warner, J. C. Running, M. Stempien, J. Clyne, and T. Horn, "A comparisson of non-radioisotopic hybridisation assay methods using fluorescent, chemiluminescent and enzyme labeled synthetic oligodeoxyribonucleotide probes," *Nucleic Acid Research* **16**(11), pp. 4937–4956, 1988.

[76] A. Maxam and W. Gilbert, "A new method of sequencing DNA," *Proceedings of the National Academy of Sciences, USA* **74**(2), pp. 560–564, 1977.

[77] F. Sanger, S. Nicklen, and A. Coulson, "DNA sequencing with chain-terminating inhibitors," *Proceedings of the National Academy of Sciences, USA* **74**(12), pp. 5463–5467, 1977.

[78] A. D. Roses, "Pharmacogenetics and the practice of medicine," *Nature* **405**(15), pp. 857–865, 2000.

[79] The International Human Genome Mapping Consortium, "A physical map of the human genome," *Nature* **409**, pp. 934–941, 2001.

[80] S. B. Carroll, "Genetics and the making of homo sapiens," *Nature* **422**, pp. 849–857, 2003.

[81] F. S. Collins, E. D. Green, A. E. Guttmacher, and M. S. Guyer, "A vision for the future of genomics research," *Nature* **422**, pp. 835–847, 2003.

[82] The International HapMap Consortium, "A haplotype map of the human genome," *Nature* **437**, pp. 1299–1320, 2005.

[83] M. E. Frazier, G. M. Johnson, D. G. Thomassen, C. E. Oliver, and A. Patrinos, "Realizing the potential of the genome revolution: The genomes to life program," *Science* **300**, pp. 290–29, 2003.

[84] A. Ulman, "Formation and structure of self-assembled monolayers," *Chemical Reviews* **96**, pp. 1533–1554, 1996.

[85] N. Zammatteo, L. Jeanmart, S. Hamels, S. Courtois, P. Louette, L. Hevesi, and J. Remacle, "Comparison between Different Strategies of Covalent Attachment of DNA to Glass Surfaces to Build DNA Microarrays," *Analytical Biochemistry* **280**(1), pp. 143–150, 2000.

[86] S. Ye and I. N. M. Day, *Microarrays and Microplates: Applications in Biomedical Sciences*, BIOS Scientific Publishers Limited, 1st ed., 2003.

[87] D. H. Geschwind, "DNA microarrays: translation of the genome from laboratory to clinic," *The Lancet Neurology* **2**, pp. 275–282, 2003.

[88] D. D. Shoemaker, E. E. Schadt, C. D. Armour, Y. D. He, P. Garrett-Engele, P. D. McDonagh, P. M. Loerch, A. Leonardson, P. Y. Lum, G. Cavet, L. F. Wu, S. J. Altschuler, S. Edwards, J. King, J. S. Tsang, G. Schimmack, J. M. Schelter, J. Koch, M. Ziman, M. J. Marton, B. Li, P. Cundiff, T. Ward, J. Castle, M. Krolewski, M. R. Meyer, M. Mao, J. Buchard, M. J. Kidd, H. Dai, J. W. Phillips, P. S. Linsley, R. Stoughton, S. Scherer, and M. S. Boguski, "Experimental annotation of the human genome using microarray technology," *Nature* **409**, pp. 922–927, 2001.

[89] L. Li, X. Wang, V. Stolc, X. Li, D. Zhang, N. Su, W. Tongprasit, S. Li, Z. Cheng, J. Wang, and X. Wang-Deng, "Genome-wide transcription analyses in rice using tiling microarrays," *Nature Genetics* **38**(1), pp. 124–129, 2006.

[90] C. J. Kim, J. K. Jeong, M. Park, T. S. Park, T. C. Park, S. E. Namkoong, and J. S. Park, "HPV oligonucleotide microarray-based detection of HPV genotypes in cervical neoplastic lesions," *Gynecologic Oncology* **89**, pp. 210–217, 2003.

[91] S. Ramaswamy and C. M. Perou, "DNA microarrays in breast cancer: the promise of personalised medicine," *The Lancet* **361**, pp. 1576–1577, 2003.

[92] P.-L. Wang, K. Ohura, T. Fujii, M. Oido-Mori, Y. Kowashi, M. Kikuchi, Y. Suetsugu, and J. Tanaka, "DNA microarray analysis of human gingival fibroblasts from healthy and inflammatory gingival tissues," *Biochemical and Biophysical Research Communications* **305**, pp. 970–973, 2003.

[93] K. E. Vrana, W. M. Freeman, and M. Aschner, "Use of microarray technologies in toxicology research," *NeuroToxicology* **24**, pp. 321–332, 2003.

[94] M. Sedlak, H. J. Edenberg, and N. W. Y. Ho, "DNA microarray analysis of the expression of the genes encoding the major enzymes in ethanol production during glucose and xylose co-fermentation by metabolically engineered saccharomyces yeast," *Enzyme and Microbial Technology* **33**, pp. 19–28, 2003.

[95] S. T. Hou, K. G. Becker, A. Baggley, G. Chen, and J. Webster, "High-density DNA microarray analysis of gene expression following transient focal cerebral ischemia in mouse," *International Congress Series* **1252**, pp. 45–56, 2003.

[96] G. Boas, "Novel microarrays could help improve drug discovery," *Biophotonics International* **12**(12), pp. 18–20, 2005.

[97] L. Stryer, *Biochemistry*, W. H. Freeman, 4th ed., 1995.

[98] M. Schena, D. Shalon, R. Heller, A. Chai, P. O Brown, and R. W. Davis, "Parallel human genome analysis: Microarray-based expression monitoring of 1000 genes," *Proceedings of the National Academy of Sciences of the United States of America* **93**(20), pp. 10614–10619, 1996.

[99] M. May, "Genotyping scales up and packs in the data," *Genomics & Proteomics* **3**(9), pp. 46–48, 2003.

[100] Affymetrix website:
http://www.affymetrix.com/products/arrays/specific/500k.affx.

[101] R. J. Redkar, N. A. Schultz, V. Scheumann, L. A. Burizo, D. A. Haines, E. Metwalli, O. Becker, and S. D. Conzone, "Signal and Sensitivity Enhancement Through Optical Interference Coating for DNA and Protein Microarray Applications," *Journal of Biomolecular Techniques* **17**(2), pp. 122–130, 2006.

[102] T. Ha, T. Enderle, D. F. Ogletree, D. S. Chemla, P. R. Selvin, and S. Weis, "Probing the interaction between two single molecules: Fluorescence resonance energy transfer between a single donor and a single acceptor," *Proceedings of the National Academy of Sciences, USA* **93**, pp. 6264–6268, 1996.

[103] T. Ha, "Single-molecule fluorescence methods for the study of nucleic acids," *Current Opinion in Structural Biology* **11**, pp. 287–292, 2001.

[104] A. A. Deniz, T. A. Laurence, M. Dahan, D. S. Chemla, P. G. Schultz, and S. Weiss, "Ratiometric single-molecule studies of freely diffusing biomolecules," *Annual Review of Physical Chemistry* **52**, pp. 233–253, 2001.

[105] Z. Foldes-Papp, U. Demel, and G. P. Tilz, "Detection of single molecules: solution-phase single-molecule fluorescence correlation spectroscopy as an ultrasensitive, rapid and reliable system for immunological investigation," *Journal of Immunological Methods* **260**, pp. 117–124, 2002.

[106] P. Serwer and S. J. Hayes, "Partially condensed DNA conformations observed by single molecule fluorescence microscopy," *Biophysical Journal* **81**, pp. 3398–3408, 2001.

[107] P. R. Bianco, L. R. Brewer, M. Corzett, R. Balhorn, Y. Yeh, S. C. Kowalczykowski, and R. J. Baskin, "Processive translocation and DNA unwinding by individual RecBCD enzyme molecules," *Nature* **409**, pp. 374–378, 2001.

[108] S. R. Garden, G. J. Doellgast, K. S. Killham, and N. J. C. Strachan, "A fluorescent coagulation assay for thrombin using a fibre optic evanescent wave sensor," *Biosensors and Bioelectronics* **19**, pp. 737–470, 2004.

[109] M. I. Daneshvar, J. M. Peralta, G. A. Casay, N. Narayanan, L. Evans-III, G. Patony, and L. Strekowski, "Detection of biomolecules in the near-infrared spectral region via fiber-optic immunosensor," *Jounral of Immunological Methods* **226**, pp. 119–128, 1999.

[110] K. L. Brogan and D. R. Walt, "Optical fiber-based sensors: applications to chemical biology," *Current Opinion in Chemical Biology* **9**, pp. 494–500, 2005.

[111] D. J. Monk and D. R. Walt, "Optical fiber-based biosensors," *Analytical and Bioanalytical Chemistry* **379**, pp. 931–945, 2004.

[112] X. Wang and U. J. Krull, "Synthesis and fluorescence studies of thiazole orange tethered onto oligonucleotide: development of a self-contained DNA biosensor on a fiber optic surface," *Bioorganic and Medicinal Chemistry Letters* **15**, pp. 1725–1729, 2005.

[113] J. R. Epstein and R. Walt, David, "Fluorescence-based fibre optic arrays: a universal platform for sensing," *Chemical Society Reviews* **32**(4), pp. 203–214, 2003.

[114] A. Almadidy, J. Watterson, P. A. E. Piunno, S. Raha, I. V. Foulds, P. A. Horgen, A. Castle, and U. Krull, "Direct selective detection of genomic DNA from coliform using a fiber optic biosensor," *Analytica Chimica Acta* **461**, pp. 37–47, 2002.

[115] J. R. Epstein, A. P. K. Leung, K.-H. Lee, and R. Walt, David, "High-density microsphere-based fiber optic DNA microarrays," *Biosensors and Bioelectronics* **18**, pp. 541–546, 2003.

[116] N. C. Seeman and A. M. Belcher, "Emulating biology: Building nanostructures from the bottom up," *PNAS* **99**, pp. 6451–6455, 2002.

[117] C. R. Lowe, "Nanobiotechnology: the fabrication and applications of chemical and biological nanostructures," *Current Opinion in Structural Biology* **10**, pp. 428–434, 2000.

[118] W. Fritzsche, "DNA-gold conjugates for the detection of specific molecular interactions," *Reviews in Molecular Biotechnology* **82**, pp. 37–46, 2001.

[119] J. Reichert, A. Csaki, J. M. Kohler, and W. Fritzsche, "Chip-based optical detection of DNA hybridisation by means of nanobead labelling," *Analytical Chemistry* **72**(24), pp. 6025–6029, 2000.

[120] Y. Li, A. W. Wark, J. H. Lee, and R. M. Corn, "Single-nucleotide polymorphism genotyping by nanoparticle-enhanced surface plasmon resonance imaging measurements of surface ligation reactions," *Analytical Chemistry* **78**(9), pp. 3158–3164, 2006.

[121] A. Csaki, R. Moller, W. Straube, J. Kohler, and W. Fritzsche, "DNA monolayer on gold substrates characterized by nanoparticle labeling and scanning force microscopy," *Nucleic Acids Research* **29**(16), 2001.

[122] C. Mirkin, R. Letsinger, R. Mucic, and J. Storhoff, "A DNA-based method for rationally assembling nanoparticles into macroscopic materials," *Nature* **382**, pp. 607–609, 1996.

[123] C. M. Neimeyer and C. A. Mirkin, *Nanobiotechnology*, Wiley-VCH, 1st ed., 2004.

[124] J. J. Storhoff, A. A. Lazarides, R. C. Mucic, C. A. Mirkin, R. L. Letsinger, and G. C. Schatz, "What controls the optical properties of DNA-linked gold nanoparticle assemblies?," *Journal of the American Chemical Society* **122**(19), pp. 4640–4650, 2000.

[125] R. A. Reynolds, C. A. Mirkin, and R. L. Letsinger, "Homogeneous, nanoparticle-based quantitative colourimetric detection of oligonucleotides," *Journal of the American Chemical Society* **122**(15), pp. 3795–3796, 2000.

[126] M. Huber, T.-F. Wei, U. R. Muller, P. A. Lefebvre, S. S. Marla, and Y. P. Bao, "Gold nanoparticle probe-based gene expression analysis with unamplified total human RNA," *Nucleic Acids Research* **32**(18), p. e137, 2004.

[127] Y. P. Bao, M. Huber, T.-F. Wei, S. S. Marla, J. J. Storhoff, and U. R. Muller, "SNP identification in unamplified human genomic DNA with gold nanoparticle probes," *Nucleic Acids Research* **33**(2), p. e15, 2005.

[128] J. J. Storhoff, A. D. Lucas, V. Garimella, Y. P. Bao, and U. R. Muller, "Homogeneous detection of unamplified genomic DNA sequences based on colorimetric scatter of gold nanoparticle probes," *Nature Biotechnology* **22**(7), pp. 883–887, 2004.

[129] T. A. Taton, C. A. Mirkin, and R. L. Letsinger, "Scanometric DNA array detection with nanoparticle probes," *Science* **289**, pp. 1757–1760, 2000.

[130] D. G. Georganopoulou, L. Chang, J.-M. Nam, C. S. Thaxton, E. J. Mufson, W. L. Klein, and C. A. Mirkin, "Nanoparticle-based detection in cerebral spinal fluid of a soluble pathogenic biomarker for Alzheimer's disease," *Proceedings of the National Academy of Sciences of the United States of America* **102**(7), pp. 2273–2276, 2005.

[131] K. Glynou, P. C. Ioannou, T. K. Christopoulos, and V. Syriopoulou, "Oligonucleotide-Functionalised Gold Nanoparticles as Probes in a Dry-Reagent Strip Biosensor for DNA Analysis by Hybridisation," *Analytical Chemistry* **75**(16), pp. 4155–4160, 2003.

[132] D. A. Schultz, "Plasmon resonant particles for biological detection," *Current Opinion in Biotechnology* **14**, pp. 13–22, 2003.

[133] S. J. Oldenburg, C. C. Genick, K. A. Clark, and D. A. Schultz, "Base pair mismatch recognition using plasmon resonant particle labels," *Analytical Biochemistry* **309**, pp. 109–116, 2002.

[134] D. J. Maxwell, J. R. Taylor, and S. Nie, "Self-assembled nanoparticle probes for recognition and detection of biomolecules," *Journal of the American Chemical Society* **124**(32), pp. 9606–9612, 2002.

[135] B. Dubertret, M. Calame, and A. J. Libchaber, "Single-mismatch detection using gold-quenched fluorescent oligonucleotides," *Nature Biotechnology* **19**, pp. 365–370, 2001.

[136] M. Urban, R. Moeller, and W. Fritzsche, "A paralled readout system for an electrical DNA-hybridization assay based on a microstructured electrode array," *Review of Scientific Instruments* **74**, pp. 1077–1081, 2003.

[137] R. Moeller and W. Fritzsche, "Chip-based electrical detection of DNA," *IEE Proceedings-Nanobiotechnology* **152**(1), pp. 47–51, 2005.

[138] C.-Y. Tsai, T.-L. Chang, C.-C. Chen, F.-H. Ko, and P.-H. Chen, "An ultra sensitive DNA detection using gold nanoparticle multilayer in nano-gap electrodes," *Microelectronic Engineering* **78-79**, pp. 546–555, 2005.

[139] S. R. Nicewarner-Pena, R. G. Freeman, B. D. Reiss, L. He, D. J. Pena, I. D. Walton, R. Cromer, C. D. Keating, and M. J. Natan, "Submicrometer metallic barcodes," *Science* **294**, pp. 137–141, 2001.

[140] J. B.-H. Tok, F. Y. S. Chuang, M. C. Kao, K. A. Rose, S. S. Pannu, M. Y. Sha, G. Chakarova, S. G. Penn, and G. M. Dougherty, "Metallic striped nanowires as multiplexed immunoassay platforms for pathogen detection," *Angewandte Chemie* **118**, pp. 1–6, 2006.

[141] D. Hoffmann, J. O'Brien, D. Brennan, and M. Loughran, "Optically encoded silicon microbeads: Detection and characterisation in a microfluidic system," *Sensors and Actuators B* **122**(2), pp. 653–658, 2007.

[142] P. S. Eastman, W. Ruan, Doctolero, R. Nuttall, G. de Feo, J. S. Park, J. S. Chu, P. Cooke, J. W. Gray, S. Li, and F. F. Chen, "Qdot nanobarcodes for multiplexed gene expression analysis," *Nano Letters* **6**(5), pp. 1059–1064, 2006.

[143] R. C. Bailey and J. T. Hupp, "Large-scale resonance amplification of optical sensing of volatile compounds with chemoresponsive visible-region diffraction gratings," *Journal of the American Chemical Society* **124**(23), pp. 6767–6774, 2002.

[144] R. C. Bailey and J. T. Hupp, "Micropatterned polymeric gratings as chemoresponsive volatile organic compound sensors: Implications for analyte detection and identification via diffraction-based sensor arrays," *Analytical Chemistry* **75**(10), pp. 2392–2398, 2003.

[145] R. C. Bailey, J.-M. Nam, C. A. Mirkin, and J. T. Hupp, "Real-time multicolor DNA detection with chemoresponsive diffraction gratings and nanoparticle probes," *Journal of the American Chemical Society* **125**(44), pp. 13541–13547, 2003.

[146] R. Jenison, H. La, A. Haeberli, R. Ostroff, and B. Polisky, "Silicon-based Biosensors for Rapid Detection of Protein or Nucleic Acid Targets," *Clinical Chemistry* **47**(10), pp. 1894–1900, 2001.

[147] A. G. Mayes, J. Blyth, R. B. Millington, and C. R. Lowe, "Metal ion-sensitive holographic sensor," *Analytical Chemistry* **74**(15), pp. 3649–3657, 2002.

[148] J. Blyth, R. B. Millington, A. G. Mayes, E. R. Frears, and C. R. Lowe, "Holographic sensor for water in solvents," *Analytical Chemistry* **68**(7), pp. 1089–1094, 1996.

[149] R. B. Millington, A. G. Mayes, J. Blyth, and C. R. Lowe, "A hologram biosensor for proteases," *Sensors and Actuators B Chemical* **33**, pp. 55–59, 1996.

[150] A. G. Mayes, J. Blyth, R. B. Millington, and C. R. Lowe, "A holographic sensor based on a rationally designed synthetic polymer," *Journal of Molecular Recognition* **11**, pp. 168–174, 1998.

[151] A. G. Mayes, J. Blyth, M. Kyrolainen-Reay, R. B. Millington, and C. R. Lowe, "A holographic alcohol sensor," *Analytical Chemistry* **71**(16), pp. 3390–3396, 1999.

[152] A. J. Marshall, J. Blyth, C. A. B. Davidson, and C. R. Lowe, "pH sensitive holographic sensors," *Analytical Chemistry* **75**(17), pp. 4423–4431, 2003.

[153] G. Saxby, *Practical Holography*, Prentice Hall: Englewood Cliffs, NJ, 2nd ed., 1994.

[154] A. J. Marshall, D. S. Young, J. Blyth, S. Kabilan, and C. R. Lowe, "Metabolite-Sensitive Holographic Biosensors," *Analytical Chemistry* **76**(5), pp. 1518–1523, 2004.

[155] A. J. Marshall, S. Kabilan, J. Blyth, and C. R. Lowe, "Analyte-responsive holograms for (bio)chemical analysis," *Journal of Physics: Condensed Matter* **18**(18), pp. S619–S626, 2006.

[156] S. Kabilan, A. J. Marshall, F. K. Sartain, M.-C. Lee, A. Hussain, X. Yang, J. Blyth, N. Karangu, K. James, J. Zeng, D. Smith, A. Domschke, and C. R. Lowe, "Holographic glucose sensors," *Biosensors and Bioelectronics* **20**, pp. 1602–1610, 2005.

[157] A. Domschke, W. F. March, S. Kabilan, and C. R. Lowe, "Initial Clinical Testing of a Holographic Non-Invasive Contact Lens Glucose Sensor," *Diabetes Technology and Therapeutics* **8**(1), pp. 89–93, 2006.

[158] P. M. St. John, R. Davis, N. Cady, J. Czajka, C. A. Batt, and H. G. Craighead, "Diffraction-based cell detection using a microcontact printed antibody grating," *Analytical Chemistry* **70**(6), pp. 1108–1111, 1998.

[159] F. Yu, S. Tian, D. Yao, and W. Knoll, "Surface plasmon enhanced diffraction for label-free biosensing," *Analytical Chemistry* **76**(13), pp. 3530–3535, 2004.

[160] F. Yu and W. Knoll, "Immunosensor with self-referencing based on surface plasmon diffraction," *Analytical Chemistry* **76**(7), pp. 1971–1975, 2004.

[161] F. Yu, D. Yao, and W. Knoll, "Surface plasmon field-enhanced fluorescence spectroscopy studies of the interaction between an antibody and its surface-coupled antigen," *Analytical Chemistry* **75**(11), pp. 2610–2617, 2003.

[162] D. Neuschafer, W. Budach, C. Wanke, and S.-D. Chibout, "Evanescent resonator chips: a universal platform with superior sensitivity for fluorescence-based microarrays," *Biosensors and Bioelectronics* **18**, pp. 489–497, 2003.

[163] J.-L. Tang, S.-F. Cheng, W.-T. Hsu, T.-Y. Chiang, and L.-K. Chau, "Fiber-optic biochemical sensing with a colloidal gold-modified long period fiber grating," *Sensors and Actuators B* **119**, pp. 105–109, 2006.

[164] Y. Sarov, K. Ivanova, T. Ivanov, B. E. Volland, and I. W. Rangelow, "Micro-fluidic analysis based on total internal reflection," *Microelectronic Engineering* **83**, pp. 1294–1297, 2006.

[165] J. Voros, J. J. Ramsden, G. Csucs, I. Szendro, S. M. De Paul, M. Textor, and N. D. Spencer, "Optical grating coupler biosensors," *Biomaterials* **23**, pp. 3699–3710, 2002.

[166] J. Piehler, A. Brandenburg, A. Brecht, E. Wagner, and G. Gauglitz, "Characterisation of grating couplers for affinity-based pesticide sensing," *Applied Optics* **36**(25), pp. 6554–6562, 1997.

[167] N. Kim, I.-S. Park, and W.-Y. Kim, "Salmonella detection with a direct-binding optical grating couple immunosensor," *Sensors and Actuators B* **121**(2), pp. 606–615, 2007.

[168] D. Shin, B. Rezek, N. Tokuda, D. Takeuchi, H. Watanabe, T. Nakamura, T. Yamamoto, and C. E. Nebel, "Photo- and electrochemical bonding of DNA to single crystalline CVD diamond," *Physica Status Solidi A* **203**(13), pp. 3245–3272, 2006.

[169] S. Moses, S. H. Brewer, L. B. Lowe, S. E. Lappi, L. B. G. Gilvey, M. Sauthier, R. C. Tenent, D. L. Feldheim, and S. Franzen, "Characterization of Single- and Double-Stranded DNA on Gold Surfaces," *Langmuir* **20**(25), pp. 11134–11140, 2004.

[170] P. Gong, G. M. Harbers, and D. W. Grainger, "Multi-technique Comparison of Immobilized and Hybridized Oligonucleotide Surface Density on Commercial Amine-Reactive Microarray Slides," *Analytical Chemistry* **78**(7), pp. 2342–2351, 2006.

[171] M. R. Linford and C. E. D. Chidsey, "Alkyl monolayers covalently bonded to silicon surfaces," *Journal of the American Chemical Society* **115**(26), pp. 12631–12632, 1993.

[172] M. R. Linford, P. Fenter, P. M. Eisenberger, and C. E. D. Chidsey, "Alkyl Monolayers on Silicon Prepared from 1-Alkenes and Hydrogen-Terminated Silicon," *Journal of the American Chemical Society* **117**(11), pp. 3145–3155, 1995.

[173] J. Terry, M. R. Linford, C. Wirgen, R. Cao, P. Pianetta, and C. E. D. Chidsey, "Determination of the bonding of alkyl monolayers to the Si(111) surface using chemical-shift, scanned-energy photoelectron diffraction," *Applied Physics Letters* **71**(8), pp. 1056–1058, 1997.

[174] J. Terry, M. R. Linford, C. Wirgen, R. Cao, P. Pianetta, and C. E. D. Chidsey, "Alkyl-terminated Si(111) surfaces: A high-resolution, core level photoelectron spectroscopy study," *Journal of Applied Physics* **85**(1), pp. 213–221, 1999.

[175] A. B. Sieval, V. Vleeming, H. Zuilhof, and E. J. R. Sudholter, "An improved method for the preparation of organic monolayers of 1-alkenes on hydrogen-terminated silicon surfaces," *Langmuir* **15**(23), pp. 8288–8291, 1999.

[176] A. B. Sieval, A. L. Demirel, J. W. Nissink, M. R. Linford, J. H. van der Maas, W. H. de Jeu, H. Zuilhof, and E. J. R. Sudholter, "Highly stable Si-C linked functionalised monolayers on the silicon (1 0 0) surface," *Langmuir* **14**(7), pp. 1759–1768, 1998.

[177] A. B. Sieval, R. Opitz, H. P. A. Maas, M. G. Schoeman, G. Meijer, F. J. Vergeldt, H. Zuilhof, and E. J. R. Sudholter, "Monolayers of 1-alkynes on the H-terminated Si(100) surface," *Langmuir* **16**(26), pp. 10359–10368, 2000.

[178] R. L. Cicero, M. R. Linford, and C. E. D. Chidsey, "Photoreactivity of unsaturated compounds with hydrogen-terminated silicon(1 1 1)," *Langmuir* **16**(13), pp. 5688–5695, 2000.

[179] H. B. Yin, T. Brown, J. S. Wilkinson, R. W. Eason, and T. Melvin, "Submicron patterning of DNA oligonucleotides on silicon," *Nucleic Acids Research* **32**(14), p. e118, 2004.

[180] H. B. Yin, T. Brown, R. Greef, S. Malis, R. W. Eason, J. S. Wilkinson, and T. Melvin, "Photo-patterning of DNA oligonucleotides on silicon surfaces with micron-scale dimensions," **7**(5461-1), SPIE, 2004.

[181] The Brown Lab, Stanford University, *M Guide to microarraying.* Website: http://cmgm.stanford.edu/pbrown/mguide/index.html.

[182] T. Goldmann and J. S. Gonzalez, "DNA-printing: utilization of a standard inkjet printer for the transfer of nucleic acids to solid supports," *Journal of Biochemical and Biophysical Methods* **42**, pp. 105–110, 2000.

[183] L. R. Allain, M. Askari, D. L. Stokes, and T. Vo-Dinh, "Microarray sampling-platform fabrication using bubble-jet technology for a biochip system," *Fresenius Journal of Analytical Chemistry* **371**, pp. 146–150, 2001.

[184] R. Mukhopadhyay, M. Lorentzen, J. Kjems, and F. Besenbacher, "Nanomechanical sensing of DNA sequences using piezoresistive cantilevers," *Langmuir* **21**(18), pp. 8400–8408, 2005.

[185] T. Okamoto, T. Suzuki, and N. Yamamoto, "Microarray fabrication with covalent attachment of DNA using Bubble Jet technology," *Nature Biotech* **18**, pp. 438–441, 2000.

[186] J. L. DeRisi, V. R. Iyer, and P. O. Brown, "Exploring the metabolic and genetic control of gene expression on a genomic scale," *Science* **278**, pp. 680–686, 1997.

[187] G. MacBeath and S. L. Schreiber, "Printing proteins as microarrays for high-throughput function determination," *Science* **289**, pp. 1760–1763, 2000.

[188] G. M. Whitesides, E. Ostuni, S. Takayama, X. Jiang, and D. E. Ingber, "Soft lithography in biology and biochemistry," *Annual Review of Biomedical Engineering* **3**, pp. 335–373, 2001.

[189] B. Michel, A. Bernard, A. Bietsch, E. Delamarche, M. Geissler, D. Juncker, H. Kind, J. P. Renault, H. Rothuizen, H. Schmid, P. Schmidt-Winkel, R. Stutz, and H. Wolf, "Printing meets lithography: Soft approaches to high-resolution patterning," *IBM Journal of Research and Development* **45**(5), pp. 697–719, 2001.

[190] A. P. Quist, E. Pavlovic, and S. Oscarsson, "Recent advances in microcontact printing," *Analytical and Bioanalytical Chemistry* **381**(3), pp. 591–600, 2005.

[191] R. S. Kane, S. Takayama, E. Ostuni, D. E. Ingber, and G. M. Whitesides, "Patterning proteins and cells using soft lithography," *Biomaterials* **20**, pp. 2363–23–76, 1999.

[192] S. A. Lange, V. Benes, D. P. Kern, J. K. H. Horber, and A. Bernard, "Microcontact Printing of DNA Molecules," *Analytical Chemistry* **76**(6), pp. 1641–1647, 2004.

[193] K.-B. Lee, S.-J. Park, C. A. Mirkin, J. C. Smith, and M. Mrksich, "Protein nanoarrays generated by dip-pen nanolithography," *Science* **295**, pp. 1702–1705, 2002.

[194] C. A. Mirkin, "Invited contribution from recipient of ACS award in pure chemistry," *Inorganic Chemistry* **39**(11), pp. 2258–2272, 2000.

[195] S. Xu, S. Miller, P. E. Laibinis, and G.-y. Liu, "Fabrication of nanometer scale patterns within self-assembled monolayers by nanografting," *Langmuir* **15**(21), pp. 7244–7251, 1999.

[196] C.-H. Jang, B. D. Stevens, P. R. Carlier, M. A. Calter, and W. A. Ducker, "Immobilised enzymes as catalytically-active tools for nanofabrication," *Journal of the American Chemical Society* **124**(41), pp. 12114–12115, 2002.

[197] L. J. Guo, "Recent progress in nanoimprint technology and its applications," *Journal of Physics D: Applied Physics* **37**, pp. R123–R141, 2004.

[198] G. McGall, J. Labadie, P. Brock, G. Wallraff, T. Nguyen, and W. Hinsburg, "Light-directed synthesis of high-density oligonucleotide arrays using semiconductor photoresists," *Proceedings of the National Academy of Sciences, USA* **93**, pp. 13555–13560, 1996.

[199] A. Douvas, P. Argitis, K. Misiakos, D. Dimotikali, P. S. Petrou, and S. E. Kakabakos, "Biocompatible photolithographic process for the patterning of biomolecules," *Biosensors and Bioelectronics* **17**, pp. 269–278, 2002.

[200] D. Falconnet, A. Koenig, F. Assi, and M. Textor, "A combined photolithographic and molecular-assembly approach to produce functional micropatterns for applications in the biosciences," *Advanced Functional Materials* **14**(8), pp. 749–756, 2004.

[201] H. Sorribas, C. Padeste, and L. Tiefenauer, "Photolithographic generation of protein micropatterns for neuron culture applications," *Biomaterials* **23**, pp. 893–900, 2002.

[202] W. S. Dillmore, M. N. Yousaf, and M. Mrksich, "A photochemical method for patterning the immobilization of ligands and cells to self-assembled monolayers," *Langmuir* **20**(17), pp. 7223–7231, 2004.

[203] Z. Yang, W. Frey, T. Oliver, and A. Chilkoti, "Light-activated affinity micropatterning of proteins on self-assembled monolayers on gold," *Langmuir* **16**, pp. 1751–1758, 2000.

[204] R. Vaidya, L. M. Tender, G. Bradley, M. J. O'Brien II, M. Cone, and G. P. Lopez, "Computer-controlled laser ablation: A convenient and versatile tool for micropatterning biofunctional synthetic surfaces for applications in biosensing and tissue engineering," *Biotechnology Progress* **14**(3), pp. 371–377, 1998.

[205] A. Schwarz, J. S. Rossier, E. Roulet, N. Mermod, and M. A. Roberts, "Micropatterning of biomolecules on polymer substrates," *Langmuir* **14**(19), pp. 5526–5531, 1998.

[206] H. Thissen, J. P. Hayes, P. Kingshott, G. Johnson, E. C. Harvey, and H. J. Griesser, "Nanometer thickness laser ablation for spatial control of cell attachment," *Smart Materials and Structures* **11**, pp. 792–799, 2002.

[207] K.-N. Lee, D.-S. Shin, Y.-S. Lee, and Y.-K. Kim, "Protein patterning by virtual mask photolithography using a micromirror array," *Journal of Micromechanics and Microengineering* **13**, pp. 18–25, 2003.

[208] S. W. Han, I. Lee, and K. Kim, "Patterning of organic monolayers on silver via surface-induced photoreaction," *Langmuir* **18**(1), pp. 182–187, 2002.

[209] M. A. Holden, S.-Y. Jung, and P. S. Cremer, "Patterning enzymes inside microfluidic channels via photoattachment chemistry," *Analytical Chemistry* **76**(7), pp. 1838–1843, 2004.

[210] A. Revzin, R. G. Tompkins, and M. Toner, "Surface engineering with poly(ethylene glycol) photolithography to create high-density cell arrays on glass," *Langmuir* **19**(23), pp. 9855–9862, 2003.

[211] N. Dontha, W. B. Nowall, and W. G. Kuhr, "Generation of Biotin/Avidin/Enzyme nanostructures with maskless photolithography," *Analytical Chemistry* **69**(14), pp. 2619–2625, 1997.

[212] S. E. Rosenwald, W. B. Nowall, N. Dontha, and W. G. Kuhr, "Laser interference pattern ablation of a carbon fiber microelectrode: Biosensor signal enhancement after enzyme attachment," *Analytical Chemistry* **72**(20), pp. 4914–4920, 2000.

[213] N. Dontha, W. B. Nowall, and W. G. Kuhr, "Development of sub-micron patterned carbon electrodes for immunoassays," *Journal of Pharmaceutical and Biomedical Analysis* **19**, pp. 83–91, 1999.

[214] S. A. Brooks, W. P. Ambrose, and W. G. Kuhr, "Micrometer dimension derivitization of biosensor surfaces using confocal dynamic patterning," *Analytical Chemistry* **71**(13), pp. 2558–2563, 1999.

[215] M. Morita, T. Ohmi, E. Hasegawa, M. Kawakami, and M. Ohwada, "Growth of native oxide on a silicon surface," *Applied Physics Letters* **68**(3), pp. 1272–1281, 1990.

[216] G. B. Birrell, D. L. Habliston, K. K. Hedberg, and O. H. Griffith, "Silver-enhanced colloidal gold as a cell surface marker for photoelectron microscopy," *The Journal of Histrochemistry and Cytochemistry* **34**(3), pp. 339–345, 1986.

[217] J. I. Goldstein, *Scanning electron microscopy and X-ray microanalysis*, New York : Springer, 3rd ed., 2003.

[218] E. Hecht, *Optics*, Addison Wesley, 3rd ed., 1998.

[219] R. A. Serway, *Physics for Scientists and Engineers, with Modern Physics*, Saunders College Publishing, 4th ed., 1996.

[220] E. Palmer C, Loewen, *Diffraction Grating Handbook*, Thermo RGL, 2002.

[221] R. D. Gunther, *Modern Optics*, Wiley, 1990.

[222] P. A. Tipler, *Physics for Scientists and Engineers*, W. H. Freeman, 1998.

[223] H. Yin, J. A. Milton, T. Brown, Q. Xiao, J. S. Wilkinson, and T. Melvin, "Incorporation of PEG on silicon and nanoparticles: optimisation for biosensing and nanoparticle assembly," *currently unpublished results* .

[224] I. K. Pitcairn, P. E. Warwick, J. A. Milton, and D. A. H. Teagle, "Method for Ultra-Low-Level Analysis of Gold in Rocks," *Analytical Chemistry* **78**(4), pp. 1290–1295, 2006.

[225] R. W. Ditchburn, *Light*, Blackie & Son Ltd, 1966.

[226] D. P. Kalogianni, V. Bravou, T. K. Christopoulos, P. C. Ioannou, and N. C. Zoumbos, "Dry-reagent disposable dipstick test for visual screening of seven leukemia-related chromosomal translocations," *Nucleic Acids Research* **35**(4), p. e23, 2007.